HELIOSEISMOLOGY AND DIAGNOSTICS OF INTERNAL MAGNETIC LAYERS

Claire-Uriel Armelle Marie Aline Foullon

A Thesis Submitted for the Degree of PhD
at the
University of St Andrews

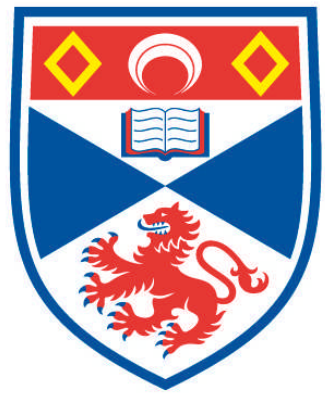

2002

HELIOSEISMOLOGY AND DIAGNOSTICS OF INTERNAL MAGNETIC LAYERS

By

Claire-Uriel Armelle Marie Aline

Foullon

Submitted in candidacy for the degree of

DOCTOR OF PHILOSOPHY

at

THE UNIVERSITY OF ST ANDREWS

SCOTLAND, U.K.

MARCH 2002

ProQuest LLC.
789 East Eisenhower Parkway
P.O. Box 1346
Ann Arbor, MI 48106 – 1346

Th E152

Claire-Uriel Armelle Marie Aline Foullon
Helioseismology and Diagnostics of Internal Magnetic Layers
Thesis directed by Professor Bernard Roberts

1. I, Claire-Uriel Armelle Marie Aline Foullon, hereby certify that this thesis, which is approximately 60,000 words in length, has been written by me, that it is a record of work carried out by me and that it has not been submitted in any previous application for a higher degree.
   date 15 March 2002 ...signature of candidate .....

2. I was admitted as a research student in September 1998 and as a candidate for the degree of Ph.D. in September 1999; the higher study for which this is a record was carried out in the University of St Andrews between 1998 and 2001.
   date 15 March 2002 ...signature of candidate .....

3. I hereby certify that the candidate has fulfilled the conditions of the Resolution and Regulations appropriate for the degree of Ph.D. in the University of St Andrews and that the candidate is qualified to submit this thesis in application for that degree.
   date 15 March 2002 ...signature of supervisor .....

4. In submitting this thesis to the University of St Andrews I understand that I am giving permission for it to be made available for use in accordance with the regulations of the University Library for the time being in force, subject to any copyright vested in the work not being affected thereby. I also understand that the title and abstract will be published, and that a copy of the work may be made and supplied to any *bona fide* library or research worker.
   date 15 March 2002 ...signature of candidate .....

Those men who lust for land
And for riches strange and new
Who love those trinkets of desire
Oh they never will have you

And they'll never know the gold
Or the copper in your hair
How could they weigh the worth
Of you so rare

Suzanne Vega, "World Before Columbus" (1996)

Table of Contents

Foreword

The paths I was given to explore when I started my doctoral research seemed all well trodden, like touristic roads in a country I was visiting for the first time. In the early days of the journey I undertook, no sign in the mathematical modelling of the solar interior could let me forebode that I was going to make discoveries of my own. This source of personal inspiration was something that I could connect with music and which helped me to appreciate both the physics and the mathematics of my models, and finally gave me the energy to go through.

My inspiration was rooted deep in the childhood, at a time when, at every school break, I would practice the recorder on the edge of the playground. Undoubtedly my mother, who gave me the instrument, paved the way, not only to my inclination to learn and play clarinet, but also to my fascination for the analogy I discovered with the seismology of the Sun. However, to arrive at the stage of doctoral research, it was her courage who inspired my determination. She gave me strength and perseverance and I thank her the most for that.

To challenge my research and my career, I have been working away from my home country, France, isolated from my maternal language mainly in Scotland and lately in Flanders. In meeting different people in the scientific community, it helped me to define my interests. I am thankful to these scientists, who at different moments instructed me and regarded me with respect or friendship. The object was not necessary related to my thesis. But it motivated me to share ideas in a field and a community I was hoping to belong to. This was particularly true of Valery Nakariakov, David Berghmans and Craig DeForest, who helped me with writing a proposal on an alternative project, which was combining theory and observations. I have learnt much from them and from this experience.

Erwin Verwichte is more than a scientist to me. So, although I omitted to acknowledge him as such, he is the person who helped me the best he could throughout the years, with me or away from me. He pushed me to debate about my work, giving me thereby a springboard to develop ideas and to become critical about them.

Conferences were particularly helpful to discuss with other scientists in the field. Meeting and discussing with Jœrgen Christensen-Daalsgaard and Mike J. Thompson

proved to be the most gratifying and inspiring moments I have had during conferences. I also appreciated the advice by phone or email of a number of scientists, who I have not met yet, like Bill Chaplin for shedding light on the frequency shift observations and Brad Hindman for sending me his numerical code computing confluent hypergeometric functions; thanks also to Jim Pintar and Sean McManus, who were very helpful in giving me access to data obtained by the Global Oscillation Network Group (GONG) project.

Moreover, through short visits in Belgium, I met with Petra Vanlommel and Vladimir Čadež, who had common interests on a close subject and whose advice was much needed and appreciated. Once I arrived for good at the *CPA* in Leuven, it was a windfall to be given some feedback, especially by Arnold Debossher and Jesse Andries. In other respects, I felt immediately 'adopted' by everyone, and it has been a pleasure to work in such friendly atmosphere for nearly one year (from December 2000 to September 2001). Such beneficial changes for my work and my moral became possible thanks to Thomas Neukirch, who I consider like a wizard who gladly opened his network *PLATON* to me, and to Marcel Goossens, who, warmly and equally gladly, opened to me the doors of his group *CPA*.

Still St Andrews will be remembered as a place where I met also very friendly people, among my colleagues and other students, and whose presence enlightened my stay there. I found much technical assistance within the group of applied mathematics and also I wish to thank Michael Ruderman and Alan Hood for their scientific interest, their advice and kindness. Finally this adventure was fastened to Bernie Roberts, who gave me the opportunity to start on the track left by his previous students William R. Campbell and Mark Daniell. I acknowledge him beyond the scope of this thesis, for I have certainly gained an understanding of his work that might influence and serve me in the future. Along the road, his investment in getting me some funding was also very much appreciated.

Globally over those three years of research, from September 1998 up to October 2001 where I started on a new position at the Royal Observatory of Belgium, funding was provided by the University of St Andrews (6.3%), the School of Mathematics and Statistics (11.6%), myself (25%), *PPARC* (28.6%) and the European Research Training Network *PLATON*, grant No. HPRN-CT-2000-00153 (34.1%).

I keep particular warm regards to Piotr Tucholka, my teacher in Geophysics at the University Paris XI in Orsay, not only for promoting my application to *PPARC*, but especially for acting as my academic home-beacon to navigate abroad. I am also ever grateful to my family who helped me to fix up the ship: my grand-parents, my sister, my uncle Arthaud and his family, Jacques, my godmother Armelle and among their sons, Alain, Yves, Bernard and spouses.

Abstract

Solar magnetic fields, as well as temperature changes, introduce pressure deviations that play a significant role in modulating the resonant frequencies of p-mode oscillations. Those pressure deviations occurring in the atmosphere or sub-surface of the Sun can explain the frequency shifts observed on the timescale of the solar activity cycle. A separate study of the contribution of internal magnetic layers can clarify the relative importance of surface effects.

Results from helioseismology provide realistic constraints for choosing parameters suitable to represent the magnetic layers buried in the solar interior and available for modelling, *i.e.* at the base of the convection zone and in the sunspots' anchoring zone. Diagnostics of the internal magnetic layers are obtained through a schematic model in which the Sun is plane-stratified. The influence of a buried magnetic field on p-modes is explored, and the nature of various waves and instabilities that can arise on such a buried magnetic field is assessed.

By treating the effects of internal magnetic layers, this thesis contributes to the building of a bridge between theories and observations. On the one hand, the theoretical analysis is explored carefully in the course of its formulation, which generates new hypotheses that were not obvious so far. On the other hand, observations help to understand which explanations of the solar cycle frequency shifts may apply.

Part I

INTRODUCTION

Chapter 1

Conditions for Infrasonic Waves in the Sun

This thesis addresses on theoretical grounds certain aspects of the subject of helioseismology, with the view to gain analytical insights and thereby explain some dynamical phenomena reported by observations. This first introductory chapter will in turn evoke essentials of helioseismology (Section 1.1), expose the mathematical formulation which will serve the purposes of this thesis (Section 1.2), and finally describe the Sun's equilibrium structure about which the dynamics takes place (Section 1.3).

1.1 Introduction to helioseismology

1. Rhythmic motions

Helioseismology started with the detection of rhythmic motions on the Sun's surface, the photosphere. Discovered in the early 1960's by R. Leighton and co-workers (Leighton et al., 1962), the solar oscillations were shown in the early 70's to result from pressure waves that echo and resonate through the Sun's interior (Ulrich, 1970; Leibacher and Stein, 1971). The Sun is made of quasi-neutral assemblies of charged particles. This state of matter, called a plasma, is the most common in the universe and exhibits properties of the collection of particles and of fluid. Because pressure provides the restoring force for the solar oscillations, they are known as p-modes, a terminology

introduced by T. G. Cowling in 1941.

Below the photospheric surface, the medium is alternatively compressed and rarefied along the direction of travel. On reaching the surface the waves cause the plasma to move up and down, resulting in changes in the wavelengths of spectral lines in the emitted light; the waves alternately compress and rarefy the surface plasma, changing its temperature and therefore its brightness (the intensity of blackbody emission is proportional to the fourth power of temperature). Acoustic waves have subtle effects: they typically cause the photosphere to rise and fall by less than 25 metres and to change temperature by just 0.005 K (Lang, 1996). The maximum velocity amplitude of a single mode is about $20\,\mathrm{cm\,s^{-1}}$, whereas the luminosity amplitudes are of order of one micromagnitude or less. Nevertheless these oscillations can be detected from tiny, periodic Doppler shifts in a well-defined spectral line (shifts that result from velocity changes of just centimetres per second) or from minuscule but regular variations in the Sun's total light output (*e.g.*, Leibacher et al., 1985; Harvey, 1995; Lang, 1996, Christensen-Dalsgaard, 1998).

Ordinary acoustic cavities, such as an organ pipe or a kettledrum, are regions of space bounded by walls that trap acoustic waves by reflecting them repeatedly. The interior of the Sun has no such walls but nonetheless has gradients of density and temperature that can reflect or refract acoustic waves. As soon as it was understood that the solar interior could act as an acoustic cavity, the analogy between solar p-modes and sound waves in an organ pipe was made (*e.g.*, Leibacher et al., 1985; Christensen-Dalsgaard et al., 1985). In a pipe, those acoustic waves with the correct wavelength characteristics are able to reinforce one another and form standing wave patterns, just as it exists for particular wavelengths in clamped strings. Similarly, the Sun vibrates like a pipe or a drum, sustaining various kinds of resonant modes of oscillation, which can be detected through their effects near the solar surface. At any given instant, the pattern of an individual mode over the solar surface is one of alternating regions of opposite sign (*e.g.*, approaching or receding flows, or higher or lower pressures/temperatures...). Constructive interference takes place between waves which find themselves in phase. The wave is reinforced and a resonance at a characteristic frequency and wavenumber

is observed.

The propagation of pressure variations through a medium such as air is particularly important when pressure changes can be detected by the auditory apparatus of the ear. The human ear produces the physiological sensation of hearing if the frequency of pressure variations is in the range from 15 Hz to about 20,000 Hz. Waves that produce such a response are called sound waves. If the frequency of a sound wave is below 15 Hz, it is called an 'infrasonic' wave. In general, an object's structure, including its size, dictates which notes, or eigenfrequencies, are generated. As far as size is concerned, the bigger a pipe, the lower the note it produces. On Earth, infrasonic waves can be generated by motions of large scale matter, such as those produced by earthquakes and volcanic activity. Intuitively the dominant oscillation frequencies on the Sun are infrasonic. A power spectrum of the solar oscillations reveals that power is concentrated around the 3.3 mHz (5 minute) wave band and extends from about 1.2 mHz to frequencies as high as 10 mHz (see Figure 1.1)[1]. Thus solar sound waves have very low frequencies with corresponding periods from minutes to hours (for reference, the fundamental radial period for the Sun is approximately one hour); human ears hear sound wave periods of milliseconds.

2. Dimension

Besides the size, one main difference between a pipe and the Sun is the dimension in which oscillations take place. Waves in an homogeneous medium obey the relation

$$\omega = ck\,, \tag{1.1}$$

connecting angular frequency ω and horizontal wavenumber k; c is the phase velocity of the wave. This implies a disturbance with wavelength $\lambda(= 2\pi/k)$. If the motion of the wave occurs in three dimensions, resolved into vertical (z) and horizontal (h) directions (*i.e.* respectively a radial direction and a direction tangent to the solar surface), then

$$\omega^2 = c^2(k_z^2 + k_h^2)\,, \tag{1.2}$$

[1]Figure 1.1 is available from World Wide Web: http://sohowww.nascom.nasa.gov/gallery/MDI/, courtesy of SOHO/MDI consortium. SOHO is a project of international cooperation between ESA and NASA.

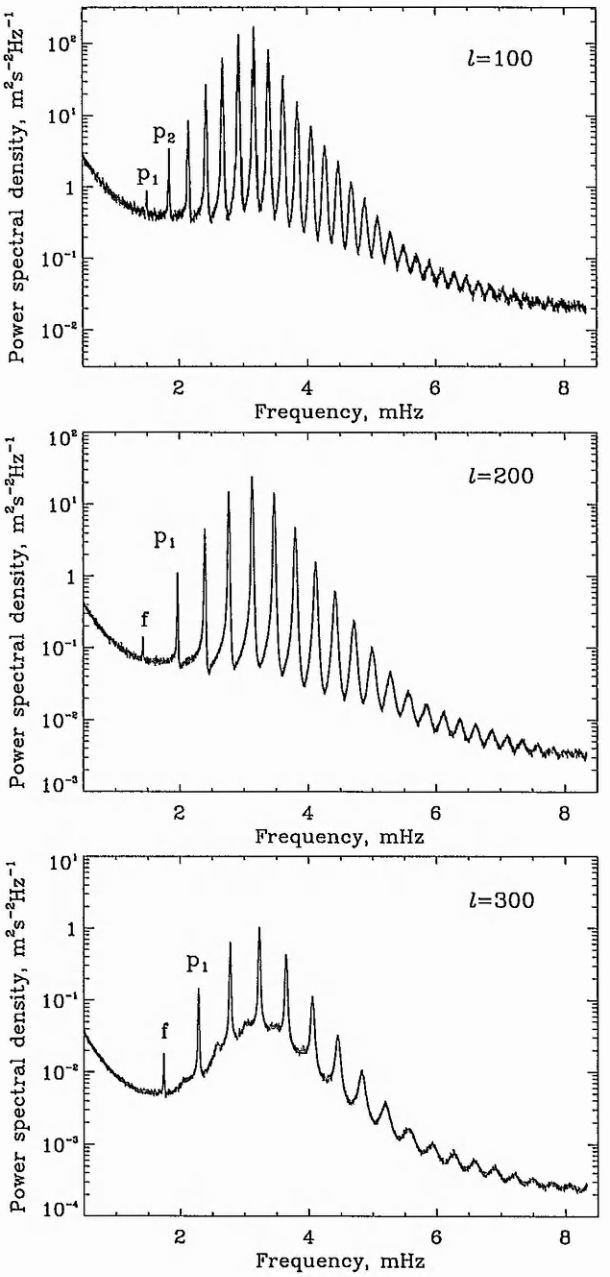

Figure 1.1: Power spectra vertical slices at degree l = 100, 200, and 300, obtained from 2 months of the SOHO/MDI Medium-l program during May/June 1996. The photospheric counterparts of the whole Sun's acoustic vibrations appear at precise frequencies, visible as sharp peaks in this spectrum, mainly around 3 mHz, corresponding to periods of about 5 min. The spectrum is dominated by the p-mode band up to the cut-off frequency ($\sim$ 5.3 mHz). Above this frequency a mode-like structure appears, corresponding to the so-called pseudo-modes or High Interference Peaks (HIPs). This has been explained by considering partial wave reflection from the atmosphere. Note the asymmetry at low frequency. Models of the upper reflection layer show similar asymmetry. The spacing of the peaks at high frequency indicates that the source of the acoustic modes is about 50 km below the photosphere.

with the wavenumbers k_z and k_h applying in their respective directions.

The spherical geometry of the Sun leads to three-dimensional standing wave patterns. They are described by spherical harmonics involving integers l, n, m. The quantisation in l is due to spherical geometry; l and k_h are related by (see, *e.g.*, Christensen-Dalsgaard, 1998)

$$k_h = \frac{\sqrt{l(l+1)}}{\mathrm{R}_\odot}, \tag{1.3}$$

where $\mathrm{R}_\odot \approx 6.96 \times 10^8$ m is the solar radius. Waves travel around, undergoing multiple reflections at their upper turning point in the photosphere. The separation between successive reflections is $2\pi\,\mathrm{R}_\odot/L$ with $L = \sqrt{l(l+1)}$, and so L is roughly the number of horizontal wavelengths along the solar circumference. This separation decreases with the horizontal wavelength as the degree l of the mode increases. In other words, modes with higher l are confined close to the solar surface.

The harmonic degree l represents the number of border lines by which the solar surface is divided by oscillations in opposite phase. On the other hand, the harmonic degree m gives information about departures of the Sun from spherical symmetry, caused for example by rotation. For a spherical oscillator, the angular component of the wave function is described by the spherical harmonics $Y_{lm}(\theta, \phi)$ of the co-latitude θ and the azimuth angle or longitude ϕ of the spherical polar coordinate, characterised by the degree l and azimuthal-order m. The spherical harmonic Y_l^m may be defined as

$$Y_l^m(\theta, \phi) = N_{lm} P_l^{|m|}(\cos\theta) e^{im\phi}, \tag{1.4}$$

where $P_l^{|m|}(x)$ denotes the associated Legendre polynomial of degree l $(= 0, 1, 2, \ldots)$ and order m $(= -l, -l+1, \ldots, 0, \ldots, l-1, l)$ and N_{lm} is a normalisation constant (see, *e.g.*, Christensen-Dalsgaard, 1998). The azimuthal order m is the number of roots of $\cos(m\phi) = 0$ in the region $0 \leq \phi < \pi$, *i.e.* the number of nodal lines that intersect the equator. Table 1.1 shows how modes are labelled according to their degree l and azimuthal order m. The spherical harmonics are depicted in Figure 1.2.

Typically acoustic modes are evident in spectrograms of the solar disk and in measurements of surface brightness. Imaged helioseismic observations are especially valuable because the surface patterns may be directly decomposed into spherical harmonic

l	m	type of modes	l nodal lines of the spherical harmonics
$l = 0$	$m = 0$	radial	no lines
$l > 0$	$m = 0$	zonal	l lines of latitude
$l > 0$	$0 < m < l$	tesseral	$l - m$ lines of latitude and m lines of longitude
$l > 0$	$m = l$	sectoral	$l = m$ lines of longitude

Table 1.1: Classification of modes according to the degree l and azimuthal order m.

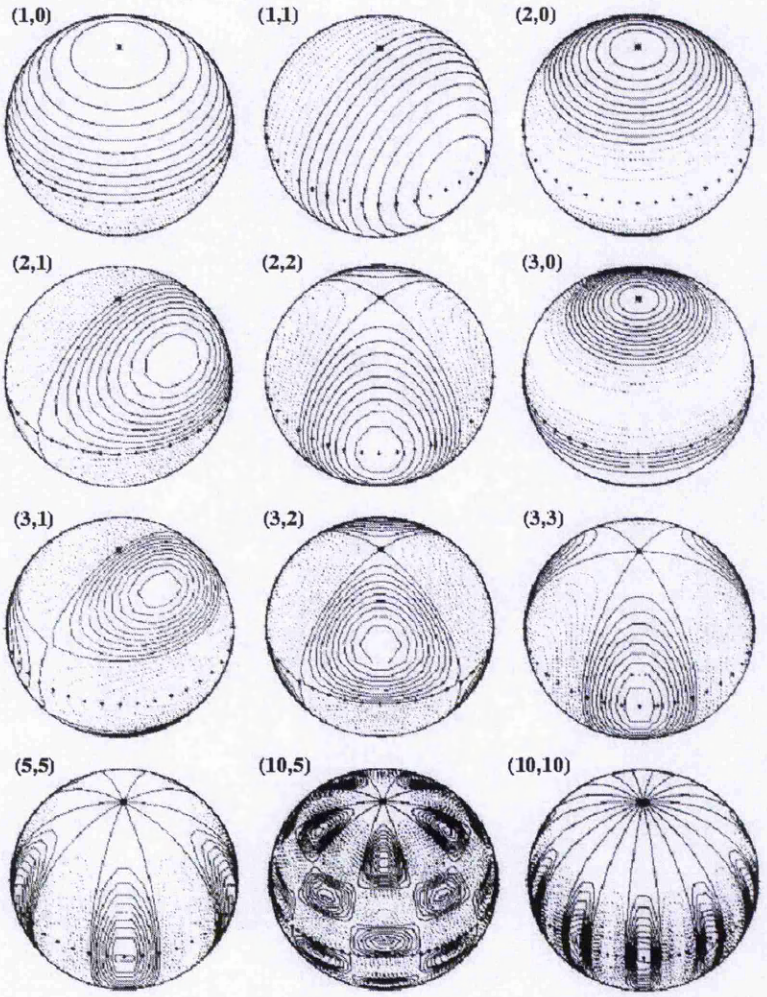

Figure 1.2: Contour plots of the real part of spherical harmonics Y_l^m, for the set of degrees (l, m) as indicated in each case. Positive contours are indicated by continuous lines and negative contours by dashed lines. The $\theta = 0$ axis has been inclined by 45 degrees towards the viewer. Adapted from Christensen-Dalsgaard, 1998.

coefficients, whose frequency spectrum may then be computed. The number of pixels across the diameter of the solar disk is roughly equal to the maximum value of l that observations can detect. Conditions in the deepest part of the Sun are probed by the lowest l's and thus require the least resolution. Besides, the oscillation patterns of high degree modes are so small that their contributions to the integrated sunlight over the whole disk cancel each other out. Therefore, whole disk measurements are sensitive only to modes with low degrees such as $l \approx 0 \sim 4$. By using a lens to average the Sun's image in a direction perpendicular to its rotation axis, one can eliminate high-angular-order spherical harmonics to leave mainly zonal harmonics with $m = 0$. Averaging the Sun's image in a direction parallel to the rotation axis, in contrast, leaves mainly information on sectoral ($\|m\| = l$) modes (Duvall and Harvey, 1984).

3. Quantisation

The wave nature of oscillations is clearly seen from the distribution of spectral power densities. To a first approximation, the Sun may be considered spherically symmetrical, ignoring its rotation. Then the azimuthal order m is taken to be zero. In the so-called diagnostic diagram, in which observed powers are shown as function of angular degree l and cyclic frequency ν (see Figure 1.3), the maximum of power lies on approximately parabolic ridges that designate the radial overtones n of the modes. In all cases the mode multiplet frequency ν_{nl} increases with l at fixed n, forming a ridge of radial order n. Broadly speaking, while l measures the horizontal component of the wavenumber, n measures the vertical component and corresponds to the number of nodal lines along a radius of the sphere.

The problem in three dimensions can be approached in one or two dimensions if it is reduced to limiting forms. In the most simple form, one-dimensional propagation in an isothermal pipe has eigenfunctions which are trigonometric functions. The multiple reflections, with harmonics in l, were first interpreted (Kahn, 1961; 1962) as the result from trapping of acoustic waves in the temperature minimum of the photosphere, either by way of ray theory or by considering the photosphere as a waveguide, which channels the mode energy horizontally, due to a temperature minimum in that layer. The ray

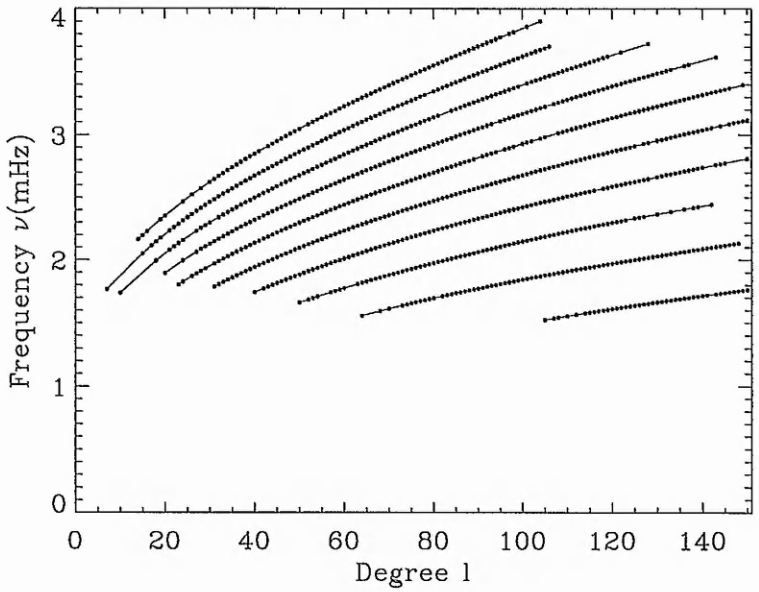

Figure 1.3: Distribution of spectral power densities, from month 50 of GONG data (see Appendix A.2). In a (l,ν) diagnostic diagram, the maximum of power lies on approximately parabolic ridges, each labelled by the radial order n, increasing with frequency, of a p-mode.

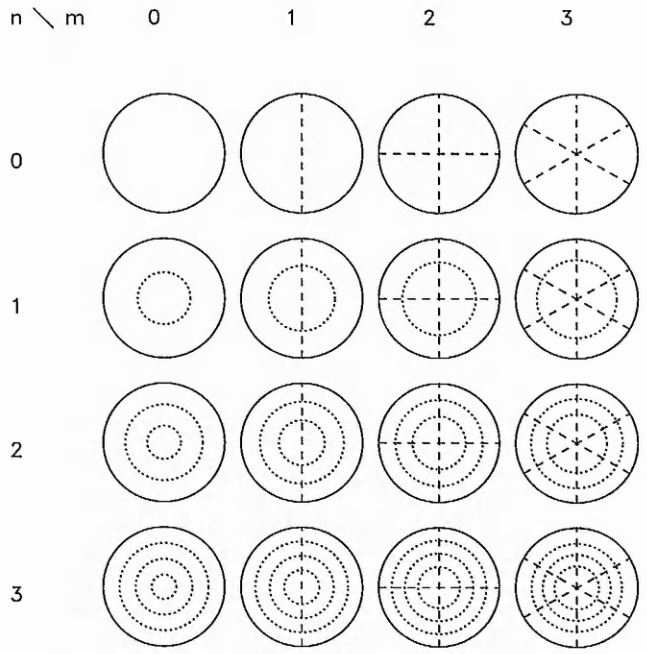

Figure 1.4: The node lines for individual resonant modes of a drum skin, which may be regarded as an equatorial cross-section of the Sun (see Figure 1.2); the azimuthal node lines (dashed) are numbered with m, the radial circular node lines (dotted) with n. After Pijpers, 2001.

theory involves trigonometric functions (Kahn, 1961), while the wave treatment involves parabolic cylinder functions (Kahn, 1962).

With $l = m$, the three-dimensional problem is reduced to an equatorial cross-section of the Sun and the quantisation in n and m is similar to the solutions of a (two-dimensional) drumskin. Figure 1.4 shows the node lines for individual resonant modes of a drum skin. These figures are called Chladni patterns in honour of 18th century physicist Ernest Chladni, who observed nodal lines on the surface of plates covered with a thin layer of sand vibrating. The acoustics of drums is described for instance by Fletcher and Rossing (1991) or Rossing (1992); the analogy between the drum skin and stellar oscillations was illustrated in particular by Pijpers (2001), from which Figure 1.4 is inspired. With $m = 0$, the problem can be reduced for $l \neq 0$ to the adiabatic acoustic oscillations of an isothermal sphere, as discussed by Lord Rayleigh in 1896 (see Gough, 1990a), or for $l = 0$ to vertical propagation in a plane-parallel polytrope (Lamb, 1909). What characterises a polytrope, as compared to the isothermal medium, is a temperature stratification. The inclusion of a temperature stratification in a one-dimension geometry plays the role of the second dimension for the isothermal propagation in a sphere. As a consequence, all the above models — drumskin, isothermal sphere, vertical propagation in an atmosphere — have in common that the harmonics in n, and possibly l or m, are obtained via Bessel functions.

Finally, for non-vertical propagation ($l \neq 0$) and in a spherically symmetric Sun ($m = 0$), a plane-parallel polytrope turns out to be a convenient model to describe the quantisation of the modes in n, as did Lamb (1932) for the Earth's atmosphere. This model is able to reproduce approximately the parabolic ridges observed in Figure 1.3. In this case, with the addition of another degree of freedom, the eigenfunctions are expressed in terms of the confluent hypergeometric functions. This possibility to describe the quantisation of the modes in l and n will be explored further in this thesis.

4. Learning about our star and the others

A star oscillates 'radially' (*cf.* Table 1.1) around its equilibrium figure, by expanding and contracting. As shown by H. Shapley in 1914, the period of such motion scales

approximately as $1/\sqrt{\bar{\rho}}$ where $\bar{\rho}$ is the mean density of the star. Moreover, as realised by R. Emden in 1907, the star oscillates 'non-radially' when deviating from its spherical shape. While a single mode provides a measure of the mean density of a star, two periods allow determination of its radius (*i.e.* its size) and therefore of its mass. Each mode that can be detected is an independent measure of the structure of the star. Hence the amount of information about the star grows with the number of modes that can be detected. Although the phenomenon of stellar pulsations has been known since 1784 (according to Harvey, 1995), the idea of using nonradial pulsations to probe stellar interiors was introduced in 1951 by P. Ledoux, who initiated the domain of asteroseismology. A detailed historical survey is given by Christensen-Dalsgaard (1998). Asteroseismology initially concentrated on stars with large amplitudes in luminosity variations, such as the Cepheids and the long period variables. But when observations from space accurately detected as many as 10^7 individual modes on the Sun (Christensen-Dalsgaard et al., 1985; Gough and Toomre, 1991), helioseismology developed at a frantic pace.

In fact, the science of helioseismology has grown rapidly, standing on the heritage of the theory of atmospheric oscillations (P. S. Laplace and H. Lamb, respectively in the beginning of the 19th and 20th century), hydrodynamics of oceans (Eckart, 1960) and a variety of methods developed by geophysicists, as quoted by Deubner and Gough (1984). Of the Sun's interior, what compares with the Earth's atmosphere, oceans and interior is its stratification in temperature and density. Pekeris perhaps personifies this understanding: famous for his work (in 1948) on the propagation of waves in the ocean, he may be also mentioned for his publications on nonradial oscillations of stars (Pekeris, 1938) as well as the propagation of a pulse in the Earth's atmosphere (Pekeris, 1948). One can view the physical processes involved in the same way that seismologists learn about the Earth's interior by monitoring waves caused by earthquakes. Temperature, composition, and motions deep in the Sun influence the oscillation periods and yield insights into conditions in the solar interior. Through imaging their internal structure, differential rotation and large-scale circulations, asteroseismology and helioseismology revolutionises the understanding of the interior and the surface of stars. Ultimately

these sciences address the reason why and how stars pulsate and nourish the topic of stellar evolution, with pulsation spectra distinguishing between different types of stars through their masses and ages (*e.g.*, Brown and Gilliland, 1994; Favata et al., 2000).

The purpose of helioseismology or asteroseismology is very similar to attempting to determine the shape and construction of a musical instrument from the sounds it makes. What will be remarkable and compelling in this thesis is to approach helioseismology through an elementary understanding of the resonance in a pipe. An ideal pipe has properties of an isothermal waveguide, which result from the combination of two states of matter, one gas and one solid: the ambient air (where the sound waves propagate) and a solid rigid tube tunnelling the sound waves towards the end. Resonance can only occur at particular frequencies, which depend upon conditions in the material of the pipe and the ambient temperature. Similarly, the pitch of the resonance for the Sun depends on the physical conditions in its interior where the sound waves travel. How it organises itself, its internal structure, may be first approached by considering the Sun as a perfect gaseous sphere. The mathematical formulation introduced in Section 1.2 will pave the way to understand later on how the characteristic frequencies are prescribed by the internal structure of the plasma.

1.2 Mathematical formulation

In this thesis, the derivation of the equations will be based on a number of assumptions, which permit progress in the mathematical analysis. A plasma will be considered as a conducting fluid without specifying its various individual species. In this single fluid approximation, each macroscopic variable is formed by adding the contributions of the various particle species in the plasma.

1. Perfect gas

The pressure arises from transfer of momentum by particles and photons. The total pressure P is therefore divided into the gas and radiation pressures. The latter is smaller than about a thousandth of the total pressure everywhere below the solar surface; at the centre of the Sun, it accounts for only 0.05% of the total pressure (*cf.*, *e.g.*, Goedbloed and Poedts, 1997). It is thus reasonable to identify the total pressure to the gas pressure p. In the interior of the Sun, where hydrogen and helium are fully ionised, the perfect gas law provides an adequate equation of state:

$$p = \frac{R}{\tilde{\mu}}\rho T, \tag{1.5}$$

where R is the gas constant ($R = 8.3145\mathrm{JK}^{-1}\,\mathrm{mol}^{-1}$) and $\tilde{\mu}$ is the mean molecular weight. Hence the temperature T could replace ρ and p, *viz.*

$$T = \frac{\tilde{\mu}}{R}\frac{p}{\rho} = \frac{p}{Nk_B}, \tag{1.6}$$

where $k_B = m_H R$ is the Boltzmann constant and $N = \rho/(\tilde{\mu}m_H)$ is the number density of particles, with m_H the mass of the hydrogen atom. Other thermodynamical variables such as q, the internal energy per unit mass, and the entropy s per unit mass are defined by the ideal gas relations:

$$q = \frac{1}{\gamma - 1}\frac{p}{\rho} = \frac{R}{(\gamma - 1)\tilde{\mu}}T, \tag{1.7}$$

$$s = C_v \ln(p\rho^{-\gamma}) + \mathrm{const}, \tag{1.8}$$

where $\gamma = C_p/C_v$ is the ratio of specific heats at constant pressure and volume, respectively.

The ratio of specific heats For a perfect gas (for which $C_p - C_v = R$), the ratio of specific heats γ is also function of the degree of freedom f. For a complete degenerate gas (no temperature dependence), the non-relativistic state[2] gives $C_v = \frac{1}{2} f R \,\mathrm{mol}^{-1}$. Therefore

$$\gamma = \frac{C_p}{C_v} = \frac{C_v + R}{C_v} = \frac{f+2}{f}. \tag{1.9}$$

Hence, for $f = 3$ degrees of freedom in a non-relativistic gas, the ratio of specific heats $\gamma = 5/3$.

The mean molecular weight $\tilde{\mu}$ measures the average weight of the constituents particles in units of m_H. For ionised hydrogen, $\tilde{\mu} = 1/2$ (1 unit m_H divided by 2 particles: proton p and electron e); for ionised helium $\tilde{\mu} = 4/3$ (4 units m_H divided by 3 particles: particle α and 2 e); and for the heavier completely ionised atoms, $\tilde{\mu} \approx 2$ (approximately $2Z_c$ units m_H divided by $Z_c + 1$ particles: 1 ion and Z_c e, where Z_c is the charge number). For a mixture of these gases (see, for example, Goedbloed and Poedts, 1997)

$$\tilde{\mu} \approx \left(2X + \frac{3}{4}Y + \frac{Z}{2}\right)^{-1}, \tag{1.10}$$

where X is the mass fraction of hydrogen, Y is the mass fraction of helium, and Z is the mass fraction of heavier elements. Hence $\tilde{\mu}$ is a function of position reflecting the abundance of different elements in the Sun and their degrees of ionisation.

2. Ideal MHD equations

Using simplified forms of the transport equations (conservation of mass, momentum, and energy) and Maxwell's electromagnetic equations, the so-called magnetohydrodynamic (MHD) theory is created. MHD is a model system designed to treat the macroscopic dynamics of an electrically neutral fluid, which is nevertheless made up of moving charged particles, and hence reacts to electric and magnetic fields. The derivation of the MHD equations is discussed in many publications and lecture notes (*e.g.*, Priest, 1982; Goedbloed, 1983; Scott, 1994; Goedbloed and Poedts, 1997; Hood, 1998; Goossens, 2001).

[2]The relativistic state gives $C_v = f R \,\mathrm{mol}^{-1}$.

The system of equations of ideal MHD consists of

1. the equation of mass continuity

$$\frac{D\rho}{Dt} + \rho\nabla \cdot \mathbf{V} = 0\,; \tag{1.11}$$

2. the momentum equation

$$\rho\frac{D\mathbf{V}}{Dt} = -\nabla p + \rho\mathbf{g} + \mathbf{j} \times \mathbf{B}\,; \tag{1.12}$$

3. an adiabatic energy equation

$$\frac{Dp}{Dt} = \frac{\gamma p}{\rho}\frac{D\rho}{Dt}\,; \tag{1.13}$$

4. and an induction equation

$$\frac{\partial \mathbf{B}}{\partial t} = \nabla \times (\mathbf{V} \times \mathbf{B})\,. \tag{1.14}$$

p and ρ retain the meanings given to them earlier, and $\mathbf{V}$, $\mathbf{g}$, $\mathbf{B}$ are respectively the velocity field, gravitational field and magnetic induction, usually referred as magnetic field. The current density $\mathbf{j}$ is given by Ampère's law

$$\mu\mathbf{j} = \nabla \times \mathbf{B}\,, \tag{1.15}$$

where μ is the magnetic permeability ($\mu = 4\pi \times 10^{-7}\,\mathrm{H\,m^{-1}}$); the advective derivative is denoted by

$$\frac{D}{Dt} \equiv \frac{\partial}{\partial t} + \mathbf{V} \cdot \nabla\,. \tag{1.16}$$

Finally, the magnetic field is governed by the solenoid constraint

$$\nabla \cdot \mathbf{B} = 0\,. \tag{1.17}$$

The momentum equation as given in Equation (1.12) is effectively Newton's equation of motion for a fluid element, which expresses the acceleration of a fluid element as caused by the pressure gradient, gravity and differs from Euler's momentum equation in the addition of the Lorentz force, which couples the fluid equations to the electromagnetic equations. It assumes here, in particular, no viscous effects.

The gravitational acceleration satisfies Poisson's equation

$$\nabla \cdot \mathbf{g} = \nabla^2 \Phi = -4\pi G\rho\,, \tag{1.18}$$

for the gravitational potential Φ, and where G is the gravitational constant ($G \approx 6.6726 \times 10^{-11}\,\mathrm{m^3\,s^{-2}\,kg^{-1}}$).

In obtaining this ideal set of MHD equations, drastic simplifications were made possible by applying non-viscous, non-dissipative and adiabatic approximations.

3. Perturbations

Advection Equations (1.11)-(1.13) contain the advective or Lagrangian time derivative, $\frac{D}{Dt}$. The significance of this derivative as opposed to the partial derivative $\frac{\partial}{\partial t}$ deserves comment. From a mathematical point of view, the advective derivative of a function $F(\mathbf{r}(t), t)$, where $\mathbf{r}$ denotes the position vector to a given point in space at a time t, is the total derivative of F:

$$\frac{dF}{dt} = \frac{\partial F}{\partial t} + \frac{d\mathbf{r}}{dt}\frac{\partial F}{\partial \mathbf{r}} = \frac{\partial F}{\partial t} + \mathbf{V} \cdot \nabla F = \frac{DF}{Dt}\,. \tag{1.19}$$

Physically, the partial derivative and the total (advective) derivative describe, each in a different way, how F evolves with time. Any quantity such as velocity, density, temperature, *etc.*, may be ascribed either to a bit of plasma or to the point that is momentarily occupied by that bit of plasma. Each conception has its way of expressing a perturbation. The description which corresponds to what is seen by a stationary observer is known as the Eulerian description. The description of an observer who follows the motion of fluid elements from given initial positions is the Lagrangian description.

The Eulerian form, denoted by a hat, is defined as a perturbation of a physical quantity at a given position $\mathbf{r}(t)$:

$$F(\mathbf{r}, t) = F_o(\mathbf{r}) + \hat{F}(\mathbf{r}, t)\,. \tag{1.20}$$

The Lagrangian form, denoted by a symbol δ, is defined by that for a given fluid element at the given position $\mathbf{r}$, but from an original position $\mathbf{r_o} = \mathbf{r}(t_o)$:

$$F(\mathbf{r}, t) = F_o(\mathbf{r_o}) + \delta F(\mathbf{r_o}, t)\,. \tag{1.21}$$

Here, the subscript o indicates that the reference frame is the unperturbed configuration.

Thus, the Lagrangian displacement ξ of a fluid parcel is a transformation of coordinates, as a function of time, from old (undisturbed, initial) to new coordinates, in

$$\mathbf{r}(\mathbf{r_o}, \mathbf{t}) = \mathbf{r_o} + \xi(\mathbf{r_o}, \mathbf{t}) ; \tag{1.22}$$

this also represents a flow $\mathbf{V} = \frac{\partial \xi}{\partial t}$ that is determined by the ideal MHD equations.

To the first order in displacement ξ,

$$F(\mathbf{r}, t) = F(\mathbf{r_o}, t) + \xi \cdot \nabla F_o(\mathbf{r}) . \tag{1.23}$$

After applying the Eulerian description (1.20) to the first term on the right-hand side of (1.23),

$$F(\mathbf{r}, t) = F_o(\mathbf{r_o}) + \hat{F}(\mathbf{r_o}, t) + \xi \cdot \nabla F_o(\mathbf{r}) , \tag{1.24}$$

the relation between the Lagrangian and Eulerian perturbations emerges:

$$\delta F(\mathbf{r}, t) = \hat{F}(\mathbf{r}, t) + \xi \cdot \nabla F_o(\mathbf{r}) . \tag{1.25}$$

The corresponding time variations are denoted by $\frac{D\delta F(\mathbf{r},t)}{Dt}$ and $\frac{\partial \hat{F}(\mathbf{r},t)}{\partial t}$ (Unno et al., 1989). The partial derivative of Equation (1.25) with respect to time leads back to the form of the advective derivative (1.16)

$$\frac{D\delta F}{Dt} = \frac{\partial \hat{F}}{\partial t} + \mathbf{V} \cdot \nabla F . \tag{1.26}$$

Applying the relation (1.25) to the velocity $\mathbf{V}$ and developing $\delta V = \frac{D\xi}{Dt}$, one obtains

$$\begin{aligned} \hat{V} &= \delta V - \xi \cdot \nabla \mathbf{V_o} \\ &= \frac{\partial \xi}{\partial t} + \mathbf{V_o} \cdot \nabla \xi - \xi \cdot \nabla \mathbf{V_o} \\ &= \frac{\partial \xi}{\partial t} - \mathbf{V_o} \times (\nabla \times \xi) . \end{aligned} \tag{1.27}$$

For a spherically symmetric Sun without rotation nor circulation, $\mathbf{V_o} = \mathbf{0}$. Then the expression (1.27) shows the equivalence of the Lagrangian and Eulerian velocities, and in addition that $\hat{V} = \frac{\partial \xi}{\partial t}$.

Adiabatic energy equation In the adiabatic approximation, energy losses or gains are ignored. Considering adiabatic processes means that the entropy s (see Equation (1.8)) convected by the fluid is constant:

$$\frac{Ds}{Dt} = 0 \qquad \text{or} \qquad \frac{D}{Dt}(p\rho^{-\gamma}) = 0\,, \tag{1.28}$$

yielding the form (1.13) of adiabatic energy equation. In terms of variable q (or T), the adiabatic energy equation (1.13) combined with the equation of mass continuity (1.11) yields the internal energy equation

$$\frac{Dq}{Dt} + (\gamma - 1)q\nabla \cdot \mathbf{V} = 0\,, \tag{1.29}$$

or

$$\rho\frac{Dq}{Dt} + p\nabla \cdot \mathbf{V} = 0\,. \tag{1.30}$$

Compressibility One important illustration of advection is the equation of mass continuity (1.11), which expresses the rate of change of density following the motion. This typical conservation equation springs from the Eulerian form, balancing the rate of change of density in a volume with the flux of the density into the volume:

$$\frac{\partial\rho}{\partial t} = -\nabla \cdot (\rho\mathbf{V})\,. \tag{1.31}$$

The amount of mass converted into energy over the entire lifetime of the star is less than 0.007 the total mass of the nuclear burning regions of the star and thus can be ignored. Also, in current standard solar models, mass loss from winds is usually not included, because the loss is negligible ($10^{-14}\,M_\odot$/year, according to Cassinelli and MacGregor, 1986) when compared to the total mass. The total mass and the mass in any given layer is, therefore, assumed to be constant during the evolution of the Sun. Substantial mass loss, of the order of several tenths of a solar mass, occurs much later in the life of the solar-type star (Guenther and Demarque, 1996).

Since $\rho = \frac{1}{\mathcal{V}}$, where $\mathcal{V}$ is the volume of unit mass, an alternative formulation of Equation (1.11) for the mass conservation is

$$\frac{1}{\mathcal{V}}\frac{D\mathcal{V}}{Dt} = \nabla \cdot \mathbf{V}\,, \tag{1.32}$$

showing that $\nabla \cdot \mathbf{V}$ is the rate of expansion of a given volume of gas, when following the motion. A plasma, like any other state of matter, whether gas, liquid or solid, exhibits some change in volume when subjected to a compressive stress. Hence $\nabla \cdot \mathbf{V}$ is usually called the compressibility, and denoted Δ. The degree of compressibility is measured by a bulk modulus of elasticity, E, defined as either

$$E = \frac{\delta p}{\delta \rho / \rho}, \qquad \text{or} \qquad E = \frac{\delta p}{-\delta \mathcal{V} / \mathcal{V}}, \qquad \text{that is} \qquad E = \frac{\delta p}{-\Delta}, \tag{1.33}$$

where δp is a Lagrangian change (see Equation (1.25)) in pressure and $\delta \rho$ or $\delta \mathcal{V}$ is the corresponding change in density or specific volume. The bulk modulus (or coefficient) of elasticity indicates the extent to which increasing pressure within the medium decreases the volume.

Fluids have elasticity (compressibility) and inertia (mass density), two characteristics required for wave phenomena in a spatially distributed physical system whose elements are coupled. Elasticity implies that any deviation from the equilibrium state of the fluid will tend to be corrected; inertia implies that the correction will tend to overshoot, producing the need for a correction in the opposite direction and hence allowing for the possibility of propagating phenomena — acoustic pressure waves. The speed of sound c in a medium depends on the medium's modulus of elasticity E and its density ρ according to the relationship

$$c = \sqrt{\frac{E}{\rho}} = \sqrt{\frac{\delta p}{\delta \rho}}. \tag{1.34}$$

Hence, by inserting the adiabatic energy equation (1.13), one can define the adiabatic sound speed c_s by

$$c_s = \sqrt{\frac{\gamma p}{\rho}}. \tag{1.35}$$

The sound speed is closely related to the temperature and, for a perfect gas, the adiabatic sound speed is given by

$$c_s^2 = \frac{\gamma R}{\tilde{\mu}} T. \tag{1.36}$$

Moreover, note from Equation (1.34) that $E = \rho c^2$. In the Sun's interior, as for liquids and solids, E is typically very large so that density and volume changes are generally very small, unless exceptionally large pressures are applied.

By the perfect gas law (1.5), the changes in pressure, density and temperature are related by

$$\frac{\delta p}{p} = \frac{\delta \rho}{\rho} + \frac{\delta T}{T}, \tag{1.37}$$

where changes in $\tilde{\mu}$ have been neglected. In the adiabatic approximation, this corresponds to

$$\frac{\delta p}{p} = \frac{\delta \rho}{\rho} + \frac{\delta [c_s^2]}{c_s^2}. \tag{1.38}$$

1.3 The Sun's equilibrium

The power source for the Sun and stars remained a mystery until the discovery of thermonuclear reactions (see the historical notes from Guenther and Demarque, 1996). The Sun's energy is generated in the core ($r \leq 0.25\,\mathrm{R}_\odot$) by thermonuclear fusion, which converts hydrogen into helium. The dependence (1.6) of pressure p on the mean molecular weight $\tilde{\mu}$ (Equation (1.10)) implies that the pressure drops when hydrogen is converted into helium. The Sun's energy diffuses slowly outward (a photon takes some hundreds of thousand years to travel from the core to the surface) in the radiative zone ($0.25\,\mathrm{R}_\odot \leq r \leq 0.713\,\mathrm{R}_\odot$), by means of atomic absorption and emission; the radiative transport is exceeded by convection in the convection zone, where the energy is carried out to the photosphere by rising and falling eddies of plasma (*e.g.*, Goedbloed and Poedts, 1997).

The distributions of the physical variables in the equilibrium state or in the unperturbed configuration are denoted by a subscript o. They are the background distributions about which the dynamics is supposed to take place. Adopting the hat notation to denote the amplitudes of the perturbations, the basic quantities are expressed as:

$p = p_o + \hat{p}$ pressure

$\rho = \rho_o + \hat{\rho}$ density

$\mathbf{B} = \mathbf{B_o} + \hat{\mathbf{B}}$ magnetic field

$\mathbf{V} = \mathbf{V_o} + \hat{\mathbf{V}}$ velocity field

$\mathbf{g} = \mathbf{g_o} + \hat{\mathbf{g}}$ gravitational field .

The dynamical timescale of the Sun is approximately one hour (the dynamical timescale is essentially $(G\bar{\rho})^{-1/2}$ where $\bar{\rho}$ is the mean density and G is the gravitational constant; see, *e.g.*, Christensen-Dalsgaard, 1998). Hence, during the Sun's 4.5 Gyr evolution, it has had ample time to establish a stationary equilibrium. A plasma is in stationary equilibrium if it does not change in time, *viz.*

$$\frac{\partial}{\partial t} \equiv 0\,. \tag{1.39}$$

Simple but fundamental laws, which govern the background distributions of the solar interior, are derived in this section. They are relations of adiabatic equilibria, ex-

pressions obtained by assuming a spherically symmetric stratification, and relations of radiative and convective equilibria. Ultimately, one can obtain the criterion for convective stability and, by introducing polytropic stratifications, one can model the solar interior in terms of linear temperature profiles, close to those given by the internal seismic structure of the Sun.

1. Adiabatic equilibria

Steady conditions Under the steady conditions ($\frac{\partial}{\partial t} = 0$), the advective derivative (1.16) is given by

$$\frac{D}{Dt} \equiv \mathbf{V_o} \cdot \nabla . \tag{1.40}$$

The equation of mass continuity (1.11) becomes

$$\nabla \cdot (\rho_o \mathbf{V_o}) = 0 , \tag{1.41}$$

the momentum equation (1.12) gives

$$\rho \mathbf{V_o} \cdot \nabla \mathbf{V_o} = -\nabla p_o + \rho_o \mathbf{g_o} + \mathbf{j} \times \mathbf{B_o} , \tag{1.42}$$

where the Lorentz force is deduced from Ampère's law (1.15), *viz.*

$$\begin{aligned} \mathbf{j} \times \mathbf{B_o} &= \frac{\nabla \times \mathbf{B_o}}{\mu} \times \mathbf{B_o} \\ &= \frac{1}{\mu}(\mathbf{B_o} \cdot \nabla)\mathbf{B_o} - \frac{1}{\mu}\nabla(\frac{B_o^2}{2}) . \end{aligned} \tag{1.43}$$

The Lorentz force is directed perpendicular to the magnetic field and is formed of two contributions: a magnetic tension force and a magnetic pressure force.

The adiabatic energy equation (1.13) reduces to

$$\mathbf{V_o} \cdot \nabla p_o = -\gamma p_o \nabla \cdot \mathbf{V_o} , \tag{1.44}$$

and the induction equation (1.14) becomes

$$\nabla \times (\mathbf{V_o} \times \mathbf{B_o}) = \mathbf{0} , \tag{1.45}$$

with the solenoid constraint

$$\nabla \cdot \mathbf{B_o} = 0 . \tag{1.46}$$

Static equilibrium In addition to the stationary condition (1.39), a plasma is in static equilibrium if

$$\mathbf{V_o} = \mathbf{0}\,. \tag{1.47}$$

Under these conditions the advective derivative

$$\frac{D}{Dt} \equiv 0\,, \tag{1.48}$$

and $\mathbf{V_o} = 0$ in the distributions (1.41)-(1.45). This time, the equation of mass continuity (1.11), the adiabatic energy equation (1.13) and the induction equation (1.14) reduce to zero. However, the momentum equation (1.12) gives the equation for a magnetostatic equilibrium, *viz.*

$$\begin{aligned} 0 &= -\nabla p_o + \rho_o \mathbf{g_o} + \mathbf{j} \times \mathbf{B_o} \\ &= -\nabla p_o + \frac{1}{\mu}\nabla(\frac{B_o^2}{2}) + \rho_o \mathbf{g_o} - \frac{1}{\mu}(\mathbf{B_o} \cdot \nabla)\mathbf{B_o}\,, \end{aligned} \tag{1.49}$$

and with the solenoid constraint as in Equation (1.46).

2. Spherically symmetric stratification

Nearly all stellar evolutionary calculations are calibrated with respect to the standard solar model. The standard solar model is derived from the conservation laws and energy transport equations, applied to a spherically symmetric gas (plasma) sphere and constrained by the luminosity, radius, age and composition of the Sun. The standard solar model is used as a test case for the stellar evolution calculation because the luminosity, radius, age and composition of the Sun are well determined. The total radiation energy output of the Sun, the solar luminosity, is $\mathrm{L}_\odot = 3.86 \times 10^{26}$ W. At the Earth, *i.e.* at a distance of 1 AU ($= 1.5 \times 10^{11}$ m), this results in a heat flux of $\mathrm{L}_\odot/[4\pi \times (1\mathrm{AU})^2] = 1.36\mathrm{kW\,m^{-2}}$, the so-called solar constant (*e.g.*, Goedbloed and Poedts, 1997).

A number of important phenomena occurring in the solar interior may be described. In the standard solar model the physics is simplified by assuming a spherically symmetric Sun: the total pressure P, the density ρ and the other physical variables are function of the radius r only. Magnetism is ignored. Furthermore, the medium is

stratified: plasma properties are structured by the competition of the outward pressure force and the inward gravitational attraction.

Temperature gradients The adiabatic sound speed is given by

$$c_s^2(r) = \frac{\gamma p_o(r)}{\rho_o(r)} = \gamma \frac{R}{\tilde{\mu}} T_o(r)\,. \tag{1.50}$$

In consequence, the sound speed gradient is related to the temperature gradient. The fundamental relation

$$-\frac{dT_o}{dr} = T_o \left(\frac{1}{\rho_o}\frac{d\rho_o}{dr} - \frac{1}{p_o}\frac{dp_o}{dr} \right) \tag{1.51}$$

follows from the equation of state (1.6), taking $\tilde{\mu}$ to be a constant.

Combining Equations (1.50) and (1.51) leads to

$$[c_s^2]' = c_s^2 \left(\frac{1}{H_P} - \frac{1}{H_\rho} \right), \tag{1.52}$$

where H_P and H_ρ are respectively the pressure and density scale-heights, defined through

$$H_P = \frac{p_o}{p_o'}, \qquad \text{and} \qquad H_\rho = \frac{\rho_o}{\rho_o'}, \tag{1.53}$$

and where the prime denotes the spatial derivative. Equation (1.52) is rewritten as the fundamental adiabatic relation

$$\frac{1}{H_P} = \frac{1}{H_\rho} + \frac{[c_s^2]'}{c_s^2}\,. \tag{1.54}$$

This relation shows, for basic quantities with gradients of same sign in the solar interior, that the pressure varies on a scale ($H_P \sim 150\,\mathrm{km}$) always shorter than both the density scale-height ($H_\rho \sim 350\,\mathrm{km}$) and the temperature scale-height, which is represented by the last term ($\frac{c_s^2}{[c_s^2]'} \sim 250\,\mathrm{km}$).

The sound speed or temperature structure of the solar interior has an effect on oscillation frequencies. In an isothermal medium, all acoustic waves propagate at the same velocity, regardless of their frequency or wavelength. Here, the frequencies of the solar oscillations are predominantly determined by the value of the local sound speed within the Sun's interior.

Density stratification The Sun is stratified under gravity. As part of an attempt to determine the surface temperature of the Sun, J. H. Lane wrote down, for the first time in 1869, the set of equations describing a gas sphere in hydrostatic equilibrium (see, *e.g.*, Guenther and Demarque, 1996; Goedbloed and Poedts, 1997),

$$\nabla p_o = \rho_o \mathbf{g_o} \,. \tag{1.55}$$

For the spherically symmetric Sun, the gas configuration in gravitational equilibrium satisfies

$$-\frac{dp_o(r)}{dr} = g_o \rho_o(r) \,, \tag{1.56}$$

where $g_o = \frac{GM(r)}{r^2}$ is the gravitational attraction due to the mass $M(r)$ enclosed inside a spherical surface of radius r.

The equilibrium relation (1.56) modifies the form (1.51) of the equation of state to the fundamental relation

$$-\frac{dT_o}{dr} = T_o \left(\frac{1}{\rho_o} \frac{d\rho_o}{dr} + \frac{\rho_o g_o}{p_o} \right) . \tag{1.57}$$

Alternatively, the pressure scale height becomes

$$H_P = \frac{c_s^2}{\gamma g_o} = \frac{R}{\tilde{\mu}} \frac{T_o}{g_o} \,, \tag{1.58}$$

and the spatial derivative of c_s^2 in Equation (1.52) is

$$[c_s^2]' = \gamma g_o \left(1 - \frac{H_P}{H_\rho} \right) . \tag{1.59}$$

3. Radiative and convective equilibria

Radiative equilibrium J. H. Lane is also credited with constructing the first physical model of the solar interior. In 1926, following the development of atomic physics and the first calculations of absorption coefficients, A. S. Eddington improved Lane's stellar models by including a description of the transport of energy by radiation. Significantly, Eddington discovered that the only way he could produce a solar model with the correct luminosity was to assume that the Sun (and presumably all stars) was composed primarily of ionised hydrogen (Guenther and Demarque, 1996).

The radiative equilibrium model can predict the static equilibrium distributions of the different variables characterising the interior of the Sun. To formulate this equilibrium, the internal energy equation (1.30) is modified to include radiative terms (see, *e.g.*, Goedbloed and Poedts, 1997; Christensen-Dalsgaard, 1998):

$$\rho\frac{Dq}{Dt} + p\Delta = -\nabla\cdot\mathbf{F} + \rho q\,; \tag{1.60}$$

$\mathbf{F} = -\lambda\nabla\mathbf{T}$ is the energy flux with thermal conduction coefficient (or conductivity) $\lambda(r)$.

In static equilibrium, the left-hand side of Equation (1.60) vanishes, so that

$$\nabla\cdot\mathbf{F_o} = \rho_o q_o\,. \tag{1.61}$$

In stellar interiors, radiation is the only significant contributor to $\mathbf{F_o}$, so that Equation (1.61) expresses a radiative equilibrium: the thermonuclear energy is transported outward by radiative transfer. By analysing the relationship of this differential equation for the temperature with the fundamental quantities of radiative transport (luminosity, radiation pressure and opacity κ, *i.e.* the absorption coefficient of the radiation per unit mass and per unit length), λ_o turns out to be related to κ through

$$\lambda_o = \frac{16\sigma}{3}\frac{T_o^3}{\kappa\rho_o}\,, \tag{1.62}$$

where $\sigma = 5.67\times10^{-8}\mathrm{W\ m^{-2}K^{-4}}$ is the Stefan-Boltzmann constant. The opacity is a microscopic quantity determined by quite a number of different processes between photons and atoms, ions, or electrons, averaged over frequency.

The standard solar model is obtained from the two second order differential equations (1.56) and (1.61) for the temperature T_o, supplemented with numerical tables of $\tilde{\mu}$, κ and q_o, and appropriate boundary conditions. This provides realistic solutions, except for the assumption of static equilibrium up to the solar surface.

Convective equilibrium Turbulent gas motions in the convection zone provide a very efficient transport of energy. The conditions for static equilibrium are violated in the convective region so that one should perhaps return to the steady conditions (1.41)-(1.44) (neglecting the magnetic field), where the flow also destroys the spherical

symmetry of the problem. However, one can define a convective equilibrium. This concept was first introduced in geophysics by Lord Kelvin in 1861, and was later codified in the stellar context by R. Emden in 1907 (Guenther and Demarque, 1996). Motions of the gas are neutrally stable with respect to convective instability if s, the value of the entropy per unit mass (1.28), is constant throughout the pertinent region of space:

$$p_o \rho_o^{-\gamma} = \text{const} \qquad \text{that is} \qquad \frac{dp_o}{dr} = \frac{\gamma p_o}{\rho_o} \left(\frac{d\rho_o}{dr} \right)_{ad}, \tag{1.63}$$

which can be rewritten as

$$\frac{p_o'}{p_o} = \gamma \frac{\rho_o'}{\rho_o}, \qquad \text{that is} \qquad \frac{1}{H_P} = \gamma \frac{1}{H_\rho}. \tag{1.64}$$

Yet, the steady and convective equilibria do concur on local scales for up or down moving eddies, where the flow $\mathbf{V_o}$ is parallel to the spherically symmetric gradients of pressure and density. With this restriction, the steady condition (1.44) from the adiabatic energy equation

$$\mathbf{V_o} \cdot \nabla p_o = \frac{\gamma p_o}{\rho_o} \mathbf{V_o} \cdot \nabla \rho_o \tag{1.65}$$

leads to the convective equilibrium (1.63).

4. Convective stability

Suppose an elementary parcel of fluid is displaced vertically, so slowly that it remains in horizontal pressure equilibrium with its surroundings. Combining the fundamental relation (1.51) with the convective equilibrium (1.63), one obtains an expression for the value of the associated temperature gradient for which the plasma can move adiabatically, *viz.*

$$-\left(\frac{dT_o}{dr} \right)_{ad} = -T_o \frac{\gamma - 1}{\gamma} \frac{1}{p_o} \frac{dp_o}{dr}. \tag{1.66}$$

Alternatively, this corresponds to

$$[c_s^2]_{ad}' = \frac{\gamma - 1}{\gamma} \frac{c_s^2}{H_P}. \tag{1.67}$$

Inserting the pressure gradient from the hydrostatic equilibrium (1.56), one finds

$$-\left(\frac{dT_o}{dr} \right)_{ad} = T_o \frac{\gamma - 1}{\gamma} \frac{\rho_o g_o}{p_o}, \tag{1.68}$$

or alternatively,

$$[c_s^2]'_{ad} = (\gamma - 1)g_o \,. \tag{1.69}$$

Hence convective instability occurs when the actual temperature gradient, $-\frac{dT_o}{dr}$, exceeds $-\left(\frac{dT_o}{dr}\right)_{ad}$, *i.e.* when the Schwarzschild (1958) criterion for convective stability, *viz.*

$$-\frac{dT_o}{dr} \leq -\left(\frac{dT_o}{dr}\right)_{ad}, \tag{1.70}$$

is violated. This is the case in the so-called convective region, where turbulent flow carries eddies of hot material up and cool material down, so as to maintain the temperature gradient close to the value given by Equation (1.68).

The Brunt-Väisälä frequency (or buoyancy frequency), defined either by

$$\omega_g^2 = \frac{g_o}{T_o}\left[\frac{dT_o}{dr} - \left(\frac{dT_o}{dr}\right)_{ad}\right], \qquad \text{or} \qquad \omega_g^2 = \frac{g_o}{\rho_o}\left[-\frac{d\rho_o}{dr} + \left(\frac{d\rho_o}{dr}\right)_{ad}\right], \tag{1.71}$$

is a measure of the stability. This corresponds to

$$\omega_g^2 = -\frac{g_o}{\rho_o}\frac{d\rho_o}{dr} - \frac{\rho_o g_o^2}{\gamma p_o}\,. \tag{1.72}$$

In terms of density scale-height and adiabatic sound speed, this corresponds to

$$\omega_g^2 = g_o\left(\frac{1}{H_\rho} - \frac{g_o}{c_s^2}\right). \tag{1.73}$$

The first term in between brackets represents the amount of work to move a blob of fluid vertically; the second term accounts for the compressibility of the fluid.

In Section 5.1, the convective stability will be generalised in the presence of a horizontal magnetic field.

5. Temperature profiles and seismic structure of the Sun

Changes in temperatures and elemental composition in the Sun affect the speed with which pressure waves travel. Thanks to the p-mode oscillations observed at the surface, helioseismology (see, *e.g.*, Gough and Toomre, 1991, for a review on the inversion techniques) provides information about these factors in the radial and latitudinal directions of the Sun, notwithstanding the presence of magnetic fields and circulation processes. In this respect, helioseismology succeeds in probing the internal seismic structure of

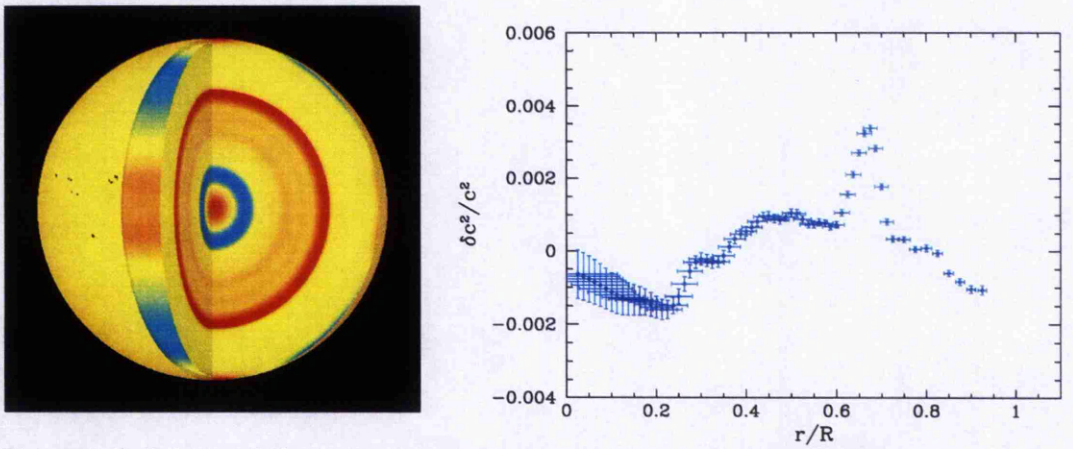

Figure 1.5: Relative differences between the squared sound speed in the Sun and in a standard solar model. (*a*) Radial and latitudinal variations; red colour corresponds to the positive variations ('hotter' regions), and blue colour corresponds to negative variations ('cooler' regions). (*b*) Radial variations; the horizontal bars show the spatial resolution, and the vertical bars are the error estimates. From Kosovichev et al., 1997. Available from World Wide Web: http://soi.stanford.edu/results/sspeed.html, courtesy of SOHO/SOI/MDI consortium. SOHO is a project of international cooperation between ESA and NASA.

the Sun as seen effectively by waves at a given period. In neglecting the magnetic field, the model of the Sun is over-simplified, but this assumption has the advantage of leading to the description of a mean spherical model, the so-called standard model, to which the solar structure inferred by helioseismic observations may be compared. Under this assumption, the solar structure is known at the level of 10^{-3} departures from the standard model, as illustrated by Figure 1.5.

A useful parameter to model the field-free convective and radiative zones is the 'polytropic' index defined as

$$m = \frac{c_s^2}{(c_s^2)'}\frac{\rho_o'}{\rho_o} = \frac{c_s^2}{(c_s^2)'}\frac{1}{H_\rho}\,. \tag{1.74}$$

m increases with the central condensation. If $m = 0$, the density is uniform. The limit $m \to \infty$ may correspond to an incompressible gas or an isothermal medium.

In combining Equation (1.74) to the fundamental relation for the hydrostatic equilibrium (1.59), one obtains

$$[c_s^2]' = \frac{\gamma g_o}{m+1}\,. \tag{1.75}$$

In the convective equilibrium (1.63),

$$p_o \propto \rho_o^\gamma\,. \tag{1.76}$$

Comparing the expression (1.75) with the adiabatic gradient (1.69), a temperature profile that is marginally stable to convective motions requires the condition that

$$m = \frac{1}{\gamma - 1} \qquad \text{or} \qquad \gamma = \frac{m+1}{m}. \tag{1.77}$$

If A is this adiabatic gradient, then

$$A = [c_s^2]'_{ad} = \frac{g_o}{m}. \tag{1.78}$$

Conditions with polytropic indices of smaller value than that given by the above adiabatic convective equilibrium would become unstable.

From Equations (1.76) and (1.77), the pressure distribution in convective equilibrium obeys

$$p_o \propto \rho_o^{\frac{m+1}{m}}, \tag{1.79}$$

or in terms of scale-heights,

$$\frac{1}{H_P} = \frac{m+1}{m}\frac{1}{H_\rho}. \tag{1.80}$$

Note that for constant g_o and within a defined region of constant ratio of specific heats γ, *i.e.* of constant adiabatic polytropic index m, the adiabatic temperature profile is linear. This is especially true for the value $\gamma = 5/3$, giving $m = 3/2$.

When the temperature gradient required to transport all the energy by radiation exceeds the adiabatic temperature gradient, the layer is unstable to convection and the material physically transports the energy outwards. Because convection is very efficient at transporting energy, it is reasonable to assume a temperature gradient A_c in the convection zone, which is not smaller than the adiabatic gradient, *i.e.* only slightly 'superadiabatic'. This is not true near the surface, where cooling is so strong that the absolute value of the temperature gradient exceeds the value given by the Schwarzschild criterion for convective stability. The real temperature gradients in this thin outer layer are significantly steeper than the adiabatic temperature gradient. The density is low enough that radiative transport must be taken into account. Apart from this region near the surface, where a substantial superadiabatic gradient is required to drive the convective flux, the bulk of the convection zone has a fairly simple structure and the condition of an adiabatic temperature gradient is quite accurately satisfied.

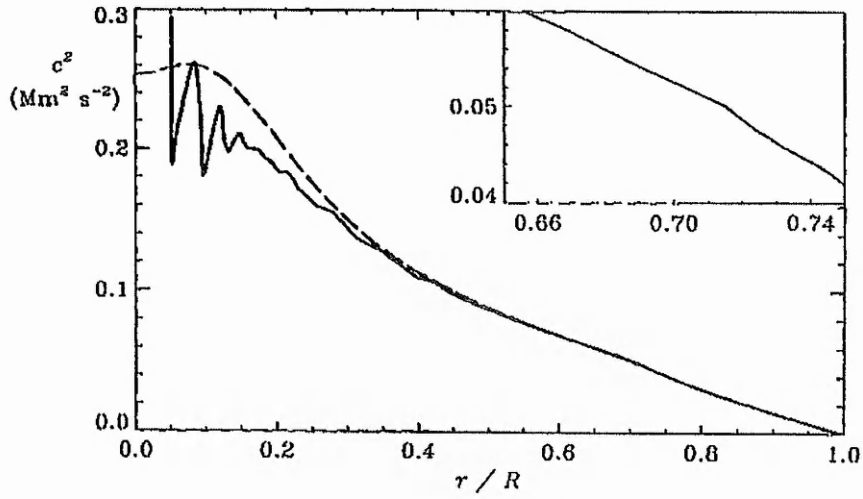

Figure 1.6: Profile of the sound speed squared in the Sun, as inferred from helioseismology by Christensen-Dalsgaard et al. (1985) (solid curve); the dashed curve shows the sound speed squared in a standard solar model for comparison. The inset shows in greater detail the inferred sound speed near the base of the convection zone. Figure in Christensen-Dalsgaard et al. (1991).

The base of the convective envelope is at $0.713 \pm 0.003\,R_\odot$ with a temperature in the range $2.15 - 2.30 \times 10^6 K$ (Christensen-Dalsgaard et al., 1991). It is usually assumed that at the base of the convection zone, the temperature gradient changes continuously between an adiabatic to a radiative 'subadiabatic' stratification with a discontinuous derivative. The sound speed gradient is closely related to the temperature gradient, due to Equation (1.50). Thus this transition from an adiabatic temperature gradient within the convection zone to a subadiabatic gradient beneath it is visible as a clear break in the gradient of the sound speed as inferred by Christensen-Dalsgaard et al. (1985), as can be seen in Figure 1.6.

Chapter 2

Dynamics of the Solar Interior

The standard model of the Sun, constrained by its seismic structure, is a reference equilibrium figure of our star. The symmetry breaking physics of magnetic fields, circulation, and rotation, in particular, are neglected in the standard model because they increase the complexity of the problem enormously and are generally not believed to affect the structure and evolution of the model by very much. Yet helioseismology is able to add a dynamic picture of the Sun's internal structure. This dynamics is especially demonstrated by the observation of variations in pressure perturbations which evolve in time and space. Specific aspects of the solar dynamics allow the development of a theoretical model, the background motivations for which are introduced in Section 2.1. In Section 2.2 these motivations are placed in context: observational results are reviewed briefly and this is followed by the basic theoretical processes proposed to explain them; further specific properties and physical justifications needed for modelling are also presented.

2.1 Premise to theoretical modelling

1. The connection between solar magnetic fields and solar p-modes

As with any astrophysical plasma, the Sun is threaded by magnetic fields, whose distribution may be measured not only in the solar atmosphere, but also in the sub-surface layers of the Sun through local helioseismology. In the photosphere, magnetic fields

are not smoothly distributed but are instead highly concentrated, inhomogeneous and everywhere clumped together into intense bundles — the sunspots — that cover only a few percent of the photosphere's surface area. This geometrically complex distribution does not simplify higher up in the chromosphere and the corona. On the contrary, the chromosphere is jagged and irregular, and the Sun's magnetism plays an important role in shaping, molding and heating the coronal gas.

Magnetic fields manifest themselves on the Sun with a regularity not fully understood. The 11-year cyclic variation of magnetic activity, first suggested in the early 1840's by Samuel Henrich Schwabe and seen through a change in the sunspot coverage, is the most obvious manifestation of solar variability. Since most forms of solar activity are magnetic in origin, they follow also this 11-year cycle, which refers to a quasi-periodic oscillation in the surface distribution of the solar magnetic field.

One of these solar cycle variations relates to the p-mode oscillation frequencies, and this aspect is of particular importance for this thesis. Indeed, a large body of helioseismic data convincingly shows that a cyclical variation in frequency has been observed on the timescale of the solar activity cycle. Note that the solar luminosity varies also with the solar cycle. The small magnitude of these changes probably justifies the assumption that the oscillation and brightness changes are not dynamically important to the cyclic activity. On the other hand, the sensitivity of the solar oscillations to the 11-year cycle is accurate enough to indicate that pressure deviations take place in the interior or atmosphere of the Sun over that period of time.

2. Solar cycle variations in p-mode frequencies

Solar-cycle-dependent frequency shifts A distinction must be introduced between the low ($0 \leq l \leq 4$), intermediate ($5 \leq l \leq 150$) and high degrees ($l > 150$). The first evidence that the frequencies of the p-modes change over the solar cycle came from the observations of low degree modes. During different time epochs, several groups have shown that the frequency shifts are well correlated with the solar activity cycle and that low degree-modes at increasingly higher frequencies become more sensitive to solar cycle effects (Woodard and Noyes, 1985; Fossat et al., 1987; Elsworth et al., 1990;

Anguera Gubau et al., 1992; Elsworth et al., 1994; Chaplin et al., 1998; Jiménez-Reyes et al., 1998). The solar cycle dependence of the intermediate degree frequencies in the p-mode spectrum was established later (Libbrecht and Woodard, 1990; Rhodes et al., 1993; Ronan et al., 1994) and, more recently, clearly confirmed by Bhatnagar et al. (1999) and Howe et al. (1999).

These observations report, over a solar cycle, peak shifts at a frequency of 3900 μHz, that are of order 750 nHz for low-degree modes (Chaplin et al., 1998) and 900 nHz for intermediate-degree modes (Libbrecht and Woodard, 1991; Howe et al., 1999). Hence it appears globally that low-l modal frequencies are slightly less affected by the solar cycle than their higher l counterparts. This is in agreement with the degree dependence of frequency shifts observed for intermediate-degree modes (Libbrecht and Woodard, 1991; Howe et al., 1999) and illustrated in Figure 2.1.

Due to the paraboloid relation between degree l and radial order n, higher n frequencies show a larger shift. This can be seen in Figure 2.2, which illustrates the frequency dependence of the frequency shifts. This figure also illustrates the correlation with solar activity.

The discovery that p-modes change over the solar cycle offers the possibility of a new diagnostic signature of that cycle, complementary to the more familiar signatures such as sunspot numbers and the butterfly diagram, but also potentially more rich of information regarding the structure of the Sun, which has been neglected in the standard solar model. Indeed, additional spatial signatures such as hysteresis have been clearly identified in the p-mode oscillations.

Hysteresis Bachmann and White (1994) have found hysteresis shapes amongst 7 indices of solar activity in their relative variations during a 20 year period. Such relations were also found in p-mode frequencies of low degree by Jiménez-Reyes et al. (1998) (see Figure 2.3). In some cases these observed hysteresis patterns start to repeat over more than one solar cycle, giving evidence that this is a normal feature of solar variability. Bachmann and White (1994) argue that hysteresis represents a real delay in the onset and decline of solar activity. In this view, Jiménez-Reyes et

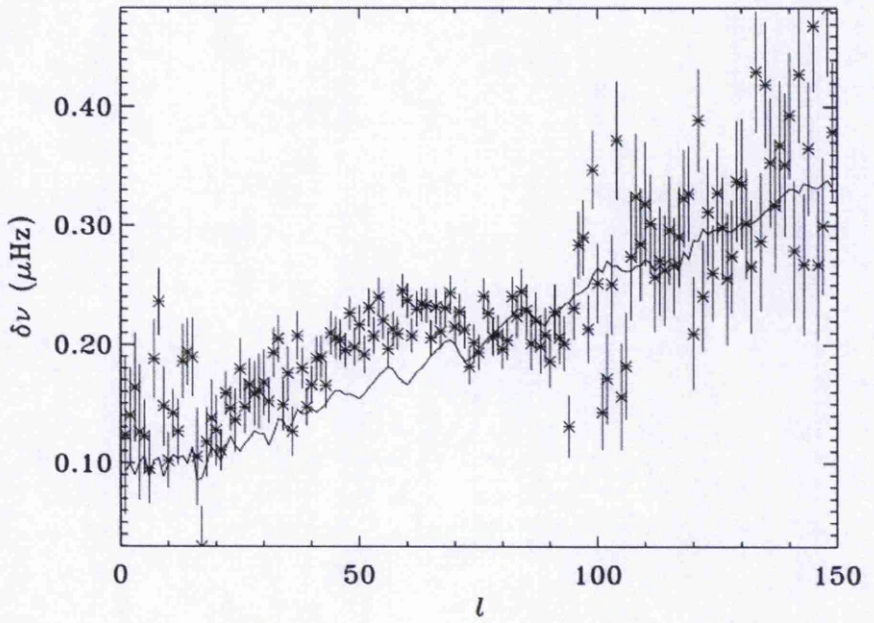

Figure 2.1: This figure from Howe et al. (1999) illustrates the l-dependence of the frequency shifts. It represents, as a function of l, the mean frequency shift between months $8-10$ and months $32-34$ of GONG data (*cf.* Appendix A.2), averaged over the frequency range 2800 to 3200μHz. The solid curves show the scaled inverse mode energy for the averaged modes.

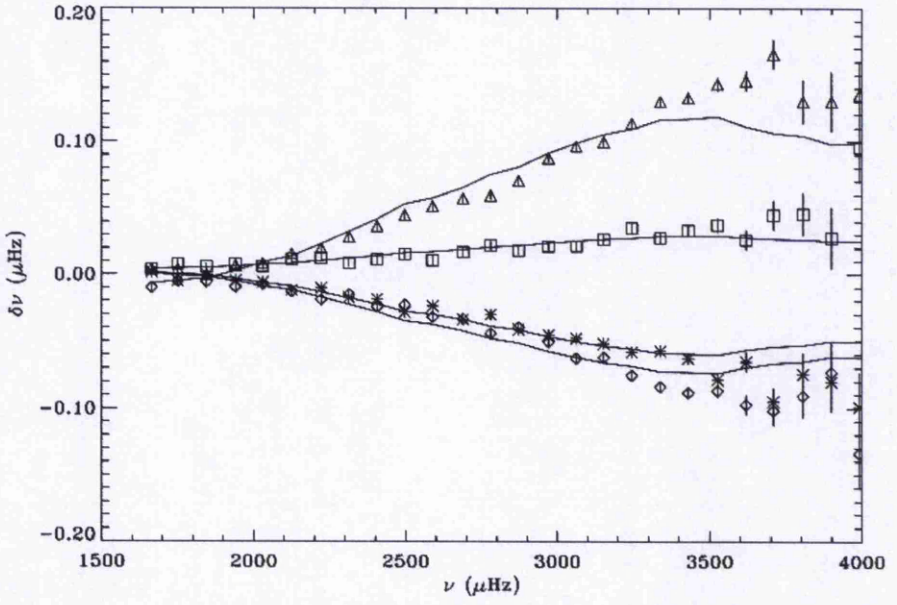

Figure 2.2: Frequency-dependence of the frequency shifts for the four independent periods months $5-7$ (stars), months $11-13$ (diamonds), months $25-27$ (squares), and months $30-32$ (triangles) of GONG data (*cf.* Appendix A.2), averaged over all l and over frequency bins of approximately 70μHz. The shifts have been calculated with respect to the mean of all four periods. The solid curves through each set of points represent linear fits to the mean inverse mode energy for the modes averaged (Howe et al. 1999).

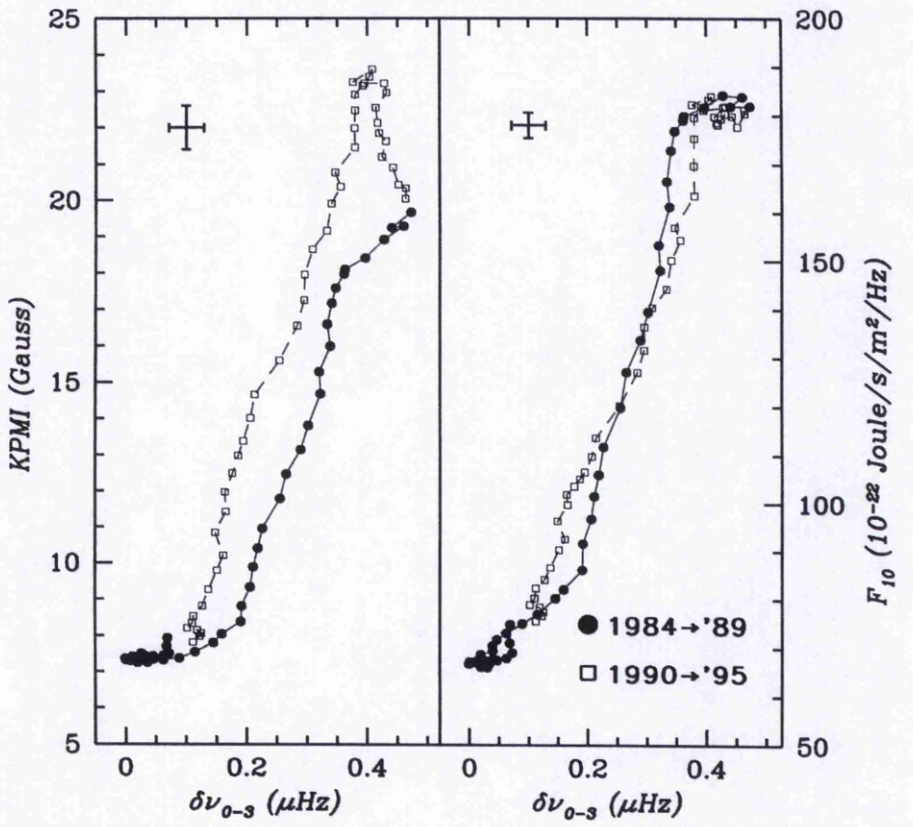

Figure 2.3: Hysteresis shapes seen in low-degree frequency shifts by Jiménez-Reyes et al. (1998). Two types of activity indices, surface magnetic field ($KPMI$) and spectral irradiance (F_{10}) are plotted against the smoothed frequency shifts $\delta\nu$.

al. (1998) suggest that the hysteresis shape could be due to time-delayed responses to one single phenomenon which can be located deep in the Sun, while Moreno-Insertis and Solanki (2000) find that the hysteresis in low-degree shifts is consistent with near surface magnetic flux distributions.

Frequency splitting coefficients The measured multiplet frequencies ν_{nlm} (for radial order n, angular degree l and azimuthal order m of the oscillation) may be fitted to a sum of Legendre polynomials P_i in m/L (where $L = \sqrt{l(l+1)}$), each weighted by the so-called splitting coefficients $\alpha_i(n,l)$, *viz.*

$$\nu_{nlm} = \bar{\nu}_{nl} + L \sum_{i=1} \alpha_i P_i \left(\frac{m}{L}\right) . \tag{2.1}$$

In this expansion, the odd-order coefficients α_i reflect the advective, latitudinally symmetric part of the perturbations caused by rotation, while the even-α's are sensitive to the solar cycle or to the latitude-dependent properties, *i.e.* they arise from asphericities, such as caused by magnetic and centrifugal forces (see, *e.g.*, Libbrecht and Woodard, 1990; 1991).

Changes in solar p-mode oscillations are not only observed in the multiplet frequencies ν_{nl} but also in the splitting coefficients $\alpha_i(n,l)$. It has been shown that the even-index frequency splitting coefficients vary with solar cycle (*e.g.*, Kuhn, 1988; Libbrecht and Woodard, 1990). The odd-index coefficients have been used to determine rotation rate as a function of latitude and radius. Through their analysis, a 1.3-year periodicity in the equatorial differential rotation at a radius of $0.72\,\mathrm{R}_\odot$ and, in antiphase, at a radius of $0.63\,\mathrm{R}_\odot$ has been reported (Howe et al., 2000a) but is still a matter of debate (Antia and Basu, 2000).

3. Background motivations

The influence of a magnetic field on p-modes may be thought of in several ways (see, *e.g.*, Roberts, 2001). First, the presence of magnetic fields affects the pressure distribution within an electrically conducting gas, and so the background equilibrium is modified. The gas pressure p_{mag} in the vicinity of a magnetic field deviates from that in a field-free Sun p_{free}. For a horizontal magnetic field confined to a flux tube or layer,

$$p_{mag} = p_{free} - \frac{B_o^2}{2\mu}\,. \tag{2.2}$$

It is as if the gas is 'evacuated' in the presence of the magnetic field. Secondly, the direction of the magnetic field is preferential in confining the wave propagation to the field lines, and so new types of perturbations, more or less subject to anisotropy, propagate. Additional forces, which depend upon the strength of the magnetic field, act on the system when it is perturbed. The effect is most simply characterised by the Alfvén speed, the basic speed with which a magnetic disturbance propagates. The sound speed and the Alfvén speed may be combined to describe a fast magnetoacoustic speed which is both super-sonic and super-Alfvénic. Finally, there is an indirect effect

due to magnetism: the temperature of the medium may be changed because of the presence of a magnetic field, thus modifying the sound speed. This effect is most clearly apparent in sunspots with their reduction in temperature (and thus sound speed), but may also occur elsewhere in more subtle ways (Roberts, 2001).

With the view that such effects can explain the cyclical variations in the global mode frequencies, it is of interest to explore how magnetic changes occurring in the solar cycle induce the observed frequency shifts. Four magnetic regions have been investigated as responsible for the changes in mode frequencies observed during the solar cycle: (*a*) the corona and the transition region above the chromosphere (*e.g.*, Vanlommel, 2001); (*b*) the canopy field of the chromosphere (*e.g.*, Campbell, 1987); (*c*) the fibril fields of the photosphere (Bogdan and Zweibel, 1985; Zweibel and Bogdan, 1986); and (*d*) the strong fields that reside in the convective overshoot region, at the base of the convection zone (Campbell, 1987; Daniell, 1998). A fifth region is now considered: (*e*) the anchorage zone of sunspots some 50 Mm below the surface.

Other non-magnetic processes can take place in these regions. With the uncertainty in the exact distribution of magnetic field both in the interior and the atmosphere, a separate study of each contribution is necessary, so as to clarify the relative importance of each physical process and each region in the determination of frequency shifts observed on the timescale of the solar activity cycle. However, in the atmosphere or sub-surface of the Sun, solar magnetic fields (a, b, c) play a significant role in modulating the resonant frequencies of p-mode oscillations: they can explain the frequency shifts observed on the timescale of the solar activity cycle.

A separate study of the contribution of internal magnetic layers can clarify the relative importance of surface effects. By treating the effects of internal magnetic layers (d, e), such as at the base of the convection zone and in the sunspots' anchoring zone, this thesis hopes to contribute to building a bridge between theories and observations, and so help to understand which explanations of solar cycle frequency shifts may be most fruitfully explored. By exploring carefully the theoretical analysis in the course of its formulation, new hypotheses that were not obvious so far may be generated. This is the main aim of this thesis.

2.2 Justifications and constraints for realistic modelling

To be as realistic as possible, one needs to assess parameters such as field strength and layer thickness of the internal magnetic layers to be modelled and which may be constrained by various physical arguments.

1. Time and spatial scales of circulation

There is as yet no satisfactory physical explanation of the length of the cycle itself, but the explanation of the solar cycle is generally considered to come from dynamo theory, which concerns the generation of magnetic fields in conducting fluids. Magnetic fields are produced by electric currents. These currents are generated within the Sun by the flow of the Sun's hot, ionised gases. Several elements that play an important role in most models of the dynamo theory will be mentioned later. Because nearly all the flows, which are observed on the Sun's surface and within its interior, may contribute in one way or another to the production of the Sun's magnetic field, it is necessary to review beforehand these hydrodynamical processes.

Besides, even when convective effects are taken into account, their treatment is uncertain (Unno et al., 1989). Indeed, there is no definitive theory for the perturbation in the convective flux, induced by the oscillations (coupling pulsation-convection). In this thesis, the perturbations in the turbulent pressure are neglected. Non-adiabatic effects, convective and radiative, are neglected all together. This is justified for radiative timescales, which are much longer than the typical period of a p-mode. Yet, convective timescales are much shorter than radiative timescales. For this reason, it is also prudent to review whether these timescales and their associated spatial scales justify the neglect of non-adiabatic effects.

Cellular flows In fact, only the granulation, with lifetimes between 5 and 15 minutes, that is one to three oscillation periods, challenges the assumption of adiabatic fluid motions. But granule cells do not occupy spatially the same regions as the p-modes. Figure 2.4 provides direct evidence for the depth of the granules, which are confined below the photospheric surface to depths ranging between 500 to 2500 km. At the

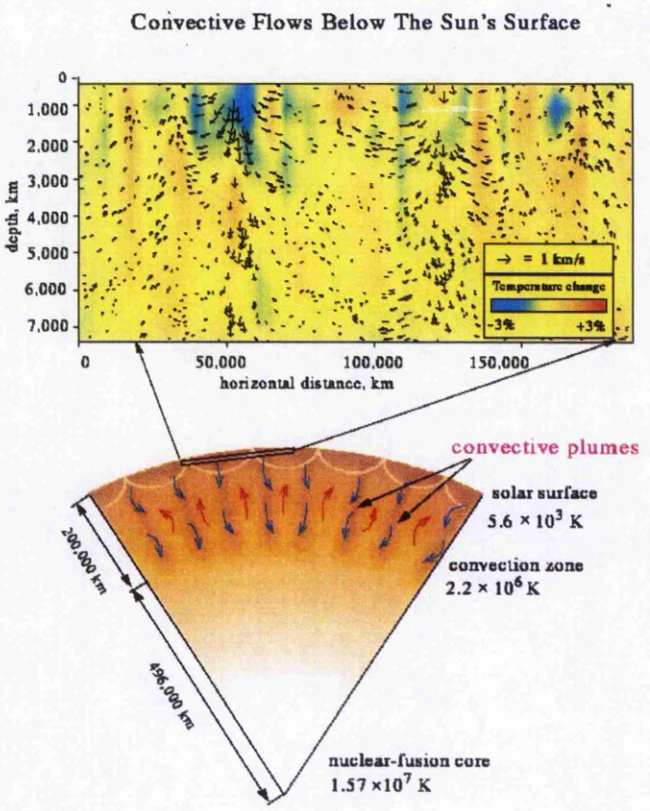

Figure 2.4:
(*a*) The top graphic is a vertical cut showing velocity and temperature variations below the solar surface derived by time-distance (travel) helioseismology on MDI data. The arrows indicate the direction and magnitude of the flow. The red and blue colouring indicates the variations of temperature, with red being hotter, and blue cooler.
(*b*) The bottom picture shows that the upper vertical cut is from a thin shell in the outer solar convection zone.
Available from World Wide Web:
http://sohowww.nascom.nasa.gov/gallery/MDI/, courtesy of SOHO/SOI/MDI consortium. SOHO is a project of international cooperation between ESA and NASA.

solar maximum, size and flow speed of the granules seem somewhat reduced, but this modulation needs further study.

Granules typically are organised into larger domains called supergranules that are more than 40,000 km across. The results of time-distance helioseismology suggests that they are shaped like pancakes, with a thickness only one-tenth of their width. The timescale of supergranulation ranges between 20 and 40 hours; for mesogranulation, it is about 2 hours.

Figure 2.4 shows also evidence of narrow plumes of cooler gases streaming downward toward the boundary with the radiative layer. The downflows are faster and, by mass conservation, narrower than the upflows. The plumes appear to originate from the middle of the supergranules, rather than at their edges. More significantly, this map shows no evidence of giant convection cells, persisting for a solar rotation period of 30 days, and which had been predicted by a popular theory called the global circulation

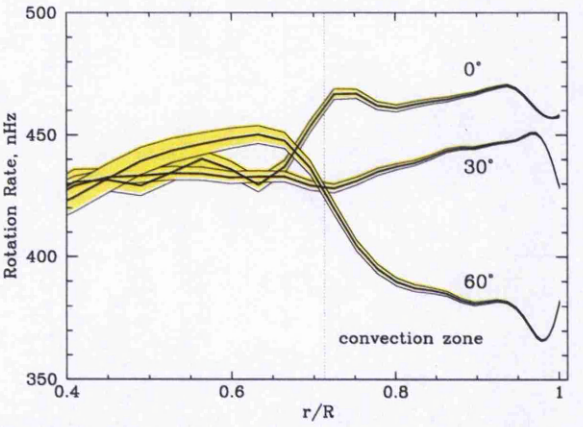

Figure 2.5: Solar rotation rate inferred from two months of MDI Medium-l data as a function of radius at three latitudes, respectively 0, 30 and 60 degrees. The formal errors are indicated by the coloured regions. From Kosovichev et al., 1997. Available from World Wide Web: http://soi.stanford.edu/results/srotation.html, courtesy of SOHO/MDI consortium. SOHO is a project of international cooperation between ESA and NASA.

model.

Axisymmetric flows The axisymmetric flows are the differential rotation and meridional circulation (Hathaway et al., 1996). The Sun rotates with an average 27-day period, but the equatorial regions rotate more rapidly (24 days) and the polar regions rotate more slowly (> 30 days). Small variations on this rotation profile occur over the course of the solar cycle. The rotation tends to be slower near solar maximum and in the hemisphere with more spots, and slower in cycles with more spots. Rotating streams, a pattern of alternating slower and faster rotation known as torsional oscillations or zonal flows, are observed in conjunction with the sunspots. These streams move toward the equator like the sunspots but appear to start earlier and at higher latitudes, with an amplitude of $5 - 10\,\mathrm{m\,s^{-1}}$, and appear to be significant down to a depth of between 0.03 to $0.1\,\mathrm{R}_\odot$ (see, *e.g.*, Hathaway et al., 1996; Schou et al., 1998; Howe et al., 2000b; Antia and Basu, 2000). Finally, meridional flows from the equator toward the poles are seen with magnitude ranging between 10 to $20\,\mathrm{m\,s^{-1}}$ (*e.g.*, Hathaway et al., 1996; Giles et al., 1997; Braun and Fan, 1998; 1999).

Helioseismology also provides estimates of how the rotation rate varies with depth. The differential rotation detected in the surface with Doppler observations persists throughout the convection zone. The maximum of the angular velocity occurs at

$r \approx 0.95\,R_\odot$. The sub-surface radial gradient changes sign from low to high latitudes (see Figure 2.5 from Kosovichev et al., 1997). The convection zone exhibits strong latitudinally dependent differential rotation, while the radiative core immediately below it rotates like a nearly (latitudinally independent) rigid body. Thus, at the interface between the base of the convection zone and the radiative region is a rather abrupt transition layer where the temperature gradient and the convective flux change rapidly with depth, with strong gradients of angular velocity as detected by helioseismic inversions of the observed splitting coefficients (*e.g.*, Brown et al., 1989; Thompson et al., 1996; Kosovichev et al., 1997; Schou et al., 1998). This shear layer, the so-called 'tachocline' (Spiegel and Zahn, 1992), is thought to be the seat of the dynamo action that may drive the solar cycle.

2. Basic theoretical processes

The dynamics of the solar convection zone, observed by helioseismology, is not precisely understood. But the basic processes of dynamo theory can explain the main lines. The following describes some phenomena and results from helioseismology that are important for placing realistic constraints on the modelling of magnetic layers buried in the solar interior.

Overshoot The convection penetrates into the radiative zone, before being deflected by pressure fluctuations associated with the opposing buoyancy forces. Following van Ballegooijen (1982), the so-called overshooting layer may be defined as the region where the average temperature gradient is subadiabatic, but where convective motions are still present and sufficiently rapid to maintain the temperature gradient essentially at the adiabatic value. Convective and radiative energy transport compete with each other in the weakly stable overshoot region. Besides the proposed solar models taking the convective overshoot into account (*e.g.*, Schmitt et al., 1984; Pitadella and Stix, 1986; Skaley and Stix, 1991; Freytag et al., 1996; Stix and Kiefer, 1997), helioseismology provides an upper estimate of the extent of overshoot in the radiative zone (Basu et al., 1994; Basu and Antia, 1994; Monteiro et al., 1994; Christensen-Dalsgaard et al., 1995;

Basu, 1997). By using a sequence of solar models to calibrate the amplitude of the signal observed in the data and associated with the discontinuities in the derivatives of the sound speed, Basu (1997) obtained an upper limit of $0.05H_P$ (2800 km) for the extent of overshoot. There is as yet no evidence for changes in the convection zone depth or extent of overshoot (Basu and Antia, 2000; 2001).

Turbulence, mixing, diffusion The strong gradient in the rotation rate is also expected to produce 'turbulence' (see, *e.g.*, Zahn, 1992), which is likely to mix material on a short timescale just below the convection zone (Richard et al., 1996). Also, sound waves speed up more than expected in this region (see Figure 1.5(*b*)), perhaps indicating that the turbulence and mixing associated with a dynamo are present. The action of mixing processes, which inhibit microscopic diffusion, is used to explain that the temperatures at the base of the convection zone are 'hotter' than solar models predict (Brun et al., 1999). The presence of magnetic fields at the base of the convection zone is not directly studied as responsible for this discrepancy. However, for any dynamo to work, diffusion is needed so that magnetic fields can reconnect to form new topologies. Moreover, slight changes are observed in the conspicuous peak over the solar cycle, which hint to an indirect effect of the magnetic field (Eff-Darwich and Korzennik, 2000).

The solar lithium/beryllium problem Standard evolutionary models of the Sun are not able to explain the observed depletion of lithium (Li 7 isotope) by a factor of 140 and beryllium (Be 9 isotope) by a factor of 2 compared to their primordial abundances. As stressed by Freytag et al. (1996), the solar Li/Be depletion is probably the result of the interplay of several transport processes. Mixing due to overshooting is regarded as one of them (Freytag et al., 1996). Turbulence generated in the tachocline is also likely to mix material in the upper radiative zone (see, *e.g.*, Zahn, 1992). And finally a magnetic field of strength of 4×10^5G just below the base of the convection zone may be needed to explain the partial depletion in abundance of Li (Parker, 1984a, b). Note however that this abundance of Li would be destroyed if the magnetic field exceeds a few times 10^5G.

Magnetic field storage at the base of the convection zone It has been argued that a relatively stable magnetic layer may reside at the bottom of the convection zone (Spiegel and Weiss, 1980; Pidatella and Stix, 1986) and presumably vary over the solar magnetic cycle. Specifically, within the stably stratified overshoot layer, flux tubes are initially stored in mechanical equilibrium in a layer of super-equipartition field, *i.e.* a field strength above an equipartition value of $10^4 G$ between magnetic energy density and kinetic energy density of the convective motions. Given its relative overlapping position in the overshoot layer, the tachocline is considered to be the most likely place for the solar dynamo. A currently favoured idea is that motions overshooting from the convection zone would carry magnetic fields into the tachocline to be stretched there into toroidal fields. If the layer were widely extended into the convection zone, convection would quickly destroy the toroidal flux. Besides, flux tubes originating near the very top of the subadiabatic layer have too low field strengths (Caligari et al., 1995). If this layer is too thin, the period of the solar cycle, which depends on the turbulent magnetic diffusion time through the layer, would be too short. A minimum thickness is therefore required, estimated to be at least $0.05\,\mathrm{R}_\odot \approx 35\,\mathrm{Mm} \approx H_P/2$ (Ruediger and Brandenburg, 1995).

Seismology of the base of the convection with splitting coefficients Because the tachocline is thought to be the site of the magnetic dynamo, there is great interest to assess its properties, essentially its location and its thickness, through an analysis of the odd-index splitting coefficients $\alpha(n,l)$ of modes of radial order n and angular degree l (Kosovichev, 1996; Gough and McIntyre, 1998; Elliott and Gough, 1999). Increasing variations with latitude are seen for the central position of the tachocline (Charbonneau et al., 1999; Basu and Antia, 2001) and possibly for its thickness (Schou et al., 1998; Antia et al., 1998; Basu and Antia, 2001), which is thought to be no more than $0.05\,\mathrm{R}_\odot$ and as small as $0.01\,\mathrm{R}_\odot$. The most recent results locate the tachocline at an equatorial central radius of about $0.693\,\mathrm{R}_\odot$, a little below the convection zone base, and suggest that a substantial part of the tachocline moves into the convection zone at higher latitudes (Charbonneau et al., 1999; Basu and Antia, 2001). At all latitudes,

the magnitude of the jump in rotation rate across the tachocline increases with solar activity (Basu and Schou, 2000).

The even-index splitting coefficients $\alpha(n,l)$ display changes over the solar cycle. Gough and Thompson (1990), who solved the adiabatic oscillation equation in a slowly rotating Sun that includes a toroidal field at the base of the convection zone, noted that the amplitudes of the even-order splitting coefficients vary as the square of the magnetic field strength. By comparing their theoretical results with changes observed by GONG, Basu (1997) deduced that the toroidal field modelled by Gough and Thompson (1990) would be of strength not larger than 3×10^5G. This result was further supported by Antia et al. (2000), who extended the formulation of Gough and Thompson (1990) by including the perturbation in the gravitational potential and assuming differential rotation in the interior, and used the more recent GONG and MDI data.

Stability analysis of toroidal flux tubes in the convection zone The value of 3×10^5G is slightly above but in broad agreement with the range $3 \times 10^4 - 10^5$G suggested by numerical simulations of active region emergence and evolution at the solar surface (see, *e.g.*, Choudhuri and Gilman, 1987; Schüssler et al., 1994; Fisher et al., 2000, and references therein). With the Coriolis force alone, rising flux tubes would be forced to move parallel to the axis of rotation and would emerge at unrealistic high latitudes. Buoyancy needs to dominate over the rotational and drag forces, allowing the flux tubes to erupt roughly along radial paths. This is achieved if the initial field strength is larger than about $10^5 G$, exceeding the equipartition value of $10^4 G$. This estimation is based on comparison between theoretical results and the observed regular properties throughout the solar cycle of

- the emergence latitude of sunspots: the restriction of sunspots to two belts of latitude (5 deg to 40 deg) above and below the equator;
- the magnitude of the tilt angle of the active regions main axis (between the connecting line of two polarities of an active region) with respect to the equator, by typically 10 deg, and its dependence on emergence latitude;

- the asymmetry between preceding and following parts of an active region (as regards morphology, stability and proper motion);
- the long intervals (approximately 50 to 100 years) with absence of activity in the form of sunspots (grand minima or Maunder minima);

Thus, the prime cause of the solar cycle is an oscillating strong magnetic field ($10^4 - 10^5 G$) of predominantly toroidal orientation and stored at the interface between the convection zone and the radiative interior.

α–ω dynamo mechanism: the global picture For sufficiently large field strengths, a magnetic buoyancy instability sets in, which leads to the eruption of magnetic loops from the overshoot layer, their subsequent rise through the convection zone and, as a by product, the emergence of bipolar pairs of sunspots at the solar surface.

Through the Coriolis force, rotation provides a diverging flow pattern with a twist that is clockwise on the northern hemisphere and anticlockwise on the southern hemisphere. As a sinking contracting parcel acquires a twist, the embedded magnetic field is also twisted, and thus poloidal loops may be formed around an initial toroidal flux element. This amounts to the creation of a net electric current parallel to the toroidal magnetic fields and producing a helicity. Through this effect, referred to as the α effect, a net poloidal magnetic field is generated from the toroidal magnetic field.

The differential rotation provides in turn a strong source of helicity injection (*e.g.*, Berger, 1999) and stretches the poloidal field into a strong toroidal field. This deformation of the field topology by differential rotation is referred as the ω effect.

Dikpati and Charbonneau (1999) combine the feature of rising of toroidal flux tubes, together with the poleward meridional flow-speeds observed at the surface and the differential rotation through the convection zone, to explore a Babcock-Leighton flux transport dynamo mechanism generating toroidal/poloidal fields from the interior/surface to the surface/interior. This model accounts for many of the global magnetic and flow features observed at the surface.

The sunspots' anchoring zone The magnetic fields observed in the solar atmosphere have their roots deep in the solar interior, where they are presumed to form a predominantly toroidal flux system. In the last 6 Mm, the density drops by a factor of 1000. As a bundle rises through the convection zone, it should expand as the pressure around it decreases, and should 'explode' into weak fragments (like a balloon). Results from time-distance helioseismology by Zhao, Kosovichev and Duvall (2001) support the idea that a downdraft beneath the sunspot holds together the loose cluster of magnetic flux tubes, thus explaining how the magnetic bundle survives the rise without being fragmented. Powerful and converging downward flows are found from 1.5 to 5 Mm beneath the surface and are believed to hold the sunspot together as long as the field is strong enough.

As the sunspots get older, they may well be disconnected from the deep fields by the frequent reconnections that occur in the first, say, 20 Mm below the photosphere (Schrijver and Title, 1999). This would indeed explain the difference between the rotation rates of the old and young sunspots (see, *e.g.*, the review by Beck, 2000). The differential rotation inside the convection zone inferred from helioseismology shows a peak angular velocity at about $r \approx 0.93\,\mathrm{R}_\odot$, that is some 49 Mm below the photosphere (*cf.* Figure 2.5). Recently the average sunspot rotation rate over more than a century has been shown to match approximately this peak value at 15 degree latitude (Javaraiah and Komm, 1999). This hints to the existence of an 'anchoring' layer, whose formation can be related to the solar cycle. Whereas a young spot would be anchored to it, like the tip of a submarine propelled on the photospheric plasma at its intrinsic speed, an older spot would be disconnected from it and be transported at a speed closer to the surface plasma flow.

The existence of a magnetic layer, where fields lines are to be anchored, was already proposed by Foukal (1972) to explain the basic rearrangement of sunspots and plage fields and the shorter rotation period of active regions compared to the photospheric gas. The minimum depth where the mechanical equilibrium occurs was deduced by Foukal to be more than 5 Mm below the photosphere.

Recently signatures of a significant perturbation at a shallow depth below the pho-

tosphere (30 Mm or ranging between 25-100 Mm with a peak at 45 Mm) have been reported (Dziembowski et al., 2000; Antia et al., 2000) but the authors could not distinguish between a thermal or a magnetic perturbation. In the latter hypothesis, estimates were given for a magnetic field of strength ranging between 2×10^4G to 3×10^4G (Antia et al., 2000) or peaking at 6×10^4G (Dziembowski et al., 2000). Developing a model close to the above conditions might prove useful to assess whether a shallow magnetic layer could contribute efficiently to the global frequency shifts observed over the solar cycle.

Outline of the thesis

Results from helioseismology provide realistic constraints for choosing parameters suitable to represent the magnetic layers buried in the solar interior. The main objective of the thesis is to explore the influence of a buried magnetic field on p-modes, and to assess the nature of various waves and instabilities that can arise on such a buried magnetic field. Diagnostics of the internal magnetic layers will be obtained through a schematic model in which the Sun is plane-stratified. This model is built up progressively in the thesis.

The dynamics of simple plane-stratified layers is considered in Part II. This part starts with Chapter 3, with a derivation of a general governing equation. In Chapter 4, basic aspects of helioseismology are described by way of a polytropic model and, in Chapter 5, the magnetohydrodynamics of isothermal magnetic layers is explored. Chapter 6 closes Part II with an investigation of some peculiar modes.

In Part III an investigation of more complicated models is undertaken. The effect of a buried magnetic field on the properties of solar oscillation modes is examined, showing also which other modes may propagate, and determining their frequency-wavenumber relationship. Analytical and numerical solutions to the dispersion relation for these modes are presented in Chapters 7 and 8 respectively. Chapter 9 provides a closer look at the boundary conditions of the field-free model of the Sun before Chapter 10 closes Part III in considering the influence of the buried magnetic field on solar oscillations.

The conclusions in Part IV raise some open questions and discussions in Chapter

11, ending with a summary of the results in Chapter 12.

Appendix A contains some reference material relevant for several chapters. Specifically, Appendix A.1 lists some useful formulas and describes the numerical methods employed; Appendix A.2 describes the GONG observations used in this thesis with their associated activity measures. Finally Appendix B contains lists of tables and figures, together with an index of topics and the bibliography.

O! Wanderers in the shadowed land
despair not! For though dark they stand,
all woods there be must end at last,
and see the open sun go past:
the setting sun, the rising sun,
the day's end or the day begun.
For east or west all woods must fail ...

John R.R. Tolkien (1892 - 1973)
"The Lord of the Rings" (1954-55), "The Old Forest"

Part II

DYNAMICS OF SIMPLE PLANE STRATIFIED LAYERS

As a preliminary to an investigation of more complicated models, this part considers the dynamics of simple plane-stratified layers. By way of a series of assumptions and restrictions, a fundamental wave equation is derived in Chapter 3. The modes of oscillation, which obey this equation in basic theoretical media, are considered attentively in the next chapters of this part. These media have in common a constant temperature gradient, but differ in the choice of this gradient and in the presence or otherwise of a magnetic field. With a non-zero temperature gradient and no field, the medium described is a field-free polytrope. With an adiabatic temperature gradient and appropriate boundary conditions, this will constitute a basic model of the field-free Sun, presented in Chapter 4. With a zero temperature gradient, the medium is isothermal. In Chapter 5, the equilibrium and the wave equations of an isothermal plasma will be studied in the presence of a magnetic field with constant Alfvén speed. These models form the building bricks to construction, in Part III, of hybrid models with one or two interfaces. Yet, before closing this part, immediate dispersion relations, which may serve to interpret the more complex model, will be presented in Chapter 6.

Chapter 3

Governing Equations

3.1 Perturbation equations

Linearisation When motions are superimposed on the equilibrium state (see Section 1.3), perturbation quantities can be expanded in power series of a small parameter ϵ ($0 \leq \epsilon < 1$) measuring amplitude, for instance

$$p = p_o + \hat{p}\,, \qquad \text{where} \quad \hat{p} = \epsilon p_1 + \epsilon^2 p_2 + \epsilon^3 p_3 + \ldots\,. \tag{3.1}$$

If only small departures from the state of stationary equilibrium are considered, then the zero-order terms in ϵ are very much larger than the respective first order terms in ϵ, and the MHD equations can be linearised. Linearisation consists of neglecting all second and higher order terms in the perturbed quantities, *i.e.* all products of perturbation quantities. Paradoxically, in a static equilibrium with $\mathbf{V_o} = 0$, the first-order term in velocity field is the only accepted perturbation much larger than its equilibrium quantity. In fact, by scaling the momentum equation in keeping the pressure gradient as the main restoring force for the p-modes, one can instead require the first-order term in velocity field to be much smaller than the local sound speed.

Typically, the largest velocity amplitude of a single p-mode of the Sun is less than a few tens of centimeters per second. For comparison, the sound speed near the photospheric surface is $c_o \approx 10\,\mathrm{km\,s^{-1}}$; in the interior, the sound speed rapidly rises with depth, while the oscillation amplitude falls. Therefore, with Mach numbers less than

10^{-4}, p-modes satisfy the linearised equations of ideal MHD (1.11)-(1.18) about a state of equilibrium (Section 1.3).

In particular, when the momentum equation (1.12) is linearised, one finds

$$\rho_o \frac{\partial \hat{\mathbf{V}}}{\partial t} = -\nabla \hat{p} + \frac{\nabla \times \mathbf{B_o}}{\mu} \times \hat{\mathbf{B}} + \frac{\nabla \times \hat{\mathbf{B}}}{\mu} \times \mathbf{B_o} + \hat{\rho} \mathbf{g_o} + \rho_o \hat{\mathbf{g}} \,. \tag{3.2}$$

Cowling approximation Changes of the gravitational field $\hat{\mathbf{g}}$ during the oscillatory motions are neglected in the so-called Cowling approximation. First demonstrated by T. G. Cowling in 1941, this neglect arises from a consideration of the solution to the perturbed Poisson's equation (1.18), *i.e.*

$$\nabla \cdot \hat{\mathbf{g}} = \nabla^2 \hat{\Phi} = -4\pi G \hat{\rho} \,, \tag{3.3}$$

where $\hat{\Phi}$ is the gravitational potential perturbation. The qualitative justification of the approximation is that the contribution from one part of the Sun to the gravitational potential perturbation $\hat{\Phi}$ is largely cancelled in non radial oscillations by the contribution of the other part of the Sun (see, *e.g.*, Unno et al., 1989; Christensen-Dalsgaard, 1998).

Approximation of the gravitational acceleration The convection zone constitutes 2.2 ± 0.2 per cent of the Sun's mass (Christensen-Dalsgaard et al., 1991). Hence, not only the gravitational acceleration $\mathbf{g_o}(z)$ decreases slowly in height in the solar atmosphere, but it increases also slowly with depth below the solar surface. At the base of the convection zone $g_o = 530\,\mathrm{m\,s^{-2}}$ (Basu et al., 1994, p.214). That is about twice as much its value at the surface, *viz.* $g_o = 274\,\mathrm{m\,s^{-2}}$. While in studies having the solar atmosphere for object the variation in $\mathbf{g_o}$ is neglected, leading to simpler equations and therefore simplifying the mathematical analysis, it is obviously not justified to assume that $\mathbf{g_o}$ is constant in a problem embodying the convection zone. However, for the sake of mathematical tractability, the simplification is made. From now on, $\mathbf{g_o}$ is noted $\mathbf{g}$. This choice of constant gravitational acceleration g precludes certainly a physical effect, that might overthrow the results obtained without it. Yet, to uncover

the processes affecting this region in a picture as realistic as possible but simple enough mathematically, this approximation is a first step. It will be of interest to investigate which difference is introduced when choosing the value of g.

Set of linearised MHD equations The resulting linearised MHD equations without background flow are

1. the equation of mass continuity

$$\frac{\partial \hat{\rho}}{\partial t} + \nabla \cdot (\rho_o \hat{\mathbf{V}}) = 0\,; \tag{3.4}$$

2. the momentum equation

$$\rho_o \frac{\partial \hat{\mathbf{V}}}{\partial t} = -\nabla \left(\hat{p} + \frac{\mathbf{B_o} \cdot \hat{\mathbf{B}}}{\mu} \right) + \frac{(\mathbf{B_o} \cdot \nabla)\hat{\mathbf{B}}}{\mu} + \frac{(\hat{\mathbf{B}} \cdot \nabla)\mathbf{B_o}}{\mu} + \hat{\rho}\mathbf{g}\,; \tag{3.5}$$

3. an adiabatic energy equation

$$\frac{\partial \hat{p}}{\partial t} + \hat{\mathbf{V}} \cdot \nabla p_o = -\gamma p_o \nabla \cdot \hat{\mathbf{V}}\,; \tag{3.6}$$

4. and an induction equation with no magnetic diffusion,

$$\frac{\partial \hat{\mathbf{B}}}{\partial t} = \nabla \times (\hat{\mathbf{V}} \times \mathbf{B_o})\,. \tag{3.7}$$

Finally, the solenoid constraint gives:

$$\nabla \cdot \hat{\mathbf{B}} = 0\,. \tag{3.8}$$

The Lorentz force in the momentum equation (3.2) was rewritten in Equation (3.5) using standard vector identities.

Pressures It is convenient to introduce the total (plasma plus magnetic) pressure

$$p_{oT} = p_o + p_m\,, \tag{3.9}$$

which, according to the magnetostatic equilibrium (1.49), obeys

$$\nabla p_{oT} = \rho_o \mathbf{g} + \frac{1}{\mu}(\mathbf{B_o} \cdot \nabla)\mathbf{B_o}\,, \tag{3.10}$$

where the gradient in magnetic pressure is equal in magnitude and of opposite direction to the magnetic pressure contribution of the Lorentz force, *viz.*

$$\nabla p_m = \nabla \frac{B_o^2}{2\mu}. \tag{3.11}$$

Note also that, from Equation (3.10), the gradient in total pressure may balance two contributions: the gravity force and the magnetic tension force.

The total pressure perturbation $\hat{p}_T$ is

$$\hat{p}_T = \hat{p} + \frac{\mathbf{B_o} \cdot \hat{\mathbf{B}}}{\mu}. \tag{3.12}$$

Then, upon derivation with respect to time, and using the adiabatic energy equation (3.6) and the induction equation (3.7) to eliminate respectively $\frac{\partial \hat{p}}{\partial t}$ and $\frac{\partial \hat{\mathbf{B}}}{\partial t}$,

$$\begin{aligned} \frac{\partial \hat{p}_T}{\partial t} &= \frac{\partial \hat{p}}{\partial t} + \frac{\mathbf{B_o}}{\mu} \cdot \frac{\partial \hat{\mathbf{B}}}{\partial t} \\ &= -\hat{\mathbf{V}} \cdot \nabla p_o - \gamma p_o \nabla \cdot \hat{\mathbf{V}} + \frac{\mathbf{B_o}}{\mu} \cdot \nabla \times (\hat{\mathbf{V}} \times \mathbf{B_o}). \end{aligned} \tag{3.13}$$

Hence, the Lagrangian rate of change in total pressure perturbation $\hat{\mathcal{P}}_T$, defined by

$$\hat{\mathcal{P}}_T \equiv \frac{D\hat{p}_T}{Dt} = \frac{\partial \hat{p}_T}{\partial t} + \hat{\mathbf{V}} \cdot \nabla p_{oT}, \tag{3.14}$$

can be expressed in two useful ways. First, using Equation (3.10),

$$\hat{\mathcal{P}}_T = \frac{\partial \hat{p}_T}{\partial t} + \hat{\mathbf{V}} \cdot \rho_o \mathbf{g} + \frac{1}{\mu} \hat{\mathbf{V}} \cdot [(\mathbf{B_o} \cdot \nabla)\mathbf{B_o}] \tag{3.15}$$

and second, using Equation (3.13),

$$\begin{aligned} \hat{\mathcal{P}}_T &= \left(\frac{\partial \hat{p}_T}{\partial t} + \hat{\mathbf{V}} \cdot \nabla p_o \right) + \hat{\mathbf{V}} \cdot \nabla p_m \\ &= -\gamma p_o \nabla \cdot \hat{\mathbf{V}} + \frac{\mathbf{B_o}}{\mu} \cdot \nabla \times (\hat{\mathbf{V}} \times \mathbf{B_o}) + \hat{\mathbf{V}} \cdot \nabla p_m \\ &= \hat{\mathcal{P}} + \hat{\mathcal{P}}_m, \end{aligned} \tag{3.16}$$

where the first term is the Lagrangian rate of change in pressure perturbation due only to the plasma, *viz.*

$$\hat{\mathcal{P}} = -\gamma p_o \nabla \cdot \hat{\mathbf{V}}; \tag{3.17}$$

and where the second term is the component of Lagrangian rate of change in pressure perturbation due only to the magnetic field

$$\hat{\mathcal{P}}_m = \frac{1}{\mu} \left[\mathbf{B_o} \cdot \nabla \times (\hat{\mathbf{V}} \times \mathbf{B_o}) + \hat{\mathbf{V}} \cdot \nabla \frac{B_o^2}{2} \right]. \tag{3.18}$$

This verifies that the magnetic component of the Lagrangian rate of change in pressure perturbation is formed of two contributions: the Eulerian rate of change in magnetic pressure perturbation and the advective change due to the equilibrium magnetic pressure force.

Equation of linearised MHD The linearised momentum equation reduces (upon derivation with respect to time and using the adiabatic energy equation, the induction equation and the equation of mass continuity to eliminate respectively $\frac{\partial \hat{p}}{\partial t}$, $\frac{\partial \hat{\mathbf{B}}}{\partial t}$ and $\frac{\partial \hat{\rho}}{\partial t}$) to the equation of linearised MHD for the rate of change of the force-operator:

$$\rho_o \frac{\partial^2 \hat{\mathbf{V}}}{\partial t^2} = \mathbf{F}(\hat{\mathbf{V}}), \tag{3.19}$$

with

$$\begin{aligned} \mathbf{F}(\hat{\mathbf{V}}) &= \nabla\left[\hat{\mathbf{V}}\cdot\nabla p_o + \gamma p_o \nabla\cdot\hat{\mathbf{V}} - \frac{\mathbf{B_o}}{\mu}\cdot\nabla\times(\hat{\mathbf{V}}\times\mathbf{B_o})\right] - \left[\nabla\cdot(\rho_o\hat{\mathbf{V}})\right]\mathbf{g} \\ &\quad + \left(\frac{\mathbf{B_o}}{\mu}\cdot\nabla\right)\left[\nabla\times(\hat{\mathbf{V}}\times\mathbf{B_o})\right] + \left[\frac{\nabla\times(\hat{\mathbf{V}}\times\mathbf{B_o})}{\mu}\cdot\nabla\right]\mathbf{B_o}. \end{aligned} \tag{3.20}$$

By using expression (3.15) for the Lagrangian rate of change in total pressure perturbation, $\mathbf{F}(\hat{\mathbf{V}})$ may be decomposed into three components, *viz.*

$$\mathbf{F}(\hat{\mathbf{V}}) = \mathbf{F}_1(\hat{\mathbf{V}}) + \mathbf{F}_2(\hat{\mathbf{V}}) + \mathbf{F}_3(\hat{\mathbf{V}}), \tag{3.21}$$

where

$$\mathbf{F}_1(\hat{\mathbf{V}}) = -\nabla\hat{\mathcal{P}}_T, \tag{3.22}$$

$$\begin{aligned} \mathbf{F}_2(\hat{\mathbf{V}}) &= -\left[\nabla\cdot(\rho_o\hat{\mathbf{V}})\right]\mathbf{g} + \nabla(\hat{\mathbf{V}}\cdot\rho_o\mathbf{g}) \\ &= \rho_o\left[-(\nabla\cdot\hat{\mathbf{V}})\mathbf{g} + \nabla(\hat{\mathbf{V}}\cdot\mathbf{g})\right], \end{aligned} \tag{3.23}$$

$$\begin{aligned} \mathbf{F}_3(\hat{\mathbf{V}}) &= \frac{1}{\mu}\Big\{(\mathbf{B_o}\cdot\nabla)\left[\nabla\times(\hat{\mathbf{V}}\times\mathbf{B_o})\right] + \left[\left[\nabla\times(\hat{\mathbf{V}}\times\mathbf{B_o})\right]\cdot\nabla\right]\mathbf{B_o} \\ &\quad + \nabla\left[\hat{\mathbf{V}}\cdot[(\mathbf{B_o}\cdot\nabla)\mathbf{B_o}]\right]\Big\}. \end{aligned} \tag{3.24}$$

The first contribution $\mathbf{F}_1$ is equal in magnitude and of opposite direction to the gradient of the Lagrangian rate of change in the total pressure perturbation; the second contribution $\mathbf{F}_2$ combines the Eulerian rate of change in the gravity force (*i.e.* here, the Eulerian rate of change in density perturbation) with the gradient of the advective

change due to the equilibrium gravity force, in cancelling out exactly their respective contribution due to the gradient in equilibrium density; the third vector $\mathbf{F}_3$ gathers the contributions due to the magnetic tension force (*i.e.* the tension force exerted by the Eulerian rate of change in the perturbed magnetic field and the gradient of the advective change due to the equilibrium magnetic tension force).

The eigenvalue problem From Equation (3.19), it is evident that the time dependence of the linearised version of MHD equations can be factored out. One approach is to reformulate Equation (3.19) as a normal mode problem. Nonlinear coupling between modes has been found theoretically to be quite small (Belvedere et al., 1983; Kumar and Goldreich, 1989). Since each mode does not interact with the other modes in the linear theory this allows the oscillations to be separated into normal modes, each uncoupled to all the rest. In this case, the time variation of all the perturbed quantities should represent harmonic disturbances that have always been present. And the damping associated to the viscosity of the solar plasma is neglected. This assumption is achieved by taking the perturbed quantities proportional to $e^{i\omega t}$, for a mode of angular frequency ω. For instance, the velocity perturbation is of the form

$$\hat{\mathbf{V}}(\mathbf{r},t) = \widetilde{\mathbf{V}}(\mathbf{r})e^{i\omega t}\,. \tag{3.25}$$

With this formulation, solutions to Equation (3.19) obey

$$-\rho_o\omega^2\widetilde{\mathbf{V}} = \mathbf{F}(\widetilde{\mathbf{V}})\,, \tag{3.26}$$

with $\widetilde{\mathbf{V}}$ no longer an explicit function of time. Equation (3.26) represents an eigenvalue problem for the eigenvalue ω^2. The operator $-\rho_o^{-1}\mathbf{F}(\widetilde{\mathbf{V}})$ is self-adjoint, or Hermitian, and as a consequence the eigenvalues ω^2 are real (see, *e.g.*, Goedbloed, 1983). Then, two types of solution exist.

Either $\omega^2 > 0$, and the motion is oscillatory and of constant (in time) amplitude. This implies a disturbance which, at any given point, has a harmonic time dependence of period $T(= 2\pi/\omega)$ and cyclic frequency $\nu(= \omega/2\pi)$.

Or $\omega^2 < 0$, and the motion is essentially exponentially growing in time. The perturbed quantities are proportional to $e^{\sigma t}$, where σ is the growth rate and such that

$\sigma^2 = -\omega^2 > 0$. This corresponds to a dynamical instability of the equilibrium. Note that the linear theory would only apply to the initial linear stages of the instability.

Hence, the real eigenfrequencies ω describe the dynamically stable oscillations, whereas complex eigenfrequencies carry information about the (exponentially growing) unstable modes. A further consequence of the operator $-\rho_o^{-1}\mathbf{F}$ being Hermitian is that the discrete modes present are orthogonal and can therefore be used as a set of basis functions to describe any small disturbance in a perturbative approach.

3.2 Assumptions and fundamental wave equation

Plane-stratified geometry Let $\mathbf{x}$, $\mathbf{y}$ and $\mathbf{z}$ represent Cartesian coordinate unit vectors: $\mathbf{xy}$ represent a local horizontal plane, while the depth is given in terms of the unit vector $\mathbf{z}$, measured downwards from the solar surface (gravity $\mathbf{g}$ acting in the positive z-direction). The medium is homogeneous and infinite in the horizontal direction, but is assumed to be of finite or semi-infinite extent in the z-direction, where it will be magnetically structured, possibly limited by boundaries and vertically stratified. The plane-parallel model corresponds to a description of a spherically symmetric Sun, stratified and structured radially.

Fourier expansion Perturbations may be Fourier analysed in the horizontal direction, though not in the vertical direction $\mathbf{z}$. The linearised isentropic velocity disturbances are then expressed in the form

$$\hat{\mathbf{V}} = (\hat{V}_x, \hat{V}_y, \hat{V}_z) = (V_x(z), V_y(z), V_z(z))\, e^{i(\omega t - \mathbf{k_h}\cdot\mathbf{r_h})}\,, \tag{3.27}$$

for horizontal wave vector $\mathbf{k_h}$ and horizontal position vector $\mathbf{r_h}$.

The complex form (3.27) represents a progressive wave-train, such that the velocity v_h of a point of constant phase $(\omega t - \mathbf{k_h}\cdot\mathbf{r_h})$ along the horizontal position vector $\mathbf{r_h}$ is

$$v_h = \frac{\omega}{k_h}\,. \tag{3.28}$$

v_h is defined as the phase velocity in the horizontal direction and the horizontal wavenumber k_h is the magnitude of the horizontal vector $\mathbf{k_h}$ and is assumed positive, *viz.* $k_h \geq 0$.

Preferential directions In the plane-stratified model, the direction **z** of gravity is already a preferential direction: it is the direction defined by the variation of equilibrium quantities of the static background. While the depth given in unit vector **z** may be directly related to the radius, in the absence of a magnetic field the horizontal direction is not preferential. The horizontal direction becomes preferential in the presence of a magnetic field (except of course if the magnetic field is orientated vertically — see Ferraro and Plumpton, 1958).

Let **xz** be the plane containing the equilibrium magnetic field. This plane contains also the direction of gravity. The orientation of the magnetic field with respect to the gravity field defines an additional preference.

$\mathbf{k_x}$ and $\mathbf{k_y}$, the x- and y-components of the horizontal wavevector, as defined in $\mathbf{k_h} = \mathbf{k_x} + \mathbf{k_y}$, have different roles to play. Assuming a horizontal direction for the magnetic field consistent with the storage of magnetic field at the base of the convection zone, the magnetic field is taken to be directed along the x-axis. Hence $\mathbf{k_x}$ indicates the direction of parallel propagation, while $\mathbf{k_y}$ corresponds to the direction of propagation perpendicular to the magnetic field lines.

Equilibrium quantities The distribution of the plasma pressure $p_o(z)$ and density $\rho_o(z)$ in the equilibrium state are related by the requirement of magnetostatic pressure balance (see Equation (3.10))

$$\frac{d}{dz}\left(p_o(z) + \frac{B_o^2(z)}{2\mu}\right) = g\rho_o(z)\,. \tag{3.29}$$

It is convenient to introduce here the Alfvén speed v_A through

$$v_A^2(z) = \frac{B_o^2(z)}{\mu\rho_o(z)}\,, \tag{3.30}$$

and define β to be the squared ratio of the sound speed $c(z)$ to the Alfvén speed $v_A(z)$, *viz.*

$$\beta = \frac{c^2(z)}{v_A^2(z)}\,. \tag{3.31}$$

β relates to the ratio between the kinetic pressure p_o and the magnetic pressure p_m, *viz.*

$$\frac{p_o}{p_m} = \frac{p_o}{B_o^2/(2\mu)}\,, \tag{3.32}$$

which conventionally is called the plasma β. Using the expression (1.50) for the adiabatic sound speed $c_s(z)$, there is proportionality between the two, *viz.*

$$\frac{p_o}{p_m} = \frac{2}{\gamma}\beta\,, \tag{3.33}$$

and so β is a measure of the importance of the magnetic field in a plasma.

Lagrangian rates of change in pressure perturbation Using the expression (1.50) for the adiabatic sound speed $c_s(z)$, the Lagrangian rate of change in pressure perturbation due only to the plasma (3.17) can be rewritten

$$\hat{\mathcal{P}} = -\gamma p_o \hat{\Delta} = -\rho_o c_s^2 \hat{\Delta} = -E\hat{\Delta}\,, \tag{3.34}$$

where $E = \rho_o c_s^2$ is the medium's modulus of elasticity and where the compressibility $\hat{\Delta}$ is defined as

$$\hat{\Delta} = \nabla \cdot \hat{\mathbf{V}} = \frac{\partial \hat{V}_x}{\partial x} + \frac{\partial \hat{V}_y}{\partial y} + \frac{\partial \hat{V}_z}{\partial z}\,. \tag{3.35}$$

The induced magnetic perturbation $\hat{\mathbf{B}}$ satisfies

$$\begin{aligned}
\frac{\partial \hat{\mathbf{B}}}{\partial t} = \nabla \times (\hat{\mathbf{V}} \times \mathbf{B_o}) &= \nabla \times (\hat{V}_z B_o \mathbf{y} - \hat{V}_y B_o \mathbf{z}) \\
&= \left[-B_o \frac{\partial \hat{V}_y}{\partial y} - \frac{\partial}{\partial z}(\hat{V}_z B_o), B_o \frac{\partial \hat{V}_y}{\partial x}, B_o \frac{\partial \hat{V}_z}{\partial x} \right] \\
&= \left[-B_o \hat{\Delta}_\perp - \hat{V}_z \frac{dB_o}{dz}, B_o \frac{\partial \hat{V}_y}{\partial x}, B_o \frac{\partial \hat{V}_z}{\partial x} \right],
\end{aligned} \tag{3.36}$$

where $\hat{\Delta}_\perp$ gathers the components of compressibility perpendicular to the magnetic field lines, *viz.*

$$\hat{\Delta}_\perp = \frac{\partial \hat{V}_y}{\partial y} + \frac{\partial \hat{V}_z}{\partial z}\,. \tag{3.37}$$

Note that the induced magnetic perturbation shows components not only in the x- and z-directions, but also in the y-direction.

The Lagrangian rate of change in pressure perturbation due only to the magnetic field (3.18) becomes

$$\begin{aligned}
\hat{\mathcal{P}}_m &= \frac{1}{\mu}\left(-B_o^2 \hat{\Delta}_\perp - B_o \hat{V}_z \frac{dB_o}{dz} + \hat{V}_z \frac{d}{dz}\frac{B_o^2}{2} \right) \\
&= -\frac{B_o^2}{\mu}\hat{\Delta}_\perp \\
&= -\rho_o v_A^2 \hat{\Delta}_\perp\,.
\end{aligned} \tag{3.38}$$

It should be noted that $\hat{\mathcal{P}}_m$, originally formed of two contributions (Eulerian rate of change and advective change), reduces to a compressive contribution of the Eulerian rate of change in the magnetic pressure perturbation. In fact the other component of the Eulerian rate of change offsets the advective change due to the equilibrium magnetic pressure force. As a result, $\hat{\mathcal{P}}_m$ compresses the volume perpendicular to the magnetic field lines through $\hat{\Delta}_\perp$. The extent to which increasing magnetic pressure decreases the volume perpendicular to the magnetic field lines is the modulus of magnetic elasticity

$$E_m = \rho_o v_A^2 \,. \tag{3.39}$$

Hence the Lagrangian rate of change in total pressure perturbation is

$$\begin{aligned} \hat{\mathcal{P}}_T &= -\left(E\hat{\Delta} + E_m\hat{\Delta}_\perp\right) \\ &= -\rho_o\left(c_s^2\hat{\Delta} + v_A^2\hat{\Delta}_\perp\right) \\ &= -\rho_o c_s^2\left(1 + \frac{1}{\beta}\frac{\hat{\Delta}_\perp}{\hat{\Delta}}\right)\hat{\Delta}\,, \end{aligned} \tag{3.40}$$

and so the effective medium's modulus of elasticity is

$$E_T = \rho_o c_s^2\left(1 + \frac{1}{\beta}\frac{\hat{\Delta}_\perp}{\hat{\Delta}}\right) = E\left(1 + \frac{1}{\beta}\frac{\hat{\Delta}_\perp}{\hat{\Delta}}\right). \tag{3.41}$$

The F-operator $\mathbf{F}(\hat{\mathbf{V}})$ in Equation (3.21) expresses the rate of change of the force-operator (see its dimensions). *This* '**F**-operator' becomes

$$\begin{aligned} \mathbf{F}(\hat{\mathbf{V}}) &= -\nabla\hat{\mathcal{P}}_T + \left[g\nabla\hat{V}_z - \hat{\Delta}\mathbf{g}\right]\rho_o \\ &\quad + \frac{B_o}{\mu}\frac{\partial}{\partial x}\left[\left(-B_o\hat{\Delta}_\perp - \hat{V}_z\frac{dB_o}{dz}\right)\mathbf{x} + B_o\frac{\partial\hat{V}_y}{\partial x}\mathbf{y} + B_o\frac{\partial\hat{V}_z}{\partial x}\mathbf{z}\right] + \frac{B_o}{\mu}\frac{\partial\hat{V}_z}{\partial x}\frac{dB_o}{dz}\mathbf{x} \\ &= -\nabla\hat{\mathcal{P}}_T + \left[g\nabla\hat{V}_z - \hat{\Delta}\mathbf{g}\right]\rho_o + \rho_o v_A^2\left[-\frac{\partial\hat{\Delta}_\perp}{\partial x}\mathbf{x} + \frac{\partial^2\hat{V}_y}{\partial x^2}\mathbf{y} + \frac{\partial^2\hat{V}_z}{\partial x^2}\mathbf{z}\right]. \end{aligned} \tag{3.42}$$

Recall that in this equation, the three different contributions of the operator **F** are respectively

$$\mathbf{F}_1(\hat{\mathbf{V}}) = -\nabla\hat{\mathcal{P}}_T\,, \tag{3.43}$$

$$\mathbf{F}_2(\hat{\mathbf{V}}) = \left[g\nabla\hat{V}_z - \hat{\Delta}\mathbf{g}\right]\rho_o\,, \tag{3.44}$$

$$\mathbf{F}_3(\hat{\mathbf{V}}) = \rho_o v_A^2\left[-\frac{\partial\hat{\Delta}_\perp}{\partial x}\mathbf{x} + \frac{\partial^2\hat{V}_y}{\partial x^2}\mathbf{y} + \frac{\partial^2\hat{V}_z}{\partial x^2}\mathbf{z}\right]. \tag{3.45}$$

Note that there is no advective change due to the equilibrium magnetic tension force since the equilibrium field lines are not curved. The term in v_A^2 in this expression is due to the tension force exerted by the Eulerian rate of change in the perturbed magnetic field.

Keeping the distinction between the three contributions of $\mathbf{F}$, the equation for the $\mathbf{F}$-operator (3.19) is projected on the $\mathbf{x}$, $\mathbf{y}$ and $\mathbf{z}$ unit vectors respectively, *viz.*

$$\frac{\partial^2 \mathbf{V}}{\partial t^2} = \frac{1}{\rho_o}\mathbf{F}_1(\hat{\mathbf{V}}) + \frac{1}{\rho_o}\mathbf{F}_2(\hat{\mathbf{V}}) + \frac{1}{\rho_o}\mathbf{F}_3(\hat{\mathbf{V}}) \tag{3.46}$$

$$\frac{\partial^2 \hat{V}_x}{\partial t^2} = c_s^2 \frac{\partial \hat{\Delta}}{\partial x} + g\frac{\partial \hat{V}_z}{\partial x} \tag{3.47}$$

$$\frac{\partial^2 \hat{V}_y}{\partial t^2} = c_s^2 \frac{\partial \hat{\Delta}}{\partial y} + v_A^2 \frac{\partial \hat{\Delta}_\perp}{\partial y} + g\frac{\partial \hat{V}_z}{\partial y} + v_A^2 \frac{\partial^2 \hat{V}_y}{\partial x^2} \tag{3.48}$$

$$\frac{\partial^2 \hat{V}_z}{\partial t^2} = -\frac{1}{\rho_o}\frac{\partial \hat{P}_T}{\partial z} + g\left(\frac{\partial \hat{V}_z}{\partial z} - \hat{\Delta}\right) + v_A^2 \frac{\partial^2 \hat{V}_z}{\partial x^2}. \tag{3.49}$$

The three different contributions of the operator $\mathbf{F}$ on each of the three spatial projections merit comment.

Due to the vertical dependence of stratification, the first contribution $\mathbf{F}_1$ in the operator simplifies on the horizontal x- and y-projections, but the term which appears on the z-projection is more complicated and is retained as it is until the very end in the derivation of the fundamental governing equation.

The second contribution $\mathbf{F}_2$ is two-fold. Through the advective change due to the equilibrium gravity force, the gravity force is a restoring force in all directions, but because the Eulerian rate of change in density perturbation is acting only on the vertical direction, the two components of $\mathbf{F}_2$ add up only on this projection (Equation (3.49)), where it results that the gravity force affects a volume involving the horizontal components of compressibility $\left(\frac{\partial \hat{V}_z}{\partial z} - \hat{\Delta}\right)$, *i.e.* a volume orthogonal to $\mathbf{g}$. In this sense, gravity indicates a preferential direction the same way magnetic fields do.

One can see from Equation (3.42) that the tension force $\mathbf{F}_3$ exerted on the x-direction by the Eulerian rate of change in the perturbed magnetic field compresses the volume perpendicular to the magnetic field lines through $\Delta_\perp$, and as such cancels out with the compressive contribution of the Eulerian magnetic pressure perturbation in $\mathbf{F}_1$. While in the direction perpendicular to the magnetic field lines, respectively

on the y- and z-projections (Equations (3.48)-(3.49)), the perturbed magnetic field exerts a parallel 'surface' tension force on the perpendicular (horizontal or vertical) displacement, through the last term in v_A^2, which cannot be eliminated. It will be shown later that these terms play a role in the propagation of Alfvén and magnetoacoustic surface waves respectively.

Fourier analysis By Fourier analysing the perturbations proportionally to $e^{i(\omega t - k_x x - k_y y)}$, the compressibility $\hat{\Delta}$ reduces to

$$\Delta = -ik_x V_x - ik_y V_y + \frac{dV_z}{dz}\,, \tag{3.50}$$

and Equations (3.47)-(3.49) reduce to

$$-\omega^2 V_x = -ik_x c_s^2 \Delta - igk_x V_z\,, \tag{3.51}$$

$$-\omega^2 V_y = -ik_y c_s^2 \Delta - ik_y v_A^2(\Delta + ik_x V_x) - igk_y V_z - k_x^2 v_A^2 V_y\,, \tag{3.52}$$

$$-\omega^2 V_z = -\frac{1}{\rho_o}\frac{d\mathcal{P}_T}{dz} + g\left(\frac{dV_z}{dz} - \Delta\right) - k_x^2 v_A^2 V_z\,. \tag{3.53}$$

V_x and V_y may be rewritten from the horizontal projections (3.51)-(3.52) in terms of V_z and Δ, *viz.*

$$-ik_x V_x = \frac{k_x^2 c_s^2}{\omega^2}\Delta + \frac{gk_x^2}{\omega^2}V_z\,, \tag{3.54}$$

$$-ik_y V_y(\omega^2 - k_x^2 v_A^2) = \left[\frac{k_y^2 c_\perp^2}{\omega^2}\Delta + \frac{gk_y^2}{\omega^2}V_z\right](\omega^2 - k_x^2 v_A^2)\,, \tag{3.55}$$

where $c_\perp(z, \omega, k_x)$ is defined through

$$c_\perp^2 = \frac{\omega^2}{\omega^2 - k_x^2 v_A^2}\left(c_s^2 + v_A^2 - \frac{k_x^2}{\omega^2}c_s^2 v_A^2\right)\,, \tag{3.56}$$

and represents the effective magnetosonic speed along the y-axis.

Alfvén wave It is important not to forget the denominator $(\omega^2 - k_x^2 v_A^2)$ in $c_\perp^2$ before simplifying Equation (3.55). If

$$\omega^2 = k_x^2 v_A^2\,, \tag{3.57}$$

then Equation (3.55) reduces to $\Delta = 0$. Further examination of Equations (3.40), (3.53) and (3.54) shows that $V_z = 0$, $V_x = 0$ and $\mathcal{P}_T = 0$. However, the disturbances in the

y-direction (*i.e.* the $\mathbf{g} \times \mathbf{B_o}$-direction) propagating parallel to the x-axis account for transversal perturbations of an Alfvén wave, driven by the magnetic tension force. The Alfvén wave, obeying the relation (3.57), is incompressible — since it has neither density nor pressure variations (in the linear limit) —, and propagates along the magnetic field lines.

Effective perpendicular magnetosonic speed If $\omega^2 \neq k_x^2 v_A^2$, Equations (3.54)-(3.55) may both look like equations for acoustic-gravity waves. The term involving g and V_z is caused by the advective change due to the equilibrium gravity force. Without this effect ($g = 0$), these equations look like equations for simple sound waves. However in the horizontal and perpendicular projection (3.55), the gradient of the Lagrangian rate of change in the total pressure perturbation (which involves the volume perpendicular to the magnetic field lines) and the magnetic tension term in v_A^2 have been combined through $c_\perp^2$.

The expression (3.56) for $c_\perp^2$ may be rewritten as

$$c_\perp^2 = (c_s^2 + v_A^2)\frac{\omega^2 - k_x^2 c_T^2}{\omega^2 - k_x^2 v_A^2}\,, \tag{3.58}$$

where the magnetohydrodynamic cusp speed $c_T(z)$ is an hybrid speed, always sub-sonic and sub-Alfvénic, defined through

$$\frac{1}{c_T^2(z)} = \frac{1}{c_s^2(z)} + \frac{1}{v_A^2(z)}\,. \tag{3.59}$$

The speed c_T happens to be the propagation speed of the longitudinal sausage modes in a straight slender magnetic flux tube (Defouw, 1976; Roberts and Webb, 1978).

In the numerator of Equation (3.58) for $c_\perp^2$, the appearance of the cusp speed is related to the magnetic pressure in the Lorentz force, while the Alfvén speed in the denominator is related to the effect of a tension in the magnetic field. These two contributions in the Lorentz force may compete against each other. In fact, one can see that the sign of $c_\perp^2$ is negative if a mode propagates with a parallel horizontal phase-speed $v_x = \frac{\omega}{k_x}$ intermediate between the cusp and the Alfvén speeds. Outside of this range, $c_\perp^2$ is positive.

For propagation perpendicular to the magnetic field lines ($k_x = 0$), $c_\perp$ corresponds to the fast magnetoacoustic speed $(c_s^2 + v_A^2)^{\frac{1}{2}}$, while for propagation along the field lines ($k_x \to \infty$), $c_\perp \to c_s$.

Therefore, it is of interest to consider the difference between the square of the effective perpendicular and the parallel sound speeds, *viz.*

$$c_\perp^2 - c_s^2 = v_A^2 \frac{\omega^2}{\omega^2 - k_x^2 v_A^2} \,. \tag{3.60}$$

It is also useful to introduce here the magnetically-modified frequency ϖ, defined by

$$\varpi^2 = \frac{c_s^2 + v_A^2}{c_s^2} \left(\omega^2 - k_x^2 c_T^2\right) = \frac{c_s^2 + v_A^2}{c_s^2} \omega^2 - k_x^2 v_A^2 \tag{3.61}$$

(note that $\varpi^2 \to \omega^2$ in the field-free limit). Then the squared ratio between $c_\perp$ and c_s is

$$\begin{aligned} \frac{c_\perp^2}{c_s^2} &= \frac{\varpi^2}{\omega^2 - k_x^2 v_A^2} \,, \\ &= \frac{\left(1 + \frac{1}{\beta}\right) \frac{\omega^2}{k_x^2 v_A^2} - 1}{\frac{\omega^2}{k_x^2 v_A^2} - 1} \,, \\ &= 1 + \frac{1}{\beta \left(1 - \frac{k_x^2 v_A^2}{\omega^2}\right)} \,. \end{aligned} \tag{3.62}$$

This ratio is illustrated in Figure 3.1, against the squared normalised parallel phase speed with respect to the Alfvén speed, $\omega^2/(k_x^2 v_A^2)$. The figure shows that at large parallel wavelengths ($k_x \to 0$), $c_\perp^2$ tends to $c_s^2 + v_A^2$; for $k_x \to \infty$, $c_\perp^2$ tends to c_s^2. The sign of $c_\perp^2$ is negative for a horizontal phase speed intermediate between the cusp and the Alfvén speeds; on the graph the limits of this range correspond respectively to where $c_\perp = 0$ and $c_\perp \to \infty$; specifically, the points which indicate where $c_\perp = 0$ are for $\omega^2/(k_x^2 v_A^2) = c_T^2/v_A^2$, while the asymptote to the limit $c_\perp \to \infty$ is given by $\omega^2/(k_x^2 v_A^2) = 1$.

Coupled ordinary differential equations V_x and V_y may then be replaced in the compressibility Δ given by Equation (3.50), giving

$$\left(1 - \frac{k_x^2 c_s^2 + k_y^2 c_\perp^2}{\omega^2}\right) \Delta = \frac{g(k_x^2 + k_y^2)}{\omega^2} V_z + \frac{dV_z}{dz} \,. \tag{3.63}$$

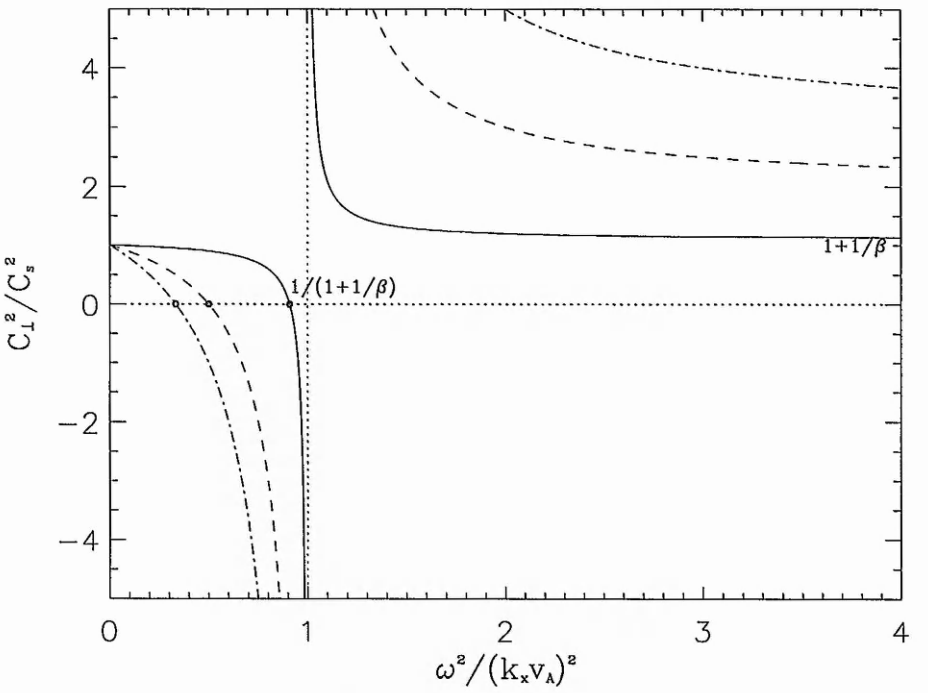

Figure 3.1: The squared ratio, $c_\perp^2/c_s^2$, between the effective perpendicular magnetosonic speed $c_\perp$ and the sound speed c_s versus the squared normalised parallel phase speed with respect to the Alfvén speed, $\omega^2/(k_x^2 v_A^2)$, for different parameters $\beta = c_s^2/v_A^2$; the plain curve is for $\beta = 10$, the dashed curve for $\beta = 1$ and the dashed-dotted curve for $\beta = 1/2$.

This equation is coupled to the vertical projection (3.53), showing the relations between the vertical velocity V_z, the compressibility Δ and the Lagrangian rate of change in total pressure perturbation $\mathcal{P}_T$. Eliminating Δ between these two equations yields the result

$$\frac{1}{\rho_o}\frac{d\mathcal{P}_T}{dz} = \left[(\omega^2 - k_x^2 v_A^2) - \frac{g^2(k_x^2+k_y^2)}{(\omega^2 - k_x^2 c_s^2 - k_y^2 c_\perp^2)}\right] V_z - \frac{g(k_x^2 c_s^2 + k_y^2 c_\perp^2)}{(\omega^2 - k_x^2 c_s^2 - k_y^2 c_\perp^2)}\frac{dV_z}{dz}. \quad (3.64)$$

Finally $\mathcal{P}_T$, derived from Equation (3.40), may be expressed in terms of V_z by using Equation (3.63) to eliminate Δ, *viz.*

$$\begin{aligned}
\mathcal{P}_T &= -\rho_o\left[c_s^2\Delta + v_A^2\left(\frac{dV_z}{dz} + \frac{k_y^2 c_\perp^2}{\omega^2}\Delta + \frac{g k_y^2}{\omega^2}V_z\right)\right] \quad (3.65)\\
&= -\rho_o\left[\left(\frac{\omega^2 c_s^2 + k_y^2 c_\perp^2 v_A^2}{(\omega^2 - k_x^2 c_s^2 - k_y^2 c_\perp^2)} + v_A^2\right)\frac{dV_z}{dz}\right.\\
&\qquad \left. + \left(\frac{g(k_x^2+k_y^2)}{(\omega^2 - k_x^2 c_s^2 - k_y^2 c_\perp^2)}\left(c_s^2 + \frac{k_y^2 c_\perp^2}{\omega^2}v_A^2\right) + \frac{g k_y^2 v_A^2}{\omega^2}\right)V_z\right]\\
&= -\rho_o\left[\frac{(c_s^2+v_A^2)(\omega^2 - k_x^2 c_T^2)}{\omega^2 - k_x^2 c_s^2 - k_y^2 c_\perp^2}\frac{dV_z}{dz}\right.
\end{aligned}$$

$$+g\left(\frac{(k_x^2+k_y^2)c_s^2+k_y^2v_A^2[1+\frac{k_x^2}{\omega^2}(c_\perp^2-c_s^2)]}{\omega^2-k_x^2c_s^2-k_y^2c_\perp^2}\right)V_z\Bigg]$$

$$= \frac{-\rho_o}{\omega^2-k_x^2c_s^2-k_y^2c_\perp^2}\left[c_s^2\varpi^2\frac{dV_z}{dz}+g\left(k_x^2c_s^2+k_y^2c_\perp^2\right)V_z\right]. \tag{3.66}$$

Fundamental wave equation Thus, the governing differential equation satisfied by the vertical velocity component V_z may be written in the form

$$\frac{1}{\rho_o}\frac{d}{dz}\left[A_1(z)\rho_o(z)\frac{dV_z}{dz}\right]+A_2(z)V_z=0\,, \tag{3.67}$$

where the coefficients A_1 and A_2 are given by

$$\begin{aligned} A_1(z) &= \frac{c_s^2\varpi^2}{\omega^2-k_x^2c_s^2-k_y^2c_\perp^2}\,, \\ &= \frac{(c_s^2+v_A^2)(\omega^2-k_x^2c_T^2)}{\omega^2-k_x^2c_s^2-k_y^2c_\perp^2}\,, \end{aligned} \tag{3.68}$$

$$\begin{aligned} A_2(z) &= (\omega^2-k_x^2v_A^2)-\frac{g^2(k_x^2+k_y^2)}{(\omega^2-k_x^2c_s^2-k_y^2c_\perp^2)} \\ &\quad +\frac{g}{\rho_o}\frac{d}{dz}\left[\rho_o(z)\frac{k_x^2c_s^2+k_y^2c_\perp^2}{\omega^2-k_x^2c_s^2-k_y^2c_\perp^2}\right]. \end{aligned} \tag{3.69}$$

General derivations related to this equation were first given by Goedbloed (1971) and Nye and Thomas (1976). The novelty in the present derivation resides in the distinction of the role played by the Lagrangian rate of change in total pressure perturbation, as well as the definition (see Equation (3.56) or (3.58)) and the emphasis on the use of $c_\perp(z)$. In fact, in the field-free limit (see Table 3.1), $c_\perp \to c_s$, consistent with the isotropic nature of the fundamental equation in that case. But also, in a more general way, the formulation of the equation is considerably simplified, thereby becoming more meaningful.

Singularities Two singularities may be defined: an Alfvén singularity ($\omega^2 = k_x^2v_A^2(z)$) and a cusp singularity ($\omega^2 = k_x^2c_T^2(z)$). These singularities are associated with the occurrence of continuous spectra in MHD (see, *e.g.*, Adam (1977a); Goedbloed (1983, 1984); Goossens (1991) and references therein). If, at a depth z, the frequency of the wave matches the Alfvén frequency (so that $c_\perp(z) \to \infty$), then $A_2(z) \to \infty$, while if the wave matches the cusp frequency (so that $c_\perp(z) \to 0$), then $A_1(z) \to 0$. Either case

	$c_\perp^2(z)$	$A_1(z)$	$A_2(z)$
$v_A = 0$	c_s^2	$\frac{c_s^2\omega^2}{\omega^2-k_h^2c_s^2}$	$\omega^2 - \frac{g^2k_h^2}{(\omega^2-k_h^2c_s^2)} + \frac{g}{\rho_o}\frac{d}{dz}\left[\rho_o(z)\frac{k_h^2c_s^2}{\omega^2-k_h^2c_s^2}\right]$
$k_y = 0$	$c_\perp^2$	$\frac{(c_s^2+v_A^2)(\omega^2-k_x^2c_T^2)}{\omega^2-k_x^2c_s^2}$	$\omega^2 - k_x^2v_A^2 - \frac{g^2k_x^2}{(\omega^2-k_x^2c_s^2)} + \frac{g}{\rho_o}\frac{d}{dz}\left[\rho_o(z)\frac{k_x^2c_s^2}{\omega^2-k_x^2c_s^2}\right]$
$k_x = 0$	$c_s^2 + v_A^2$	$\frac{(c_s^2+v_A^2)\omega^2}{\omega^2-k_y^2(c_s^2+v_A^2)}$	$\omega^2 - \frac{g^2k_y^2}{\omega^2-k_y^2(c_s^2+v_A^2)} + \frac{g}{\rho_o}\frac{d}{dz}\left[\rho_o(z)\frac{k_y^2(c_s^2+v_A^2)}{\omega^2-k_y^2(c_s^2+v_A^2)}\right]$

Table 3.1: Coefficients of the fundamental equation in three cases: a field-free medium ($v_A = 0$); and, for the case $v_A \neq 0$, when propagation is either parallel ($k_y = 0$) or perpendicular ($k_x = 0$) to the applied field.

corresponds to a zero coefficient function of $\frac{d^2V_z}{dz^2}$ in the governing differential equation, and this describes a singularity.

Parallel and perpendicular propagations in the horizontal direction When the analysis is restricted to motions that have a horizontal wave vector parallel or perpendicular to the horizontal equilibrium magnetic field, A_1 and A_2 simplify (see Table 3.1). This has the mathematical convenience of leading to a simple governing wave equation.

Taking $k_y = 0$ in Equation (3.67), it can be seen that any interaction of acoustic oscillations with local Alfvén oscillations is removed (*i.e.* there is no Alfvén singularity) and that the wave equation is possibly singular only at positions in the cusp continuum, defined by the variation of $c_T(z)$. This is the singularity discussed by Adam (1977a), who apparently was the first to notice it in his thesis in 1974.

However, in taking $k_x = 0$ instead, *i.e.* for motions in the yz- plane, all singularities are withdrawn. For purposes concerned with simple mathematical treatments to understand primary effects of the magnetic field other than resonances, one can see already an interest to study the perpendicular rather than the parallel propagation in the horizontal direction.

Outline Equation (3.67) is *a priori* a second order differential equation with non-constant coefficients, whose analytic complexity is a first step to overcome and understand. This is accomplished in Chapter 4 in the field-free limit and in passing to another variable, or in Chapter 5 by restricting the propagation to parallel or perpendic-

ular directions and by assuming constant coefficients. By applying them to media with appropriate background equilibrium profiles, these reduced forms of the fundamental equation (3.67) contain sufficient information to reveal a number of basic properties of the modes of oscillation sustained by these media.

A traveller who refuses to pass over a bridge until he has personally tested the soundness of every part of it is not likely to go far; something must be risked, even in mathematics.

Horace Lamb (1849 - 1934)

Chapter 4

Aspects of Helioseismology

In this chapter, several aspects of helioseismology will be inferred by considering the hydrostatic equilibrium of a plane-stratified semi-infinite region of fluid in the Cartesian system (x, y, z), with z measured downwards from the solar surface (at $z = 0$). In Section 4.1, simple aspects of wave propagation are deduced by way of Lamb's equation for a field-free plasma stratified under gravity. An analytic solution to this equation may be obtained in particular for a polytropic profile. Taking non-isothermal stratification into account rather than the spherical geometry, the azimuthal order m introduced earlier is here taken to be zero. In what follows, m will instead be used to denote the polytropic index (see Section 1.3), used to determine sound speed, density and pressure profiles. For non-vertical propagation ($l \neq 0$), a plane-parallel polytrope is a convenient model to describe the quantisation of the modes in integer order n. This is accomplished in Section 4.2, considering appropriate boundary conditions. In addition to the p-modes, low-frequency modes (called g-modes) are obtained.

4.1 Lamb's equation and polytropic stratification

Lamb's equation The governing equation for V_z in a field-free plasma is given by Equation (3.67), taking v_A and c_T to be zero. But this equation possesses a complex structure, even in the field-free limit. It proves more convenient to describe the motion in terms of the compressibility Δ.

In the field-free limit, $\beta \to \infty$ and $\mathcal{P}_T \to \mathcal{P}$, giving from Equation (3.34),

$$\Delta = \frac{-\mathcal{P}}{\rho_o c_s^2}\,. \tag{4.1}$$

Furthermore, the derivative of $\mathcal{P}$ gives

$$\begin{aligned} -\frac{1}{\rho_o c_s^2}\frac{d\mathcal{P}}{dz} &= \frac{d\Delta}{dz} - \frac{\mathcal{P}}{\rho_o c_s^2}\left(\frac{\rho_o'}{\rho_o} + \frac{(c_s^2)'}{c_s^2}\right) \\ &= \frac{d\Delta}{dz} + \frac{\gamma g}{c_s^2}\Delta\,. \end{aligned} \tag{4.2}$$

Hence the set of coupled ordinary differential equations (3.63) and (3.53) taken in the field-free limit gives, upon using (4.2) to eliminate $\frac{d\mathcal{P}}{dz}$, the relationships between the vertical velocity V_z and the compressibility Δ:

$$\frac{dV_z}{dz} + \frac{gk_h^2}{\omega^2}V_z = \left(1 - \frac{k_h^2 c_s^2}{\omega^2}\right)\Delta \tag{4.3}$$

and

$$(\omega^4 - g^2k_h^2)V_z = g(k_h^2c_s^2 - \gamma\omega^2)\Delta - \omega^2 c_s^2\frac{d\Delta}{dz}\,. \tag{4.4}$$

Assuming that $\omega^4 \neq g^2k_h^2$, V_z may be eliminated from Equations (4.3) and (4.4) to obtain the governing second-order differential equation for Δ (Lamb, 1932), namely

$$\frac{d^2\Delta}{dz^2} + \left(\frac{c_s^2(z)'}{c_s^2(z)} + \gamma\frac{g}{c_s^2(z)}\right)\frac{d\Delta}{dz} + \left[\frac{\omega^2 - k_h^2c_s^2(z)}{c_s^2(z)} + \frac{gk_h^2}{\omega^2}\left((\gamma-1)\frac{g}{c_s^2(z)} - \frac{c_s^2(z)'}{c_s^2(z)}\right)\right]\Delta = 0\,. \tag{4.5}$$

Standard form of the wave equation Several simple but important ideas of helioseismology are mathematically understood by way of this equation rewritten in the standard form (see, *e.g.*, Deubner and Gough, 1984)

$$\frac{d^2Q}{dz^2} + K^2(z)Q = 0\,, \tag{4.6}$$

where $Q(z) = \sqrt{\rho_o(z)}c_s^2(z)\Delta$ and

$$K^2(z) = \frac{\omega^2 - \omega_a^2}{c_s^2(z)} + k_h^2\left(\frac{\omega_g^2}{\omega^2} - 1\right)\,. \tag{4.7}$$

Here the buoyancy frequency ω_g, as defined in Equation (1.73), is given by

$$\omega_g^2 = \frac{g}{H_\rho} - \frac{g^2}{c_s^2(z)}\,, \tag{4.8}$$

which can be developed (using the fundamental relation (1.52)) to give

$$\omega_g^2 = \frac{g}{c_s^2(z)} \left[(\gamma - 1)g - [c_s^2(z)]' \right] ; \tag{4.9}$$

here ω_a^2 is a modification of the squared acoustic cut-off frequency, ω_o^2 (Lamb, 1909), defined through

$$\begin{aligned} \omega_o^2 &= \frac{c_s^2(z)}{4H_\rho^2} \\ &= \frac{(\gamma g - [c_s^2(z)]')^2}{4c_s^2(z)} \\ \omega_a^2 &= \omega_o^2(1 + 2H_\rho') . \end{aligned} \tag{4.10}$$

Solar p-modes derive many of their properties from the vertical inhomogeneity of the solar interior, as well as from the action of the buoyancy force. For a field-free medium stratified under gravity, the density stratification has two important implications, each leading to the addition of an extra term in the basic wave equation (1.2), rewritten here for clarity:

$$k_z^2 = \frac{\omega^2}{c_s^2} - k_h^2 . \tag{4.11}$$

By comparison to k_z in Equation (4.11), K in Equation (4.7) involves the acoustic cut-off frequency and the gravity cut-off frequency. These extra terms need to be introduced. For a detailed investigation on the propagation of acoustic-gravity waves, see Moore and Spiegel (1964).

Acoustic cut-off frequency From Equation (1.56), variations of equilibrium quantities typically take place over a pressure scale height H_P. If the propagation is over distances much smaller than H_P, the stratification effects are small. On the other hand, when the wavelength of a wave is much longer than H_P, changes in density along the direction of propagation modify the information conveyed by the acoustic wave. This accounts for the existence of the acoustic cut-off frequency ω_a (Equation (4.10)), below which acoustic disturbances can no longer propagate.

Throughout most of the solar interior, the oscillations can be regarded as being adiabatic, *i.e.* the material motions that arise from the acoustic waves are not accompanied by an exchange of radiative energy with the environment. The pressure distribution

in convective equilibrium (see Equation (1.54)) shows that the existence of a cut-off frequency is not solely due to the pressure stratification produced by the external gravity. A temperature stratification in a non-isothermal atmosphere can generate such a cut-off as well. In the case of three dimensional wave propagation, the cut-off frequency depends also on the horizontal wavenumber.

Buoyancy or Brunt-Väisälä cut-off frequency The physical significance for the buoyancy frequency, ω_g, follows from the 'blob' argument for convective stability: if a blob of fluid is rising adiabatically, its behaviour depends on whether the local density of the element is greater or smaller than its new surroundings. ω_g^2 is proportional to the difference between $|d\rho/dz|$ and $|d\rho/dz|_{ad}$ (see Equation (1.71)).

When $\omega_g^2 > 0$ the element is heavier than its surroundings, and so it sinks, but may overshoot and oscillate about its equilibrium position. Slow sloshings of material are mediated by gravity, like waves on the ocean, rather than by pressure as in the case of sound waves. This type of wave is called a *gravity wave* or g-mode, since gravity serves to provide the restoring force for the motion.

When $\omega_g^2 < 0$, the density of a rising element falls off more rapidly than that of its surroundings and gravity acts to enhance the motion, forcing the element away from equilibrium; the medium is said to be *convectively unstable.*

Propagation behaviour In the Sun, the temperature $T_o(z)$ increases rapidly with depth. Thus, as an acoustic wave propagates inward, it is *refracted*: the inwardly increasing sound speed causes deeper parts of the wave front to travel more quickly than less deep parts and, as a consequence, the direction of propagation (orthogonal to the wave front) is rotated until it is pointing towards the solar surface. The inner boundaries of the resonant cavity result from the refraction of waves back towards the surface. The depth to which the p-modes penetrate is the acoustical cavity depth. The radius of deepest penetration is also called the lower turning point. It is commonly said that beneath the lower turning point, there exists a zone of avoidance that the wave never samples. However this is not strictly correct. The solutions $Q(z)$ are oscillatory when $K^2(z) > 0$ and evanescent (exponential or hyperbolic type) when $K^2(z) < 0$; the

division between propagation and evanescence occurs at the lower turning point (or cavity depth) $z = z_t$ where

$$K^2(z_t) = 0\,. \tag{4.12}$$

For a wave to be able to propagate in the vertical (or radial) direction, it must have $K^2(z) > 0$. From Equation (4.7), this condition is satisfied in two different regimes: at large frequency ω, in the regime of acoustic modes; and at small frequency ω, in the regime of gravity modes. Indeed, the first term in Equation (4.7), *viz.*

$$\frac{\omega^2 - \omega_a^2(z)}{c_s^2(z)}\,, \tag{4.13}$$

is positive for $\omega^2 > \omega_a^2$ and dominates at high frequencies above the acoustic cut-off, while the second term, *viz.*

$$k_h^2 \left(\frac{\omega_g^2(z)}{\omega^2} - 1 \right)\,, \tag{4.14}$$

is positive for $\omega^2 < \omega_g^2$ and dominates at low frequencies below the buoyancy cut-off.

At low frequency below the buoyancy cut-off, buoyancy dominates, producing internal gravity waves. Note that gravity waves cannot propagate in convective regions. The frequency of g-modes approaches a finite limit, which is the maximum value of the buoyancy frequency ω_g beneath the convection zone, where g-modes are 'believed' to be confined. Certainly, g-modes remain undetected. They seem not to be excited to observable amplitudes at the Sun's surface, perhaps owing to the extremely small amplitudes associated with the motions they induce. On the other hand, pressure fluctuations dominate at high frequencies above the acoustic cut-off, producing acoustic waves — the p-modes — which have proved to be the major focus of study. The remainder of this section is mainly concerned with these modes.

For $\omega_g < \omega_a$, the terms (4.13) and (4.14) are of opposite sign for a given frequency ω. And so the passage from propagation to evanescence, which defines a lower or upper turning point, occurs when one negative term offsets the other positive term. Hence, in the range of frequencies comprised between the buoyancy and the acoustic cut-off frequencies, $K^2(z) < 0$. The solutions with real values of ω and k_h are *evanescent* waves in the z-direction, which means that they propagate horizontally and have amplitudes that decay exponentially with height or depth. If ω is imaginary, the motion grows

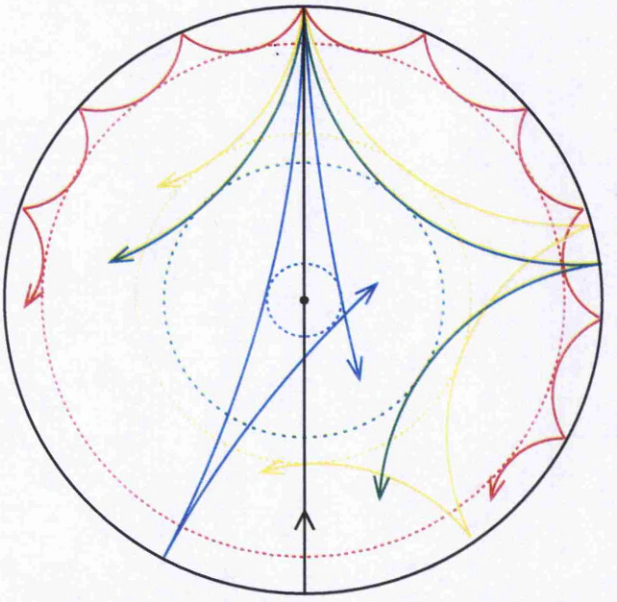

Figure 4.1: In this cross-section of the Sun, the curves show the ray paths followed by various sound waves at a fixed frequency of 3 mHz. Depending on their direction of propagation near the surface, sound waves penetrate to various depths. The different ray paths correspond to different values of the degree l: in red $l = 75$, in yellow $l = 25$, in green $l = 20$, in blue $l = 2$, and in black $l = 0$. In each case, the dotted circle indicates the turning point of the oscillation. Inspired by a graph from the web-site 'Helio- and Asteroseismology', by TAC, Aarhus University, Denmark (http://www.obs.aau.dk/helio_outreach/english/).

exponentially with time; this is the case of instability, corresponding here to convective motions.

Refraction at the lower turning point By noting the vertical dependence of the cut-off frequencies, a number of general properties may be determined through an examination of Equation (4.7). The acoustic cut-off frequency $\omega_a \sim \frac{1}{\sqrt{T_o}}$, and so decreases with depth. As a consequence, the first term (4.13) in (4.7) remains positive for low frequencies as the depth increases, which means that low-frequency modes are trapped farther below the solar surface than high-frequency modes. In the acoustic regime $\omega^2 > \omega_a^2 > \omega_g^2$, and the second term (4.14) in (4.7) is negative. Its amplitude is proportional to k_h. Therefore, at fixed frequency ω, this negative term is larger for high k_h^2 (*i.e.* high l) than for low k_h (*i.e.* low l). For the first term to offset the second term, smaller values of $c_s(z)$ are required at high l than at low l. This means that lower l modes propagate deeper into the solar interior than those with higher l. In

other words, if waves travel steeply downward, they are refracted less strongly than if they penetrate at a more oblique angle: with a low frequency, *i.e.* a large period, they take more time to bounce back to the surface (see Figure 4.1).

Reflection at the upper turning point Whether the pulsational wave is completely reflected (*standing wave*) or leaks into space as a *running wave* depends upon the surface conditions. The upper reflection boundaries are defined by the abrupt change in sound speed associated with the steep temperature gradient in the superadiabatic region just below the surface. Because of the decreasing density and temperature, the acoustic cut-off frequency ω_a rises very rapidly towards the surface. At the temperature minimum, where $T_o \simeq 4300\text{K}$, $c_s \simeq 8\,\text{km}\,\text{s}^{-1}$ and $H_P \simeq 120\,\text{km}$, the highest acoustic cut-off frequency occurs for $\omega_a/(2\pi) \simeq 5.3$ mHz.

The assumption of a standing wave solution requires that the (sound) wave coming up from the solar interior undergoes perfect reflection. Below the acoustic cut-off, waves are reflected near the surface forming an acoustic cavity inside the Sun. If ω_g is neglected in (4.14), this term reduces to $-k_h^2$. So at fixed degree l, the higher the frequency, the larger is the acoustic cut-off frequency ω_a at which waves may suffer reflection; thus the upper turning point of high-frequency waves is closer to the surface than it is for low-frequency waves. At fixed frequency ω, the wave is reflected for decreasing values of ω_a as l increases. Thus waves of low l turn higher up than waves of high l.

p-mode cavities Hence p-modes are trapped in spherical-shell cavities, starting essentially at the visible surface and extending inward. A cavity is delimited at its upper extreme by the reflective properties of the photosphere and chromosphere (see Section 9.3) and at its lower extreme by the increasing sound speed in the convection zone. Depending on frequency and degree, these modes sample different but overlapping regions of the solar interior.

A single mode having an intermediate frequency has characteristics of acoustic, gravity, and evanescent waves in different regions within a Sun-like star. This is well illustrated by the propagation diagram in Figure 4.2.

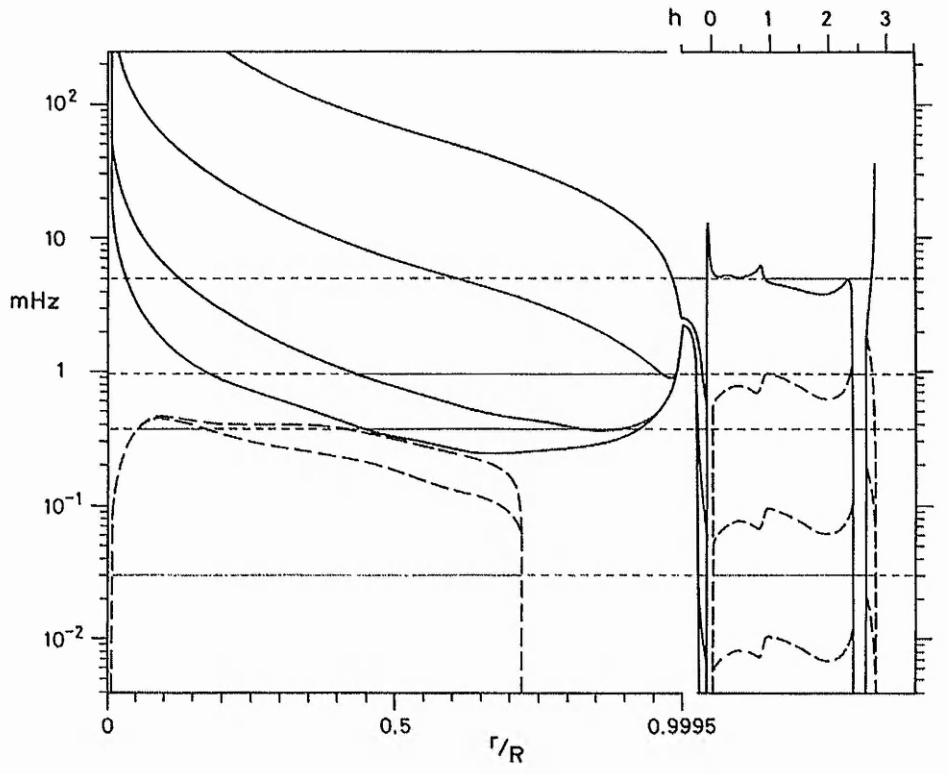

Figure 4.2: Propagation diagram for a model of the Sun from Deubner and Gough (1984, Figure 1, see references therein). The corona is not included. Solid curves represent $\omega_a/(2\pi)$, and dashed curves $\omega_g/(2\pi)$, in the regions where the critical frequencies are real. The lower abscissa scale extends to $r/\,\mathrm{R}_\odot = 0.9995$; beyond that value, the scale is expanded by a factor of 100 and indicated on the upper boundary of the diagram: the independent variable is the height h above the photosphere measured in units $10^{-3}\,\mathrm{R}_\odot$. The cut-off curves are for $l = 1$, 5, 50 and 500. In all cases, ω_a and ω_g are increasing functions of l at fixed $r/\,\mathrm{R}_\odot$, which permits the identification of the curves: in the interior the ω_g curves for $l = 5$, $l = 50$, and $l = 500$ are essentially indistinguishable, as are all four ω_a curves in the atmosphere, where $\omega_a/(2\pi) \simeq 5.3$ mHz. The thin horizontal lines represent normal modes; they are continuous in zones of propagation and dashed in evanescent regions. From low to high frequency, the modes represented are a high-degree ($l \gtrsim 25$) g-mode, g_1 ($l = 1$), p_4 ($l = 5$) and p_6 ($l = 500$).

General polytrope Introducing the sound speed c_o at $z = 0$ and the temperature scale height $z_o = \frac{c_o^2}{(c_s^2)'}$, the profile for the square of the sound speed in hydrostatic equilibrium is (see Equation (1.75))

$$\begin{aligned} c_s^2(z) &= c_o^2 + (c_s^2)'z \\ &= \frac{\gamma g}{m+1}(z_o + z)\,, \qquad z \geq 0\,. \end{aligned} \tag{4.15}$$

From Equation (4.9), the buoyancy frequency ω_g is then given in the polytropic case by

$$\begin{aligned} \omega_g^2 &= \frac{g^2}{(m+1)c_s^2}\left(m(\gamma-1)-1\right) \\ &= \frac{g}{mH_\rho}\left(\frac{\gamma-1}{\gamma}m-\frac{1}{\gamma}\right). \end{aligned} \tag{4.16}$$

Hydrostatic equilibrium combined with the gas law (1.54) gives

$$\frac{1}{H_P}=\frac{1}{H_\rho}+\frac{1}{z+z_o}, \tag{4.17}$$

and Equation (1.74) gives

$$\frac{1}{H_\rho}=\frac{m}{z+z_o}. \tag{4.18}$$

These last two equations are equivalent to

$$\frac{p_o'}{p_o} = \frac{m+1}{z+z_o}, \tag{4.19}$$

$$\frac{\rho_o'}{\rho_o} = \frac{m}{z+z_o}. \tag{4.20}$$

Finally the acoustic frequency ω_a, defined in Equation (4.10), may be developed:

$$\begin{aligned} \omega_o^2 &= \left(\gamma\frac{m}{m+1}\right)^2\frac{g^2}{4c_s^2(z)} \\ &= \left(\gamma\frac{m}{m+1}\right)\frac{mg}{4(z+z_o)} \\ \omega_a^2 &= \omega_o^2\left(1+\frac{2}{m}\right) \\ &= \left(\gamma\frac{m}{m+1}\right)\frac{(m+2)g}{4(z+z_o)}. \end{aligned} \tag{4.21}$$

Constant polytropic index Assuming a constant ratio of specific heats γ, and because g is constant, the temperature profile or the profile for the square of the sound speed is linear with depth z if the polytropic index m is constant. Figure 4.3 provides a sketch of such a field-free polytrope.

In this case (if the polytrope has constant polytropic index), the pressure and density profiles have power-law distributions given explicitly by

$$\begin{cases} p_o(z) = p_s(1+\frac{z}{z_o})^{m+1} \\ \rho_o(z) = \rho_s(1+\frac{z}{z_o})^m \end{cases} \qquad z \geq 0\,, \tag{4.22}$$

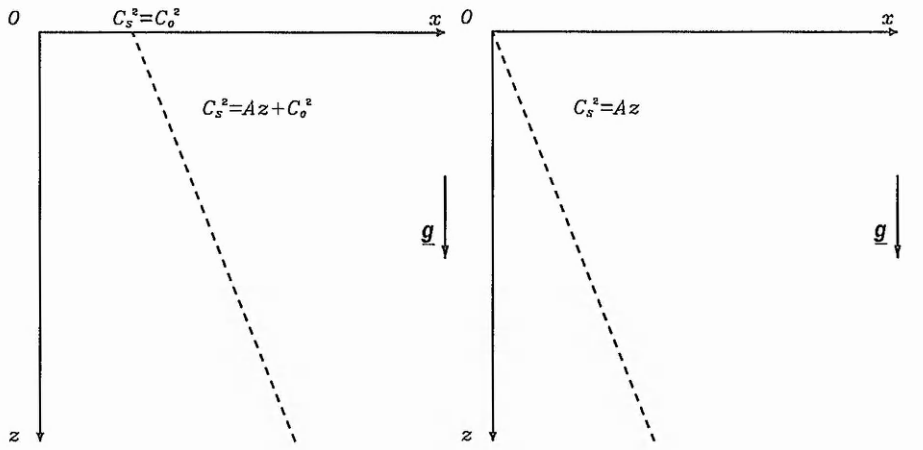

Figure 4.3: Simple plane-stratified models representing a field-free polytropic interior with (a) non-vanishing sound speed ($c_o^2 \neq 0$) at $z = 0$ or (b) a vanishing sound speed ($c_o^2 = 0$) at $z = 0$.

where p_s and ρ_s are the plasma pressure and density at $z = 0$ (and $z_o \neq 0$ or ∞).

In the special case of $p_s = 0$, a vanishing pressure at $z = 0$ (and consequently for $c_o^2 = 0$, a vanishing sound speed at $z = 0$), the model looks like the one described in Figure 4.3(b) and $z_o = 0$. One can rewrite Equations (4.19)-(4.20) with $z_o = 0$ and obtain the power-law distributions for the pressure and density profiles by introducing p_p and ρ_p, the plasma pressure and density at a lower boundary, at $z_p = \mathrm{R}_\odot$ for instance, *viz.*

$$\begin{cases} p_o(z) = p_p(\frac{z}{z_p})^{m+1} \\ \rho_o(z) = \rho_p(\frac{z}{z_p})^m \end{cases} \qquad z \geq 0. \tag{4.23}$$

In the case $\omega^4 \neq g^2 k_h^2$, the Lamb equation (4.5) applied to the linear profile (4.15) may be transformed into

$$Z\frac{d^2\Delta}{dZ^2} + (m+2)\frac{d\Delta}{dZ} + \left(\Upsilon + \frac{m+2}{2} - \frac{Z}{4}\right)\Delta = 0\,, \tag{4.24}$$

where $Z = 2k_h(z + z_o)$; the parameter Υ is determined by

$$\begin{aligned} 2\Upsilon &= \frac{m+1}{\gamma}\Omega^2 + \left(\frac{\gamma-1}{\gamma}m - \frac{1}{\gamma}\right)\frac{1}{\Omega^2} - (m+2) \\ &= \frac{m+1}{\gamma}\Omega^2 + k_h(z+z_o)\frac{\Omega_g^2}{\Omega^2} - (m+2)\,. \end{aligned} \tag{4.25}$$

The expression

$$\Omega^2 = \frac{\omega^2}{gk_h}\,, \tag{4.26}$$

introduced in Equation (4.25), is the normalised frequency squared and will be used extensively in what follows; also $\Omega_g^2 = \frac{\omega_g^2}{gk_h}$ denotes the normalised buoyancy frequency squared.

Confluent hypergeometric equation The differential equation (4.24) may be further transformed by writing

$$\psi = \Delta e^{k_h(z+z_o)} = \Delta e^{Z/2}\,, \tag{4.27}$$

resulting in a form of the confluent hypergeometric equation known as Kummer's equation:

$$Z\frac{d^2\psi}{dZ^2} + (m+2-Z)\frac{d\psi}{dZ} + \Upsilon\psi = 0\,. \tag{4.28}$$

The general solution of Equation (4.28) can be given under different forms (Slater, 1960). A closer look at these different forms is taken in Section 9.2. For the moment, the following form is adopted:

$$\psi = \alpha_1 M(-\Upsilon, m+2, Z) + \beta_1 U(-\Upsilon, m+2, Z)\,, \qquad Z \geq 0. \tag{4.29}$$

The functions M and U are respectively the *Kummer* and *Tricomi* confluent hypergeometric functions. See Appendix A.1. For non-integer values of the polytropic index (*e.g.*, for a convectively neutral medium, $m = 3/2$ when $\gamma = 5/3$), $m+2$ is not an integer. It can be easily verified that the Wronskian W,

$$W\{M(-\Upsilon, m+2, Z), U(-\Upsilon, m+2, Z)\} = -\frac{\Gamma(m+2)}{\Gamma(-\Upsilon)}\frac{e^Z}{Z^{m+2}}\,, \tag{4.30}$$

is non-zero for $\Upsilon \neq 0, 1, 2, \ldots$. And so the functions M and U are linearly independent provided Υ is not an integer. This is an essential property for understanding the polytropic model.

If Υ is not an integer, then the functions M and U are linearly independent (their Wronskian $W \neq 0$) and in the general case they are both solutions to retain.

If Υ is an integer, then the functions M and U are linearly dependent (the Wronskian $W = 0$): in that case, the M and U functions terminate as forms of generalised Laguerre polynomials, which are proportional (see Appendix A.1, Equations (A.18) and (A.19)),

viz.

$$M(-\Upsilon, m+2, Z) = \frac{\Upsilon!}{(m+2)_\Upsilon} L_\Upsilon^{(m+1)}(Z)\,, \tag{4.31}$$

and

$$\begin{aligned} U(-\Upsilon, m+2, Z) &= (-1)^\Upsilon (m+2)_\Upsilon M(-\Upsilon, m+2, Z) \\ &= (-1)^\Upsilon \Upsilon! L_\Upsilon^{(m+1)}(Z)\,. \end{aligned} \tag{4.32}$$

Here a choice must be made between these two functions, or some linear combination of them, and this choice depends on the boundaries in place.

4.2 p- and g-modes in a polytrope

The two outer boundaries of this medium are the upper boundary surface at $z = 0$ and the centre of the star.

Upper boundary condition The outer boundary of the Sun is ill defined. Inaccuracies in solar model calculations are generated near the solar surface, the mode frequencies being most sensitive to the surface structure (because the sound speed is lowest there). Moreover, the surface layers of the Sun are the most difficult to model accurately because they exhibit a wide range of complex dynamical phenomena, in many of which magnetism plays an important role.

Since pressure and density near the solar surface decrease steeply outwards, it is reasonable to assume that pressure essentially vanishes at the surface. The free surface must move with the plasma and not independently of it. In linear theory, this may be formulated as $\frac{DP}{Dt} = 0$ at $z = 0$ (Lamb, 1932, Ref.3, p.363). Therefore, an illustrative upper boundary surface is given by the use of a reflective outer boundary condition for the Lagrangian rate of change in total pressure perturbation:

$$\mathcal{P}_T = 0 \qquad \text{at } z = 0\,. \tag{4.33}$$

The requirement of vanishing Lagrangian pressure perturbation at the surface isolates the solar interior from the solar atmosphere. This allows a study of the effect of a buried magnetic field on p-modes, without the complications introduced by surface effects.

For a field-free surface, the boundary condition (4.33) reduces to

$$c_s^2(z)\rho_o(z)\Delta = 0 \qquad \text{at} \quad z = 0\,. \tag{4.34}$$

For a discussion or use of this condition, see, *e.g.*, Pekeris (1938, p.194), Christensen-Dalsgaard (1980, p.768), Unno et al. (1989, Equation (21.24), p.215), Gough and Thompson (1990, p.27), Smeyers et al. (1996, Equation (8), p.106). For vanishing sound speed at the surface, *i.e.* $c_o = 0$, the surface condition is sufficient but not necessary.

The centre of the Sun The boundary conditions in the centre of the Sun are not better defined. Schmitz and Steffens (1999) assume vanishing (or at least finite) Lagrangian pressure perturbations. This will be discussed further in Section 9.2. But for the moment, it is the kinetic energy density (i.e. kinetic energy per unit volume) associated with a perturbation, which is taken to vanish deep below the surface, *viz.*

$$E = \frac{1}{2}\rho(z)V_z^2(z) \to 0 \qquad \text{as} \quad z \to \infty\,. \tag{4.35}$$

Taking the square root of E, and linearising, this corresponds to looking at the condition that

$$E_o^{1/2} \sim C^{st}\rho_o^{1/2}(z)V_z(z) \to 0 \qquad \text{as} \quad z \to \infty\,. \tag{4.36}$$

Expression for the vertical velocity amplitude Substituted back in Equation (4.27), the solution (4.29) for ψ gives in turn the compressibility:

$$\Delta = e^{-Z/2}\left[\alpha_1 M(-\Upsilon, m+2, Z) + \beta_1 U(-\Upsilon, m+2, Z)\right]\,, \qquad Z \geq 0. \tag{4.37}$$

For $\Omega^4 \neq 1$, V_z is obtained from Equations (4.4) and (4.27) in the normalised form

$$V_z = \frac{e^{-k_h(z+z_o)}}{(1-\Omega^4)}\frac{\gamma}{k_h}F(\psi)\,, \qquad z > 0, \tag{4.38}$$

where

$$\begin{aligned} F(\psi) = &\ \tfrac{k_h c_s^2(z)}{\gamma g}\left[2\Omega^2\psi' - (\Omega^2+1)\psi\right] + \Omega^2\psi\,, && z > 0 \\ = &\ \tfrac{k_h(z+z_o)}{m+1}\left[2\Omega^2\psi' - (\Omega^2+1)\psi\right] + \Omega^2\psi\,, && z > 0 \\ = &\ \tfrac{Z}{2(m+1)}\left[2\Omega^2\psi' - (\Omega^2+1)\psi\right] + \Omega^2\psi\,, && Z > 0\,; \end{aligned}$$

here ψ' denotes the derivative of the function $\psi(Z)$ with respect to Z, evaluated at $Z = 2k_h(z + z_o)$.

In what follows, M, U, M' and U' are also evaluated at Z and defined as

$$M = M(-\Upsilon, m+2, Z), \quad U = U(-\Upsilon, m+2, Z), \tag{4.39}$$

$$M' = M'(-\Upsilon, m+2, Z), \quad U' = U'(-\Upsilon, m+2, Z), \tag{4.40}$$

where the prime denotes the derivative of M or U with respect to Z. In the general case, when the functions M and U are linearly independent, substituting the solution (4.29) for ψ into Equation (4.38) yields

$$V_z = \frac{e^{-k_h(z+z_o)}}{(1-\Omega^4)} \frac{\gamma}{k_h} \left[\alpha_1 F(M) + \beta_1 F(U)\right], \qquad z > 0. \tag{4.41}$$

Solutions from the boundary conditions Boundary conditions are always independent. It is obvious that the boundary condition at $z \to +\infty$ is independent from the boundary condition at $z \to 0$ because the value of z_o has no effect in the expression of $(z + z_o)$ when $z \to \infty$. In particular $Z \sim 2k_h z \to \infty$ as $z \to \infty$. The asymptotic expansions (A.16) and (A.17) for M and U given in Appendix A.1 are applied to the expression (4.41) for $V_z(z)$. The asymptotic expansions of a function M and its derivative are equivalent, *viz.*

$$M' \sim M \sim \frac{\Gamma(m+2)}{\Gamma(-\Upsilon)} Z^{-\Upsilon-m-2} e^Z, \qquad Z \to \infty, \tag{4.42}$$

while the derivative of the Tricomi U function (see Equation (A.11) behaves as

$$U' \sim \Upsilon Z^{\Upsilon-1} \sim \Upsilon \frac{U}{Z}, \quad \text{when} \quad U \sim Z^{\Upsilon}, \qquad Z \to \infty. \tag{4.43}$$

Therefore, one gets

$$F(M) \sim \zeta Z M, \qquad F(U) \sim \eta Z U, \qquad Z \to \infty, \tag{4.44}$$

where

$$\zeta = \frac{\Omega^2 - 1}{2(m+1)}, \qquad \eta = -\frac{\Omega^2 + 1}{2(m+1)}. \tag{4.45}$$

Together with the expression (4.23) for $\rho_o(z)$, expression (4.36) for the linearised kinetic energy density E_o gives

$$E_o^{1/2} \sim C^{st} Z^{m/2} e^{-Z/2} \left[\zeta\alpha_1 \frac{\Gamma(m+2)}{\Gamma(-\Upsilon)} Z^{-\Upsilon-m-1} e^Z + \eta\beta_1 Z^{\Upsilon+1}\right], \qquad z \to \infty. \tag{4.46}$$

Although the expression (4.46) appears not to have been derived explicitly in the literature, it is central to any formal understanding of the seismology of the Sun, as the remainder of this section will prove. The problem of a plane-parallel layer with constant gravity and a uniform temperature gradient was first discussed by Lamb (1932) and applied, for instance, by Pekeris (1948) in models of the Earth's atmosphere. Subsequently it was applied to the case of unstable g-modes by Spiegel and Unno (1962), and to the solar 5-min oscillations by Gough (1977), Christensen-Dalsgaard (1980) and Deubner and Gough (1984).

Now there are two possibilities for the linearised kinetic energy density E_o to vanish as $z \to \infty$, namely

- $\Gamma(-\Upsilon) \to \infty$, which is equivalent to $\Upsilon = 0$ or any positive integer,

  or

- $\alpha_1 = 0$.

At the surface boundary of the domain or where the domain is bounded by an interface in the interior, the Lagrangian pressure perturbation is required to be finite (*e.g.*, it is zero at the solar surface). This corresponds to a finite compressibility Δ.

Suppose Υ is an integer. Then the compressibility $\Delta \neq 0$. At the surface the requirement (4.34) of null Lagrangian rate of change in pressure perturbation is therefore satisfied only if the sound speed vanishes, *i.e.* $z_o = 0$. However these solutions would be finite and could be valid at an interface in the interior.

Suppose Υ is not an integer. Only the following special cases allow selection of a solution. First of all, at the surface boundary of the domain, if the third argument of the confluent hypergeometric functions was $Z_o = 2k_h z_o = 0$, the U function only diverges (see Equation (A.15)), causing the compressibility Δ (together with $\mathcal{P}$) to diverge. Thus it is necessary to choose the M function, so that the solution remains valid for all arguments Z. This case is only possible if the medium is bounded by an interface in the interior. Otherwise Υ has to be a non-negative integer. Secondly, if $z_o \neq 0$ at the surface boundary of the domain, then in a medium not bounded by any interface in the interior, the condition at ∞ applies and is satisfied only if one selects

the U function and discards the M function ($\alpha_1 = 0$).

Modes of oscillations in a simple polytrope Thus when the medium is not bounded by any interface in the interior and has vanishing sound speed at the surface, the condition to avoid that U diverges at the singular point $Z = Z_o = 0$ is to discard U and then the solution to Lamb's equation for a polytrope is

$$\Delta = \alpha_1 e^{-k_h z} M(-\Upsilon, m+2, 2k_h z)\,. \tag{4.47}$$

The boundary condition as $z \to \infty$ requires the M functions to terminate in the form of generalised Laguerre polynomials (see Equation 4.31), and the parameter Υ has to be a non-negative integer.

From Equation (4.25), this implies the eigenvalue equation

$$\frac{m+1}{\gamma}\Omega^4 - (m+2+2\Upsilon)\Omega^2 + k_h z \Omega_g^2(z) = 0\,, \tag{4.48}$$

for Υ zero or a positive integer. Equation (4.48) is quadratic in Ω^2, corresponding to the two classes of solutions — the acoustic and gravity waves — and revealing also the parabolic dependence $\omega^2 \sim k_h$. Setting $\Upsilon = n - 1$, with $n = 1, 2, 3...$, the discrete solutions in n are

$$\Omega^2 \equiv \Omega_n^2 = \frac{\gamma}{2}\frac{m}{(m+1)}\left[1 + \frac{2n}{m} \pm \sqrt{\left(1+\frac{2n}{m}\right)^2 - \frac{4}{m^2}\left(\frac{\gamma-1}{\gamma}m - \frac{1}{\gamma}\right)}\right]. \tag{4.49}$$

In the dimensional form, these solutions are $\omega \equiv \omega_n$ and are functions of k_h (or equivalently the degree l), and so they are also written $\omega \equiv \omega_{nl}$, with $n > 0$.

The solutions corresponding to p-modes are for the positive sign in front of the square root in Equation (4.49), *i.e.* with Ω_n^2 greater than the first term before the square root; and those corresponding to g-modes are for the negative sign, *i.e.* Ω_n^2 smaller than the first term. The g-modes may have $\omega_{nl}^2 > 0$, when they represent stationary gravity waves, or $\omega_{nl}^2 < 0$, when they represent convective modes, depending on whether ω_g^2 (or equivalently $(\gamma-1)m-1$) is positive or negative (see Equation (4.16)). In a convectively stable region, where the buoyancy frequency is real, Equation (4.49) indicates that buoyancy acts in opposition to the acoustic restoring force and decreases the frequency of the p-modes. On the other hand, the acoustic influence on g-modes augments $\omega_{n,l}$.

Radial order of a mode The integer n specifies the number of zeros the mode has within the cavity and is called the radial mode number (in contrast with the angular degree l). The ensemble of resonant modes with the same number of vertical wavelengths trapped in the cavity is often referred to as a 'vertical mode' (see Leibacher and Stein, 1981). In highly condensed polytropes, however, the behaviour of the Brunt-Väisälä frequency throughout the medium is a determining factor for the appearance of mixed modes, and the number of nodes cannot in general be used as a basis for classification of the modes. On the basis of phase diagrams (showing velocity versus pressure perturbations) used by geophysicists (see Eckart, 1960), Scuflaire (1974) gave a criterion to identify the order of the mode in presence of extra nodes. The phase differences between vertical displacement and pressure fluctuation decrease with height for p-modes and increase for g-modes. The number of zero-crossings of the pressure fluctuations (counting them positively or negatively according to the sense of rotation in the phase diagram) is used as an index to classify the modes.

Adiabatic polytrope Except very close to the surface, the stratification of the convective outer layers of the Sun is close to being adiabatic. With the assumption of an adiabatic stratification, one could expect to obtain a good approximation to the p-mode eigenfrequencies for sufficiently high l. In this case, the buoyancy (4.16) is reduced to zero, *viz.*

$$\omega_g^2 = 0\,, \tag{4.50}$$

requiring that the ratio of specific heats γ and the polytropic index m are related by (see also Section 1.3)

$$\gamma = \frac{m+1}{m}\,. \tag{4.51}$$

In particular, with $\gamma = \frac{5}{3}$, a plane-stratified polytrope is marginally stable to convective motions for polytropic index $m = \frac{3}{2}$. Also, the expression (4.25) for 2Υ reduces to

$$2\Upsilon = m\Omega^2 - (m+2)\,, \tag{4.52}$$

and the solutions of a field-free adiabatic polytrope are the p-modes, with

$$\Omega^2 = \Omega_n^2 \equiv 1 + \frac{2n}{m} \tag{4.53}$$

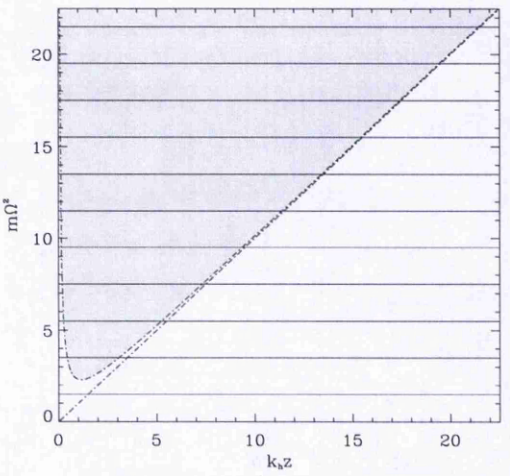

Figure 4.4: Normalised diagnostic diagram for a simple adiabatic polytrope, showing horizontal discrete ridges $m\Omega_n^2 = m + 2n$, the Lamb frequency $m\Omega^2 = k_h z$ and the acoustic cut-off from Equation (4.56), separating the shaded domain of propagation from the unshaded domain of evanescence.

for integer $n > 0$. For analytic understanding, the normalised form of the diagnostic diagram (see Figure 4.4) is convenient. The p-mode ridges are here horizontal and represent frequency levels $m\Omega_n^2$ of radial order n.

Equation (4.21) shows that the squared acoustic cut-off frequency, $\omega_a^2(z)$, decreases with depth as

$$\omega_a^2(z) = \frac{g(m+2)}{4z} \,. \tag{4.54}$$

Then the vertical wavenumber K (from Equation (4.7)) is given by

$$K^2(z) = \frac{k_h}{z}\left[m\Omega^2 - k_h z - \frac{m(m+2)}{4k_h z}\right] . \tag{4.55}$$

The normalised form (4.55) for $K^2(z)$ was first given in Foullon (1999, p.91, Equation (15)); although this is not a complicated expression to derive, it would seem not to have been given in any earlier publication. The last term in this expression corresponds to the contribution due to the acoustic cut-off. The division between propagation and evanescence occurs at a depth $z = z_t$ where $K^2(z_t) = 0$, *i.e.*

$$m\Omega^2 = k_h z_t + \frac{m(m+2)}{4k_h z_t} \,. \tag{4.56}$$

In neglecting the acoustic cut-off for small wavelengths ($k_h \to \infty$), or equivalently at large depth ($z \to \infty$), the depth z_t is determined by the Lamb frequency $\omega = k_h c_s(z_t)$;

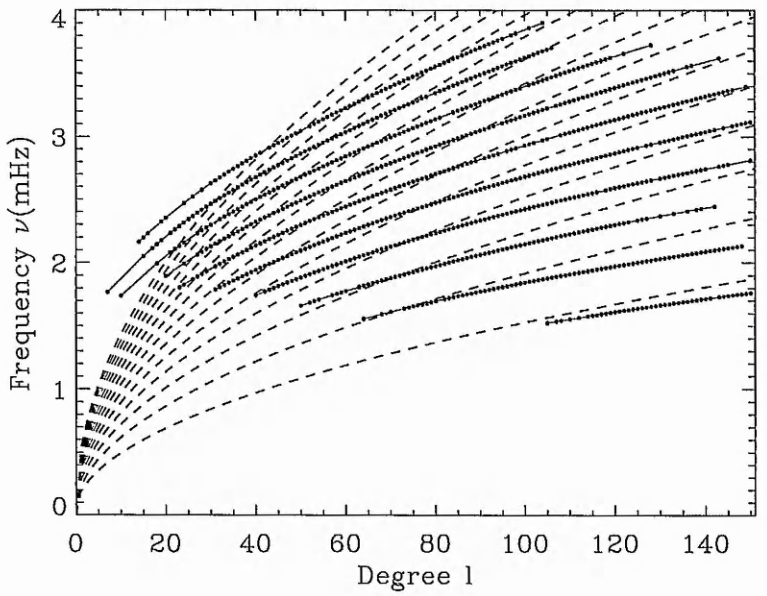

Figure 4.5: Dimensional diagnostic diagram showing in broken lines the discrete ridges for a simple adiabatic polytrope, as in Figure 4.4, and in plain lines the ridges drawn from GONG observations of power spectra (in full circles, from month 50 of GONG data, see Appendix A.2), as in Figure 1.3.

in normalised form, this is

$$m\Omega^2 = k_h z_t \,. \tag{4.57}$$

From Equation (4.53) and (4.57), it appears that the cavity depth of a mode of high radial order n or high degree l occurs at

$$z_t \simeq \frac{2n+m}{k_h} \sim \frac{2n+m}{l} \mathrm{R}_\odot \,. \tag{4.58}$$

It makes clear that high-degree modes are concentrated in the outer layers of the Sun (or Sun-like star). This result is also approximately true for a more realistic model, in agreement with a nearly adiabatic stratification of the upper convection zone (see Gough, 1990a). Figure 4.5 illustrates the similarity but also reveals a mismatch between the modes of the simple adiabatic polytrope and the p-mode observations. This mismatch may be attributed to boundary effects, which will be discussed in Chapter 9.

Outline p- and g-modes can also be obtained with an isothermal stratified atmosphere serving as a waveguide, as discussed in Chapter 6. But the plane-parallel polytrope with constant gravity and uniform temperature gradient is a convenient and more

realistic model to describe basic aspects of helioseismology. For this reason, it has been used extensively in model calculations of the effects of surface magnetism on p-modes (see Section 10.1) and, in this thesis, it will be used similarly to study the effect of internal magnetism (leaving aside studies of surface effects to other models). In Part III, it will be possible to insert a buried magnetic layer between two polytropic layers, or at least to form a hybrid model where the magnetic layer is in contact with a polytrope. Indeed, the presence of the polytrope in all these hybrid models is a principal ingredient in order to reproduce the solar p-modes as realistically as possible.

The properties of waves propagating in the buried magnetic field should be detailed beforehand. The next chapter inquires into the magnetohydrodynamics of isothermal layers and investigates specifically the case of constant Alfvén speed, restricting the propagation to parallel or perpendicular directions. The previous study of Lamb's equation rewritten in a standard form was useful to describe a number of properties of the wave in a field-free plasma stratified under gravity, and to reveal in particular the existence of acoustic and gravity cut-off frequencies. This will be a useful reference in the following investigation which, despite the simplification in choosing the plasma to be isothermal, is complicated by the presence of a magnetic field.

Chapter 5

Magnetohydrodynamics of Isothermal Layers

5.1 Preliminaries

1. Motivations and outline

The Lorentz force affects the equilibrium state of a conducting gas and is another restoring force of the dynamics. Recall that

$$\mathbf{j} \times \mathbf{B} = \frac{1}{\mu}(\mathbf{B} \cdot \nabla)\mathbf{B} - \frac{1}{\mu}\nabla(\frac{B^2}{2}), \tag{5.1}$$

so two terms emerge in the Lorentz force: the first term represents the effect of a tension in the magnetic field (this force appears when the field lines are curved) and the second term represents a magnetic pressure (this force appears when B varies from place to place).

For a straight horizontal magnetic field, the equilibrium of the plasma is not affected by the magnetic tension, since the equilibrium field lines are not curved. But, as revealed through the derivation of the fundamental equation (3.67) in Chapter 3, the magnetic tension plays a role in the dynamics of non-parallel propagating waves and surface waves which propagate at a magnetic interface. By contrast, the magnetic pressure affects both the equilibrium state and the dynamics of non-parallel propagating waves. Except for the surface waves, this chapter is devoted to these aspects. The

surface waves appear in layered models with a magnetic interface as will be seen in Section 8.2.

Originally, the dynamics of a horizontally stratified conducting medium was studied for constant sound and Alfven speeds by Yu (1965), who derived a general dispersion relation by performing Fourier analysis in all directions, including the vertical direction with wavenumber k_z. But even without Fourier analysis in the z-direction, the assumption of constant sound and Alfvén speeds allows in fact the reduction of the fundamental equation (3.67) to an equation with constant coefficients. Gaining an easier mathematical treatment, this approach may also be adequate and usefully exploited to model a thin buried layer of magnetic field in the solar interior; this will be discussed in Part III.

Studies of the 'magneto-atmospheric waves', as Yu called them, have either been based upon a dispersion relation for plane waves (as Yu did) or have sought analytical or numerical solutions for particular model atmospheres; see the review on magneto-atmospheric waves by Thomas (1983), where the results obtained by Yu (1965) may also be found.

Yu's dispersion relation (his Equation (26)) is of third order in ω^2, and therefore yields three different modes by which a wave can travel: the acoustic and gravity modes, modified by the presence of the magnetic field, and an hydromagnetic mode, which does not appear in the field-free case, and which is influenced only to a minor extent by compressibility and gravity.

While the fundamental equation (3.67) for perpendicular propagation ($k_x = 0$) is devoid of resonances, one can avoid the difficulties of a slow spectrum for parallel propagation ($k_y = 0$) if the plasma is isothermal and if in addition the horizontal magnetic field is structured in such a way as to produce a constant Alfvén speed, in which case the slow spectrum collapses to a single point ($\omega^2 = k_x^2 c_T^2$).

However, the problem of a cusp singularity $\omega_T^2 = k_x^2 c_T^2(z)$ for $k_y = 0$ is not avoided if the horizontal magnetic field is assumed to be uniform. For wave propagation parallel to a uniform horizontal magnetic field, an exact solution of the hypergeometric type may be given, as pointed out independently by Nye and Thomas (1976) and Adam (1977a).

For this profile, the correspondence between the cusp singularity and singularities in the hypergeometric equation is discussed in detail by Adam (1977a); later references are given in the review by Thomas (1983, p.336) and more recent discussions are undertaken by Vanlommel (2001). Such an atmosphere was also discussed in the context of vertical propagation by Musielak et al. (1989).

In the circumstances when the sound and Alfvén speeds are taken to be constant, there is no particular reason why the mathematical modelling of plane-stratified layers including a magnetic field started with the study of parallel propagation (Nye and Thomas, 1974; Campbell, 1987; Campbell and Roberts, 1989; Miles and Roberts, 1992) rather than perpendicular. The anisotropic nature of the magnetic field was ignored and the two dimensionality in the (x, z) plane was simply assumed as an absence of preferential horizontal direction with respect to the vertical stratification (Campbell, 1987, p. 32) . When more sophisticated models were developed, with non-constant profiles for the Alfvén speed, the assumption of parallel propagation was maintained (Nye and Thomas, 1976; Adam, 1977a; Evans, 1990; Miles et al., 1992; Vanlommel, 2001). Either the belief that 'the y-dependence of perturbation quantities in no way affects the basic phenomenon of critical levels' (Adam, 1977a, p. 294) went on for a long time or there was lack of specifying and establishing that, in order to avoid any interaction of acoustic oscillations with local Alfvén oscillations, it was also possible to consider the case of perpendicular propagation ($k_x = 0$) (this was not mentioned so far, for instance in the recent work done by Tirry (1998), Pintér (1999) or Vanlommel (2001), who all argue that the case of parallel propagation ($k_y = 0$) is the only solution to avoid the Alfvén singularity). In passing to non-parallel propagation in the horizontal direction, the analysis was extended to arbitrary (k_x, k_y) (Gonzalez and Gratton, 1991; Jain and Roberts, 1994a). Despite a preliminary investigation to the case for which $k_x = 0$ given by Chen and Lykoudis (1972), such models did not benefit from earlier results studying the wave propagation perpendicular to the magnetic field lines, altough those might have been easier to obtain in the first place.

In other respects, however, for analyses based upon a local dispersion relation for plane waves, the difference between parallel and perpendicular propagation was already

addressed by Yu (1965), who found that the magneto-gravity mode changes its character at high wavenumbers for perpendicular propagation, 'because of the binding of the magnetic lines, which becomes much larger than the other forces and consequently dominates the motion'. Also Gilman (1970), who explored the criterion for instability through magnetic buoyancy in stellar interiors, illustrated the case of constant sound and Alfvén speeds, and particularly the difference between the respective limits for parallel and perpendicular motions. Yu and Gilman's results were recovered recently by Pintér et al. (1999). Besides, it seems that considering the case of perpendicular propagation to a horizontal magnetic field presents some advantages to understand some solar phenomena (see Adam, 1977b).

There is no doubt that the analysis for the case of perpendicular propagation is complementary to the study of wave propagation in the parallel direction. It turns out that the assumption of parallel propagation has some important physical drawbacks, which could not be ascertained without discussing the case of perpendicular propagation.

In the remainder of this section, the equilibrium state and the stability criterion are presented. Then, in Section 5.2, some understanding to the dynamics of plane-stratified magnetic layers will be acquired by reducing the governing wave equation derived in Chapter 3 for respectively parallel ($k_y = 0$) and perpendicular ($k_x = 0$) propagations. The mathematical analysis of these cases will be simplified by choosing the plasma to be isothermal and structured in such a way as to produce a constant Alfvén speed. Where appropriate, this analysis will be discussed in relationship with the physical results and references previously introduced.

2. Equilibrium state

Magnetically-modified scale-height The pressure distribution within an electrically conducting gas is affected by the presence of magnetic field. Magnetostatic pressure balance for a horizontal magnetic field requires (see Equation (3.29))

$$\frac{d}{dz}\left(p_o(z) + \frac{B_o^2(z)}{2\mu}\right) = g\rho_o(z)\,, \tag{5.2}$$

which is rewritten in the form

$$\frac{d}{dz}\left[\left(c_s^2(z)+\frac{\gamma}{2}v_A^2(z)\right)\frac{\rho_o(z)}{\gamma}\right]=g\rho_o(z)\,. \tag{5.3}$$

One particular consequence of magnetostatic pressure balance is that a horizontal field which increases with depth is able to 'hold up' more mass against gravity than would be possible in its absence. This shows up particularly in the special case where the plasma is isothermal and the magnetic field is structured in such a way as to produce a constant Alfvén speed. If

$$c_c=\sqrt{\frac{\gamma p_o(z)}{\rho_o(z)}} \tag{5.4}$$

denotes the adiabatic sound speed of the isothermal medium and

$$v_A=\frac{B_o(z)}{\sqrt{\mu\rho_o(z)}} \tag{5.5}$$

is its constant Alfvén speed, then Equation (5.3) can be rewritten as

$$\left(\frac{c_c^2}{\gamma}+\frac{v_A^2}{2}\right)\frac{d\rho_o(z)}{dz}=g\rho_o(z)\,. \tag{5.6}$$

Hence, in such case, the density profile from an arbitrary reference depth $z=z_p$ is

$$\rho_o(z)=\rho_o(z_p)e^{\frac{z-z_p}{H_o}}\,, \tag{5.7}$$

where the magnetically modified scale-height H_o obtained from Equation (5.6) is given by

$$\frac{1}{H_o}=\frac{\rho_o'}{\rho_o}=\frac{g}{\frac{c_c^2}{\gamma}+\frac{v_A^2}{2}}\,. \tag{5.8}$$

To compare the scale-height H_o with the scale-height H of an isothermal medium in the absence of a magnetic field, given by (see Equation (1.58))

$$\frac{1}{H}=\frac{g\gamma}{c_c^2}\,, \tag{5.9}$$

it is useful to define a magnetically-modified adiabatic exponent Γ_o, through

$$\frac{1}{H_o}=\frac{g\Gamma_o}{c_c^2}\,. \tag{5.10}$$

Then the magnetically-modified adiabatic exponent is

$$\Gamma_o=\frac{\gamma}{1+\frac{\gamma}{2\beta}}\,,\quad \beta=\frac{c_c^2}{v_A^2}\,, \tag{5.11}$$

where β (defined in the general case in Equation (3.31)) is the squared ratio of the sound speed c_c to the Alfvén speed v_A.

In the presence of a magnetic field, the density scale-height H_o is increased from H by a factor $1 + \frac{\gamma}{2\beta}$. Keeping in mind that the inverse of the density scale-height is a measure of the steepness of the density gradient, this corresponds to a decrease of the density gradient in the presence of a magnetic field, *viz.*

$$\frac{H}{H_o} = \frac{\Gamma_o}{\gamma} = \frac{1}{1 + \frac{\gamma}{2\beta}} < 1 . \tag{5.12}$$

This is due to the fact that the mass of the medium is supported in part by the magnetic pressure.

Other equilibrium profiles Note that the density scale-height equals the total pressure scale-height,

$$\begin{aligned} \frac{1}{H_o} &= \frac{p'_{oT}}{p_{oT}} \\ &= \frac{p'_o + p'_m}{p_o + p_m} . \end{aligned} \tag{5.13}$$

The condition of isothermality (that $\gamma p_o(z)/\rho_o(z)$ is constant), means that the density and plasma pressure vary on the same scale-height (see also the fundamental adiabatic relation (1.54)), *viz.*

$$\frac{1}{H_o} = \frac{p'_o}{p_o} . \tag{5.14}$$

Therefore in such medium the plasma pressure $p_o(z)$, the magnetic pressure $p_m(z)$, the total pressure $p_{oT}(z)$ and the density $\rho_o(z)$ all vary on the same scale-height H_o.

Moreover, from the particular condition of constant Alfvén speed (5.5), the profile for the magnetic field strength is a square root function of the density profile ($B_o \propto \rho_o^{\frac{1}{2}}$). Thus the magnetic field strength $B_o(z)$ increases with depth and varies on a scale of $2H_o$, *viz.*

$$B_o(z) = B_o(z_p) e^{\frac{z - z_p}{2H_o}} . \tag{5.15}$$

3. Stability criterion

General criterion for convective stability The decrease of the density gradient by the presence of the magnetic field plays a major role in destabilising the stratified

medium. Convective instability in the case of a horizontal magnetic field was first considered by Newcomb (1961) and derived from the energy principle of Bernstein et al. (1958); see, for example, the discussion in Appendix B of Hughes and Cattaneo (1987). Yu (1966) interpreted the results of Newcomb by following the reasoning of Schwarzschild (1958). Newcomb's general criterion for stability is that

$$\frac{1}{\rho_o}\frac{d\rho_o}{dz} > \frac{\rho_o g}{\gamma p_o}. \tag{5.16}$$

This is the most stringent condition which corresponds to the stability criterion against the most unstable displacement. This displacement is the 'quasi-interchange' displacement, that reduces to pure translations in the limit of $k_x \to 0$ (Newcomb, 1961; Yu, 1966). Yu (1965) also shows that it is the hydromagnetic mode which induces the instability with $k_x \to 0$. For perpendicular propagation ($k_y \to \infty$, $k_x = 0$), the hydromagnetic mode reduces to a neutral stable mode, in which the motion is purely translational along the magnetic field lines. Hence, the perturbation for which the medium is the least stable corresponds to an interchange of long tubes of magnetic lines.

Newcomb's criterion may be viewed in terms of the physical significance of the magnetic buoyancy frequency $\tilde{\omega}_{g\|}$ for parallel propagation. For the case of an isothermal layer with constant Alfvén speed, this magnetic buoyancy frequency (see the connection with the Brunt-Väisälä frequency ω_g of Equation (1.3)) is given by:

$$\begin{aligned} \tilde{\omega}_{g\|}^2 &= g\left(\frac{1}{\rho_o}\frac{d\rho_o}{dz} - \frac{\rho_o g}{\gamma p_o}\right) \\ &= \frac{g}{H_o} - \frac{g^2}{c_c^2} \\ &= \frac{g^2}{c_c^2}(\Gamma_o - 1)\,. \end{aligned} \tag{5.17}$$

The buoyancy frequency $\tilde{\omega}_{g\|}$ relates to g-modes ($\tilde{\omega}_{g\|}^2 > 0$) and instability ($\tilde{\omega}_{g\|}^2 < 0$). Thus the stability criterion is

$$\frac{1}{\Gamma_o} = \frac{gH_o}{c_c^2} < 1\,, \qquad i.e. \quad \Gamma_o > 1\,. \tag{5.18}$$

This result is also obtained by Yu (1965) (see his Equation (28)) from derivation of the dispersion relation for an infinite medium in three dimensions.

This gives stability (see also Equation (30) in Yu, 1965) for

$$\gamma > \frac{1}{1-\frac{1}{2\beta}}, \tag{5.19}$$

or instability (as in Gilman, 1970, §VI (a), on top of p.1025) for

$$\frac{1}{\beta} > 2(1-\gamma^{-1}). \tag{5.20}$$

Another way to express the criterion is to consider the critical state $\tilde{\omega}_{g\|} = 0$ (see also Thomas and Nye, 1975, Equation (7)), for which

$$\beta_{crit} = \frac{\gamma}{2(\gamma-1)}. \tag{5.21}$$

All the above criteria are equivalent, but might not appear like this in the literature.

The criterion (5.19) is useful to see that when no magnetic field is present ($\beta \to \infty$), the medium is stable unless $\gamma < 1$. This is consistent with Schwarzchild's criterion for convective stability under adiabatic perturbations in the absence of magnetic field (*i.e.* Equation (5.16) in the field-free limit):

$$\frac{1}{\rho_o}\frac{d\rho_o}{dz} > \frac{1}{\gamma p_o}\frac{dp_o}{dz}. \tag{5.22}$$

Indeed, in the isothermal case the density and pressure scale-heights being equal, the criterion for stability, $\gamma > 1$, is recovered.

Destabilising influence of magnetism in a stratified medium For finite β, the minimum value of γ required for a stable medium increases and approaches infinity as $\beta \to \frac{1}{2}$. This means that the presence of the magnetic field tends to destabilise the medium, and the larger the field strength, the more potentially unstable the medium becomes.

The reason for the destabilisation due to the magnetic field can be seen by using Newcomb's criterion (5.16) or inspecting the buoyancy frequency expression (5.17). The second term is unaffected by the presence of the magnetic field, provided the sound speed remains the same, whereas the magnitude of the first term (the density gradient or the inverse of the density scale-height) is decreased by the presence of the magnetic field. As a result $\tilde{\omega}_{g\|}^2 < \omega_g^2$. Indeed, the density gradient is not as steep as in

the field-free case (see Equation (5.12)). This decrease of the density gradient makes the medium less stable.

Furthermore, using the equation of magnetostatic equilibrium (5.2), Newcomb's stability criterion (5.16) may alternatively be expressed in a more explicit way, *viz.*

$$\frac{g}{c_s^2}\frac{d}{dz}\ln(B_o) < \frac{\omega_g^2}{v_A^2}, \tag{5.23}$$

as was shown by Thomas and Nye (1975) or Acheson (1979). Here the right-hand side represents the stabilising effect of conventional buoyancy forces, while the left-hand side represents the destabilising influence of the magnetic field distribution that diminishes sufficiently rapidly with height.

Thus magnetism has a destabilising influence in a stratified medium as long as the horizontal magnetic field is nonuniform and $\frac{dB_o}{dz} > 0$. This is the case for the isothermal medium with constant Alfvén speed (see Equation (5.15)). A field that decreases with depth (or increases with height), *i.e.* with $\frac{dB_o}{dz} < 0$, can on the contrary stabilise the medium (see, *e.g.*, Thomas and Nye, 1975). Instabilities due to magnetic buoyancy were originally proposed by Parker (1955) as the cause for the rising of magnetic flux tubes from the base of the convection zone to the solar surface, and their eventual emergence as active regions at the surface of the Sun. The distortion of field lines due to magnetic buoyancy has been extensively studied to explain the escape of magnetic flux from stellar interiors (Gilman, 1970; Acheson, 1979; Hughes, 1985), but was originally studied as responsible for the structure of interstellar magnetic field (Parker, 1966; 1967).

Undular and interchange modes Without the restriction to constant sound and Alfvén speed, the Parker instability is more generally classified into two modes depending on the geometric nature of the perturbation and underlying a two-dimensional view of the possible dynamics (see, *e.g.*, Hughes and Cattaneo, 1987). One is the translational or interchange mode (or Rayleigh-Taylor type mode), which has no variation in the field-aligned direction (the perturbed magnetic field lines remain in the direction of the field). The other is the undular mode, in which the perturbed field lines are wavy. A mixed mode containing both undular and interchange characteristics exists if

the equilibrium has line-tied boundaries in the x-direction.

With no variation in the field-aligned direction, the most unstable modes are those for which the wavenumber in the $\mathbf{g} \times \mathbf{B_o}$-direction is infinitely large (*i.e.* $k_y \to \infty$). In this respect, interchange (or Rayleigh-Taylor type) modes are more unstable than undular modes (Yu, 1965; Parker, 1967; Gilman, 1970; Hughes, 1985; Hughes and Cattaneo, 1987; Pintér et al., 1999). Similarly, mixed modes are the most unstable for $k_y \to \infty$ (Parker, 1967).

But this first picture of the effect of magnetic buoyancy should be taken with care. In particular, as was pointed out by Hughes and Cattaneo (1987), the magnetic instability for undular modes as applied to a magnetic layer is interpreted erroneously from considering the behaviour of an isolated magnetic flux tube. Moreover, while undular modes rely on an increase of B_o with depth, interchange modes rely on an increase of B_o/ρ_o with depth. As was shown by Shubert (1968) by a linear stability analysis or Acheson (1979) by a simple interchange argument, the criterion of unstable interchange modes is

$$\frac{g}{c_s^2}\frac{d}{dz}\ln\left(\frac{B_o}{\rho_o}\right) > \frac{\omega_g^2}{v_A^2}. \tag{5.24}$$

Hence, for only slightly less stringent conditions than those needed for interchange modes, undular modes can set in when interchange modes are stable (Acheson, 1979; Hughes, 1985; Hughes and Cattaneo, 1987). In fact, for the isothermal medium threaded by a horizontal magnetic field with constant Alfvén speed,

$$\frac{d}{dz}\ln\left(\frac{B_o}{\rho_o}\right) = -\frac{1}{2H_o} < 0\,. \tag{5.25}$$

Thus, before considering the stability aspects of this magnetic layer as part of a more complex model, which will be the subject of Section 7.2, the general stability criterion will prove to be sufficient for the following discussion.

5.2 Wave equations and cut-off frequencies

1. General wave equation and solutions

Before reducing the governing wave equation derived in Chapter 3 for respectively parallel ($k_y = 0$) and perpendicular ($k_x = 0$) propagations, it is instructive to simplify the fundamental equation (3.67) when the sound and Alfvén speeds are constant, *viz.*

$$\frac{d^2V_z}{dz^2} + \frac{1}{H_o}\frac{dV_z}{dz} + A_oV_z = 0\,, \tag{5.26}$$

where

$$A_o = \frac{A_2}{A_1} = \frac{\omega^2 - k_x^2c_c^2 - k_y^2c_\perp^2}{c_\perp^2} + \frac{k_x^2c_c^2 + k_y^2c_\perp^2}{c_\perp^2(\omega^2 - k_x^2v_A^2)}\left[\frac{g}{H_o} - \frac{g^2(k_x^2+k_y^2)}{k_x^2c_c^2 + k_y^2c_\perp^2}\right]. \tag{5.27}$$

Standard form With the transformation $W(z) = V_z e^{\frac{z-z_p}{2H_o}}$, where z_p is an arbitrary reference depth in the stratified medium, Equation (5.26) assumes the standard form

$$\frac{d^2W(z)}{dz^2} + \kappa^2 W(z) = 0\,; \tag{5.28}$$

κ^2 is independent of depth z and, after identification of its different components, can be cast in a form that allows the connection to the K^2 in the general field-free case (see Equation (4.7)), *viz.*

$$\begin{aligned}
\kappa^2 &= A_o - \frac{1}{4H_o^2} \\
&= \frac{\omega^2 - \tilde{\omega}_a^2}{c_\perp^2} + \left(\frac{k_x^2c_c^2 + k_y^2c_\perp^2}{c_\perp^2}\right)\frac{\tilde{\omega}_g^2 - (\omega^2 - k_x^2v_A^2)}{(\omega^2 - k_x^2v_A^2)}\,, \qquad (5.29)\\
&= \frac{\frac{\omega^2}{\varpi^2}(\omega^2 - k_x^2v_A^2) - \omega_{ao}^2}{c_c^2} + \left(\frac{k_x^2c_c^2 + k_y^2c_\perp^2}{c_\perp^2}\right)\frac{\tilde{\omega}_g^2 - (\omega^2 - k_x^2v_A^2)}{(\omega^2 - k_x^2v_A^2)}\,, \\
&= \frac{\frac{\omega^4}{\varpi^2} - \omega_{ao}^2}{c_c^2} + \left(\frac{k_x^2c_c^2 + k_y^2c_\perp^2}{c_c^2}\right)\frac{\tilde{\omega}_g^2 - \varpi^2}{\varpi^2} + k_y^2\frac{v_A^2}{c_c^2}\frac{\omega^2}{(\omega^2 - k_x^2v_A^2)}\,. \qquad (5.30)
\end{aligned}$$

Here $\tilde{\omega}_a$ is the magnetically modified acoustic cut-off for an isothermal medium, defined through

$$\tilde{\omega}_a^2 = \frac{c_\perp^2}{4H_o^2} = \omega_{ao}^2\frac{\varpi^2}{\omega^2 - k_x^2v_A^2}\,, \tag{5.31}$$

$$\text{with} \qquad \omega_{ao}^2 = \frac{c_c^2}{4H_o^2} = \frac{g^2\Gamma_o^2}{4c_c^2}\,; \tag{5.32}$$

	$v_A = 0$	$k_y = 0$	$k_x = 0$
$c_\perp^2$	c_c^2	$c_\perp^2$	$c_c^2 + v_A^2$
H_c	H	H_o	H_o
ϖ^2	ω^2	ϖ^2	$\frac{(c_c^2+v_A^2)}{c_c^2}\omega^2$
$\tilde{\omega}_a^2$	$\omega_a^2 = \frac{c_c^2}{4H^2}$	$\tilde{\omega}_a^2$	$\tilde{\omega}_{a\perp}^2 = \frac{c_c^2+v_A^2}{4H_o^2}$
$\tilde{\omega}_g^2$	$\omega_g^2 = \frac{g}{H} - \frac{g^2}{c_c^2}$	$\tilde{\omega}_{g\|}^2 = \frac{g}{H_o} - \frac{g^2}{c_c^2}$	$\tilde{\omega}_{g\perp}^2 = \frac{g}{H_o} - \frac{g^2}{c_c^2+v_A^2}$
κ^2	$\frac{\omega^2-\omega_a^2}{c_c^2} + k_h^2\frac{\omega_g^2-\omega^2}{\omega^2}$	$\frac{\frac{\omega^4}{\varpi^2}-\omega_{ao}^2}{c_c^2} + k_x^2\frac{\tilde{\omega}_{g\|}^2-\varpi^2}{\varpi^2}$	$\frac{\omega^2-\tilde{\omega}_{a\perp}^2}{c_c^2+v_A^2} + k_y^2\frac{\tilde{\omega}_{g\perp}^2-\omega^2}{\omega^2}$
$\lim_{k_h\to 0}\omega_+^2$	$\omega_a^2 = \frac{c_c^2}{4H^2}$	$\tilde{\omega}_{a\perp}^2 = \frac{c_c^2+v_A^2}{4H_o^2}$	$\tilde{\omega}_{a\perp}^2 = \frac{c_c^2+v_A^2}{4H_o^2}$
$\lim_{k_h\to\infty}\omega_+^2$	$k_h^2 c_c^2$	$k_x^2\max(c_c^2, v_A^2)$	$k_y^2(c_c^2 + v_A^2)$
$\lim_{k_h\to 0}\omega_-^2$	0	0	0
$\lim_{k_h\to\infty}\omega_-^2$	0	$k_x^2\min(c_c^2, v_A^2)$	0

Table 5.1: Elements of the magneto-atmospheric wave equation and associated cut-off frequencies in certain limiting cases, corresponding to the field-free limit ($v_A = 0$), parallel propagation ($k_y = 0$) and perpendicular propagation ($k_x = 0$).

$\tilde{\omega}_g$ is the magnetically modified buoyancy frequency given by

$$\tilde{\omega}_g^2 = \frac{g}{H_o} - \frac{g^2(k_x^2 + k_y^2)}{k_x^2 c_c^2 + k_y^2 c_\perp^2}\,; \tag{5.33}$$

ϖ^2 was defined in Section 3.2 (Equation (3.61)) and is the squared magnetically modified frequency:

$$\begin{aligned}\varpi^2 &= \frac{c_c^2 + v_A^2}{c_c^2}(\omega^2 - k_x^2 c_T^2) \\ &= \omega^2\left(1 + \frac{1}{\beta}\right) - k_x^2 v_A^2\,.\end{aligned} \tag{5.34}$$

It can easily be verified that indeed the two vertical wavenumbers K and κ are equal in the isothermal field-free case. The different forms (5.29) and (5.30) of κ^2 give an explicit magnetic version of K^2 which may prove more appropriate for parallel (Equation (5.30)) or perpendicular propagations (Equation (5.29)). Table 5.1 gives a summary of the elements of the magneto-atmospheric wave equation for the isothermal field-free limit, as well as for further limiting cases, namely for parallel and perpendicular propagation. Associated cut-off frequencies, added in this table for completeness, are discussed later in this section.

Solutions Note that it is not necessary to develop a differential equation similar to the Lamb equation, in terms of $\mathcal{P}_T$ in a magnetic region. Indeed, wary of the fact that its expression is rather complicated, once the solution for V_z is obtained, which has the general form

$$V_z = e^{-\frac{z}{2H_o}} \left[D_1 e^{i\kappa z} + D_2 e^{-i\kappa z} \right] , \tag{5.35}$$

where D_1 and D_2 are arbitrary constants, it is possible to obtain $\mathcal{P}_T$ (from Equation (3.66)), which is a linear combination of V_z and $\frac{dV_z}{dz}$.

Evanescent modes ($\kappa^2 < 0$, *i.e.* $4A_oH_o^2 < 1$) are of the form

$$V_z = D_1 e^{\Lambda^+ z} + D_2 e^{\Lambda^- z} , \tag{5.36}$$

with

$$\Lambda^{\pm} = \frac{-1 \pm \sqrt{1 - 4A_oH_o^2}}{2H_o} = \frac{-1}{2H_o} \pm \kappa_e , \tag{5.37}$$

where

$$\kappa_e = \frac{\sqrt{1 - 4A_oH_o^2}}{2H_o} . \tag{5.38}$$

Oscillatory modes ($\kappa^2 > 0$, *i.e.* $4A_oH_o^2 > 1$) are of the form

$$V_z = e^{\frac{-z}{2H_o}} \left[D_1 \sin(\kappa_b z) + D_2 \cos(\kappa_b z) \right] . \tag{5.39}$$

where

$$\kappa_b = \frac{\sqrt{4A_oH_o^2 - 1}}{2H_o} . \tag{5.40}$$

2. Propagation behaviour and cut-off frequencies

The sign of κ^2 indicates the spatial behaviour of the modes. The cut-off frequencies separating domains of evanescence and oscillatory propagation may be conveniently studied in the cases of parallel and perpendicular propagation.

Parallel propagation Where the medium is stable (*i.e.* when $\tilde{\omega}_{g\|}^2 > 0$), an examination of κ^2 for $k_y = 0$ gives

$$\kappa^2 = \frac{\frac{\omega^4}{\varpi^2} - \omega_{ao}^2}{c_c^2} + k_x^2 \frac{\tilde{\omega}_{g\|}^2 - \varpi^2}{\varpi^2} , \tag{5.41}$$

which shows that if $\varpi^2 < 0$, *i.e.* $\omega^2 < k_x^2 c_T^2$, then $\kappa^2 < 0$. Therefore low-frequency MHD modes of phase speed less than the cusp speed have an evanescent behaviour. The cusp frequency $\omega_T = k_x c_T$ is a cut-off, which does not show up in a field-free region, where the cusp speed is reduced to zero, nor for perpendicular motions ($k_x = 0$).

For modes with $\varpi^2 > 0$, *i.e.* with frequencies above the cusp frequency, then the reasoning is similar to that presented in Section 4.1 for the field-free Lamb's Equation, but free from the vertical dependence of the cut-off frequencies. Two different regimes satisfy the condition of wave propagation ($\kappa^2 > 0$): at large frequency ω, in the regime of magnetoacoustic modes; at small frequency $\omega > \omega_T$ in the regime of magnetogravity modes.

As well as below the cusp frequency ω_T, evanescent modes ($\kappa^2 < 0$) exist between the two cut-offs of high and low-frequency, given by the equation $\kappa^2 = 0$ or $4A_o{H_o}^2 = 1$, *viz.*

$$\begin{aligned} & \omega^4 - (k_x^2 c_c^2 + \omega_{ao}^2)\varpi^2 + k_x^2 c_c^2 \tilde{\omega}_{g\|}^2 && = 0\,, \\ \textit{i.e.}\quad & \omega^4 - \left(1 + \tfrac{1}{\beta}\right)\left(k_x^2 c_c^2 + \omega_{ao}^2\right)\omega^2 + k_x^2 c_c^2 \left[\tilde{\omega}_{g\|}^2 + \tfrac{1}{\beta}\left(k_x^2 c_c^2 + \omega_{ao}^2\right)\right] && = 0\,, \\ \text{or}\quad & \omega^4 - \left(c_c^2 + v_A^2\right)\left(k_x^2 + \tfrac{1}{4H_o^2}\right)\omega^2 + k_x^2 c_c^2 \left[\tilde{\omega}_{g\|}^2 + v_A^2\left(k_x^2 + \tfrac{1}{4H_o^2}\right)\right] && = 0\,. \end{aligned} \quad (5.42)$$

The two solutions of the ω^2-quadratic equation (5.42) are denoted ω_+^2 and ω_-^2 and correspond to the 'plus' and 'minus' modes with no vertical propagation discussed in Nye and Thomas (1974), where the wave equation is Fourier analysed in the vertical direction. Here, whatever the form,

$$\begin{aligned} \omega_\pm^2 &= \frac{1}{2}\left(1 + \frac{1}{\beta}\right)\left(k_x^2 c_c^2 + \omega_{ao}^2\right) \\ &\quad \pm \frac{1}{2}\sqrt{\left(1 + \frac{1}{\beta}\right)^2 \left(k_x^2 c_c^2 + \omega_{ao}^2\right)^2 - 4k_x^2 c_c^2 \left[\tilde{\omega}_{g\|}^2 + \frac{1}{\beta}\left(k_x^2 c_c^2 + \omega_{ao}^2\right)\right]} \\ &= \frac{1}{2}\left(c_c^2 + v_A^2\right)\left(k_x^2 + \frac{1}{4H_o^2}\right) \\ &\quad \pm \frac{1}{2}\sqrt{\left(c_c^2 + v_A^2\right)^2 \left(k_x^2 + \frac{1}{4H_o^2}\right)^2 - 4k_x^2 c_c^2 \left[\tilde{\omega}_{g\|}^2 + v_A^2\left(k_x^2 + \frac{1}{4H_o^2}\right)\right]}\,. \end{aligned} \quad (5.43)$$

Perpendicular propagation For $k_x = 0$, the magnetically modified Brunt-Väisälä frequency for perpendicular propagation, $\tilde{\omega}_{g\perp}$ (see Chen and Lykoudis, 1972), may be

written in various forms, *viz.*

$$\tilde{\omega}_{g\perp}^2 = \frac{g}{H_o} - \frac{g^2}{c_c^2 + v_A^2} = \frac{g^2}{c_c^2}\left[\Gamma_o - \frac{1}{1+\frac{1}{\beta}}\right] \tag{5.44}$$

$$= \frac{g}{H_o} - \frac{1}{\left(1+\frac{1}{\beta}\right)}\frac{g^2}{c_c^2} = \tilde{\omega}_{g\parallel}^2 + \frac{1}{(\beta+1)}\frac{g^2}{c_c^2}. \tag{5.45}$$

One may show that $\tilde{\omega}_{g\parallel}^2 \leq \tilde{\omega}_{g\perp}^2 \leq \omega_g^2$.

Moreover, for $k_x = 0$, ϖ^2 reduces to

$$\varpi^2 = \omega^2 \frac{c_c^2 + v_A^2}{c_c^2} = \omega^2\left(1 + \frac{1}{\beta}\right), \tag{5.46}$$

so that there exists no frequency domain where $\varpi^2 < 0$, contrary to the case of parallel propagation. As a result, one should not expect to find for perpendicular propagation the evanescent domain below the cusp frequency that exists for parallel propagation.

The vertical wavenumber of the standard form (5.28) of the wave equation is given by

$$\kappa^2 = \frac{\frac{\omega^4}{\varpi^2} - \omega_{ao}^2}{c_c^2} + k_y^2 \frac{\tilde{\omega}_{g\perp}^2 - \omega^2}{\omega^2}. \tag{5.47}$$

Rewritten in the form

$$\kappa^2 = \omega^2\left[\frac{k_y^2}{\omega^2} - \frac{1}{c_c^2\left(1+\frac{1}{\beta}\right)}\right]\left(\frac{\omega_{gy}^2}{\omega^2} - 1\right) - \frac{1}{4}\left[\frac{\tilde{\omega}_{g\perp}^2}{g} - \frac{g}{c_c^2\left(1+\frac{1}{\beta}\right)}\right]^2, \tag{5.48}$$

one obtains Equation (20) of Chen and Lykoudis (1972).

Because $\tilde{\omega}_{g\perp}^2 \geq \tilde{\omega}_{g\parallel}^2$, $\tilde{\omega}_{g\perp}^2$ is always positive where $\tilde{\omega}_{g\parallel}^2 > 0$. For stable modes ($\omega^2 > 0$), Equation (5.47) indicates the two regimes for wave propagation ($\kappa^2 > 0$) and the regime for evanescence ($\kappa^2 < 0$) in the direction perpendicular to the magnetic field. The equation $\kappa^2 = 0$, *viz.*

$$\begin{aligned} \omega^4 - \tfrac{c_c^2+v_A^2}{c_c^2}(k_y^2 c_c^2 + \omega_{ao}^2)\omega^2 + k_y^2\left(c_c^2 + v_A^2\right)\tilde{\omega}_{g\perp}^2 &= 0, \\ i.e.\quad \omega^4 - \left(c_c^2 + v_A^2\right)\left(k_y^2 + \tfrac{1}{4H_o^2}\right)\omega^2 + k_y^2\left(c_c^2 + v_A^2\right)\tilde{\omega}_{g\perp}^2 &= 0, \end{aligned} \tag{5.49}$$

yields the two cut-off frequencies

$$\begin{aligned} \omega_\pm^2 &= \frac{1}{2}\left(1+\frac{1}{\beta}\right)\left(k_y^2 c_c^2 + \omega_{ao}^2\right) \pm \frac{1}{2}\sqrt{\left(1+\frac{1}{\beta}\right)^2\left(k_y^2 c_c^2 + \omega_{ao}^2\right)^2 - 4k_y^2(c_c^2 + v_A^2)\tilde{\omega}_{g\perp}^2} \\ &= \frac{1}{2}\left(c_c^2 + v_A^2\right)\left[k_y^2 + \frac{1}{4H_o^2} \pm \sqrt{\left(k_y^2 + \frac{1}{4H_o^2}\right)^2 - \frac{4k_y^2\tilde{\omega}_{g\perp}^2}{(c_c^2 + v_A^2)}}\right]. \end{aligned} \tag{5.50}$$

3. Asymptotic behaviour

The asymptotic behaviour of ω_+ and ω_- in the long and short horizontal wavelength limits is useful to place bounds on the domains where the modes (respectively, magnetoacoustic and magnetogravity) may propagate. It is also instructive to see whether these bounds differ between parallel and perpendicular propagation.

Parallel propagation The asymptotic behaviour of ω_+ and ω_- in the long and short horizontal wavelength limits is such that

$$\omega_\pm^2 \sim \frac{1}{2}\left[\frac{c_c^2+v_A^2}{4H_o^2} \pm \frac{c_c^2+v_A^2}{4H_o^2}\right], \quad \text{for} \quad k_x \to 0\,; \tag{5.51}$$

$$\omega_\pm^2 \sim \frac{k_x^2}{2}\left[\left(c_c^2+v_A^2\right) \pm \sqrt{\left(c_c^2-v_A^2\right)^2}\right], \quad \text{for} \quad k_x \to \infty\,. \tag{5.52}$$

Hence as $k_x \to 0$, the magnetoacoustic mode has a finite cut-off frequency, below which the mode is evanescent, while the magnetogravity mode approaches zero, *viz.*

$$\omega_+^2 \sim \frac{c_c^2+v_A^2}{4H_o^2}, \qquad \omega_-^2 \sim 0\,. \tag{5.53}$$

For $k_x \to \infty$, the plus and minus cut-off frequencies approach the dispersion lines for the pure acoustic and pure Alfvén modes, *viz.*

$$\omega_+^2 \sim k_x^2 \max(c_c^2, v_A^2)\,, \qquad \omega_-^2 \sim k_x^2 \min(c_c^2, v_A^2)\,. \tag{5.54}$$

For a weak magnetic field, the high frequency separation ω_+ approaches the line $\omega = k_x c_c$ (the Lamb mode in the field-free case) from above, and the low frequency separation ω_- approaches the line $\omega = k_x v_A$ also from above. This can be seen from examining Equation (5.41) for $\kappa^2 = 0$ in the high and low frequency limits, giving respectively

$$\omega_+^2 \sim k_x^2 c_c^2 + \omega_{ao}^2 \tag{5.55}$$

and

$$\omega_-^2\left(1+\frac{1}{\beta}\right) - k_x^2 v_A^2 \sim \frac{k_x^2 c_c^2 \tilde{\omega}_{g\|}^2}{k_x^2 c_c^2 + \omega_{ao}^2}\,. \tag{5.56}$$

For large k_x, the magnetic buoyancy dominates at low frequency (rather than at high frequency), and the behaviour (5.56) is approximately

$$\omega_-^2 \sim \frac{k_x^2 v_A^2 + \tilde{\omega}_{g\|}^2}{1+\frac{1}{\beta}}\,. \tag{5.57}$$

Hence the magnetogravity mode with parallel propagation differs from the non-magnetic case by not having a limiting frequency as $k_x \to \infty$.

Perpendicular propagation In the long wavelength limit, it is obvious that the magnetoacoustic and the magnetogravity modes with perpendicular propagation ($k_y \to 0$) have the same cut-off frequencies (5.53) as for parallel propagation ($k_x \to 0$). In both cases, the plus cut-off has a limit which corresponds to the perpendicular acoustic cut-off $\tilde{\omega}_{a\perp}$.

On the other hand, for $k_y \to \infty$, the plus cut-off frequency approaches the dispersion line for the fast magnetoacoustic mode, while the minus cut-off frequency approaches zero, *viz.*

$$\omega_+^2 \sim k_y^2(c_c^2 + v_A^2)\,, \qquad \omega_-^2 \sim 0\,. \tag{5.58}$$

As for parallel propagation, one can show that these limits are approached from above rather than below by examining Equation (5.47) when $\kappa^2 = 0$. The high and low frequency limits are approached as

$$\omega_+^2 \sim k_y^2(c_c^2 + v_A^2) + \tilde{\omega}_{a\perp}^2 \tag{5.59}$$

and

$$\omega_-^2 \sim \frac{k_y^2 c_c^2 \tilde{\omega}_{g\perp}^2}{k_y^2 c_c^2 + \omega_{ao}^2}\,. \tag{5.60}$$

For large k_y, the behaviour (5.60) is approximately

$$\omega_-^2 \sim \tilde{\omega}_{g\perp}^2\,. \tag{5.61}$$

Contrary to what Chen and Lykoudis (1972) write, the modified buoyancy frequency $\tilde{\omega}_{g\perp}$ corresponds exactly to the asymptotic frequency obtained by Yu (1965) taken in the perpendicular direction. In dimensional form, the frequency N obtained by Yu is given by (see also Thomas, 1983, p.331)

$$\begin{aligned} N^2 &= \frac{g^2}{c_c^2}\left[\frac{\gamma - 1 + \frac{\gamma}{2\beta}}{\left(1+\frac{\gamma}{2\beta}\right)\left(1+\frac{1}{\beta}\right)}\right], \\ i.e. \qquad N^2 &= \frac{g^2}{c_c^2}\left[\frac{\gamma}{1+\frac{\gamma}{2\beta}} - \frac{1}{1+\frac{1}{\beta}}\right], \\ &= \frac{g^2}{c_c^2}\left[\Gamma_o - \frac{1}{1+\frac{1}{\beta}}\right] = \tilde{\omega}_{g\perp}^2\,. \end{aligned} \tag{5.62}$$

Unstratified limit Note that in both cases, parallel and perpendicular, the buoyancy frequency acts in decreasing the plus cut-off ω_+, while it augments the minus cut-off ω_-. In the limit of no stratification ($H_o \to \infty$, $g \to 0$), $\tilde{\omega}_a^2 \to 0$, $\tilde{\omega}_g^2 \to 0$, the vertical wavenumber κ simplifies, yielding the relation

$$\kappa^2 = \frac{\omega^2}{c_\perp^2} - \frac{k_x^2 c_c^2 + k_y^2 c_\perp^2}{c_\perp^2},$$

$$i.e. \qquad \omega^2 = k_x^2 c_c^2 + (k_y^2 + \kappa^2) c_\perp^2, \tag{5.63}$$

$$\text{or} \qquad \omega^4 - (k_x^2 + k_y^2 + \kappa^2)(c_c^2 + v_A^2)\omega^2 + c_c^2 v_A^2 (k_x^2 + k_y^2 + \kappa^2) k_x^2 = 0. \tag{5.64}$$

Equation (5.64) is in a form which corresponds to the completely Fourier-analysed dispersion relation for magnetoacoustic waves (taking $\kappa = k_z$ — see, *e.g.*, the review by Stein and Leibacher, 1974, p.412). But Equation (5.63) also nicely demonstrates that, whereas a wave propagates at the sound speed in the horizontal parallel direction, it propagates at the effective perpendicular magnetosonic speed $c_\perp$ in both (horizontal and vertical) perpendicular directions.

The cut-off frequencies for which $\kappa^2 = 0$ are the two roots of the quadratic equation

$$\omega^2(\omega^2 - k_x^2 v_A^2) - (k_x^2 \omega^2 + k_y^2 \varpi^2) c_c^2 + k_x^4 c_c^2 v_A^2 = 0,$$

$$i.e. \qquad \omega^4 - (k_x^2 + k_y^2)(c_c^2 + v_A^2)\omega^2 + c_c^2 v_A^2 (k_x^2 + k_y^2) k_x^2 = 0. \tag{5.65}$$

The cut-off frequencies for parallel propagation are given by

$$\omega^4 - k_x^2 \left(c_c^2 + v_A^2\right) \omega^2 + k_x^4 c_c^2 v_A^2 = 0, \tag{5.66}$$

and reduce to the same pure acoustic and Alfvén modes as the asymptotic behaviour (5.54) at $k_x \to \infty$.

For perpendicular propagation, the cut-off frequencies are given by

$$\omega^4 = \omega^2 k_y^2 (c_c^2 + v_A^2), \tag{5.67}$$

which correspond to the two poles (5.58) as when $k_y \to \infty$ in the stratified medium, *i.e.* a fast magnetoacoustic mode with $\omega^2 = k_y^2(c_c^2 + v_A^2)$ and $\omega^2 = 0$.

These correspond to the fast and slow magnetoacoustic cut-off frequencies in a homogeneous atmosphere. Hence for large k_x or large k_y, *i.e.* small horizontal wavelengths, magneto-atmospheric waves propagate as if they were in a locally homogeneous magnetised plasma with negligible gravitational effects and no density stratification.

4. Field-free isothermal layer

Wave equation For a field-free plane-stratified layer with isothermal sound speed c_c, the fundamental wave equation (3.67) in terms of the vertical velocity amplitude V_z — or the equation for a medium of constant sound and Alfvén speeds (5.26) — reduces to the second order differential equation

$$\frac{d^2V_z}{dz^2} + \frac{1}{H}\frac{dV_z}{dz} + AV_z = 0\,, \tag{5.68}$$

while Lamb's equation (4.5) in terms of the compressibility Δ for $\omega^4 \neq g^2k_h^2$ becomes (Pekeris, 1948; Price, 1996)

$$\frac{d^2\Delta}{dz^2} + \frac{1}{H}\frac{d\Delta}{dz} + A\Delta = 0\,, \tag{5.69}$$

with the same coefficients; H is the density scale-height, *viz.*

$$H = \lim_{\beta\to\infty} H_o = \frac{c_c^2}{\gamma g}\,, \tag{5.70}$$

and $A = \lim_{\beta\to\infty} A_o$ may be written either in dimensional or normalised form, *viz.*

$$\begin{aligned} A &= \frac{\omega^2 - k_h^2c_c^2}{c_c^2} + \frac{k_h^2}{\omega^2}\left(\frac{g}{H_o} - \frac{g^2}{c_c^2}\right)\,, \\ &= \frac{k_h}{\gamma H_o}\left(\Omega^2 + \frac{\gamma-1}{\Omega^2}\right) - k_h^2\,. \end{aligned} \tag{5.71}$$

In the standard form of the wave equation, the vertical wavenumber κ is given by

$$\kappa^2 = \frac{\omega^2 - \omega_a^2}{c_c^2} + k_h^2\frac{\omega_g^2 - \omega^2}{\omega^2}\,. \tag{5.72}$$

Given that the general solutions of these equations contain each two independent arbitrary constants, the amplitude of the vertical velocity V_z is not necessarily proportional to the compressibility Δ.

Cut-off frequencies Starting from the equations for a medium of constant sound and Alfvén speeds, one may note also that, for large β,

$$\frac{\tilde\omega_{g\perp}^2}{\omega_{ao}^2} \sim \frac{\tilde\omega_{g\parallel}^2}{\omega_{ao}^2} = \frac{\Gamma_o^2}{4(\Gamma_o - 1)} \sim \frac{\gamma^2}{4(\gamma-1)} = \frac{\omega_g^2}{\omega_a^2}\,, \tag{5.73}$$

which is close to 1.0416 for $\gamma = \frac{5}{3}$. For a non-magnetic isothermal medium, the cut-off frequencies given by $\kappa^2 = 0$ — or by the field-free limit of Equation (5.42) or (5.49), *viz.*

$$\omega^4 - \left(k_h^2 c_c^2 + \omega_a^2\right) \omega^2 + k_h^2 c_c^2 \omega_g^2 = 0\,, \tag{5.74}$$

reduce to the acoustic and gravity cut-off frequencies of an isothermal atmosphere (Moore and Spiegel, 1964).

Conclusions

In this chapter, the dynamics of plane-stratified isothermal magnetic layers, structured in such a away as to produce a constant Alfvén speed, has been investigated so as to illustrate the anisotropic nature of magneto-atmospheric waves. Table 5.1 summarises the asymptotic limits of the associated cut-off frequencies. One of the most striking features is that the anisotropic acoustic cut-off opens a window for evanescent waves below the cusp frequency, which cannot exist for perpendicular propagation. On the other hand, at small wavelength, the oscillatory modes propagating perpendicular to the field lines have higher frequencies (above the dispersion line for the fast magnetoacoustic mode) than the parallel oscillatory modes (greater than the pure acoustic mode). Furthermore, the effective buoyancy frequency is also anisotropic. It is lowered in the presence of the magnetic field, but more so for parallel than for perpendicular propagation. This must affect the nature of instabilities, if they occur.

With such preliminary analysis, the dynamics of hybrid plane-stratified models will be explored further in Part III. But the dispersion relations which are presented in Chapter 6 may serve also to aid interpretation of more complex models. In particular, those relations for an isothermal magnetic waveguide yield noteworthy p- and g-modes, whose identified properties will be useful to disentangle and explain later the properties of modes in a multi-layer model which includes a magnetic layer. In this chapter also, fundamental and Lamb modes in an isothermal magnetic layer will be obtained and discussed in connection with those for a polytropic layer. Graphical solutions of these peculiar modes will also serve to illustrate the cut-off frequencies that were discussed above.

Chapter 6

Peculiar Modes

Based on the previously discussed wave equations for a polytropic layer or an isothermal plane-stratified medium with constant Alfvén speed, dispersion relations are developed in this section, with the intention to give some insight into the case when hybrid models are considered in Part III.

In preparation to this, it will be useful to adopt a normalised notation with respect to gravity. This choice explains itself by noting that this is the restoring force of gravity which is not altered and is common to both types of layer.

6.1 p- and g-modes in a magnetised isothermal waveguide

p- and g-modes If an isothermal medium with constant Alfvén speed is bounded by horizontal rigid walls, without energy radiated through these reflecting boundaries, then the propagating solutions are the oscillatory body modes ($4A_oH_o^2 > 1$) of the form (5.39), with $V_z = 0$ at each boundary. It follows that for an isothermal layer of breadth h,

$$\kappa_b = \frac{n\pi}{h}, \quad \text{where } n = 1, 2, 3, \ldots \tag{6.1}$$

This may be solved in the restricted cases of parallel and perpendicular propagations.

For parallel propagation ($k_y = 0$), Equation (6.1) develops into the form

$$\omega^4 - \left[k_x^2 c_c^2 + \omega_a^2 + c_c^2 \left(\frac{n\pi}{h}\right)^2\right] \varpi^2 + k_x^2 c_c^2 \tilde{\omega}_{g\|}^2 = 0\,, \tag{6.2}$$

i.e.

$$\omega^4 - \left(c_c^2 + v_A^2\right)\left[k_x^2 + \frac{1}{4H_o^2} + \left(\frac{n\pi}{h}\right)^2\right]\omega^2 + k_x^2 c_c^2\left[\tilde{\omega}_{g\|}^2 + v_A^2\left(k_x^2 + \frac{1}{4H_o^2} + \left(\frac{n\pi}{h}\right)^2\right)\right] = 0\,. \tag{6.3}$$

For perpendicular propagation ($k_x = 0$), Equation (6.1) becomes

$$\omega^4 - \left(c_c^2 + v_A^2\right)\left[k_y^2 + \frac{1}{4H_o^2} + \left(\frac{n\pi}{h}\right)^2\right]\omega^2 + k_y^2(c_c^2 + v_A^2)\tilde{\omega}_{g\perp}^2 = 0\,. \tag{6.4}$$

Finally, the field-free limit ($\beta \to \infty$) of Equation (6.1) corresponds to

$$\omega^4 - \left[k_h^2 c_c^2 + \omega_a^2 + c_c^2\left(\frac{n\pi}{h}\right)^2\right]\omega^2 + k_h^2 c_c^2 \omega_g^2 = 0\,, \tag{6.5}$$

which gives the solutions in a field-free isothermal waveguide.

Equations (6.3)-(6.5) are ω^2-quadratic equations, whose solutions are the p-modes and the g-modes. The solutions of order $n = 0$ correspond, in the magnetic case, to the 'plus' and 'minus' cut-off frequencies given by Equation (5.43) for parallel propagation and by Equation (5.50) for perpendicular propagation. In the field-free case, the solutions correspond to the acoustic and gravity cut-offs of an isothermal atmosphere (see Equation (5.74)). The high frequency or acoustic cut-off (the larger solution with $n = 0$) corresponds to the lowest limit of the p-mode sturmian sequence, while the low frequency or gravity cut-off (the lower solution with $n = 0$) corresponds to the highest limit of the g-mode anti-sturmian sequence.

The quantisation in n obtained for a waveguide provides a means to generate the p-modes in an isothermal stratified atmosphere. This may serve in particular to study the effect of magnetic fields on solar oscillations. This idea may be found also in Banerjee et al. (1995), for when the magnetic field is vertically aligned.

Normalised notation In order to compare the p- and g-modes obtained in an isothermal layer with those obtained in the polytropic case, the normalised frequency Ω^2 and terms more generally defined may be used as appropriate: for instance, $\Omega^2 = \omega^2/gk_x$ for parallel propagation and $\Omega^2 = \omega^2/gk_y$ for perpendicular propagation, so that the two cases may be treated in parallel.

Another notation of interest may be further introduced, which will serve the analysis and further developments in Part III: the constant sound speed is expressed as

$$c_c^2 = \frac{\gamma g z_p}{m+1} = \frac{g z_p}{m}\,, \tag{6.6}$$

with $\gamma = 5/3$ and $m = 1/(\gamma - 1) = 3/2$; z_p is a given reference depth in the medium. Then the scale-height

$$H_o = \frac{z_p}{m\Gamma_o}\,, \tag{6.7}$$

and so on.

As a result, the waveguide dispersion relation (6.3) for parallel modes may be rewritten as

$$m\Omega^4 - \left(1+\frac{1}{\beta}\right)\left[k_x z_p + \frac{\frac{m^2{\Gamma_o}^2}{4} + \left(n\pi\frac{z_p}{h}\right)^2}{k_x z_p}\right]\Omega^2 + \left[m(\Gamma_o - 1) + \frac{(k_x z_p)^2 + \frac{m^2{\Gamma_o}^2}{4} + \left(n\pi\frac{z_p}{h}\right)^2}{m\beta}\right] = 0\,, \tag{6.8}$$

while for perpendicular modes, the relation (6.4) corresponds to

$$m\Omega^4 - \left(1+\frac{1}{\beta}\right)\left[k_y z_p + \frac{\frac{m^2{\Gamma_o}^2}{4} + \left(n\pi\frac{z_p}{h}\right)^2}{k_y z_p}\right]\Omega^2 + m\left[\Gamma_o\left(1+\frac{1}{\beta}\right) - 1\right] = 0\,. \tag{6.9}$$

And the limit $\beta \to \infty$ gives the solutions in a field-free isothermal waveguide, *viz.*

$$m\Omega^4 - \left[k_h z_p + \frac{\frac{(m+1)^2}{4} + \left(n\pi\frac{z_p}{h}\right)^2}{k_h z_p}\right]\Omega^2 + 1 = 0\,. \tag{6.10}$$

Graphical solutions These equations may then be solved graphically: the diagnostic diagrams $(m\Omega^2, k_h z_p)$ shown in Figures 6.1, 6.2 and 6.3 depend on two parameters, namely β and z_p/h. The diagrams go in pairs. The two graphs in Figure 6.1 are for $\beta = 10$ and $\frac{z_p}{h} = 1$; Figure 6.2 is for $\beta = 10$ and $\frac{z_p}{h} = 2$; and in Figure 6.3, $\beta = 100$ and $\frac{z_p}{h} = 1$. In each figure, the purpose of the first diagram is to show the p-mode ridges, while the second diagram is a snapshot of the g-modes. Discrete ridges of order $n = 1$, 2 and 3 are shown in dashed, dash-dotted and dash-triple-dotted lines respectively; the plain lines are the cut-off frequencies separating the shaded domain of propagation from the unshaded domain of evanescence; three codes of colours – red, green and black – refer respectively to parallel propagation (pink-grey shading and red

lines), perpendicular propagation (green hatching and green lines) and the field-free limit (grey shading and black lines); for reference, the Lamb frequency $m\Omega^2 = k_h z_p$ is represented as a thin dotted line.

The p- and g-mode solutions exist only in the shaded oscillatory domain. For the g-modes with parallel propagation, this domain is reduced by the evanescent window below the cusp frequency. Hence it appears that the parallel g-modes never become unstable, but in fact do not propagate if their analytic solution, as given by Equation (6.8), is below the cusp cut-off frequency. However, the g-modes with perpendicular propagation may become unstable (see Equation (6.9) for $\Omega^2 \to 0$) for

$$\Gamma_o < \frac{1}{\left(1 + \frac{1}{\beta}\right)}, \tag{6.11}$$

which corresponds to the general instability criterion for perpendicular propagation (when the buoyancy frequency $\tilde{\omega}^2_{g\perp} < 0$; see Equation (5.44)).

The p-mode ridges are affected by the anisotropic nature of the magneto-atmospheric cut-off frequency. Indeed the cut-off frequencies may be considered as the fundamental ridges of order $n = 0$, and so the p-modes, in particular, are affected by this anisotropy. Hence, in Figure 6.1, one can clearly see that the p-modes propagating perpendicular to the field lines cannot cross the dispersion line for the fast magnetoacoustic mode at large $k_h z_p$, (*i.e.* small wavelength compared to the pressure scale-height H_o), contrary to the parallel p-modes which follow the field-free ridge in the limit of the pure acoustic mode. On the other hand, at large wavelength compared to the pressure scale-height H_o (*i.e.* $k_h z_p \to 0$), the parallel and perpendicular p-modes have the same magneto-atmospheric cut-off frequency, and so their ridges come nearer together. This observation is particularly important in order to consider the influence of magnetism on p-mode frequencies. For $k_h z_p \to 0$, this effect will be the same for parallel or perpendicular propagations, while it appears that the perpendicular p-modes will yield the largest shifts as $k_h z_p \to \infty$, in comparison to the parallel p-modes, which should yield the smallest shifts. Furthermore, one may note that the magnetic effects on the p-modes are larger as n increases and are difficult to distinguish on such diagrams as soon as $\beta = 100$ (see Figure 6.3).

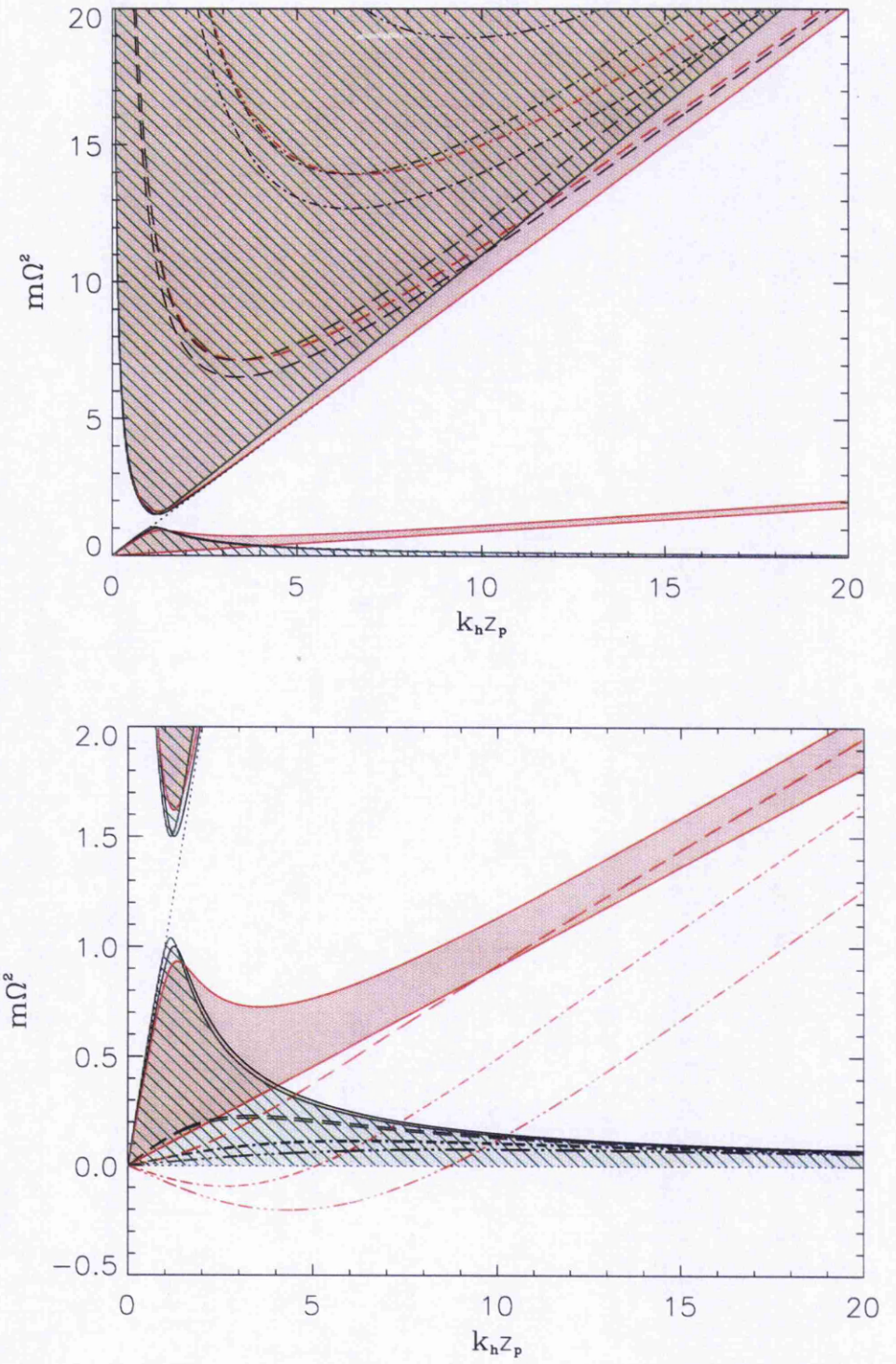

Figure 6.1: Normalised diagnostic diagrams $(m\Omega^2, k_h z_p)$ for an isothermal waveguide stratified under gravity and threaded by a horizontal magnetic field of constant Alfvén speed; $\beta = 10$ and $\frac{z_p}{h} = 1$.

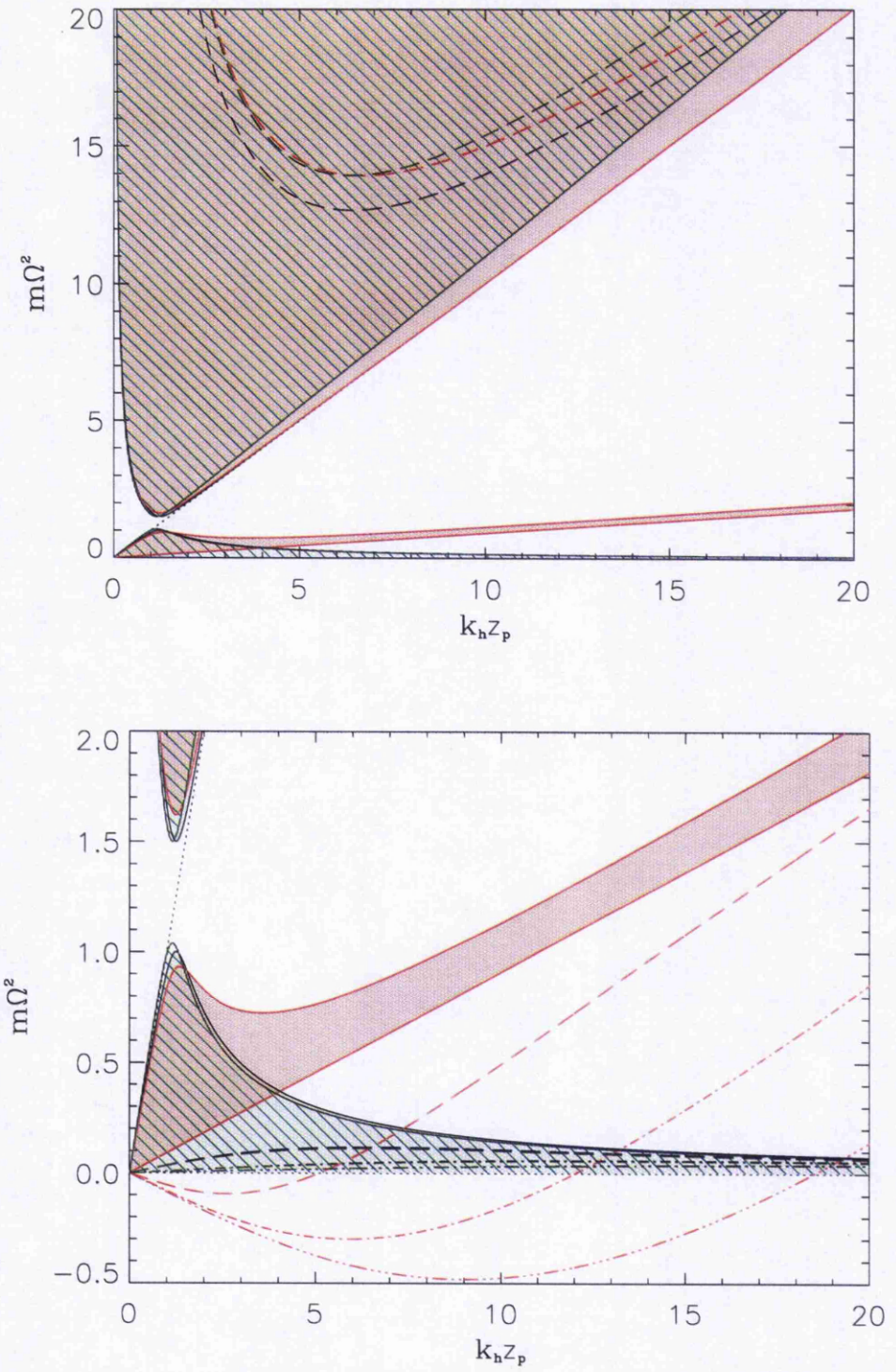

Figure 6.2: Normalised diagnostic diagrams $(m\Omega^2, k_h z_p)$ for an isothermal waveguide stratified under gravity and threaded by a horizontal magnetic field of constant Alfvén speed; $\beta = 10$ and $\frac{z_p}{h} = 2$.

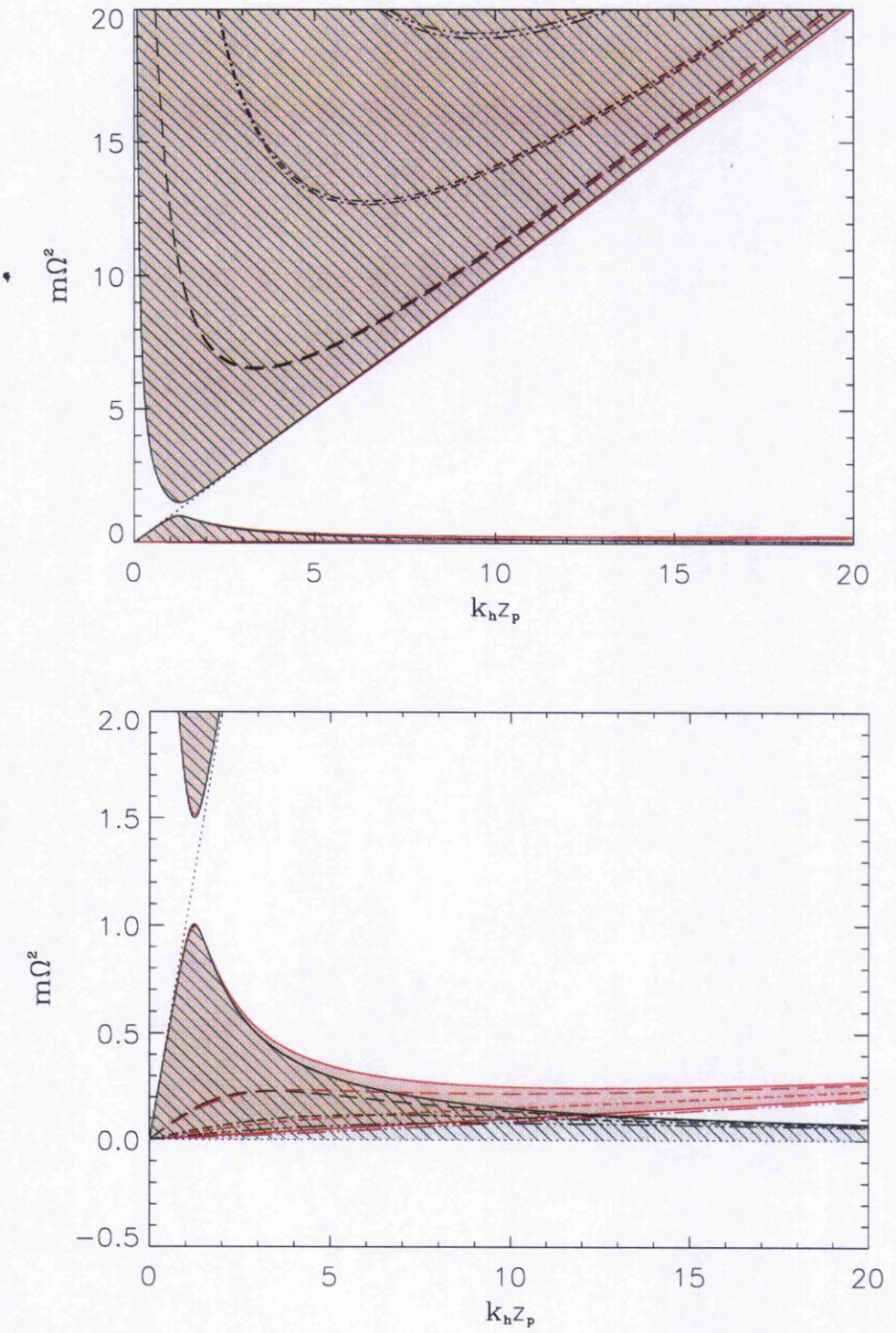

Figure 6.3: Normalised diagnostic diagrams $(m\Omega^2, k_h z_p)$ for an isothermal waveguide stratified under gravity and threaded by a horizontal magnetic field of constant Alfvén speed; $\beta = 100$ and $\frac{z_p}{h} = 1$.

The parameter $\frac{z_p}{h}$ is a factor to the radial order n in the waveguide equations (6.8)-(6.10), and therefore characterises the spacing between the ridges. For illustration, Figure 6.2 differs from Figure 6.1 by the choice of this parameter, which is multiplied by two. As a consequence, the p- and g-mode ridges of order $n = 1$ in Figure (6.2) correspond exactly to the ridges of order $n = 2$ in Figure (6.1). The physical meaning of the parameter $\frac{z_p}{h}$ may be interpreted as follows: the thinner is the layer as compared to the pressure scale-height (*i.e.* $h \ll z_p$), the more the ridges are spaced in the frequency diagram, which means that the frequencies are generally higher. By analogy, h plays the same role as the length of a pipe: 'short' pipes produce higher notes than 'long' pipes; and z_p plays the role of the temperature: at lower temperature, the notes produced by a pipe are lower.

6.2 Fundamental and Lamb modes

1. An isothermal field-free region bounded by a free surface

One may consider the modes of oscillations for an isothermal field-free region bounded by a free surface. The kinetic energy density to the first order, *viz.*

$$E_o \sim \left[D_1 e^{i\kappa z} + D_2 e^{-i\kappa z}\right]^2 , \tag{6.12}$$

vanishes at $z \to \infty$ if one chooses the evanescent disturbances with $D_1 = 0$ and

$$\kappa_e = \frac{\sqrt{1-4AH^2}}{2H} = \sqrt{\frac{1}{4H^2} + k_h^2 - \frac{k_h}{\gamma H}\left(\Omega^2 + \frac{\gamma - 1}{\Omega^2}\right)} . \tag{6.13}$$

Note that in this case, V_z is proportional to Δ.

The condition for a free-moving oscillation at the surface corresponds to the vanishing amplitude of the compressibility, *i.e.* from Equation (4.3),

$$\Lambda^- = -\frac{1}{2H} - \kappa_e = -\frac{k_h}{\Omega^2} . \tag{6.14}$$

Substituting in the expression (6.13) for κ_e, the associated dispersion relation is

$$(\Omega^4 - 1)(\Omega^2 - \gamma k_h H) = 0 . \tag{6.15}$$

In dimensional form, these roots are respectively

$$\omega^4 = g^2 k_h^2 , \qquad \text{and} \qquad \omega^2 = k_h^2 c_c^2 . \tag{6.16}$$

Eliminating the unstable root $\omega^2 = -gk_h$, two modes are solutions of this isothermal field-free atmosphere: the first one, with $\omega^2 = gk_h$, which has no zero crossings, is called the 'fundamental' or the f-mode, and the second, with $\omega^2 = k_h^2 c_c^2$, is the Lamb mode.

While the Lamb mode oscillation can exist at all frequencies, it will be shown that in the f-mode oscillation only frequencies above a critical value ω_f can propagate (see, *e.g.*, Pekeris, 1948).

2. Fundamental mode

Lamb's equation shows that $\Omega^4 = 1$ cannot be introduced as a possible solution. However it is a solution in a field-free isothermal medium when working with the variable

V_z. The stable mode with $\Omega^2 = 1$, *i.e.*

$$\omega^2 = g k_h \,, \tag{6.17}$$

satisfies

$$\frac{dV_z}{dz} + k_h V_z = \left(1 - \frac{k_x c_s^2(z)}{g}\right) \Delta \tag{6.18}$$

and

$$\left(k_h c_s^2(z) - \gamma g\right) \Delta - c_s^2(z) \frac{d\Delta}{dz} = 0 \,. \tag{6.19}$$

Two temperature profiles are of interest here, the polytropic profile and the isothermal profile, which may be viewed as a special case of the polytropic profile with $m \to \infty$. They will be treated alongside each other: on the left-hand side for a polytropic layer and on the right-hand side for an isothermal field-free layer.

Equations (6.18) and (6.19) become:

$$\frac{dV_z}{dz} + k_h V_z = \left(1 - \frac{\gamma k_h (z+z_o)}{m+1}\right) \Delta \,; \qquad \frac{dV_z}{dz} + k_h V_z = (1 - \gamma k_h H)\, \Delta \,; \tag{6.20}$$

$$\frac{d\Delta}{dz} + \left(\frac{m+1}{z+z_o} - k_h\right) \Delta = 0 \,; \qquad \frac{d\Delta}{dz} + \left(\frac{1}{H} - k_h\right) \Delta = 0 \,. \tag{6.21}$$

The differential equations (6.21) have each solutions of the form (assuming a constant polytropic index for the polytropic case),

$$\Delta = C \frac{e^{k_h z}}{(z + z_o)^{m+1}} \,; \qquad \Delta = C e^{\frac{-z}{H}} e^{k_h z} \,, \tag{6.22}$$

with an arbitrary constant C.

The condition (4.34) at the surface $z = 0$ is satisfied provided that the compressibility $\Delta = 0$ at $z = 0$. It follows that $C = 0$ and then the compressibility $\Delta = 0$ for all z. Therefore, Equations (6.20) simplify and in both cases the amplitude of the vertical velocity is

$$V_z = D e^{-k_h z} \,, \tag{6.23}$$

where D is a constant.

At infinity, the kinetic energy density E behaves to the first order as

$$E_o \sim z^m e^{-2k_h z} \,; \qquad E_o \sim e^{(\frac{1}{H} - 2k_h) z} \,, \tag{6.24}$$

which satisfies the condition that $E_o \to 0$ as $z \to \infty$ in the polytropic case; but in the isothermal case E_o vanishes as $z \to \infty$ provided

$$2k_h H > 1\,. \tag{6.25}$$

The requirement (6.25) may be interpreted as the existence of a cut-off Ω_f such that

$$\Omega^2 = 1 < \Omega_f^2 = 2k_h H\,, \tag{6.26}$$

or, in the dimensional form (with $\Omega_f^2 = \omega_f^2/gk_h$), to the criterion for propagation that

$$\omega^2 < \omega_f^2 = 2k_h^2 Hg = \frac{2k_h^2 c_c^2}{\gamma}\,. \tag{6.27}$$

One may also note the agreement with the requirement for a surface wave to propagate on the interface between two isothermal and stratified regions. If H_l and H_u are the density scale-heights of respectively the lower and upper region, then this requirement is (Miles and Roberts, 1992, Equation (56))

$$\frac{1}{2H_l} < k_h < \frac{1}{2H_u}\,. \tag{6.28}$$

For $H_l = H$ and $H_u \to 0$ Equation (6.28) recovers the requirement (6.25) for the model studied here.

The fundamental is therefore the longest vertical wavelength mode and is a surface wave that propagates horizontally and decays more or less exponentially with depth. Like a surface water wave, it is nearly incompressible (for $k_h\,\mathrm{R}_\odot \gg 1$), and its frequency and horizontal scale are related by the dispersion relation (6.17). The f-mode is frequently observed at high l, where its surface amplitude is greater (Libbrecht and Woodard, 1991). For the modes of oscillation of the polytropic model, it may be regarded as an extension of the p-modes, *i.e.* one of the special cases of non-radial oscillations, forming another lower frequency ridge with $n = 0$ (Deubner and Gough, 1984).

3. Magneto-atmospheric f-modes

As for the field-free case, one may consider modes of oscillations for a magnetised region with constant sound and Alfvén speeds bounded by a free surface. Similarly, the kinetic

energy density vanishes at $z \to \infty$ for evanescent disturbances with $D_1 = 0$. The nature of the modes will be deduced from the boundary condition at the surface (Equation (4.33)) for two cases of interest, namely parallel and perpendicular propagation. The Lagrangian rate of change in total pressure perturbation for parallel propagation is

$$\begin{aligned} \mathcal{P}_T &= -\rho_o \left(c_c^2 \Delta + v_A^2 \frac{dV_z}{dz} \right) \\ &= -\frac{\rho_o c_c^2}{\omega^2 - k_x^2 c_c^2} \left[\varpi^2 \frac{dV_z}{dz} + g k_x^2 V_z \right] ; \end{aligned} \tag{6.29}$$

for perpendicular propagation it is

$$\begin{aligned} \mathcal{P}_T &= -\rho_o \left[c_c^2 \Delta + v_A^2 \left(\frac{dV_z}{dz} + \frac{k_y^2 (c_c^2 + v_A^2)}{\omega^2} \Delta + \frac{g k_y^2}{\omega^2} V_z \right) \right] , \\ &= -\frac{\rho_o (c_c^2 + v_A^2)}{\omega^2 - k_y^2 (c_c^2 + v_A^2)} \left[\omega^2 \frac{dV_z}{dz} + g k_y^2 V_z \right] . \end{aligned} \tag{6.30}$$

To allow a uniform notation, similar to the one adopted for the polytropic case, the normalised form is adopted and the two cases of parallel and perpendicular propagation are treated simultaneously, respectively on the left and right-hand sides. The surface boundary condition reduces respectively (for $\omega^2 \neq k_x^2 c_c^2 + k_y^2 c_\perp^2$) to

$$\widetilde{\Omega}^2 \frac{dV_z}{dz} + k_x V_z = 0 ; \qquad \Omega^2 \frac{dV_z}{dz} + k_y V_z = 0 ; \tag{6.31}$$

here $\widetilde{\Omega}^2 = \varpi^2 / g k_x$. This in turn leads to the dispersion relations

$$\widetilde{\Omega}^2 \left(-\frac{1}{2H_o} - \kappa_e \right) + k_x = 0 ; \qquad \Omega^2 \left(-\frac{1}{2H_o} - \kappa_e \right) + k_y = 0 ; \tag{6.32}$$

that is, with $\kappa_e > 0$,

$$\kappa_e^2 = \left(\frac{k_x}{\widetilde{\Omega}^2} - \frac{1}{2H_o} \right)^2 ; \qquad \kappa_e^2 = \left(\frac{k_y}{\Omega^2} - \frac{1}{2H_o} \right)^2 , \tag{6.33}$$

which, by substituting κ_e yields respectively for parallel propagation

$$\left[\Omega^2 - \frac{k_x^2 c_c^2}{g} \right] \left[\Omega^4 - \frac{k_x (v_A^2 + c_T^2)}{g} \Omega^2 - \left(1 - \frac{k_x^2 c_c^2 (v_A^2 - c_T^2)}{g^2} \right) \right] = 0 ; \tag{6.34}$$

and for perpendicular propagation

$$\left[\Omega^2 - \frac{k_y (c_c^2 + v_A^2)}{g} \right] \left[\Omega^4 - 1 \right] = 0 . \tag{6.35}$$

Therefore the perpendicular modes with $\omega^4 = g^2 k_y^2$ are found here again as solutions, while in the parallel direction, two solutions exist which satisfy

$$\begin{aligned} \Omega^4 - \frac{k_x(v_A^2 + c_T^2)}{g}\Omega^2 - \left(1 - \frac{k_x^2 v_A^2 c_T^2}{g^2}\right) &= 0\,, \\ i.e. \quad \omega^4 - k_x^2(v_A^2 + c_T^2)\omega^2 - k_x^2\left(g^2 - k_x^2 v_A^2 c_T^2\right) &= 0\,. \end{aligned} \tag{6.36}$$

It should be noted that this dispersion relation yields the locus $\omega^4 = g^2 k_x^2$ in the field-free limit ($\beta \to \infty$) or (to first order) in the long wavelength limit ($k_x \to 0$). Equation (6.36) has roots

$$\omega^2 = \frac{1}{2}\left[k_x^2(v_A^2 + c_T^2) \pm \sqrt{4k_x^2 g^2 + k_x^4(v_A^2 - c_T^2)^2}\right]. \tag{6.37}$$

The mode with the positive sign in front of the square root may be called a magneto-atmospheric f-mode, while the one with a negative sign corresponds to the unstable solution $\omega^2 = -gk_x$ in the field-free limit. It may also be noted that in the unstratified limit ($g \to 0$), these modes correspond respectively to $\omega^2 = k_x^2 v_A^2$ and $\omega^2 = k_x^2 c_T^2$.

The requirement $\kappa_e > 0$ implies that (respectively for parallel and perpendicular propagations)

$$\begin{aligned} & \widetilde{\Omega}^2 < 2k_x H_o\,; && \Omega^2 < 2k_y H_o\,; \\ i.e. \quad & \Omega^2 < \frac{k_x c_T^2}{g}\left(1 + \frac{2\beta}{\Gamma_o}\right); && \Omega^2 < \frac{2k_y c_c^2}{g\Gamma_o}\,; \\ \text{or} \quad & \omega^2 < 2k_x^2 c_T^2\left(1 + \frac{\beta}{\gamma}\right); && \omega^2 < \frac{2k_y^2 c_c^2}{\Gamma_o} = 2k_y^2 c_c^2\left(\frac{1}{\gamma} + \frac{1}{2\beta}\right). \end{aligned} \tag{6.38}$$

This expression gives a cut-off $\tilde{\omega}_f$ below which the mode can propagate. Respectively for parallel and perpendicular propagations, this cut-off is such that

$$\tilde{\omega}_{f\parallel}^2 = 2k_x^2 c_c^2\left(\frac{\frac{1}{\gamma} + \frac{1}{\beta}}{1 + \frac{1}{\beta}}\right); \qquad \tilde{\omega}_{f\perp}^2 = 2k_y^2 c_c^2\left(\frac{1}{\gamma} + \frac{1}{2\beta}\right). \tag{6.39}$$

In the field-free limit,

$$\lim_{\beta\to\infty} \tilde{\omega}_f^2 = \frac{2k_h^2 c_c^2}{\gamma} = (2k_h H)(k_h g)\,, \tag{6.40}$$

which corresponds to $\Omega_f^2 = 2k_h H$ as seen previously in Equation (6.26).

Note that $\tilde{\omega}_{f\parallel}^2 > \omega_f^2$ since $\gamma > 1$; also $\tilde{\omega}_{f\perp}^2 > \omega_f^2$ always. Besides, for $\gamma = \frac{5}{3}$, one can find that $\tilde{\omega}_{f\parallel}^2 < \tilde{\omega}_{f\perp}^2$. This favours the transmission of a greater part of the magneto-atmospheric f-mode in the perpendicular direction.

4. Magneto-atmospheric Lamb modes

When $\omega^2 = k_x^2 c_c^2 + k_y^2 c_\perp^2$, one may simplify the analysis and study alongside the cases of parallel and perpendicular propagations. Equation (3.63) becomes respectively

$$\frac{dV_z}{dz} + \frac{1}{\Gamma_o H_o} V_z = 0\,; \qquad \frac{dV_z}{dz} + \frac{1}{\Gamma_o H_o (1+\frac{1}{\beta})} V_z = 0\,; \tag{6.41}$$

where the magnetic Lamb frequencies for respectively parallel and perpendicular propagations are given in the normalised form by

$$\Omega^2 = \frac{k_x c_c^2}{g} = k_x \Gamma_o H_o\,; \qquad \Omega^2 = \frac{k_y (c_c^2 + v_A^2)}{g} = k_y \Gamma_o H_o \left(1 + \frac{1}{\beta}\right). \tag{6.42}$$

Equations (6.41) possess each a solution of the form

$$V_z = C e^{\frac{-z}{\Gamma_o H_o}}\,; \qquad V_z = C e^{\frac{-z}{\Gamma_o H_o (1+\frac{1}{\beta})}}, \tag{6.43}$$

where C is a constant.

At infinity, the kinetic energy density E behaves to the first order as

$$E_o \sim e^{\left(1-\frac{2}{\Gamma_o}\right)\frac{z}{H_o}}\,; \qquad E_o \sim e^{\left(1-\frac{2}{\Gamma_o (1+\frac{1}{\beta})}\right)\frac{z}{H_o}}. \tag{6.44}$$

For parallel propagating modes, $E_o \to 0$ as $z \to \infty$ provided $\Gamma_o < 2$; this condition is met if $\gamma < 2$ since $\Gamma_o < \gamma$. For perpendicular modes, the condition is met for any value of γ.

The boundary condition at the surface (4.33) is satisfied as well since the dispersion relations (6.34) and (6.35) possess the respective magnetic Lamb modes as one of their roots. This shows that magneto-atmospheric Lamb modes may well exist.

5. Graphical solutions

In the same normalised notation adopted for the magnetic isothermal waveguide, the diagnostic diagrams of Figure 6.4 illustrates the fundamental and Lamb modes discussed in this section for $\beta = 10$. The colour codes and the representation of the cut-off frequencies are identical to those of the waveguide diagrams. In contrast to the waveguide diagrams, the fundamental and Lamb modes lie in the unshaded evanescent domains. Their dispersion lines are respectively dashed and dotted. In each case —

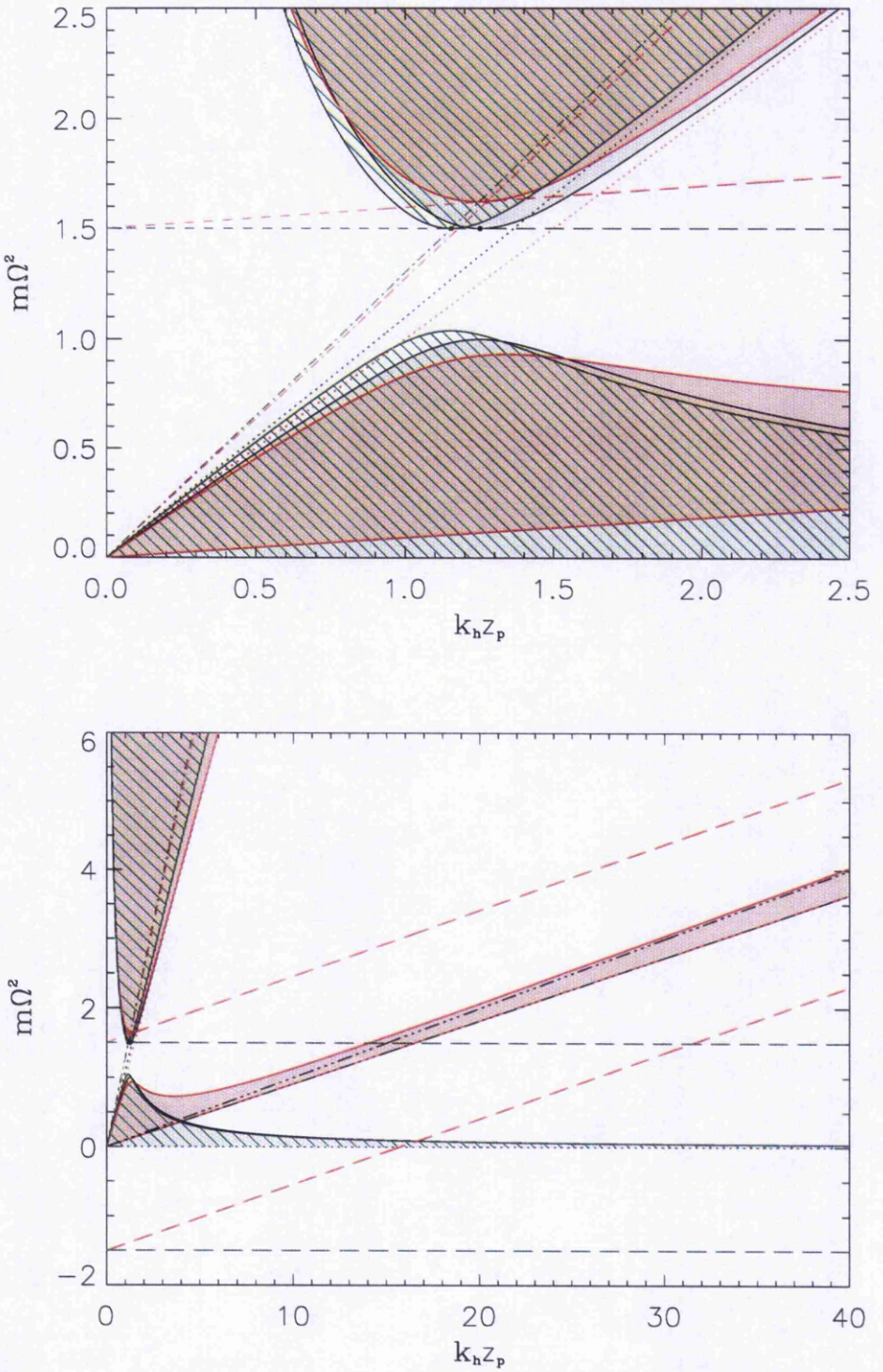

Figure 6.4: Normalised diagnostic diagrams $(m\Omega^2, k_h z_p)$ for an isothermal region stratified under gravity and threaded by a horizontal magnetic field of constant Alfvén speed; $\beta = 10$.

the parallel and perpendicular propagations and the field-free limit — the fundamental mode, the plus atmospheric cut-off frequency and the fundamental cut-off frequency (represented by dash-dotted lines and given by Equation (6.27) in the field-free case and Equation (6.39) in the magnetic case) intersect in one point indicated by a full circle. The dispersion lines where the f-mode cannot propagate are dashed less broadly than where it does propagate. The lower graph enlarges the upper graph to show the two solutions of the quadratic equation (6.36). The unstratified limits of these modes, respectively the Alfvén frequency and the cusp frequency are shown (normalised) as dash-triple-dotted black lines. While the dispersion line of the stable mode runs at large $k_h z_p$ parallel to the Alfvén frequency, the dispersion line for the 'unstable'mode runs parallel to the cusp frequency and eventually becomes stable (see, *e.g.*, Equation (6.36) for $\omega \to 0$) for

$$k_x z_p \geq m\sqrt{\beta(\beta+1)}\,. \tag{6.45}$$

But not yet weary are our feet,
Still round the corner we may meet
A sudden tree or standing stone
That none have seen but we alone.

John R.R. Tolkien (1892 - 1973)
"The Lord of the Rings" (1954-55), "Three is Company"

Part III

DIAGNOSTICS OF INTERNAL MAGNETIC LAYERS

This part explores the dynamics of hybrid plane-stratified models that include as many as three separate plasma layers, such as described in Part II and within the range in depth z from $z = 0$ to $z = +\infty$; the models may include a field-free zone, may be truncated or include an horizontal magnetic field. Except in certain special cases, these various models can be derived from two general three-layer models. The theoretical foundations of these layered models are established in Chapter 7. In Chapter 8, some first applications are developed: the dispersion relations are adapted to field-free layered models and diagnostic diagrams for more or less realistic model conditions are obtained for waves propagating parallel to the magnetic field lines. Because the magnetic field and layer thickness are presumed to vary over a solar cycle, a comparative study of these diagrams, with those of standard field-free models, may serve finally to draw diagnostics of the internal magnetic layers (still for parallel propagation). Namely the effects of internal layers on the global solar oscillations manifest in the form of frequency shifts, which might be compared with observations. This is the subject of Chapter 10, where, in addition, an analytical approximation of these effects will confirm the numerical results for parallel propagation and will serve to evaluate the amplitude of the shifts for perpendicular propagation. Before embarking in Chapter 10, Chapter 9 will help to guide the expectancy by giving a closer look at the boundary conditions of the field-free model of the Sun.

Chapter 7

Theoretical Foundations of Layered Models

The models consist of a hydrostatically stratified polytrope, below which is a slab of magnetic field, underlaid either by a polytropic or isothermal region that is field-free; see Figure 7.1. Within the magnetic slab, which lies between depths $z = z_p$ and $z = z_q$, the plasma is assumed to be isothermal and the horizontal magnetic field is structured in such a way as to produce a constant Alfvén speed. Above the slab, for $0 \leq z \leq z_p$, the square of the sound speed, $c_s^2(z)$, has a linear profile and is zero at the solar surface $z = 0$: $c_s^2(z) = \frac{g}{m}z$. The sound speed is assumed to be continuous across each magnetic interface, giving $c_s^2(z) = c_c^2 = \frac{g}{m}z_p$ within the slab (for $z_p \leq z \leq z_q$). Below the magnetic slab, in $z \geq z_p$, the sound speed squared is again either taken to be linear in depth, with the same gradient as in the upper region, or is assumed constant.

These three-layer models of the solar interior are subject to six boundary conditions: two at each interface between a magnetic and a field-free region at $z = z_i$, one at the surface $z = 0$, and one as $z \to \infty$. While the outer boundary conditions were described in Part II (Section 4.2), the equilibrium properties across interfaces and the dynamical coupling between adjacent regions is formulated in Section 7.1, so as to obtain the general dispersion relations for the three-layer models. The stability of the models is examined in Section 7.2.

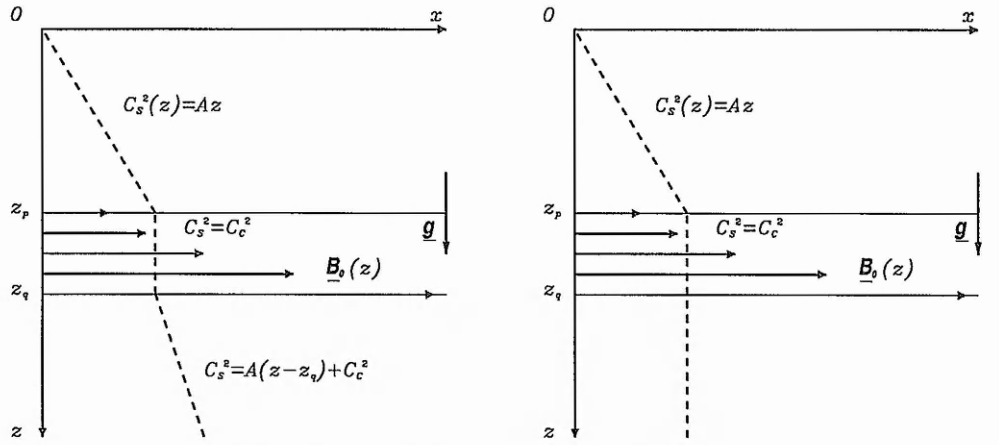

Figure 7.1: Three-Layer Models. A field-free polytropic medium $0 \leq z \leq z_p$ lies above an isothermal magnetic slab of constant Alfvén speed $z_p \leq z \leq z_q$ on top of either (*a*) a field-free polytrope or (*b*) an isothermal field-free region $z \geq z_q$.

7.1 Interfaces and general dispersion relations

1. Properties across interfaces

Jump in hydrostatic pressure Consider an interface at $z = z_i$ between a magnetic region and a field-free region. A physical quantity at this interface is denoted in the magnetic region by the script '*mag*' and in the field-free region by the script '*free*'.

The total pressure is continuous across the interface, *viz.*

$$p_o^{mag} + \frac{B_o^2(z_i)}{2\mu} = p_o^{free}. \tag{7.1}$$

From the expressions (1.50) and (3.30) for the sound speed $c_s(z)$ and the Alfvén speed $v_A(z)$, *viz.*

$$c_s^2(z) = \frac{\gamma p_o(z)}{\rho_o(z)}, \qquad v_A^2(z) = \frac{B_o^2(z)}{\mu\rho_o(z)},$$

it follows that, at $z = z_i$,

$$\rho_o^{mag}\left(\frac{[c_s^{mag}]^2}{\gamma} + \frac{v_A^2}{2}\right) = \rho_o^{free}\frac{[c_s^{free}]^2}{\gamma}. \tag{7.2}$$

Therefore, between a magnetic and a field-free region, there is a jump in the hydrostatic pressure

$$\frac{p_o^{mag}}{p_o^{free}} = \frac{(\rho_o c_s^2)\,|_{mag}}{(\rho_o c_s^2)\,|_{free}} = \frac{1}{1+\frac{\gamma}{2\beta}} = \frac{\Gamma_o}{\gamma}, \tag{7.3}$$

where Γ_o is the magnetically-modified adiabatic exponent (see Equation (5.11)) denoted by

$$\Gamma_o = \frac{2\beta\gamma}{2\beta+\gamma}, \tag{7.4}$$

and $\beta = [c_s^{mag}]^2/v_A^2$ is the ratio between the squared sound and Alfvén speeds at $z = z_i$ within the magnetic region.

This jump in hydrostatic pressure corresponds in fact to a jump in the modulus of elasticity $E = \rho_o c_s^2$ due only to the plasma. Γ_o was previously obtained in the study of the equilibrium state and in the context of the stability analysis of an isothermal magnetic medium with constant Alfvén speed. It arises here without assumptions about the profiles for the sound and Alfvén speeds, and thus the properties across the horizontal magnetic/field-free interface may be explored without a loss of generality.

Two extreme cases can be considered: either the sound speed is continuous across the interface or the density is continuous. This yields a jump in the physical quantity that is not required to be continuous. In either case the magnitude of this jump is the same.

A magnetic discontinuity with continuous density yields a jump in sound speed,

$$\frac{[c_s^{mag}]^2}{[c_s^{free}]^2} = \frac{\Gamma_o}{\gamma}. \tag{7.5}$$

A magnetic interface with continuous sound speed yields a jump in density,

$$\frac{\rho_o^{mag}}{\rho_o^{free}} = \frac{\Gamma_o}{\gamma}. \tag{7.6}$$

Note that since $\Gamma_o < \gamma$, the physical quantity in the magnetic fluid is always smaller than in the field-free fluid.

Coupling of adjacent wavefields At any interface in the medium, both the velocity amplitude of the disturbance V_z and the Lagrangian rate of change in pressure perturbation $\mathcal{P}_T$ must be continuous. The ratio of these two linear disturbances is known as the normal acoustic admittance $V_z/\mathcal{P}_T$, measuring the reaction of the wave back on the vibrating interface. The inverse ratio $\mathcal{P}_T/V_z$ is the normal acoustic impedance (see Morse and Feshbach, 1953, Part I, §3.3, p.311). These denominations come from the

analogy with electrical circuits, where the two continuous functions are the electric potential or voltage U (corresponding to $\mathcal{P}_T$) and the electrical current I (corresponding to V_z). And matching these quantities, between two terminals of an electrical system or at an acoustic interface, is known as 'impedance matching' and can be used to reconstruct the system if the impedance is independent of amplitude. By taking at an interface the continuity of the normal acoustic impedance, the two conditions of continuity are condensed into one. Furthermore, the information conveyed by the normal acoustic impedance about a medium is to allow subsequently the decomposition of the dispersion relation in meaningful parts. And this will prove useful to derive and understand dispersion relations in more specific or limiting cases.

Hence, at an interface between a magnetic region and a field-free region, the wave dynamics is coupled by the condition

$$\frac{V_z}{\mathcal{P}_T} \mid_{mag} = \frac{V_z}{\mathcal{P}} \mid_{free} ; \tag{7.7}$$

the field-free part is

$$\frac{V_z}{\mathcal{P}} \mid_{free} = \frac{V_z}{-\rho_o c_s^2 \Delta} \mid_{free} , \tag{7.8}$$

while the magnetic part is (see Equation (3.40))

$$\frac{V_z}{\mathcal{P}_T} \mid_{mag} = \frac{V_z}{-\rho_o c_s^2 \left(\Delta + \frac{1}{\beta} \Delta_\perp \right)} \mid_{mag} . \tag{7.9}$$

Equating expressions (7.8) and (7.9), and substituting in the jump in hydrostatic pressure (7.3) by assuming either continuity in temperature (*i.e.* sound speed) or continuity in density, the coupling relation at the magnetic interface (7.7) is reduced to

$$\mathcal{D} \mid_{free} = \mathcal{D}_o \mid_{mag} , \tag{7.10}$$

where $\mathcal{D}(\Omega^2, k_x, k_y, c_s^2(z))$, the non-magnetic part, is the ratio V_z/Δ for a field-free medium, *viz.* (see Equation (4.4) for $\Omega^4 \neq 1$)

$$\mathcal{D} = \frac{1}{\Omega^4 - 1} \left[\frac{c_s^2}{g} - \frac{\gamma \Omega^2}{k_h} - \frac{c_s^2 \Omega^2}{g k_h} \frac{1}{\Delta} \frac{d\Delta}{dz} \right] , \tag{7.11}$$

and $\mathcal{D}_o(\Omega^2, k_h, c_s^2(z), \beta(z))$ is the magnetic part (that depends upon the ratio $\beta = c_s^2/v_A^2$), which is developed from the general Equation (3.66), *viz.*

$$\mathcal{D}_o = \frac{\gamma}{\Gamma_o} \frac{V_z}{\left(\Delta + \frac{1}{\beta} \Delta_\perp \right)} ,$$

$$= \frac{Q}{P\frac{1}{V_z}\frac{dV_z}{dz} + R}, \tag{7.12}$$

where

$$\begin{aligned} P &= \left(1+\frac{1}{\beta}\right)\left(\Omega^2 - \frac{k_x^2 c_T^2}{g k_h}\right), \\ Q &= \frac{\gamma}{\Gamma_o}\left(\Omega^2 - \frac{k_x^2 c_s^2 + k_y^2 c_\perp^2}{g k_h}\right), \\ R &= \frac{k_x^2 c_s^2 + k_y^2 c_\perp^2}{c_s^2}. \end{aligned} \tag{7.13}$$

Here, the cusp speed c_T and the perpendicular magnetosonic speed $c_\perp$ may be expressed through

$$c_T^2 = \frac{c_s^2}{1+\beta} \qquad c_\perp^2 = c_s^2\left(1+\frac{1}{\beta}\right)\frac{\Omega^2 - \frac{k_x^2}{g k_h}\frac{c_s^2}{(1+\beta)}}{\Omega^2 - \frac{k_x^2}{g k_h}\frac{c_s^2}{\beta}}. \tag{7.14}$$

In particular, for parallel propagation ($k_y = 0$),

$$P = \left(1+\frac{1}{\beta}\right)\left(\Omega^2 - \frac{k_x c_s^2}{g(\beta+1)}\right), \qquad Q = \frac{\gamma}{\Gamma_o}\left(\Omega^2 - \frac{k_x c_s^2}{g}\right), \qquad R = k_x. \tag{7.15}$$

As for perpendicular propagation ($k_x = 0$),

$$P = \left(1+\frac{1}{\beta}\right)\Omega^2, \qquad Q = \frac{\gamma}{\Gamma_o}\left(\Omega^2 - \left(1+\frac{1}{\beta}\right)\frac{k_y c_s^2}{g}\right), \qquad R = \left(1+\frac{1}{\beta}\right)k_y. \tag{7.16}$$

Note that in the field-free limit, P, Q and R reduce to

$$P = \Omega^2, \qquad Q = \Omega^2 - \frac{k_h c_s^2}{g}, \qquad R = k_h. \tag{7.17}$$

2. General dispersion relations

To obtain the dispersion relations, one can develop the coupling condition of adjacent wavefields (7.10) at one interface $z = z_i$:

$$\mathcal{D}\left(R + P\frac{1}{V_z}\frac{dV_z}{dz}\right) - Q = 0. \tag{7.18}$$

The expression $\frac{1}{V_z}\frac{dV_z}{dz}$ evaluated at $z = z_i$ depends upon the nature of the modes in the isothermal magnetic region with constant Alfvén speed. For evanescent modes,

$$\frac{1}{V_z}\frac{dV_z}{dz} = \frac{D_1\Lambda^+ e^{\Lambda^+ z_i} + D_2\Lambda^- e^{\Lambda^- z_i}}{D_1 e^{\Lambda^+ z_i} + D_2 e^{\Lambda^- z_i}}; \tag{7.19}$$

and for oscillatory modes,

$$\frac{1}{V_z}\frac{dV_z}{dz} = \frac{D_1\left(\frac{-1}{2H_o}\sin(\kappa_b z_i) + \kappa_b\cos(\kappa_b z_i)\right) + D_2\left(\frac{-1}{2H_o}\cos(\kappa_b z_i) - \kappa_b\sin(\kappa_b z_i)\right)}{D_1\sin(\kappa_b z_i) + D_2\cos(\kappa_b z_i)}. \tag{7.20}$$

Here D_1 and D_2 are arbitrary constants (different for evanescent and oscillatory modes).

With these expressions, the requirement (7.18) yields: for evanescent modes,

$$D_1[(R+P\Lambda^+)\mathcal{D}-Q]e^{\Lambda^+ z_i} + D_2[(R+P\Lambda^-)\mathcal{D}-Q]e^{\Lambda^- z_i} = 0\,; \tag{7.21}$$

and for oscillatory modes,

$$\begin{aligned} & D_1\left[\left(\left(R-\frac{P}{2H_o}\right)\mathcal{D}-Q\right)\sin(\kappa_b z_i) + P\mathcal{D}\kappa_b\cos(\kappa_b z_i)\right] \\ + \quad & D_2\left[\left(\left(R-\frac{P}{2H_o}\right)\mathcal{D}-Q\right)\cos(\kappa_b z_i) - P\mathcal{D}\kappa_b\sin(\kappa_b z_i)\right] = 0\,. \end{aligned} \tag{7.22}$$

Taking $z_i = z_p$ and $z_i = z_q$ in turn leads to dispersion relations as follows: for evanescent modes,

$$\mathcal{E}_p^-\mathcal{E}_q^+ e^{2\kappa_e(z_q-z_p)} - \mathcal{E}_p^+\mathcal{E}_q^- = 0\,, \tag{7.23}$$

where

$$\mathcal{E}_p^\pm = (R+P\Lambda^\pm)\mathcal{D}_p - Q\,, \qquad \mathcal{E}_q^\pm = (R+P\Lambda^\pm)\mathcal{D}_q - Q\,; \tag{7.24}$$

and for oscillatory modes,

$$[\mathcal{F}_q\mathcal{F}_p + (P\kappa_b)^2\mathcal{D}_q\mathcal{D}_p]\sin(\kappa_b(z_q-z_p)) - PQ\kappa_b(\mathcal{D}_q-\mathcal{D}_p)\cos(\kappa_b(z_q-z_p)) = 0\,, \tag{7.25}$$

where

$$\mathcal{F}_p = \left(R-\frac{P}{2H_o}\right)\mathcal{D}_p - Q\,, \qquad \mathcal{F}_q = \left(R-\frac{P}{2H_o}\right)\mathcal{D}_q - Q\,. \tag{7.26}$$

P, Q and R are defined in (7.13); $\mathcal{D}_p$ and $\mathcal{D}_q$ are the field-free parts given by Equation (7.11), applied respectively for a polytropic medium at $z_i = z_p$ and for an isothermal field-free region or a polytrope at $z_i = z_q$.

These dispersion relations may also simply be written as a general one, *viz.*

$$\mathcal{E}_p^-\mathcal{E}_q^+ e^{2i\kappa(z_q-z_p)} - \mathcal{E}_p^+\mathcal{E}_q^- = 0\,, \tag{7.27}$$

where $\kappa = -i\kappa_e$ and $\kappa = \kappa_b$ for respectively evanescent and oscillatory modes in the isothermal magnetic layer; the other terms are defined above (Equation (7.24)) with

$$\Lambda^\pm = -\frac{1}{2H_o} \pm i\kappa\,. \tag{7.28}$$

In particular, for oscillatory modes, the equivalence of the dispersion relations (7.25) and (7.27) may be verified in a straight-forward way.

The general dispersion relation (7.27) and the method by which it was obtained are the first key results in this chapter.

By comparison, one would have to solve with the full matrix approach the determinant of a 6×6-matrix in the present case (the wave equations associated with each of the three layers admit solutions, with each two arbitrary constants, and the medium is subject to six boundary conditions). In applying the continuity of the normal acoustic impedance, the method provides instead a convenient and still exact way to obtain the dispersion relation. Incidentally, the impedance matching method is far advanced to decompose the wavefields in a set of incident or exciting, transmitted and scattered acoustic impedances and to study more complicated physics involving multiple scattering and absorption of acoustic waves (see Keppens, 1995a, b).

Here the derivation of the dispersion relation in meaningful parts is an advantage to explore further its nature, in order to make clearer the various interface modes a buried magnetic layer gives rise to. The dispersion relation (7.27) may be compared to the transmittance of a four-terminal network, where the magnetic slab corresponds to an electrical system or black box with two input and two output terminals. The respective input and output impedances are given by the field-free parts $\mathcal{D}_p$ and $\mathcal{D}_q$ (which, strictly speaking, have been defined for convenience as normal acoustic admittances multiplied by a factor $-E$, where E is the modulus of elasticity at the field-free interface).

Field-free parts At each interface $z = z_i$ the ratio V_z/Δ for a field-free medium (7.11), *viz.*

$$\mathcal{D} = \frac{1}{\Omega^4 - 1}\left[\frac{c_s^2}{g} - \frac{\gamma\Omega^2}{k_h} - \frac{c_s^2\Omega^2}{gk_h}\frac{1}{\Delta}\frac{d\Delta}{dz}\right], \tag{7.29}$$

may be considered for some relevant cases.

The requirement of free-moving surface leads to a study of the isolated effect of a buried magnetic field on p-modes. This is readily obtained for vanishing sound speed at the surface, leading to select solutions in terms of the Kummer M function,

$$\mathcal{D}_p = \mathcal{D}_a = \frac{\gamma z_p}{(m+1)(\Omega^4 - 1)}\left[1 - \frac{(m+1)}{k_h z_p}\Omega^2 + \Omega^2 - 2\Omega^2\frac{M'}{M}\right]. \tag{7.30}$$

For a polytrope below z_q (see Figure 7.1(a)), the requirement of vanishing kinetic energy density at $z \to \infty$ is satisfied by selecting the Tricomi U function. And so,

$$\mathcal{D}_q = \mathcal{D}_b = \frac{\gamma z_p}{(m+1)(\Omega^4-1)}\left[1 - \frac{(m+1)}{k_h z_p}\Omega^2 + \Omega^2 - 2\Omega^2\frac{U'}{U}\right]. \tag{7.31}$$

In Equations (7.30) and (7.31) and in all Part III, M, U, M' and U' are evaluated at $Z = 2k_h z_p$ and defined as

$$M = M(-\Upsilon, m+2, Z), \quad U = U(-\Upsilon, m+2, Z), \tag{7.32}$$

$$M' = M'(-\Upsilon, m+2, Z), \quad U' = U'(-\Upsilon, m+2, Z), \tag{7.33}$$

where the prime denotes the derivative of M or U with respect to Z.

The expression V_z/Δ in an isothermal region is given by

$$\begin{aligned}\mathcal{D}_c &= \frac{1}{\Omega^4-1}\left[\frac{c_c^2}{g} - \frac{\gamma\Omega^2}{k_h} - \frac{c_c^2\Omega^2}{gk_h}\frac{1}{\Delta}\frac{d\Delta}{dz}\right] \\ &= \frac{\gamma}{k_h(\Omega^4-1)}\left[\frac{k_h z_p}{m+1} - \Omega^2 - \frac{z_p}{m+1}\Omega^2\frac{1}{\Delta}\frac{d\Delta}{dz}\right] \\ &= \frac{\gamma}{k_h(\Omega^4-1)}\left[k_h H - \Omega^2 - H\Omega^2\frac{1}{\Delta}\frac{d\Delta}{dz}\right],\end{aligned} \tag{7.34}$$

where the density scale-height

$$H = \frac{c_c^2}{\gamma g} = \frac{z_p}{m+1}. \tag{7.35}$$

Now $\frac{1}{\Delta}\frac{d\Delta}{dz}$ depends upon the nature of the solutions in the isothermal field-free region: for evanescent modes, at $z = z_i$

$$\frac{1}{\Delta}\frac{d\Delta}{dz} = \frac{D_1\Lambda_i^+ e^{\Lambda_i^+ z_i} + D_2\Lambda_i^- e^{\Lambda_i^- z_i}}{D_1 e^{\Lambda_i^+ z_i} + D_2 e^{\Lambda_i^- z_i}}; \tag{7.36}$$

and for oscillatory modes, at $z = z_i$,

$$\frac{1}{\Delta}\frac{d\Delta}{dz} = \frac{D_1\left(\frac{-1}{2H_o}\sin(\kappa_b z_i) + \kappa_b\cos(\kappa_b z_i)\right) + D_2\left(\frac{-1}{2H_o}\cos(\kappa_b z_i) - \kappa_b\sin(\kappa_b z_i)\right)}{D_1\sin(\kappa_b z_i) + D_2\cos(\kappa_b z_i)}. \tag{7.37}$$

For the isothermal region below z_q (see Figure 7.1(b)), the requirement of vanishing kinetic energy density at $z \to \infty$ is satisfied by selecting the evanescent mode and evanescent solution Λ_i^- (see Equation (5.37)), so that $\mathcal{D}_q$ may be given by

$$\mathcal{D}_q = \mathcal{D}_i = \frac{\gamma}{k_h(\Omega^4-1)}\left[\frac{k_h z_p}{m+1} - \Omega^2 - \frac{z_p}{m+1}\Omega^2\Lambda_i^-\right]. \tag{7.38}$$

7.2 Stability aspects

The jump in hydrostatic pressure across a magnetic discontinuity, as was described earlier, implies that if the sound speed is taken to be continuous, the field-free fluid is always denser than in the magnetic region at such interface. In the general layered models that are investigated here, the field-free polytropic upper layer overlies a magnetic layer at the interface $z = z_p$. At this interface, the jump in density (7.6) yields a magnetic buoyancy force of $(\rho_{free} - \rho_{mag})g$ per unit volume. Consequently the 'top-heavy' equilibrium state may be unstable.

The magnetic buoyancy force, which occurs when a fluid supports a denser fluid against gravity, yields an instability, whereupon the two fluids tend to interchange positions. This instability is referred to either as the magnetic buoyancy instability or as the hydromagnetic Rayleigh-Taylor instability (see, *e.g.*, Chandrasekhar, 1961). It is obvious that this instability is due to the presence of the magnetic field. Unstable modes exist for a magnetic field of strength greater than a critical field strength B_{crit}. The first maximum field strength that one want to know is the one obtained when the magnetic pressure is neglected: taking $p_o^{mag} = 0$,

$$B_{max}^2 = 2\mu p_o^{free} . \tag{7.39}$$

This limit is not physical. The instability can occur for a smaller critical field strength if one takes the magnetic pressure into account. If instead the expression for the total pressure balance is developed, *viz.*

$$\begin{aligned} \frac{B_o(z_i)^2}{2\mu} &= p_o^{free} - p_o^{mag} , \\ &= p_o^{free}\left(1 - \frac{p_o^{mag}}{p_o^{free}}\right) , \\ &= \frac{p_o^{free}}{1 + \frac{2\beta}{\gamma}} , \end{aligned} \tag{7.40}$$

one finds that unstable modes can occur for $\beta < \beta_{crit}$; in terms of field strength, instability may occur for a magnetic field strength $B_o(z_i)$ greater than

$$B_{crit} = \sqrt{\frac{2\mu p_o^{free}}{1 + \frac{2\beta_{crit}}{\gamma}}} = B_{max}\sqrt{\frac{1}{1 + \frac{2\beta_{crit}}{\gamma}}} . \tag{7.41}$$

The natural criterion for magnetic buoyancy which occurs in an isothermal magnetised plasma (see Equation (5.21)) is given by

$$\beta_{crit} = \frac{\gamma}{2(\gamma - 1)} \,. \tag{7.42}$$

Substituting Equation (7.42) into Equation (7.41) yields the value

$$\begin{aligned} B_{crit} &= \sqrt{\frac{\gamma - 1}{\gamma}} B_{max} \,, \\ i.e. \qquad B_{crit} &= \sqrt{\frac{2}{5}} B_{max} \,, \qquad \text{for} \quad \gamma = \frac{5}{3} \,. \end{aligned} \tag{7.43}$$

The criterion for instability at the interface of a hybrid model might certainly differ from this one, because properties of those interfaces in contact with a polytropic stratification are not simply isothermal, which suggests that those interfaces might react differently to perturbations. Before showing solutions of the dispersion relation (7.27) in some applied cases, it is therefore useful to ascertain on purely theoretical grounds the equilibrium or dynamical conditions for which the instability at a magnetic interface takes place. One way of proceeding is to look for the state of marginal stability, obtained by taking $\Omega^2 = 0$ in the dispersion relation. In this limit, the field-free parts converge to the same value, *viz.*

$$\mathcal{D}_a \,,\ \mathcal{D}_b \text{ and } \mathcal{D}_i \to -\frac{\gamma z_p}{m+1} \,, \qquad \Omega^2 \to 0 \,, \tag{7.44}$$

and so, one can easily deduce that $\mathcal{E}_p^- \sim \mathcal{E}_q^-$ and $\mathcal{E}_p^+ \sim \mathcal{E}_q^+$. Therefore, for $\kappa \neq 0$, this leaves two possibilities to investigate: either the marginal solution for $\mathcal{E}_p^- \sim \mathcal{E}_q^- \sim 0$ or the marginal solution for $\mathcal{E}_q^+ \sim \mathcal{E}_p^+ \sim 0$.

When the magnetic layer is chosen to be isothermal and structured in such a way as to produce a constant Alfvén speed, the stability criterion may be solved for two extreme cases, namely parallel and perpendicular wave propagations. In particular, the behaviour of $P\Lambda^{\pm} = P(-\frac{1}{2H_o} \pm i\kappa)$ as $\omega^2 \to 0$ must be examined in each case.

State of marginal stability for perpendicular propagation When $k_x = 0$, the marginal asymptotic limit of the kernel κ may be given, *viz.*

$$\kappa^2 \sim -\frac{\omega_{ao}^2}{c_c^2} + k_y^2 \frac{\tilde{\omega}_{g\perp}^2}{\omega^2} \,, \qquad \omega^2 \to 0 \,, \tag{7.45}$$

together with the magnetic terms (see Equation (7.16))

$$P \sim \left(1+\frac{1}{\beta}\right)\frac{\omega^2}{gk_y}, \quad Q \sim -\frac{\gamma}{\Gamma_o}\left(1+\frac{1}{\beta}\right)\frac{k_y c_c^2}{g}, \quad \omega^2 \to 0 \qquad \text{and} \quad R = \left(1+\frac{1}{\beta}\right)k_y\,. \tag{7.46}$$

One can deduce from these results that

$$P\Lambda^{\pm} \sim \pm\left(1+\frac{1}{\beta}\right)\frac{\tilde{\omega}_{g\perp}}{g}\omega^2 \sim 0\,, \qquad \omega^2 \to 0\,. \tag{7.47}$$

In fact, it was shown in Chapter 5, that low-frequency modes propagating perpendicularly to the magnetic field lines do not exhibit evanescent behaviour, contrary to the parallel propagating modes. And so, independently to the marginal limit of the solution $\Lambda^{\pm}$, the marginal solutions for $\mathcal{E}_p^- \sim \mathcal{E}_q^- \sim 0$ and for $\mathcal{E}_q^+ \sim \mathcal{E}_p^+ \sim 0$ are identical for perpendicular propagation: the state of marginal stability is given by

$$-\frac{\gamma z_p}{m+1} \sim \frac{Q}{R}\,|_{k_x=0}\,, \qquad i.e. \quad \frac{\gamma}{\Gamma_o} \to 1\,, \qquad \omega^2 \to 0\,, \tag{7.48}$$

which is the general criterion (7.42) for magnetic buoyancy to occur in the isothermal magnetised plasma. It is actually a less stable criterion for perpendicular propagating modes than when the medium is not connected to a field-free layer. Hence the interface has a destabilising influence on the modes with $k_x = 0$.

State of marginal stability for parallel propagation For $k_y = 0$,

$$\begin{aligned} \kappa^2 &\sim -\frac{\omega_{ao}^2}{c_c^2} + k_x^2\frac{\tilde{\omega}_{g\|}^2 + k_x^2 v_A^2}{k_x^2 v_A^2}\,, \qquad \omega^2 \to 0\,, \\ &\sim k_x^2 - k_{ag}^2 \qquad \text{where} \quad k_{ag}^2 = \frac{g^2}{c_c^4}\left[\frac{\Gamma_o^2}{4} + \beta(\Gamma_o - 1)\right], \qquad \omega^2 \to 0\,, \end{aligned} \tag{7.49}$$

and the magnetic terms reduce to (see Equation (7.15))

$$P \sim -\frac{1}{\beta}\frac{k_x c_c^2}{g}, \qquad Q \sim -\frac{\gamma}{\Gamma_o}\frac{k_x c_c^2}{g}, \qquad \omega^2 \to 0 \qquad \text{and} \quad R = k_x\,. \tag{7.50}$$

It follows that the marginal solutions for $\mathcal{E}_p^- \sim \mathcal{E}_q^- \sim 0$ and for $\mathcal{E}_q^+ \sim \mathcal{E}_p^+ \sim 0$ correspond to

$$\begin{aligned} P\Lambda^{\pm} + k_x &\sim \tfrac{\gamma}{\Gamma_o}k_x\,, \\ i.e. \quad \Lambda^{\pm} &\sim \beta\tfrac{g}{c_c^2}\left(1-\tfrac{\gamma}{\Gamma_o}\right) = -\tfrac{\gamma g}{2c_c^2}\,, \qquad \omega^2 \to 0\,. \end{aligned} \tag{7.51}$$

Now $\Lambda^{\pm} = -\frac{\Gamma_o g}{2c_c^2} \pm i\kappa$, so

$$\pm i\kappa \sim \frac{g}{2c_c^2}(\Gamma_o - \gamma)\,, \qquad \omega^2 \to 0\,. \tag{7.52}$$

But $\Gamma_o < \gamma$ for a magnetised layer, and so for the evanescent modes ($\kappa^2 \sim k_x^2 - k_{ag}^2 < 0$) only the solutions with Λ^- may lead to instabilities, with

$$k_x^2 \sim k_{ag}^2 - \frac{g^2}{4c_c^4}(\Gamma_o - \gamma)^2\,, \qquad \omega^2 \to 0\,; \tag{7.53}$$

while for oscillatory modes ($\kappa^2 \sim k_x^2 - k_{ag}^2 > 0$),

$$k_x^2 \sim k_{ag}^2 + \frac{g^2}{4c_c^4}(\Gamma_o - \gamma)^2\,, \qquad \omega^2 \to 0\,, \tag{7.54}$$

Replacing k_{ag}^2 from Equation (7.49), one gets

$$k_x^2 \sim k_{ag}^2 \pm \frac{g^2}{4c_c^4}(\Gamma_o - \gamma)^2 = \frac{g^2}{c_c^4}\left[\frac{\Gamma_o^2}{4} + \beta(\Gamma_o - 1) \pm \left(\frac{\Gamma_o - \gamma}{2}\right)^2\right]. \tag{7.55}$$

Hence, noting that $c_c^2/(\gamma g)$ is the pressure scale-height H at the field-free interface, the dispersion relation around $\omega^2 = 0$ yields respectively: for the evanescent modes given by Λ^- (*i.e.*, with the negative sign inside the square brackets),

$$\begin{aligned}(k_x H)^2 \sim \frac{\Gamma_o - 1}{\gamma^2}\beta + \frac{\Gamma_o}{2\gamma} - \frac{1}{4} &= \left[\Gamma_o\left(1 + \frac{\gamma}{2\beta}\right) - 1\right]\frac{\beta}{\gamma^2} - \frac{1}{4} \\ &= \frac{\gamma - 1}{\gamma^2}\beta - \frac{1}{4}\,;\end{aligned} \tag{7.56}$$

and for the oscillatory modes (with the positive sign),

$$(k_x H)^2 \sim \frac{\Gamma_o^2}{2\gamma^2} + \frac{\Gamma_o - 1}{\gamma^2}\beta - \frac{\Gamma_o}{2\gamma} + \frac{1}{4} = \frac{\Gamma_o}{\gamma}\left(\frac{\Gamma_o}{2\gamma} - 1\right) + \frac{\gamma - 1}{\gamma^2}\beta + \frac{1}{4}\,. \tag{7.57}$$

The two equations above describe the state of marginal stability that the magnetic layer could reach for parallel propagating modes. Equation (7.56) solves the relation $\mathcal{E}_q^- \sim \mathcal{E}_p^- \sim 0$ when $\kappa = -i\kappa_e$, while Equation (7.57) is relevant to describe all relations $\mathcal{E} \sim 0$ when $\kappa = \kappa_b$. For a given model with a pressure scale-height H at the field-free interface, the magnetic instability occurs for values of the plasma β generally smaller than a critical parameter β_{crit} which is function of the parallel wavenumber k_x and generally differs from the value of Equation (7.42). In Figure 7.2, β_{crit} is shown in plain and dashed-dotted lines versus the wavenumber combination $(k_x H)^2$, illustrating respectively Equation (7.56) and (7.57) (for $\gamma = \frac{5}{3}$).

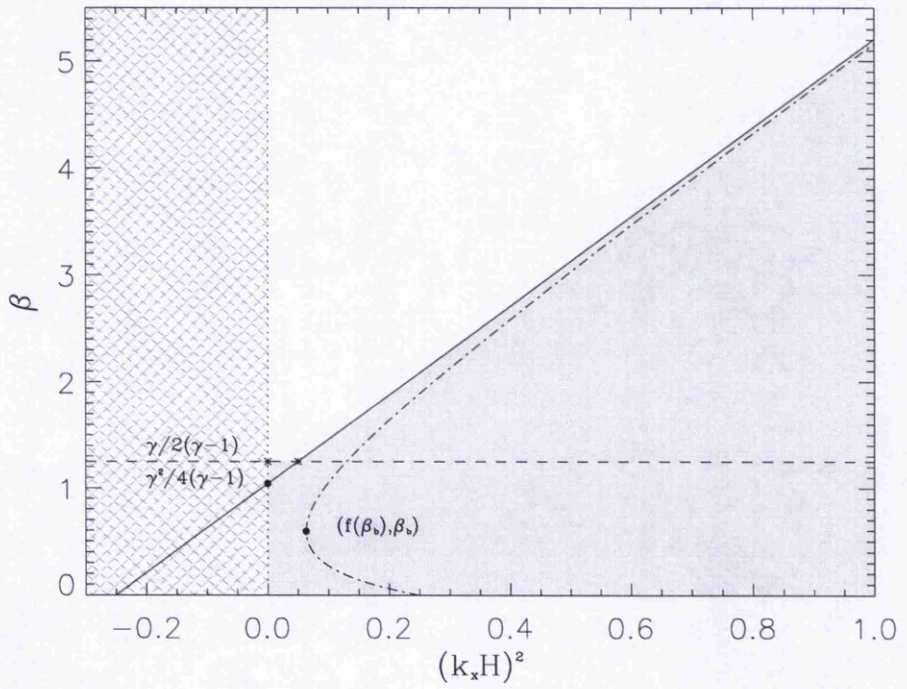

Figure 7.2: The state of marginal stability is described by the critical parameter β_{crit} in the β versus $(k_x H)^2$ plane. For parallel propagating modes, respectively evanescent disturbances and oscillatory modes in the magnetic layer, β_{crit} is shown in plain and dashed-dotted lines versus the wavenumber combination $(k_x H)^2$. The horizontal dashed line represents the natural parameter β_{crit} below which the layer is magnetically buoyant (and also the perpendicular modes may become unstable). The overall allowed region for unstable parallel and perpendicular modes ($\omega^2 < 0$) is shaded; the cross-hatched region is not physical. Points indicated in the graph are discussed in the main text.

Equation (7.56) gives a straight line in the β versus $(k_x H)^2$ plane, while Equation (7.57) is an hyperbolic type of equation, which may be studied analytically. For large parallel wavelength ($k_x H \ll 1$), oscillatory modes are more stable than evanescent modes. As $k_x H \to 0$, the evanescent mode in the layer becomes unstable for β smaller than

$$\beta_{crit} = \frac{\gamma^2}{4(\gamma - 1)} \approx 1.0416\,, \tag{7.58}$$

while for oscillatory modes there exists a regime where they are never unstable. The longest wavelength where the instability might still occur is obtained by determining an extremum to the function

$$f(\beta) = \frac{\Gamma_o}{\gamma}\left(\frac{\Gamma_o}{2\gamma} - 1\right) + \frac{\gamma - 1}{\gamma^2}\beta + \frac{1}{4}\,. \tag{7.59}$$

Resolving the point β_b for which $\frac{df}{d\beta}(\beta_b) = 0$ yields the value

$$\beta_b = \sqrt[3]{\frac{\gamma^4}{4(\gamma-1)}} - \frac{\gamma}{2} \approx 0.5916\,. \tag{7.60}$$

And so the stable regime for oscillatory modes of parallel wavelengths is given by

$$(k_x H)^2 < f(\beta_b) \approx 0.06299\,. \tag{7.61}$$

On the other hand, for large β or small parallel wavelengths ($k_x H \gg 1$),

$$\lim_{\beta\to\infty} f(\beta) = \frac{\gamma-1}{\gamma^2}\beta\,, \tag{7.62}$$

and so the criterion for instability becomes nearly the same for both types of modes. But the evanescent mode remains the most unstable.

Interpretation The stability aspects of the three-layer model may be interpreted in looking to the physical meaning of the marginal relation $\mathcal{E}_q^- \sim \mathcal{E}_p^- \sim 0$ for evanescent modes, by considering a semi-infinite magnetic isothermal region below z_p.

Indeed, $\mathcal{E}_p^- = 0$ when $\kappa = -i\kappa_e$ corresponds to the dispersion relation for a two-layer model with a semi-infinite magnetic isothermal region below z_p (see Figure 7.3(a)). The boundary condition at infinity requires to choose the evanescent mode and evanescent disturbance. Hence the condition of continuity (7.10) at the interface $z = z_p$ yields the dispersion relation (see also Foullon (1999) in the case of parallel propagation)

$$\mathcal{D}_a = \frac{Q}{P\Lambda^- + R}\,. \tag{7.63}$$

This two-layer model may be viewed as a limiting case ($z_q \to \infty$) of the general three-layer models (*cf.* Figures 7.1). The associated dispersion relation in this limit (see Equation (7.27)) is $\mathcal{E}_p^-\mathcal{E}_q^+ = 0$. Since only the surface mode solution and the evanescent disturbance is relevant, the dispersion relation is given by $\mathcal{E}_p^- = 0$, corresponding to Equation (7.63).

The reason why there is no instabilities allowed by the marginal relation $\mathcal{E}_q^+ \sim \mathcal{E}_p^+ \sim 0$ for evanescent modes may also be interpreted, by considering a semi-infinite magnetic isothermal region above z_q.

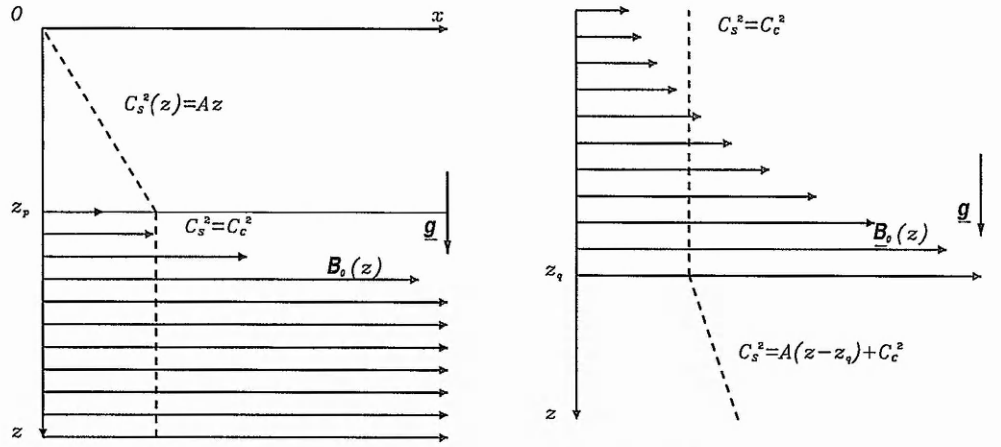

Figure 7.3: Two-Layer Models. (*a*) Two-layer model of a polytropic medium $0 \leq z \leq z_p$ overlying a semi-infinite isothermal magnetic region with constant Alfvén speed.(*b*) A semi-infinite isothermal magnetic region with constant Alfvén speed $z \leq z_q$ lies above a polytropic medium.

The dispersion relation $\mathcal{E}_q^+ = 0$ corresponds to a somewhat symmetric configuration, and may be viewed as the limiting case ($z_p \to -\infty$) of the general three-layer model (see Figures 7.1(*a*) and 7.3(*b*)) where $\mathcal{D}_q = \mathcal{D}_b$, *viz.*

$$\mathcal{D}_b = \frac{Q}{P\Lambda^+ + R}. \tag{7.64}$$

The dispersion relation (7.64) is very similar in form to the dispersion relation (7.63), except that the functions U arising here replace the functions M, and Λ^+ replaces Λ^-. The case $k_y = 0$ was examined by Campbell and Roberts (1989), treating the effect of a magnetic chromosphere on p-modes propagating parallel to the magnetic field lines.

The 'chromospheric' configuration is 'bottom heavy' and therefore should not be subject to a magnetic Rayleigh-Taylor instability. In fact, it was shown earlier (see Equation (7.52)), that the evanescent mode with Λ^+ is not subject to any instability.

Discussion It is not surprising that the marginal stability of the three-layer model and the one for the two-layer model of Figure 7.3(*a*) correspond for the evanescent solution in the layer, since the 'top-heavy' equilibrium state at $z = z_p$ might be unstable to the same mode.

As $k_x \to 0$, unstable modes with parallel propagation ($k_y = 0$) may arise for a parameter β smaller than β_{crit} given by Equation (7.58). In fact, this value may be

related to the field-free Brunt-Väisälä and acoustic cut-off frequencies through (see Equation (5.73), p.110)

$$\beta_{crit} = \frac{\gamma^2}{4(\gamma-1)} = \frac{\omega_g^2}{\omega_a^2}\,. \tag{7.65}$$

Using the β_{crit} of Equation (7.58) in Equation (7.41), one would get unstable modes for a field strength $B_o(z_p)$ greater than

$$\begin{aligned} B_{crit} &= \sqrt{\frac{3(\gamma-1)}{3\gamma-2}}B_{max}\,, \\ i.e. \qquad B_{crit} &= \frac{2}{3}B_{max}\,, \qquad \text{for} \quad \gamma = \frac{5}{3}\,. \end{aligned} \tag{7.66}$$

But the layer itself, as well as modes with perpendicular propagation ($k_x = 0$), may be already unstable for

$$B_{crit} = \sqrt{\frac{2}{5}}B_{max} < \frac{2}{3}B_{max}\,. \tag{7.67}$$

Evanescent modes propagating parallel to the field-lines become more unstable than the perpendicular modes for

$$\begin{aligned} (k_x H)^2 &> \frac{1}{2\gamma} - \frac{1}{4} \\ i.e. \qquad (k_x H)^2 &> 0.05 \qquad \text{for} \quad \gamma = \frac{5}{3}\,. \end{aligned} \tag{7.68}$$

In fact, the magnetic interface stabilises these modes against long wavelengths such that $(k_x H)^2 < 0.05$ but destabilises them against the shorter wavelengths such that $(k_x H)^2 > 0.05$.

For a realistic model of the Sun which includes an internal magnetic layer, the next chapter will show that one cannot attain such field strengths. It is therefore more relevant to know for which wavenumber k_c, one may approach a state of instability, *i.e.* such that

$$(k_c H)^2 = \frac{\gamma-1}{\gamma^2}\beta - \frac{1}{4}\,. \tag{7.69}$$

Chapter 8

First Applications

All the information about the propagation of a given wave mode is contained in the appropriate dispersion relation, which relates the angular frequency ω to the horizontal wavenumber k_h. The general dispersion relation (7.27) was explored in a way to identify the different wavefield contributions (Section 7.1) and discuss stability aspects (Section 7.2). Its form will eventually be useful to work out an analytical approximation to the effect of the buried layer in a polytrope (see Section 10.3). But as a first application, the dispersion relation developed in Section 7.1 is adapted in Section 8.1 to the particular case of field-free layered models. A complicated dispersion relation may be difficult to interpret without a graphical representation. In Section 8.2, diagnostic diagrams are presented and discussed for specified models that include a magnetic layer and are obtained for more or less realistic parameters. For these models, only the case of parallel propagation ($k_y = 0$) is treated.

8.1 Standard field-free layered models

The three-layer model presented in Figure 8.1(a) is the field-free limit ($\beta \to \infty$) of the three-layer model discussed earlier (see Figure 7.1(a)). The dispersion relations for field-free models may be easily obtained from the general dispersion relation (7.27), but they can also be obtained in a much simpler form. Besides, there exists cases of interest, where the dispersion relation must be derived independently from the more

general case. For instance, Figure 8.1(b) shows a two-layer model with a field-free isothermal region below z_p truncated at z_q; this is a special case of the three-layer model of Figure 8.1(a), with the same condition of continuity at the interface $z = z_p$, but with a particular condition at the wall $z = z_q$. To derive this dispersion relation, the boundary condition at the field-free interface $z = z_q$ must be reconsidered.

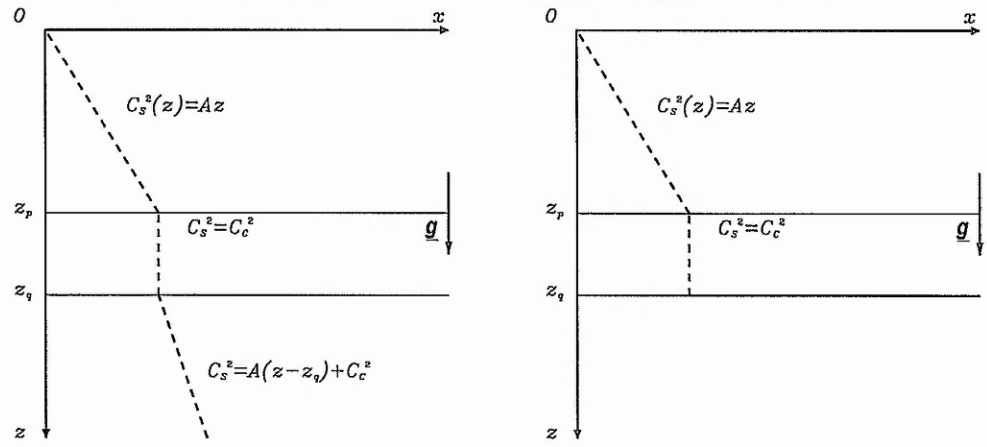

Figure 8.1: (a) Three-layer field-free model: an isothermal slab $z_p \leq z \leq z_q$ lies between two polytropes $0 \leq z \leq z_p$ and $z \geq z_q$. (b) Two-layer field-free model: a truncated isothermal region $z_p \leq z \leq z_q$ lies at the base of a polytrope $0 \leq z \leq z_p$.

1. Field-free interface

In the field-free limit, an interface at $z = z_i$ is no longer subject to a jump in hydrostatic pressure. However such a field-free interface with continuous sound speed may be considered subject to a discontinuity in temperature gradient. With respect to the positive z-direction, a physical quantity at $z = z_i$ is denoted in the region below the interface by the script '$-$' and in the region above it by the script '$+$'.

If the sound speed $c_s(z)$ is continuous across z_i, the matching of the normal acoustic impedance across $z = z_i$, as in Equation (7.7), corresponds also to the condition of continuity of V_z and Δ, *viz.*

$$\frac{V_z}{\Delta}\Big|_+ = \frac{V_z}{\Delta}\Big|_- , \qquad \text{that is} \quad \mathcal{D}\,|_+ = \mathcal{D}\,|_- \ . \tag{8.1}$$

From Equation (4.4), which can be rewritten in the normalised form

$$(\Omega^4 - 1)V_z = \left(\frac{c_s^2}{g} - \frac{\gamma\Omega^2}{k_h}\right)\Delta - \frac{c_s^2\Omega^2}{gk_h}\frac{d\Delta}{dz}, \tag{8.2}$$

it can be deduced that $\frac{d\Delta}{dz}$ is also continuous. Therefore the condition (8.1) is equivalent to the requirement

$$\frac{1}{\Delta}\frac{d\Delta}{dz}\mid_{+} = \frac{1}{\Delta}\frac{d\Delta}{dz}\mid_{-} . \tag{8.3}$$

The continuity of Δ and $\frac{d\Delta}{dz}$ may be combined in the condition that $\frac{d\ln\Delta}{dz}$ is continuous across the interface. This is the form used by Pekeris (1948) and Price (1996).

Polytropic/isothermal interface Consider now an interface at $z = z_i$ between a polytropic region and an isothermal region. A physical quantity at this interface is denoted in the polytrope by the script '*poly*' and in the isothermal region by the script '*iso*'. The condition of continuity across a field-free interface (polytrope/isothermal layer) at $z = z_i$ is

$$\mathcal{D}\mid_{poly} = \mathcal{D}_c\mid_{iso} . \tag{8.4}$$

$\mathcal{D}_c$ is the field-free isothermal part defined in Equation (7.34) and $\mathcal{D}\mid_{poly}$ may be in turn $\mathcal{D}_a$ and $\mathcal{D}_b$ respectively at $z_i = z_p$ and $z_i = z_q$ (see Equations (7.30) and (7.31)).

Developing $\mathcal{D}_a = \mathcal{D}_c$ at $z_i = z_p$ and $\mathcal{D}_b = \mathcal{D}_c$ at $z_i = z_q$ yields respectively

$$\frac{1}{\Delta}\frac{d\Delta}{dz}\mid_{z=z_p^+} = 2k_h\frac{M'}{M} - k_h ; \tag{8.5}$$

$$\frac{1}{\Delta}\frac{d\Delta}{dz}\mid_{z=z_q^-} = 2k_h\frac{U'}{U} - k_h ; \tag{8.6}$$

M, U, M' and U' are defined in Equations (7.32)-(7.33).

Field-free truncation Finally, the condition $V_z = 0$ at $z = z_i$ for a field-free truncated interface corresponds to

$$\mathcal{D} = 0 . \tag{8.7}$$

The condition of continuity across a truncated interface at $z_i = z_q$ is given by $\mathcal{D}_c = 0$, *viz.*

$$\frac{1}{\Delta}\frac{d\Delta}{dz}\mid_{z=z_q^-} = \frac{k_h}{\Omega^2} - \frac{1}{H_o} . \tag{8.8}$$

Finally, note that the case $\omega^4 = g^2k_h^2$ (*i.e.* $\Omega^4 = 1$), which is a singularity in the field-free equation, must be treated separately.

2. Dispersion relations

According to the nature of the solutions in the isothermal layer of thickness $h = z_q - z_p$ (see Equations (7.36) and (7.37)), the dispersion relations for the model of Figure 8.1(a) are: for evanescent modes,

$$\epsilon_p^- \epsilon_q^+ e^{2\kappa_e h} - \epsilon_p^+ \epsilon_q^- = 0\,, \tag{8.9}$$

where

$$\epsilon_p^\pm = \left(k_h + \Lambda_i^\pm\right) M - 2k_h M'\,, \qquad \epsilon_q^\pm = \left(k_h + \Lambda_i^\pm\right) U - 2k_h U'\,; \tag{8.10}$$

for oscillatory modes,

$$[f_q f_p + \kappa_b^2 UM]\sin(\kappa_b h) - 2k_h\kappa_b(UM' - MU')\cos(\kappa_b h) = 0\,, \tag{8.11}$$

where

$$f_p = \left(k_h - \frac{1}{2H_o}\right) M - 2k_h M'\,, \qquad f_q = \left(k_h - \frac{1}{2H_o}\right) U - 2k_h U'\,. \tag{8.12}$$

For the truncated model of Figure 8.1(b), the dispersion relations are: for evanescent modes,

$$\epsilon_p^- \delta^+ e^{2\kappa h} - \epsilon_p^+ \delta^- = 0\,, \tag{8.13}$$

where

$$\epsilon_p^\pm = \left(k_h + \Lambda_i^\pm\right) M - 2k_h M'\,, \qquad \delta^\pm = k_h H_o - \Omega^2 - H_o\Omega^2\Lambda_i^\pm\,; \tag{8.14}$$

for oscillatory modes,

$$[\delta_q f_p + \kappa_b^2 M]\sin(\kappa_b h) - \kappa_b(M\delta_q - f_p)\cos(\kappa_b h) = 0\,, \tag{8.15}$$

where

$$f_p = \left(k_h - \frac{1}{2H_o}\right) M - 2k_h M'\,, \qquad \delta_q = \frac{1}{2H_o} - \frac{k_h}{\Omega^2}\,. \tag{8.16}$$

But one can obviously generalise the dispersion relation (8.9) or (8.13) as for the general magnetic model.

3. Semi-infinite field-free isothermal region below z_p

In Figure 8.2, a two-layer model is considered with a semi-infinite field-free isothermal region below z_p.

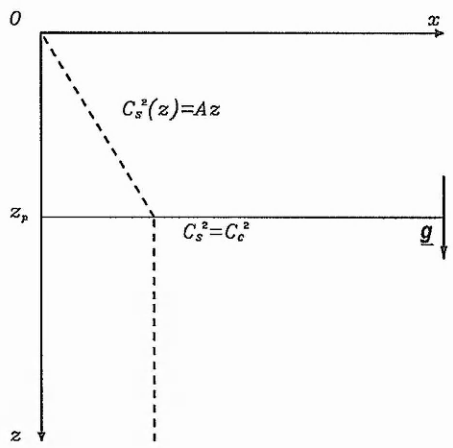

Figure 8.2: Two-layer field-free model: a polytropic medium $0 \leq z \leq z_p$ overlying a semi-infinite isothermal region.

For $\Omega^4 \neq 1$, the condition of continuity across an interface, given in Equation (8.3), is

$$\frac{1}{\Delta}\frac{d\Delta}{dz}\Big|_{z=z_p^+} = \frac{1}{\Delta}\frac{d\Delta}{dz}\Big|_{z=z_p^-} . \tag{8.17}$$

The boundary condition at infinity requires to choose the surface mode solution and an evanescent disturbance. Thus Equation (8.17) gives the dispersion relation

$$\Lambda_i^- = 2k_h\frac{M'}{M} - k_h . \tag{8.18}$$

Equation (8.18) is equivalent to

$$\epsilon_p^- = (k_h + \Lambda_i^-)M - 2k_h M' = 0 , \tag{8.19}$$

which is also

$$\mathcal{D}_a = \mathcal{D}_i , \tag{8.20}$$

where $\mathcal{D}_a$ and $\mathcal{D}_i$ are the field-free parts given by Equation (7.11), applied respectively for a polytropic medium at $z_i = z_p$ and for an isothermal field-free region at $z_i = z_q$. Written out, $\mathcal{D}_a = \mathcal{D}_i$ is

$$\frac{z_p}{m(\Omega^4-1)}\left[1 - \frac{m+1}{k_h z_p}\Omega^2 + \Omega^2 - 2\frac{M'}{M}\Omega^2\right] = \frac{z_p}{m(\Omega^4-1)}\left[1 - \frac{m+1}{k_h z_p}\Omega^2 - \frac{\Lambda_i^-}{k_h}\Omega^2\right] . \tag{8.21}$$

The two-layer model of Figure 8.2 is a limiting case of models discussed earlier. Specifically it corresponds to the three-layer model of Figure 7.1(b) in the absence of

the middle layer (*i.e.* for $z_q \to z_p$ or $h \to 0$); the two-layer model of Figure 7.3 in the field-free limit ($\beta \to \infty$); the field-free models of Figure 8.1 for $z_q \to \infty$.

1. In the limit $z_q \to z_p$, the dispersion relations (7.23) - (7.26) become

$$PQ\kappa(\mathcal{D}_i - \mathcal{D}_a) = 0\,; \tag{8.22}$$

$$PQ\kappa_b(\mathcal{D}_i - \mathcal{D}_a) = 0\,. \tag{8.23}$$

   P and Q are defined in (7.13), κ in (5.38) and κ_b in (5.40). These values set to zero are artificial roots left from carrying the limit operation. Hence this limit recovers $\mathcal{D}_a = \mathcal{D}_i$.

2. In the limit of a field-free region underlying the polytrope ($\beta \to \infty$), the magnetically-modified adiabatic exponent $\Gamma_o = \gamma/(1+\gamma/2\beta) \to \gamma$, the scale height $H_o = \rho_o/\rho_o' = z_p/m\Gamma_o \to \frac{z_p}{m+1}$ and $A_o \to \frac{k_h}{z_p}\left[m\Omega^2 - k_h z_p + \frac{1}{\Omega^2}\right]$, with the same formal expression for $\Lambda_i^- = \frac{-1-\sqrt{1-4A_oH_o^2}}{2H_o}$.

   The expression $\mathcal{D}_a = \mathcal{D}_i$ and the dispersion relation for a model with magnetic field (7.63) differ on their right-hand side. Thus one must check that

$$\lim_{\beta\to\infty} \frac{\frac{\gamma}{\Gamma_o}(\Omega^2 - \frac{k_x z_p}{m})}{(1+\frac{1}{\beta})(\Omega^2 - \frac{k_x z_p}{m(\beta+1)})\Lambda^- + k_x} = \frac{z_p}{m(\Omega^4-1)}\left[1 - \frac{m+1}{k_h z_p}\Omega^2 - \frac{\Lambda_i^-}{k_h}\Omega^2\right], \tag{8.24}$$

   which corresponds (with $k_x = k_h$) to

$$\left[\Lambda_i^- z_p\Omega^2 - k_h z_p + (m+1)\Omega^2\right](\Lambda_i^-\Omega^2 + k_h) = k_h(m\Omega^2 - k_h z_p)(1-\Omega^4) \tag{8.25}$$

   this reduces to a quadratic equation for Λ_i^- in the isothermal case, *viz.*

$$(\Lambda_i^-)^2 + \tfrac{(m+1)}{z_p}\Lambda_i^- + \tfrac{k_h}{z_p}(m\Omega^2 - k_h z_p + \tfrac{1}{\Omega^2}) = 0\,,$$

$$i.e. \qquad (\Lambda_i^-)^2 + \tfrac{1}{H_o}\Lambda_i^- + A_o = 0\,. \tag{8.26}$$

   This demonstrates that the dispersion relation (7.63) in the field-free limit is equivalent to $\mathcal{D}_a = \mathcal{D}_i$.

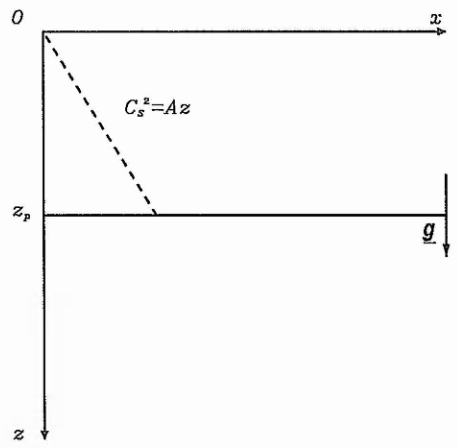

Figure 8.3: A truncated field-free polytrope $0 \leq z \leq z_p$.

3. In the limit $z_q \to \infty$, only the evanescent solutions are considered and the dispersion relation (8.9) - (8.10) for the model of Figure 8.1(a) becomes

$$\epsilon_p^- \epsilon_q^+ = 0\,; \tag{8.27}$$

for the model of Figure 8.1(b), where $V_z(z_q) = 0$, the dispersion relation (8.13) - (8.14) become

$$\epsilon_p^- \delta^+ = 0\,. \tag{8.28}$$

Only the evanescent disturbance given by Λ_i^- is physical, and so the dispersion relation is $\epsilon_p^- = 0$.

Note that at ∞, despite the fact that the boundary condition $V_z = 0$ is less strong than the kinetic energy density requirement $\rho {V_z}^2 \to 0$, the dispersion relation $\epsilon_p^- = 0$ is recovered.

4. Truncated field-free polytrope

Finally, Figure 8.3 represents a field-free polytrope for which $V_z = 0$ at a depth $z = z_p$. Thus the dispersion relation is

$$\left[1 - \frac{m+1}{k_x z_p}\Omega^2 + \Omega^2\right] M - 2\Omega^2 M' = 0\,. \tag{8.29}$$

This model is a limiting case of the model of Figure 8.1(b) for $z_q \to z_p$. In this limit, the dispersion relations (8.13) - (8.16) become

$$\epsilon_p^- \delta^+ - \epsilon_p^+ \delta^- = 0 \tag{8.30}$$

where

$$\epsilon_p^{\pm} = \left(k_x + \Lambda_i^{\pm}\right) M - 2k_x M' \,, \qquad \delta^{\pm} = k_x H_o - \Omega^2 - H_o \Omega^2 \Lambda_i^{\pm} \,; \tag{8.31}$$

and

$$\kappa_b (M \delta_q - f_p) = 0 \,, \tag{8.32}$$

where

$$f_p = \left(k_x - \frac{1}{2H_o}\right) M - 2k_x M' \,, \qquad \delta_q = \frac{1}{2H_o} - \frac{k_x}{\Omega^2} \,. \tag{8.33}$$

Both lead to the dispersion relation of a truncated field-free polytrope (8.29), along with $\kappa_e = 0$ or $\kappa_b = 0$ (the acoustic and gravity cut-offs in the isothermal layer), which are artificial roots left over from carrying the limit operation.

Note finally that Equation (8.29) may be found in Pekeris (1948, see his Equation (42)) for a model of the Earth's atmosphere where the ground level is at $z = z_p$.

8.2 Applied and numerical solutions

Solving the dispersion relation numerically consists of computing the function and finding its roots. In the present case, this implies the evaluation of confluent hypergeometric functions. Instead of computing the dispersion relation and the special functions it contains, it is sometimes easier and more productive to solve the differential equations and match the boundary conditions numerically. This method is especially valuable at singularities, in the Alfvén and cusp continua — where the ideal approximation breaks down — in order to introduce resistive effects at these points (see models of the solar atmosphere, *e.g.*, Tirry, 1998; Vanlommel, 2001). But this does not always give convincing results (see Pintér, 1999) and, by narrowing the search to solutions such as the f-, p- and g-modes, this method can disregard the presence of other modes, such as surface waves and instabilities. Favouring the painstaking method, which would give all the modes, the diagnostic diagrams which are presented in this section result from computing the confluent hypergeometric functions numerically and solving the dispersion relation via a root finding program (see Appendix A.1).

1. Model parameters

Figure 8.4 and Table 8.1 describe the different models whose dispersion relation is solved and for which diagnostic diagrams are shown. Five distinct models are investigated, referred respectively as *model A*, *model B*, *tachocline model (a)*, *tachocline model (b)* and *shallow field model*. Models A and B are physically unrealistic but provide some useful results that are a guide for other cases. The parameters for the tachocline model and the shallow field model are chosen as realistic as possible to best represent the two magnetic field configurations described in Section 2.2: the tachocline model includes a magnetic layer assumed to reside at the base of the convection zone at $z = z_p$, with field strength of 300 kG; the shallow field model includes the sunspot's anchoring zone ranging between depths $z = z_p$ and $z = z_q$, with field strength of 30 kG at $z = z_p$.

Three variants of the general dispersion relation (7.27) are used (the respective equilibrium configurations are shown in Figure 8.4). Model A is solved for $z_q \to \infty$, *i.e.* with the relation (7.63). For an isothermal region below z_q, the same dispersion

Model A

Model B

Tachocline model (a)

Tachocline model (b)

Shallow field model

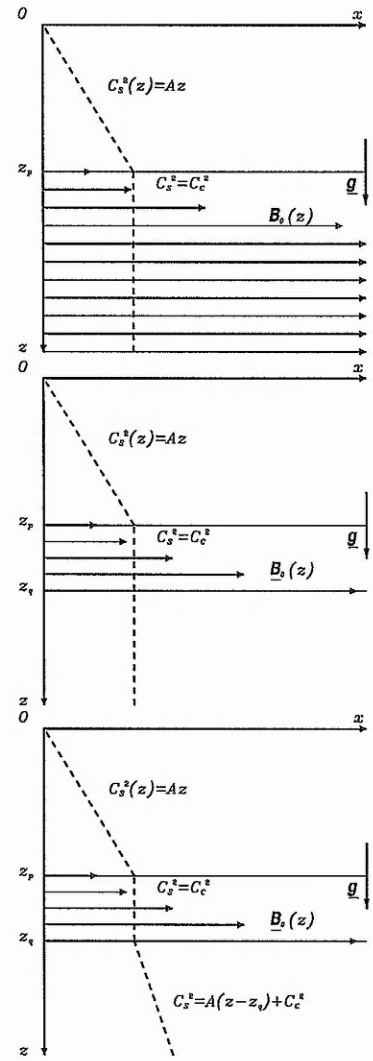

Figure 8.4: Sketch of equilibrium configurations for the models indicated to the left of each sketch and whose conditions are specified in Table 8.1

Model parameters		Model A	Model B	Tachocline model	Shallow field model
z_p	(km)	272239			35036
$z_p/\,\mathrm{R}_\odot$		0.3911			0.0503
c_c	($\mathrm{km\,s^{-1}}$)	223			80
$H(z_p)$	(km)	108896			14014
$H(z_p)/\,\mathrm{R}_\odot$		0.1564			0.0201
p_o^{free}	(Pa)	5.25855×10^{12}			5.23298×10^{10}
B_{max}	(kG)	36354			3626
B_{crit}	(kG)	22992			2293
$B_o(z_p)$	(kG)	500	5000	300	30
v_A	($\mathrm{km\,s^{-1}}$)	3.360	33.598	2.016	0.725
β	($= c_c^2/v_A^2$)	4404.559	44.054	12236.368	12176.864
$\frac{\rho_o^{free}}{\rho_o^{mag}} - 1 = \frac{\gamma}{2\beta}$	($\times 10^{-5}$)	18.9198	1 891.6211	6.8103	6.8436
$k_c z_p$		81.2729	8.0323	135.4732	135.1433
k_c	($\mathrm{Mm^{-1}}$)	0.2953	0.0295	0.4976	3.857
$k_c\,\mathrm{R}_\odot$		205.53	20.53	346.33	2684.43
$h/\,\mathrm{R}_\odot$		0	0.3	0.05	
h/z_p		0	0.767	0.128	0.994
z_q	(km)	$\to \infty$	481 036	307 039	69 836
$z_q/\,\mathrm{R}_\odot$			0.6911	0.4411	0.1003
$[c_s^2]'$ for $z > z_q$	($\mathrm{m\,s^{-2}}$)	0		(a) 0 or (b) A	A

Table 8.1: Specified model conditions used to solve the dispersion relation and analyse diagnostic diagrams. The first list of parameters are related to the field-free side of the upper magnetic interface: the depth z_p, the sound speed c_c, the pressure scale-height $H(z_p)$, the hydrostatic pressure p_o^{free} and the critical field strengths B_{max} and B_{crit}. The second set of parameters are related to the magnetic side: the field strength $B_o(z_p)$, the constant Alfvén speed v_A, the ratio β between the squared sound speed and the Alfvén speed, the density jump at the magnetic interface $\rho_o^{free}/\rho_o^{mag}$ and the critical wavenumber k_c. The last set of parameters describe properties of the model below this interface: the thickness h of the layer, how thick is this layer as seen from the surface through the ratio h/z_p, the depth z_q of the lower magnetic interface and the gradient for the sound speed squared $[c_s^2]'$ beyond z_q.

relation applies for both Model B and the tachocline model (a) allowing for a change in parameters only; this relation involves the field-free part $\mathcal{D}_q$ given by Equation (7.38). For a polytrope below z_q, the same can be said for the tachocline model (b) and the shallow field model, for which the field-free part $\mathcal{D}_q$ is given by Equation (7.31).

The value for the sound speed at the base of the convection zone is determined, from helioseismic inversion techniques, by Christensen-Dalsgaard et al. (1991), who give $c_c = 223 \pm 2\,\mathrm{km\,s^{-1}}$. By assuming $g = 274\,\mathrm{m\,s^{-2}}$, the gradient with respect to z for the squared sound speed $c_s^2(z)$ for $0 \leq z \leq z_p$ is $A = \frac{g}{m} = 0.183\,\mathrm{m\,s^{-2}}$, and the depth z_p is deduced through the relation $c_c^2 = Az_p$ (see Equation (6.6)). Inversely, for the shallow field model, the sound speed $c_c = 80\,\mathrm{km\,s^{-1}}$ was chosen so as to obtain z_p and z_q in the range identified to be the seat of a significant perturbation (Dziembowski et al., 2000; Antia et al., 2000). In both the tachocline model (b) and the shallow field model, the thickness of the layer is $0.05\,\mathrm{R}_\odot$. For the shallow field model, this corresponds to a magnetic layer ranging from 35 Mm down to 70 Mm. It may be noted that this shallow layer extends up to where the torsional oscillations appear to be significant (see Section 2.2). The hydrodynamic pressures are chosen to match the sound speeds in agreement with the solar model of Guenther et al. (1992), thus setting conditions as close as possible to those in the solar interior.

The wave equation in the magnetic layer was greatly simplified in assuming the sound and Alfvén speeds to be constant. This assumption is justified for a thin magnetic layer, of thickness h small compared to the pressure scale-height, *i.e.* $h \ll H_o$. Note that the ratio $\beta = c_c^2/v_A^2$ in the realistic magnetic slab is very large. In these conditions, because $H_o \gtrsim H(z_p)$ (see Equation (5.12)), only the tachocline model meets the assumption of a thin magnetic layer, as can be seen in Table 8.1.

Also in Table 8.1, B_{max} and B_{crit} were calculated from Equations (7.39) and (7.67) respectively. One can speculate that in a spherical model B_{crit} would be reduced. But spherical effects are not likely to be significant in the shallow field model, where B_{crit} is rather large to explain the buoyant instability of magnetic flux tubes. However Section 7.2 showed that instabilities can set in for wavenumbers greater than a critical wavenumber k_c (given by Equation (7.69)). The closest integer less than or equal to the

value of $k_c\,R_\odot$ in Table 8.1 gives an estimate of the degree l above which instabilities may set in for the different models. For instance, instabilities in the tachocline may occur for $l \geqslant 346$, while in a shallow field they could occur for $l \geqslant 2684$. Thus, in a shallow field, this instability criterion would apply efficiently against short wavelengths. As the field strength increases at the base of the convection zone, instabilities would set in for longer wavelengths.

2. Diagnostic diagrams

Results for model A and tachocline model (a) and (b) are given in the form of normalised and dimensional diagnostic diagrams, respectively in Figures 8.5 and 8.6, with the specific equilibrium configuration recalled to the left of each diagnostic diagram in Figure 8.5. In both types of diagram, each full circle represents a mode of degree l, where l has been increased from the degree $l = 1$. The limits of the range examined, $0.1 \leq \Omega^2 \leq 15$, are indicated by thin broken lines in the third figure (tachocline (b)) of Figure 8.6.

All dispersion relations considered are functions of the dimensionless combination $k_x z_p$ and, for models with a magnetic layer of thickness h, they are also function of the dimensionless ratio h/z_p. Thus increasing l, *i.e.* increasing k_x, amounts to increasing z_p and h in the dispersion relations. In other words, the investigation of the dispersion relation through a range in degree l is equivalent to increasing z_p and h at fixed l.

In the normalised diagnostic diagrams (Figure 8.5), solutions $m\Omega^2$ of the various dispersion relations are plotted versus $k_x z_p$. The roots (in full circles) of each of the dispersion relations converge for increasing l to discrete horizontal ridges Ω_n^2 in broken lines, given by Equation (4.53) and such that $\Omega_n^2 = 1 + \frac{2n}{m}$ for radial order n. Similarly, in the dimensional diagnostic diagrams of Figure 8.6 (cyclic frequency ν against degree l), these roots are aligned on the ridges of p-modes for high degree l and deflected from them as the degree decreases. That the roots collapse on the ridges of p-modes for high degree l or when $k_x \to \infty$ confirms the results (4.53) on the basis of a simple polytrope model where $z_p \to \infty$.

The roots are deflected from the ridges as the degree decreases and in particular close

to the Lamb dispersion line. The modes for a model with magnetic field differ slightly from their field-free counterparts, but the diagnostic diagrams are indistinguishable. The tiny frequency shifts which one can obtain by comparing the two will be discussed in Chapter 10. But, it may be noted at this point that the shifts are more prominent close to the Lamb dispersion line and that, when modes are allowed in the oscillatory domain, the shifts peak mostly on the other side of the Lamb separatrix.

f-modes For $\omega^2 = gk_x$, the equations for field-free plane-stratified layers (6.20)-(6.21) taken at an interface $z = z_p$ between a polytrope and an isothermal region must be equivalent. Thus the f-mode exists as long as the boundary conditions, at the surface and at infinity, are satisfied. The vertical velocity amplitude, V_z, is determined in Equation (6.23) as

$$V_z = De^{-k_x z}, \qquad z \geq 0, \tag{8.34}$$

where D is the amplitude of V_z at $z = 0$. From the condition that the kinetic energy density vanishes at infinity in an isothermal region, the f-mode propagates (see Equation (6.25)) provided

$$k_x z_p > \frac{m\gamma}{2}. \tag{8.35}$$

Thus, for $m = \frac{3}{2}$ and $\gamma = \frac{m+1}{m}$, the f-mode propagates provided $k_x z_p > 5/4 = 1.25$. With $z_p \sim 0.3911\,\mathrm{R}_\odot$, the f-mode could not exist as a pure mode (it would thus become leaky) for degree $l \leq 3$.

In Model A, the isothermal region is magnetised, but as seen in Figures 8.5 and 8.6, a magneto-atmospheric f-mode exists as a pure mode with $\omega^2 \sim gk_x$ ($\Omega^2 \sim 1$), except at low degree or low wavenumber. In a single magnetic isothermal region, the criterion for propagation of the parallel magneto-atmospheric f-mode is given by Equation (6.38) or (6.39), *viz.*

$$k_x z_p > \frac{m}{2}\left(\frac{1+\frac{1}{\beta}}{\frac{1}{\gamma}+\frac{1}{\beta}}\right). \tag{8.36}$$

For model A, $\beta \sim 4404.559$ (see Table 8.1), this corresponds to $k_x z_p > 1.2498$ or $l > 3$, which agrees with the numerical results.

The diagrams of Figure 8.5 and 8.6 for the tachocline models or Figure 8.7 for a shallow field model exhibit a magneto-atmospheric f-mode with no apparent cut-off

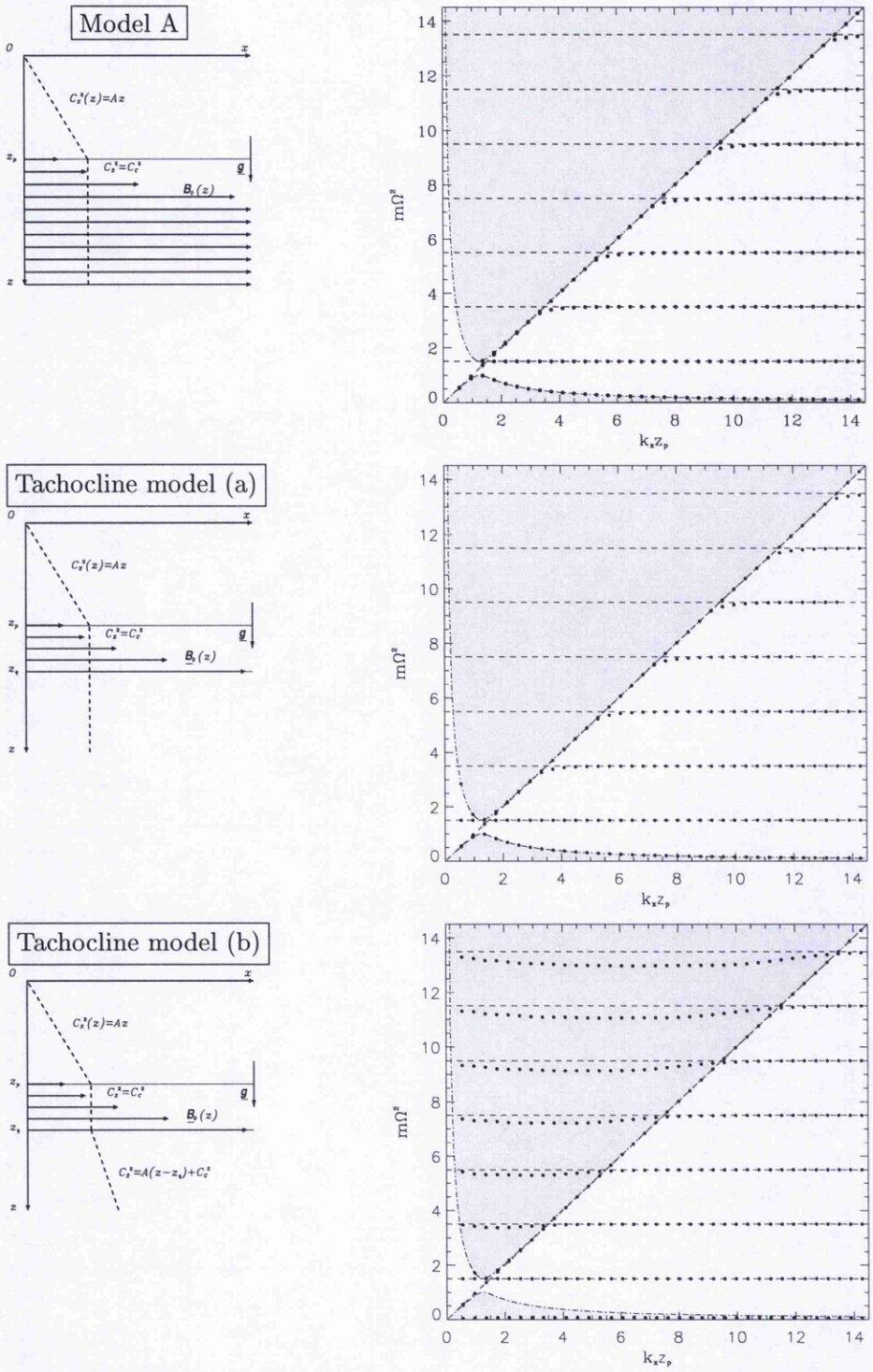

Figure 8.5: Normalised diagnostic diagrams ($m\Omega^2$ against $k_x z_p$) for model A and tachocline models with (a) an isothermal region or (b) a polytropic region below the magnetic slab. Equilibrium configurations are sketched to the left of the diagnostic diagrams.

Model A

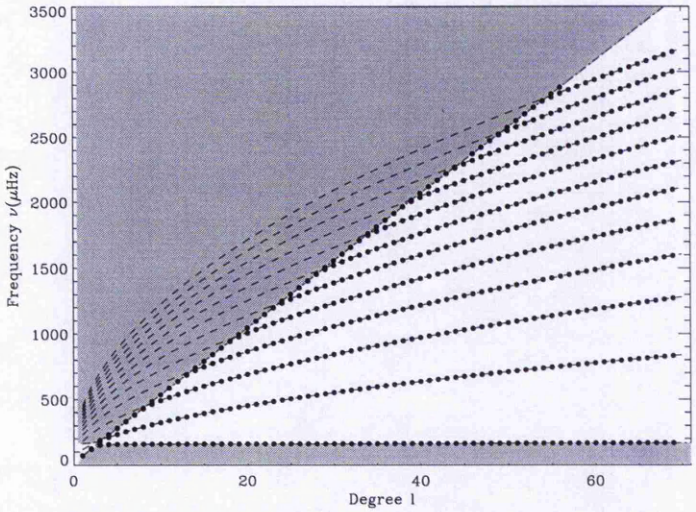

Tachocline model (a)

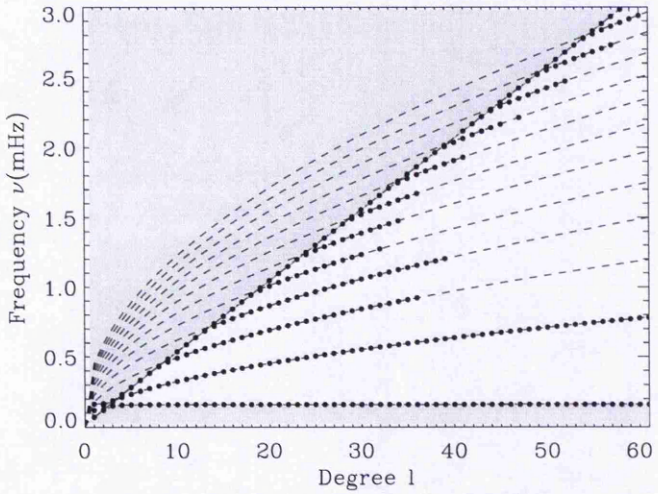

Tachocline model (b)

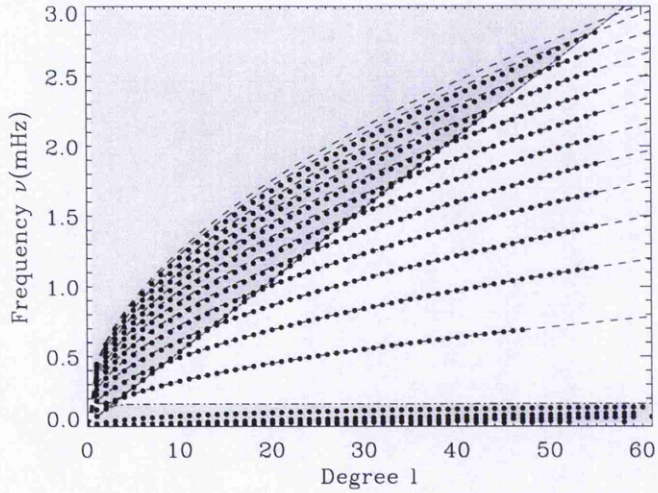

Figure 8.6: Dimensional diagnostic diagrams (cyclic frequency ν against degree l) for model A and tachocline models (a) and (b), treated in Figure 8.5.

frequency at low-degree. This difference with model A is associated with the presence of an additional magnetic interface at $z = z_q$, which opens the possibility of an evanescent disturbance (with $D_1 \neq 0$ and $\Lambda^+ = -\frac{1}{2H_o} + \kappa_e$). Hence the condition which determines the value of the cut-off frequency and which arises in Equation (6.32), p.123, namely that $\kappa_e > 0$ in the magnetic region, no longer applies for a slab.

p- and g-modes With the presence of a second magnetic interface at $z = z_q$, the isothermal layer may support (oscillatory) body waves. The plus cut-off frequencies in the magnetic and field-free regions are indistinguishable because of the high value of β. For the tachocline model (a), the oscillatory modes in the magnetic layer are concealed because of the presence of the isothermal field-free region below it. But allowing for an increasing temperature profile in the region below the slab, the p- and g-modes which are oscillatory in the layer undergo refraction. These modes belong to the shaded oscillatory domain in the diagrams for the tachocline model (b) in Figures 8.5 or 8.6 and for the shallow field model in Figure 8.7.

In the limit $z_q \to z_p$, the dispersion relation (7.27) for a magnetic slab embedded between two polytropes reduces to

$$(UM' - U'M)\kappa = 0\,. \tag{8.37}$$

$UM' - U'M$ is the Wronskian of M and U, which is null when M and U are linearly dependent, that is for Υ integer. These roots are therefore the p-modes, given by Equation (4.53). This also means that the slab is ignored if seen from the surface ($k_x \to \infty$) or from the centre of the star ($k_x \to 0$).

As seen in Figure 8.7, the effect of the isothermal layer is stronger for a shallow field model. This is explained by considering the effect of the isolated layer, which is an isothermal waveguide as described in Section 6.1. From Equation (6.3), the effect of this layer depends upon the ratio $\frac{z_p}{h}$. This parameter is a measure of the ratio between the pressure scale-height in the layer and the thickness of the layer. In other terms, $\frac{h}{z_p}$ indicates how thick the layer is as seen from the surface. Obviously, the thinner is the layer, the less the modes are affected by it. With $\frac{h}{z_p} = 0.994$, the effect for the shallow field model is much larger than with $\frac{h}{z_p} = 0.128$ for the tachocline model (see Table

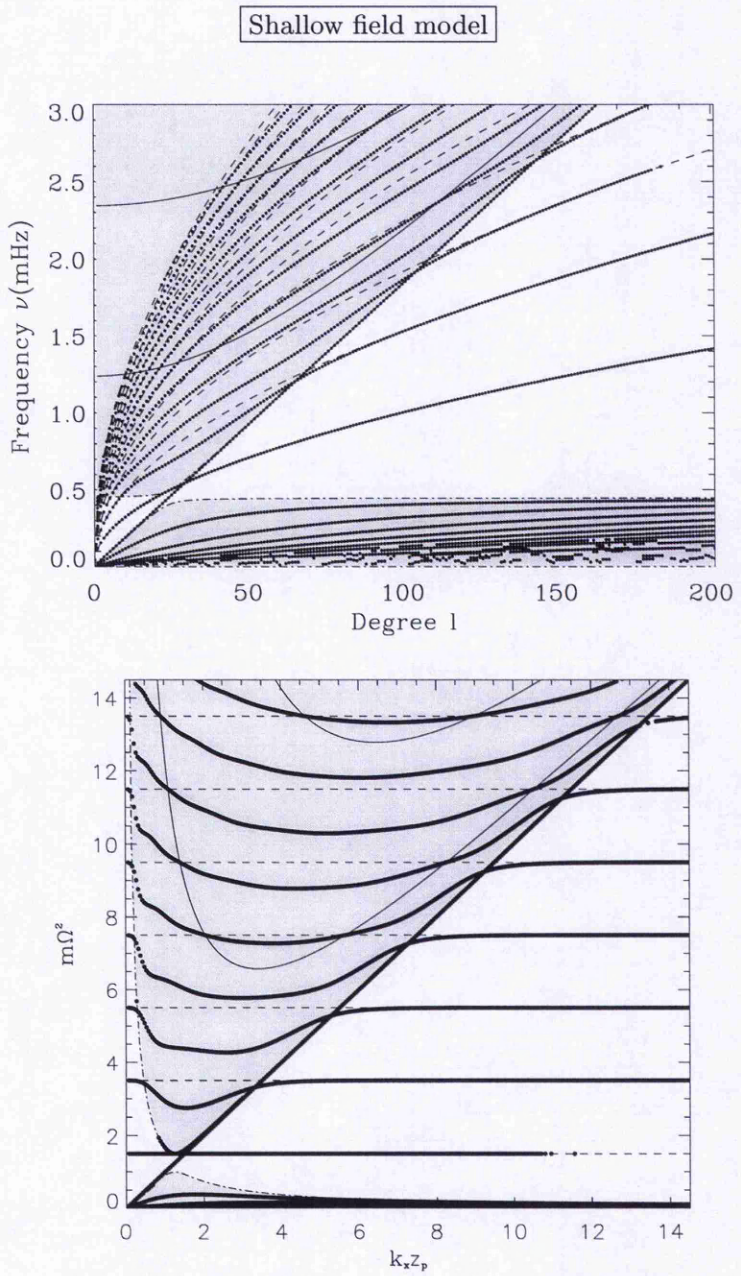

Figure 8.7: Diagnostic diagrams (l,ν) and ($k_x z_p$,$m\Omega^2$) for the shallow field model, showing the p-modes as full circles (see Figure 8.8 for a snapshot of the g-modes). The oscillatory domains are shaded. p-modes in a simple polytrope and in a waveguide with the same conditions as in the magnetic slab (with $k_y = 0$) are represented respectively in dashed and plain lines. The bold ridges of the hybrid layers pass through the intersection points of the ridges of the simple layers.

8.1). Because the frequencies of the isolated isothermal waveguide increase with the ratio $\frac{z_p}{h}$, it is with the diagnostic diagrams for the shallow field model (Figure 8.7) that

the waveguide ridges can be overplotted on the results of the more complex model, and then an elegant phenomenon may be the best observed: the ridges of the hybrid layers pass through the intersection points of the ridges of the single layers. This phenomenon is also obtained for the tachocline model (looking at higher frequencies). It was also seen by Steffens and Schmitz (2000) in a model of the solar atmosphere and in the absence of magnetic field.

Since there are no g-modes in the single polytrope (with $\omega_g = 0$), the g-modes of the hybrid layers would approach the g-modes of the isothermal waveguide as $\omega \to 0$. A snapshot of the g-modes for the shallow field model in Figure 8.8 supports this suggestion. In this figure also, the g-modes of model B may propagate in the light shaded oscillatory domain allowed by the presence of the second magnetic discontinuity at $z = z_q$, but are forbidden to propagate in the dark shaded oscillatory domain due to the isothermal region below the magnetic layer. In addition to the g-modes, Figure 8.8 shows, in the case of model B, the presence of surface waves in the unshaded evanescent domain. Before interpreting the results, the nature of these waves needs to be understood.

3. Surface waves

Single magnetic interface The discontinuity in magnetic field, as it appears in several of the models at a single magnetic interface, may support the propagation of magneto-atmospheric surface waves. The presence of such waves is due to the parallel tension force exerted by the magnetic field in the yz-plane perpendicular to the magnetic field lines (see Equations (3.48)-(3.49)). They are shear waves revealed analytically by the characteristic term in k_x^2, which is equivalent to a parallel surface tension.

Their propagation may be studied in the restricted case of zero gravity. In this case, Wentzel (1979) investigated the limits for both parallel ($k_y = 0$) and perpendicular propagation ($k_x = 0$). Non-parallel propagation ($k_x \neq 0$ and $k_y \neq 0$) was investigated later (Somasundaram and Uberoi, 1982; Jain and Roberts, 1991).

For parallel propagation, disturbances in the y-direction, accounting for the terminated Alfvén wave, are decoupled from the others. And so the magneto-atmospheric

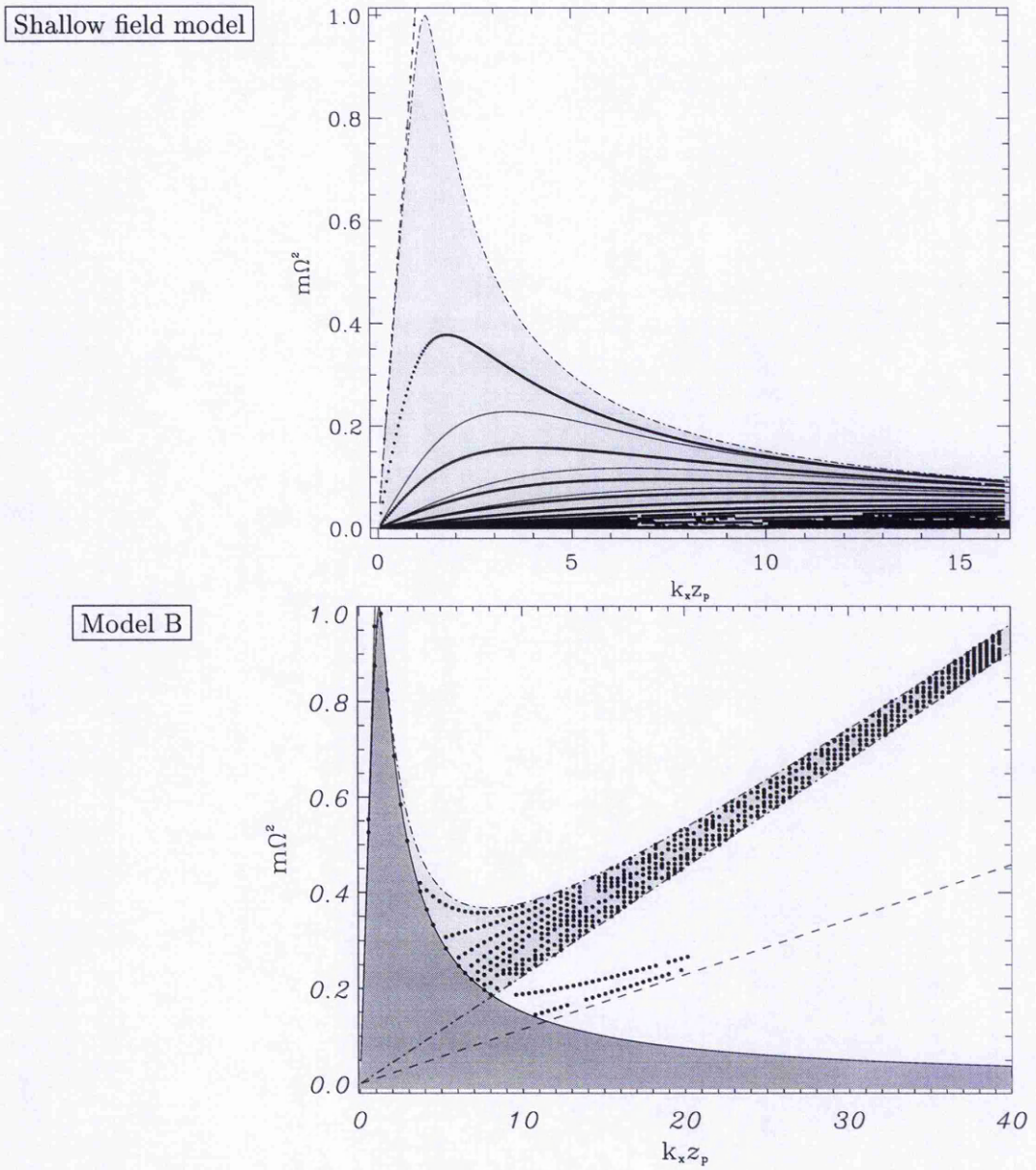

Figure 8.8: Normalised diagnostic diagrams showing the g-modes for the shallow field model and model B. The legend is as in Figure 8.7. The evanescent domain due to the isothermal region below the magnetic slab in model B is shaded in a darker grey. For model B also, the dashed diagonal line represents the dispersion line for the kink speed (8.45) adapted to the problem of the plane-stratified layers.

surface wave is connected to disturbances in the vertical z-direction only. For this reason, the properties of parallel magnetoacoustic surface waves in isothermal media could be investigated not only in zero-gravity studies (Wentzel, 1979; Roberts, 1981a;

Lee and Roberts, 1986; Miles and Roberts, 1989) but also in the presence of gravity, when the magnetic field is structured in such a way as to produce a constant Alfvén speed (Miles and Roberts, 1992) or is uniform (Miles et al., 1992).

A magnetic slab Body waves occur as motions throughout the medium. And so, when the magnetised plasma is bounded by another inhomogeneity, such as an interface parallel to the first one, body modes may propagate in the magnetic slab that is formed.

For parallel propagation and in the case of zero gravity and isothermality, an isolated slab of uniform magnetic field with an identical environment on each side of the slab has been investigated either when the environment is field-free (Roberts, 1981b; Rae and Roberts, 1983) or when it is magnetised (Edwin and Roberts, 1982). For perpendicular propagation, see Singh and Talwar (1993). For parallel propagation and for a slab of thickness h, where quantities are specified by the subscript 'o' in the slab and by the subscript 'e' in the environment, the resulting dispersion relation is

$$\frac{\rho_o}{\rho_e}\left(\frac{\omega^2-k_x^2v_{Ao}^2}{\omega^2-k_x^2v_{Ae}^2}\right)+\frac{m_o}{m_e}\left\{\begin{matrix}\tanh\\ \coth\end{matrix}\right\}m_o\frac{h}{2}=0\,, \tag{8.38}$$

where m_i for $i=o,e$ is defined through

$$m_i^2=\frac{k_x^2c_{si}^2-\omega^2}{c_{\perp i}^2}\,,\qquad c_{\perp i}^2=\frac{\omega^2}{\omega^2-k_x^2v_Ai^2}\left(c_{si}^2+v_{Ai}^2-\frac{k_x^2}{\omega^2}c_{si}^2v_{Ai}^2\right)\,. \tag{8.39}$$

The two modes are respectively the sausage (with tanh function) and kink modes (with coth function), corresponding to the eigenfunction V_z being an odd or even function of z. Solutions with $m_o^2>0$ are surface waves, and those with $m_o^2<0$ are body waves. The outer boundary conditions imposed require that $m_e^2>0$, which implies solutions for (a) $\omega/k_x<c_{se}$ and $c_{\perp e}^2>0$ or (b) $\omega/k_x>c_{se}$ and $c_{\perp e}^2<0$.

When the environment is field-free ($v_{Ae}=0$, $v_{Ao}=v_A$), only case (a) applies. In this case, for solutions with $m_o^2>0$ (like at a single interface; see Roberts, 1981a), the slab always supports a slow surface wave satisfying $\omega/k_x<\min(c_{To},c_{se})$. But if $c_{se}>c_{so}$ and $v_A>c_{so}$, then a second mode may propagate with a longitudinal phase speed satisfying $c_{so}<\omega/k_x<\min(c_{se},v_A)$; this is the fast surface wave. In general, a slab may support both fast and slow surface waves ($m_o^2>0$) and fast and slow body waves ($m_o^2<0$).

The limit $h \to \infty$ in Equation (8.38) gives the dispersion relation for surface waves propagating parallel to a single magnetic interface, subject to the condition that $m_o > 0$ and $m_e > 0$ (Roberts, 1981a), *viz.*

$$\frac{\omega^2}{k_x^2} = \frac{\rho_o m_e v_{Ao}^2 + \rho_e m_o v_{Ae}^2}{\rho_o m_e + \rho_e m_o} \,. \tag{8.40}$$

Thus compressible surface waves on a single interface have a phase speed that is intermediate between the Alfvén speeds of the two media.

In the limit of an incompressible fluid ($c_s \to \infty$), $m_i \to k_x$, and the dispersion relation (8.38) becomes

$$\frac{\rho_o}{\rho_e}\left(\frac{\omega^2 - k_x^2 v_{Ao}^2}{\omega^2 - k_x^2 v_{Ae}^2}\right) + \left\{\begin{matrix}\tanh\\ \coth\end{matrix}\right\}\frac{k_x h}{2} = 0\,; \tag{8.41}$$

if in addition the environment is field-free ($v_{Ae} = 0$, $v_{Ao} = v_A$), it becomes

$$\frac{\omega^2}{k_x^2} = \frac{\rho_o}{\rho_o + \rho_e \left\{\begin{matrix}\tanh\\ \coth\end{matrix}\right\}\frac{k_x h}{2}} v_A^2 \,. \tag{8.42}$$

In this limit it appears that surface waves exist with sub-Alfvénic phase-speeds.

The limit $h \to \infty$ in Equation (8.41) is consistent with the result, for a single interface between two incompressible fluids, that a surface wave propagates at a speed that is intermediate between the Alfvén speeds of the two media, just as in the compressible case *viz.*

$$\frac{\omega^2}{k_x^2} = c_k^2 = \frac{\rho_o v_{Ao}^2 + \rho_e v_{Ae}^2}{\rho_o + \rho_e}\,; \tag{8.43}$$

the horizontal phase speed of the wave is the kink speed c_k.

The limit $h \to \infty$ or $k_x \to \infty$ in Equation (8.42) or the case of a field-free environment ($v_{Ae} = 0$, $v_{Ao} = v_A$) in Equation (8.43) yields the result for a single magnetic interface between two uniform and incompressible fluids (Uberoi, 1972), *viz.*

$$\frac{\omega^2}{k_x^2} = c_k^2 = \frac{\rho_o v_A^2}{\rho_o + \rho_e} \,. \tag{8.44}$$

Magneto-atmospheric surface waves In plane-stratified problems, only for very large and unrealistic field strengths and layer thickness was it possible to detect the presence of magneto-atmospheric surface waves. At the interfaces between the magnetic slab and two outer polytropes, such as in the tachocline model (b) or the shallow field

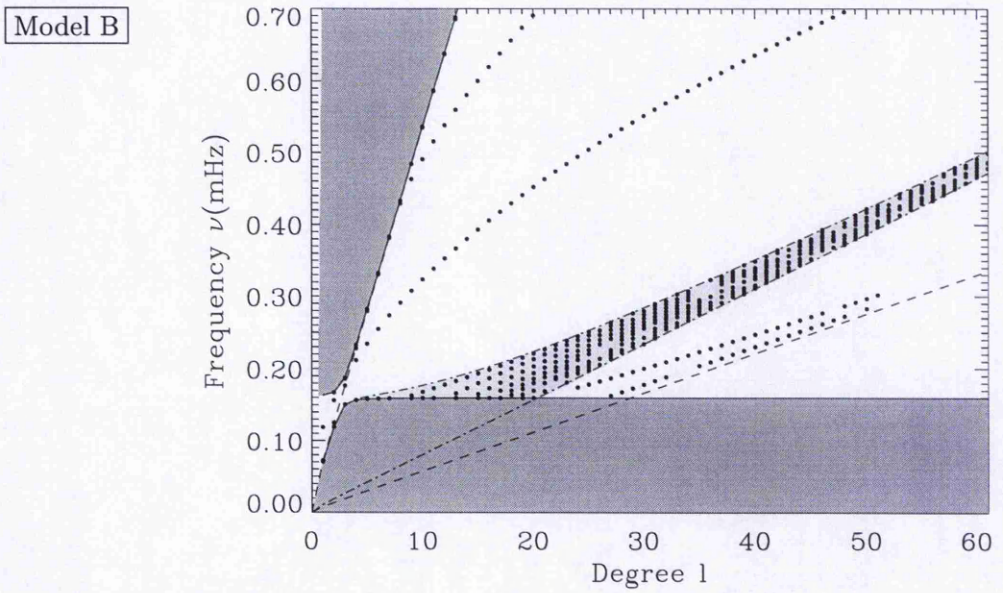

Figure 8.9: Dimensional diagnostic diagram (l, ν) showing low frequency modes (g-modes and surface waves) for model B. As in Figure 8.8 for model B, the dashed line represents the dispersion line for the kink speed (8.45) adapted to the problem of the plane-stratified layers.

model, it was not possible to find such surface waves. However, Daniell (1998), with a similar model which differs by a non-vanishing sound speed at the boundary surface, obtained surface waves but for unrealistic model parameters (taking $c_c = 191\,\mathrm{km\,s^{-1}}$ and $v_A = 306\,\mathrm{km\,s^{-1}}$ for $B_o(z_p) = 30\mathrm{MG}$).

In Figure 8.8 for model B, the dashed diagonal line represents the dispersion line for the kink speed (8.44) translated to the problem of the plane-stratified layers at the magnetic interface with the jump in density (7.6), for which

$$c_k^2 = \frac{c_c^2}{2\beta + \frac{\gamma}{2}}\,. \tag{8.45}$$

The two surface modes, propagating with horizontal phase speeds between the kink and the cusp speeds, are believed to be the sausage and kink surface waves in the plane-stratified problem; by analogy to the uniform medium, the phase speed of the sausage surface mode is lower than its kink counterpart. As $k_x \to \infty$, the phase speeds of the two modes approach the kink speed c_k ($\sim 23.646\,\mathrm{km\,s^{-1}}$).

This may be viewed also in Figure 8.9, a dimensional (l, ν) diagram, and in the upper graph of Figure 8.10, which shows the same results in a phase speed diagram. In Table 8.1, the critical value for instability was $k_c z_p \sim 8.0323$ for model B. This value

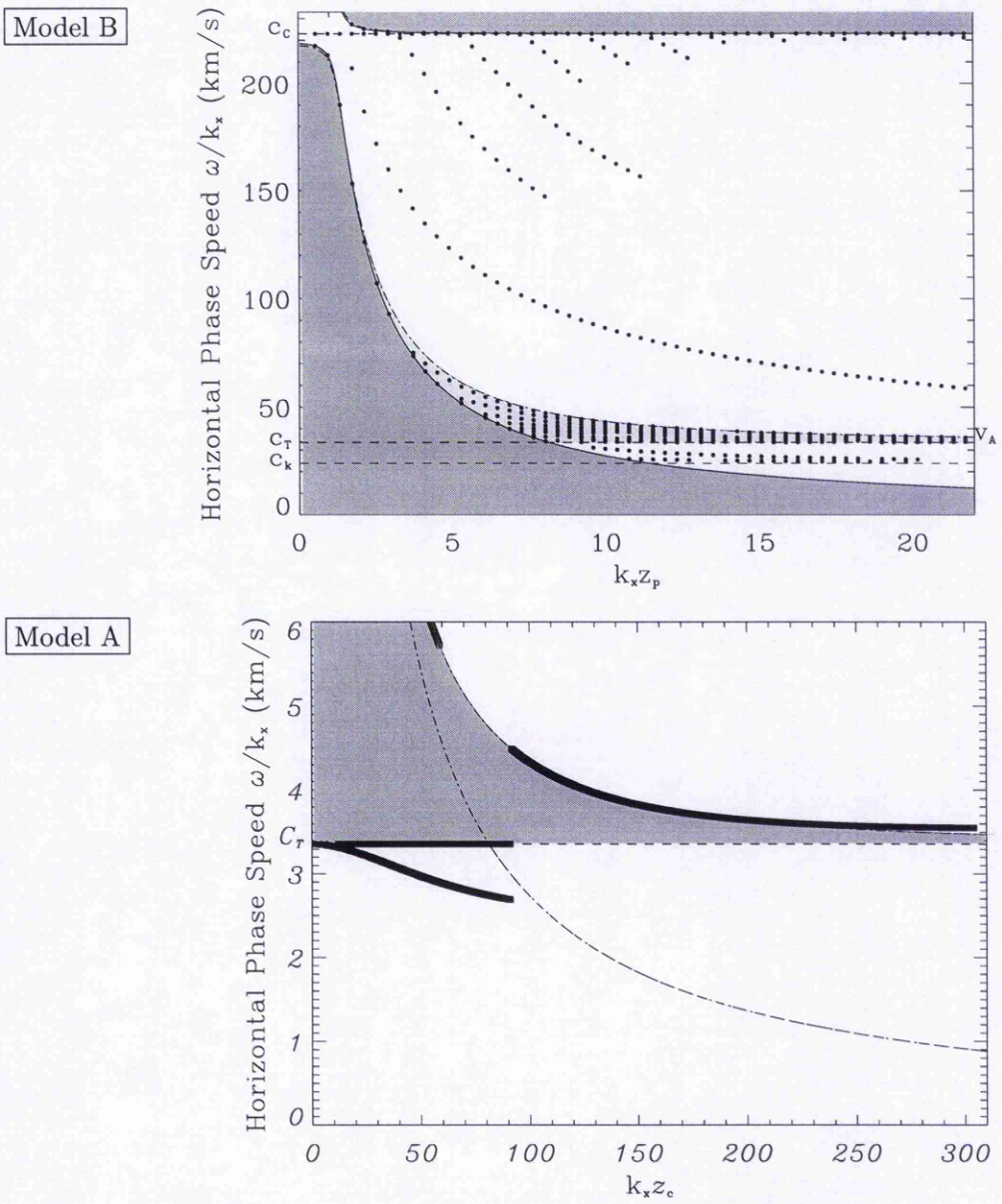

Figure 8.10: Phase speed diagrams showing surface waves for models B and A.

corresponds to the point where the evanescent window below the cusp speed opens up (see the upper graph of Figure 8.10). But the dark shaded oscillatory domain, due to the isothermal region, prevents instability setting in.

The phase speed diagram for model A is given in Figure 8.10 and shows two surface waves. One surface wave propagates at the cusp speed; the other propagates at a speed intermediate between the cusp and the kink speeds and corresponds to the surface wave found by Campbell (1987). Contrary to the treatment in Campbell, this surface

wave was computed for very high wavenumbers, beyond $k_c z_p \sim 81.2729$ for model A. As with model B, this critical value for instability corresponds to the intersection between the cusp speed and the lower cut-off for an isothermal field-free region, which here is artificial but is represented by a dotted line in the relevant diagram of Figure 8.10. Beyond this point, the surface wave does not become unstable. The phase speed $c_k \sim 2.376\,\mathrm{km\,s^{-1}}$ is also not reached at large wavenumbers. However, around $k_x z_p \sim 91 > k_c z_p$, the mode of phase speed c_T and the slow surface mode of phase speed below c_T stop propagating in that region, while a related mode of phase speed above the minus cut-off and above v_A appears (with a jump at higher phase speeds in the data). The following is an attempt to interpret this result.

For the case of an hybrid isothermal model, with a magnetic layer overlaid by a field-free region, the dispersion relation is of the form

$$\frac{\omega^2}{k_x^2} = \frac{\rho_o}{\rho_o - \rho_e \frac{m_o^2}{m_e^2}\frac{\Lambda_e^+}{\Lambda_o^-}} v_A^2 - \frac{\frac{\rho_e c_e^2}{k_x^2 c_e^2 - \omega^2} - \frac{\rho_o c_o^2}{k_x^2 c_o^2 - \omega^2}}{\rho_e \frac{\Lambda_e^+}{m_e^2} - \rho_o \frac{\Lambda_o^-}{m_o^2}} g\,, \tag{8.46}$$

where $\Lambda^{\pm}$ are the typical evanescent solutions in an isothermal region, field-free or with constant Alfvén speed. Equation (8.46) is inspired by Miles and Roberts (1992), but is slightly different here with regards to the geometry.

With a polytropic stratification in the field-free medium, in contact to an isothermal magnetic layer, with continuous sound speed c_c at the interface, as in model A, the dispersion relation (7.63) gives, in a similar form,

$$\frac{\omega^2}{k_x^2} = \frac{\rho_o}{\rho_o - \rho_e \frac{m_o^2}{m_e^2}\frac{1}{\Lambda_o^- \mathcal{D}_a}} v_A^2 - \frac{\left(\rho_e \frac{c_c^2}{g\mathcal{D}_a} - \rho_o\right)\left(\frac{c_c^2}{k_x^2 c_c^2 - \omega^2}\right)}{\frac{\rho_e}{m_e^2 \mathcal{D}_a} - \rho_o \frac{\Lambda_o^-}{m_o^2}} g\,. \tag{8.47}$$

For large k_x,

$$m_o\,,\ m_e\,,\ \Lambda_e^+ \to k_x\,, \qquad \Lambda_o^- \to -k_x\,, \qquad \mathcal{D}_a \to \frac{-c_c^2}{g}\,. \tag{8.48}$$

In this limit, Equation (8.46) for the isothermal stratification recovers the kink mode with phase speed c_k (see Equation (8.44)), while the dispersion relation (8.47), for a hybrid model with a polytropic field-free region, exhibits a mode which propagates with phase speed

$$\frac{\omega}{k_x} \sim v_A\,, \qquad k_x \to \infty\,. \tag{8.49}$$

This suggests that the unexpected mode visible in the lower diagram of Figure 8.10, for $k_x z_p \gtrsim 91$, is akin to a (fast) kink mode.

Conclusion

Diagnostic diagrams give visual evidence of variety of modes, which cohabit in a hybrid model. Each mode may be related to the proper medium or the characteristic of the model that brings it out: the f- and p-modes spring from the polytropic stratification(s); the g-modes from the isothermal layer; and the surface waves and possibly (for very large field-strength or wavenumbers) unstable modes arise from the inhomogeneity due to the presence of the isothermal magnetic layer. Yet, cohabitation of these modes implies a 'settlement' by mutual influences. Modes produced in an isolated layer are modified by any inserted or neighbouring layer when they are produced in a hybrid model. The effect on the p-modes is of particular interest, because, together with the f-mode, p-modes are the only observed modes on the Sun. They are seen to exhibit some changes over the solar cycle which may be related to changes in the solar atmosphere. But how changes in the solar interior influence the global solar oscillations is a question that can be addressed with the buried magnetic layer model and that will be explored in Chapter 10. However it is actual practice to begin with reckoning the limits of a model. This concerns in particular the problematic boundaries at the centre and the surface of a star, which are discussed for the Sun in the following chapter.

You do ill if you praise, but worse if you censure, what you do not understand.

Leonardo da Vinci (1452 - 1519)

Chapter 9

A Closer Look at Boundary Conditions

9.1 Preamble

The problem of non-radial adiabatic oscillations in hydrostatic equilibrium was first derived in spherical geometry and analytically by Pekeris (1938) who included the perturbation of the gravitational potential. After Cowling formulated in 1941 the approximation which bears his name (see Section 3.1), Robe (1968) showed by numerical calculations that the eigenfrequencies, obtained by neglecting the perturbation of the gravitational potential in the so-called Cowling approximation, differ at most by a few percent from the eigenfrequencies of the full system. For large degree l or for very large p-mode or very small g-mode frequencies (in both limits the eigenfunctions possess a large number of nodes in the radial direction), the difference is much less than 1%. In spherical geometry and keeping the perturbation in the gravitational potential, accurate frequencies of polytropic models were computed by, for instance, Christensen-Dalsgaard and Mullan (1994).

A less accurate but useful approach is to consider the mathematical modelling of a physical problem as a tool to arrive at some understanding of this problem. In this approach, keeping the model as close as possible to reality is not usually possible without making assumptions. The fundamental equation (3.67) is based on a series of

assumptions and restrictions. Some of these are well justified, such as linearisation in the case of the Sun and the use of the Cowling approximation for a field-free plasma. Other restrictions might have greater physical drawbacks. In particular the ill-defined boundaries at the surface and the centre of the Sun, which are crucial for the resonant properties of the global oscillations, offer much less certainty and must be ascertained before carrying the modelling of the solar oscillations further.

To understand the effects of boundary conditions, it is instructive to examine first an idealised one-dimensional example in some detail so as to bring out some of the concepts in their simplest form. This is achieved in considering the longitudinal wave motion on a string or in a pipe with finite length L, *i.e.* a string or a pipe with both ends terminated in some way (see, *e.g.*, Marion and Hornyak, 1982). Standing waves in gas-filled pipes are set up just as they are on terminated strings. In pipes, the pressure wave is prevented from spreading out and dissipating geometrically by being confined by the walls of the pipe.

Wave propagation on a string that is under a tension $\mathbf{T}$, or sound wave propagation excited by blowing air in a pipe, can be analysed in a simple way, assuming harmonic waves with wavenumber k in the Fourier-analysed form

$$w(z) = A\sin(kz) + B\cos(kz)\,, \tag{9.1}$$

where A and B are arbitrary constants. The $z-$axis is taken to coincide with the long axis of the pipe or with the string in its rest position. Here the wave function $w(z)$ represents either the pressure perturbation for the model of a pipe or the displacement of the string in a direction perpendicular to the z-axis for the model of a string.

A familiar example of systems with strings is the family of stringed musical instruments, while pipes belong to the family of wind instruments. The problem of adiabatic stellar oscillations is completely analogous to the vibrating string or the resonating pipe problems. The boundary conditions applied to the string or the pipe will serve as an analogy to a consideration of different boundary conditions at the centre or surface of the Sun.

The string For the model of a string, the wave function w corresponds to the displacement of the string in a direction perpendicular to the z-axis. One end of the string is fastened to a fixed support, so that at $z = 0$,

$$w(0) = 0\,. \tag{9.2}$$

Two different boundary conditions are considered at the other end of the string, at $z = L$. Either the string is fixed, or it is attached to a ring that slides without friction on a perpendicular shaft. In the first case, the boundary condition is

$$w(L) = 0\,. \tag{9.3}$$

In the second case, because the ring slides frictionlessly, the perpendicular component of the force $T_\perp = -T\frac{\partial w}{\partial z}$ is zero, and so the boundary condition is

$$\frac{\partial w}{\partial z}|_{z=L} = 0\,. \tag{9.4}$$

The fixed boundary condition (9.2) at $z = 0$ yields $B = 0$, which, together with the boundary conditions (9.3) or (9.4) at $z = L$, define the harmonic solutions, *i.e.* a sequence of wavenumbers $k = k_n$ with wavelengths $\lambda = \lambda_n = 2\pi/k_n$ with $n = 1, 2, 3 \ldots$. In the first case, with boundary condition (9.3) applied,

$$\sin(kL) = 0\,, \tag{9.5}$$

yielding

$$kL = n\pi\,, \qquad \lambda_n = \frac{2L}{n}\,. \tag{9.6}$$

In the second case, with boundary condition (9.4) applied,

$$\cos(kL) = 0\,, \tag{9.7}$$

yielding

$$kL = (2n-1)\frac{\pi}{2}\,, \qquad \lambda_n = \frac{4L}{2n-1}\,. \tag{9.8}$$

The pipe What happens when a positive pressure pulse of air gets to the end of the pipe depends on whether the pipe is open or closed. The effects of the pipe termination on the waves are identical to the effects of the two boundary conditions at one end of

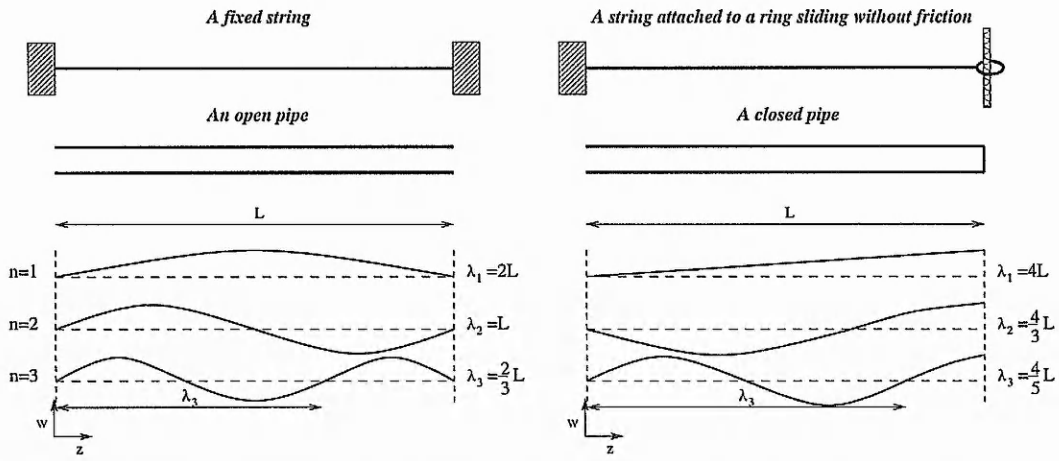

Figure 9.1: Wave propagation on strings or in pipes, with finite length L. The solid line represents the wave function w, corresponding to the string displacement or the acoustic pressure, for the fundamental ($n = 1$), the second and the third harmonics. The dashed line corresponds to the string in its rest position or the constant pressure outside the pipe; nodes (in displacement or in pressure) are the positions where the wave function intersects this line.

the string. The difference is that for a pipe, the wave function w corresponds to the pressure perturbation $\delta p = -\rho_o c_s^2 \partial\xi/\partial z$, and $\partial w/\partial z$ is akin to the displacement ξ.

At the driven opening at $z = 0$ and at the open end at $z = L$, the pressure is essentially constant and equal to the ambient pressure. When the excess pressure gets to the open end, there is still high pressure in the pulse, but average pressure outside. This large pressure difference over a small distance pushes the excess air out of the pipe, leaving a negative pressure — a *rarefaction*— of air in the pipe which then propagates back. An open end and the driven opening of a pipe (although it is not as large as a completely open end) are therefore akin to a string fixed at the end: the reflection is inverted.

At a closed pipe, the air molecules bang into the end wall and bounce off; there is still an excess of pressure there and this excess pressure propagates back. Therefore, the closed pipe requires zero displacement of gas matter and is akin to the frictionless sliding ring.

Musical instruments have many modes because the vibrating element (whether it is the body of the instrument or a column of air) is distributed over a whole area or volume. The frequency of the vibration must be integral multiples of the fundamental. The two different boundary conditions yield two different fundamentals and so two

different series of harmonics (see Figure 9.1). This comment underlines the importance of well-defined boundary conditions. As will be shown in this chapter, this applies in the modelling here for the choice of boundary conditions at the centre of the Sun and more particularly for the surface boundary condition.

Stiffness forces and friction A real musical instrument produces a much more complicated sound when it produces a 'tone'. Dispersion is introduced by stiffness forces and friction. If the system is somewhat stiff (like stiff strings of the low section of the piano), then the higher resonances will not vibrate as harmonics. Besides, slightly broadened bands of frequencies may be produced by damping a single resonance. This latter phenomenon is associated with friction. Internal friction is displayed by molecules in any solid and is the force that causes any oscillating object, such as a piano string or a tuning fork, to stop oscillating. In liquids and gases, internal friction is called viscosity. As with the viscosity of the solar plasma, the internal friction in a string will be neglected; external forces of friction are also not considered. However, one may consider stiffness forces provided by the support of the string at $z = L$.

When the stiffness of the non-rigid support is involved for sidewise motion, the perpendicular component of the tension force $T_\perp$ is non zero and is proportional to the displacement w:

$$T_\perp = -T\frac{\partial w}{\partial z} = K_s w\,, \tag{9.9}$$

where K_s is the coefficient of stiffness (see Morse and Feshbach, 1953, Part II, §11.1, p.1344). Hence, a combination of the two previous boundary conditions must be applied at $z = L$, *viz.*

$$\frac{\partial w}{\partial z}|_{z=L} + \vartheta w(L) = 0\,, \tag{9.10}$$

where $\vartheta = \frac{K_s}{T}$ is a measure of the stiffness. When $\vartheta \to 0$, the ring moves vertically along the shaft without external forces except the tension in the string. When $\vartheta \to \infty$, the termination of the string at $z = L$ is infinitely stiff and cannot move.

Applying the condition (9.10) to the wave function (9.1) (with $B = 0$) yields the dispersion relation

$$\sin(kL) + \tfrac{k}{\vartheta}\cos(kL) = 0\,, \tag{9.11}$$

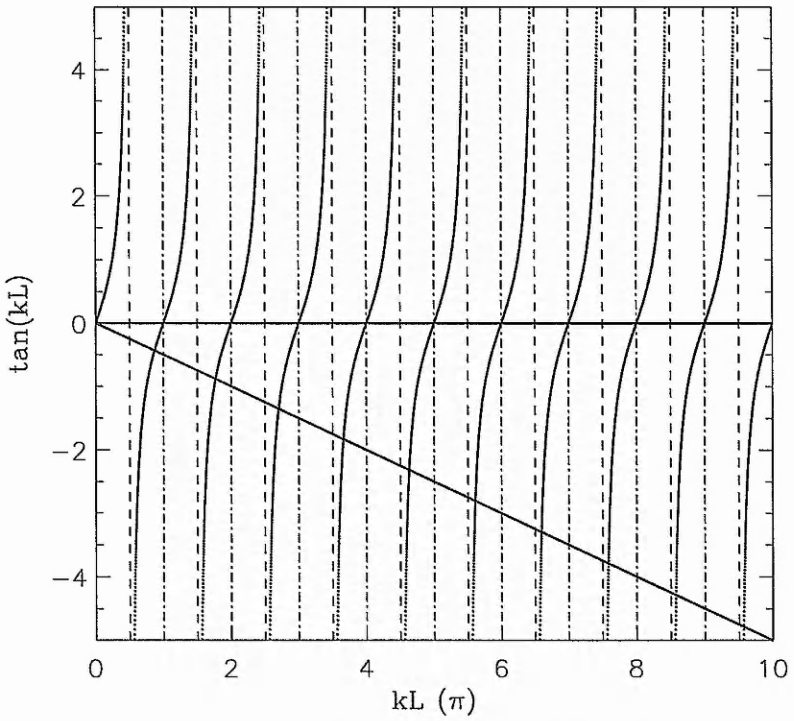

Figure 9.2: Graphical representation solving the dispersion relation (9.12) for a string attached to a ring sliding with stiffness. The roots of the dispersion relation are the abscissa positions where the tan function and the straight line of slope $-1/\vartheta L$ intersect. For this example, $\vartheta = 2\pi/L$. The asymptotes of the tan function are dashed lines; they indicate the positions of the roots for which the ring is sliding without stiffness. The dash-dotted lines indicate the positions of the roots for which the ring is infinitely stiff (*i.e.* the string is fixed).

$$i.e. \qquad \tan(kL) = -\tfrac{k}{\vartheta}\,. \tag{9.12}$$

The form of the dispersion relation (9.12) suggests the superposition of two graphs (see Figure 9.2): namely of the tan function and the straight line of slope $-1/\vartheta L$, plotted against kL. The asymptotes of the tan function indicates harmonics for which the sliding string is not stiff ($\vartheta \to 0$). The intersection points of the tan function with the line of slope $-1/\vartheta L$ approach these solutions (Equation (9.8)) for large k. For small k, this line cuts the tan function close to its roots, that is close to the harmonics (Equation (9.6)) when the string is fixed ($\vartheta \to \infty$).

Hence, by simple means, it appears that a combination of two different boundary conditions yield intermediate solutions, which converge between the two independent truncation values at large and small wavelengths. In the light of this simple approach, the boundary conditions at the centre and at the surface of a Sun-like star are examined

more carefully in the forthcoming sections of this chapter. This investigation will serve to shed some light on the formal understanding of the seismology of the Sun, which was presented in Chapter 4.

9.2 The centre of the Sun

1. Limits of planar geometry and finite depth boundary conditions

Although much literature exists for treating the problem of magnetic fields in spherical geometry (*e.g.*, Gough and Thompson, 1990; Cunha and Gough, 2000), the mathematical modelling of the solar interior with planar geometry gives the possibility to include a magnetic field with greater simplicity than in spherical geometry. Christensen-Dalsgaard (1980) worked out the adiabatic non-radial stellar oscillations in spherical geometry but also in Cartesian models, for modes trapped near the surface. Through this work, he showed the inaccuracies between the two geometries for low degree modes. Hence, in the context of the expectation that low-degree modes should be the modes most affected by the presence of magnetic fields in the solar interior (Roberts and Campbell, 1986), the planar geometry of the Sun is an approximation to bear in mind *a posteriori*. It does not indicate a complete lack of applicability but rather cautions against the deduced consequences for low-degree modes.

To substantiate this discussion, one may consider the modes of oscillation of a field-free truncated polytrope for which the sound speed vanishes at the surface, hence ignoring the surface effects. Then the solution to Lamb's equation for such a polytrope is expressed in terms of the Kummer M function (see Section 4.2). This model is recalled on the left graph of Figure 9.3.

The dispersion relation for a polytrope with a rigid wall boundary condition, such that $V_z = 0$ at a depth $z = z_p$ (see Equation (8.29)), is

$$\left[1 - 2\frac{(m+1)}{Z_p}\Omega^2 + \Omega^2\right] M(-\Upsilon, m+2, Z_p) - 2\Omega^2 M'(-\Upsilon, m+2, Z_p) = 0\,, \qquad (9.13)$$

where $Z_p = 2k_h z_p$, and where the prime denotes the derivative with respect to $Z = 2k_h z$. Another possibility to truncate the medium is to allow a freely moving surface at depth $z = z_p$, requiring that the rate of change in Lagrangian pressure perturbation is zero there. This condition leads to the dispersion relation

$$M(-\Upsilon, m+2, Z_p) = 0\,. \qquad (9.14)$$

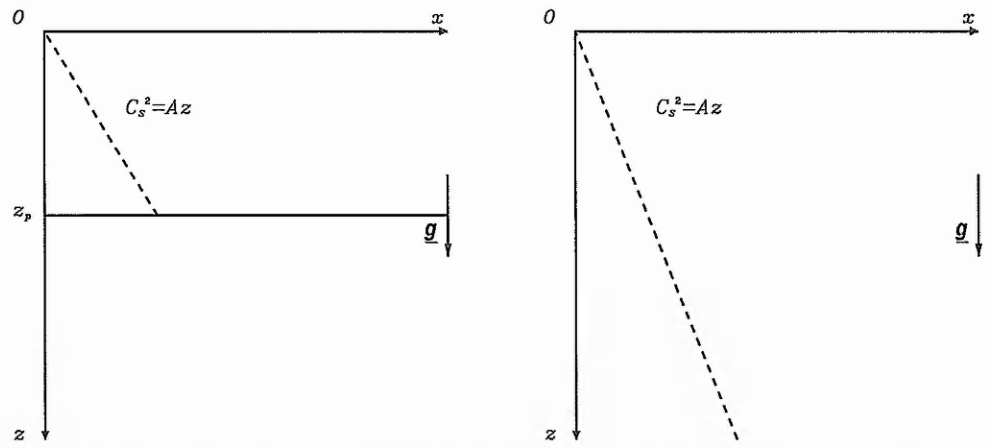

Figure 9.3: (*left*) A truncated polytrope $0 \leq z \leq z_p$ and (*right*) a simple polytropic medium. In both field-free models, the sound speed vanishes at the surface.

Both truncated media are like waveguides and can be compared to resonant cavities, such as the closed and open pipes. A rigid wall boundary condition with $V_z = 0$ at $z = z_p$ corresponds to the boundary condition of a closed pipe, while the condition of free-moving surface at $z = z_p$ corresponds to the boundary condition of an open pipe (the wave sees a pressure discontinuity that reflects it and produces an antinode).

The depth $z = z_p$ at which the boundary condition is applied may be arbitrary deep ($z_p \to \infty$). In that limit, the wall boundary condition ($V_z = 0$) is akin to the requirement of vanishing kinetic energy density ($\rho V_z^2 \to 0$), while the free-moving surface ($\mathcal{P} = 0$) is akin to a vanishing (or at least finite) Lagrangian pressure perturbation at the centre of the star, as assumed by Schmitz and Steffens (1999). In the simple polytrope, sketched in the right graph of Figure 9.3, both boundary conditions are expected to yield the same results as $z_p \to \infty$, giving p-modes of radial order n with frequencies given by

$$m\Omega_n^2 = m + 2n\,. \tag{9.15}$$

For a polytropic medium truncated at a finite depth z_p, a wave of given wavenumber k_h is refracted at the so-called cavity depth (see Equation (4.56)). The depth $z = z_p$ of this cavity, or the 'turning point' where wave-like solutions become evanescent, is approximately given by

$$m\Omega^2 \sim k_h z_p + \frac{m(m+2)}{4k_h z_p}\,. \tag{9.16}$$

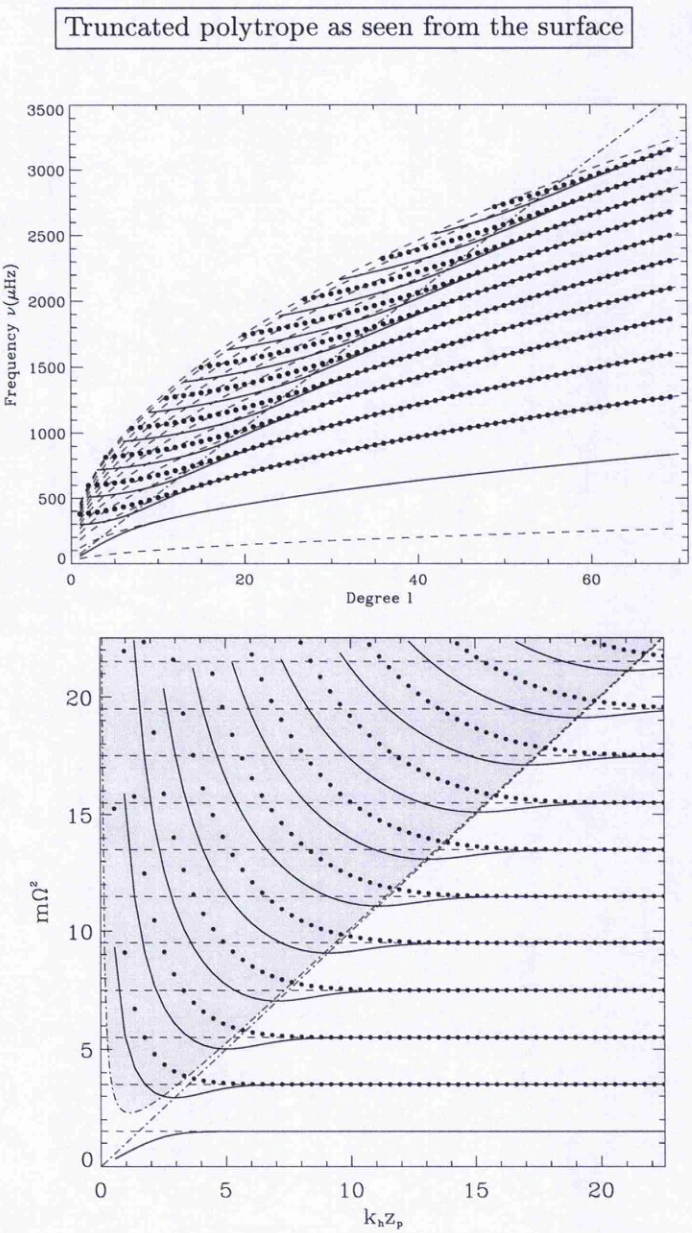

Figure 9.4: Diagnostic diagrams (l,ν) and $(k_h z_p, m\Omega^2)$ for the truncated model. p-modes in a simple polytrope, in a polytrope truncated by a rigid wall (with $V_z = 0$ at $z = z_p$), or by a free-moving surface (with $\Delta = 0$ at $z = z_p$) are represented respectively in dashed lines, plain lines and full circles. The oscillatory domain at $z = z_p$ is shaded in the normalised diagram; the dispersion line for the Lamb frequency is dash-dotted. The upper diagram is for $z = z_p$ corresponding to the base of the convection zone (*i.e.* $z_p \approx 0.391\,\mathrm{R}_\odot$); each full circle represents a multiplet frequency ν_{nl}.

When $k_h z_p \to \infty$, the cavity depth would indicate the theoretical behaviour of waves satisfying the vanishing kinetic energy density at ∞. Therefore, from Equations

(9.15) and (9.16),

$$m\Omega^2 \sim m\Omega_n^2 \sim k_h z_p + O\left(\frac{1}{k_h z_p}\right), \qquad k_h z_p \to \infty. \tag{9.17}$$

Thus this demonstrates the behaviour:

$$\Omega^2 = \Omega_n^2 + O\left(\frac{1}{k_h z_p}\right), \qquad k_h z_p \to \infty. \tag{9.18}$$

One may consider the depth z_p to be at the base of the convection zone or at the centre of the Sun (note that, for a spherically symmetric star in thermal and hydrostatic balance, Balmforth et al. (1996) have formulated their boundary condition to be a rigid wall at radius $0.17\,\mathrm{R}_\odot$). The normalised diagram in Figure 9.4 illustrates the behaviour (9.18) for these finite depths. The eigenfrequencies are deflected from the discrete levels (9.15) by a frequency shift which is positive when $m\Omega^2$ is much larger than $k_h z_p$, *i.e.* in the oscillatory domain. The dash-dotted curve, which delimits the shaded oscillatory domain, takes the acoustic cut-off (4.10) into account, *viz.*

$$m\Omega^2 = k_h z_p + \frac{m(m+2)}{4k_x z_p}. \tag{9.19}$$

Only in the case of a rigid wall truncation, these shifts are negative near the Lamb separatrix $m\Omega^2 = k_h z_p$, drawn as a dash-dotted line on the diagnostic diagram and which approximately separates (for high Ω^2) the oscillatory domain from the exponential domain. The f-mode does not appear for a truncated polytrope with free-moving surface boundary conditions both at $z = 0$ and at $z = z_p$. Because for the f-mode $\Delta = 0$ for all z (see Section 6.2, p.121), the boundary with $\Delta = 0$ at $z = z_p$ is trivially satisfied. However, the f-mode is present for a polytrope with a rigid wall truncation at $z = z_p$. In this case, the standard f-mode frequency (given by $\omega^2 = gk_h$) is reduced at low degree l and approaches the Lamb dispersion line with decreasing k_h and Ω. For this same truncated polytrope, the evanescent modes of higher radial orders resemble the f-mode decaying behaviour, but unlike the f-mode, the oscillatory criterion is met and the p-modes respond as body modes. The lower and the closer to the Lamb frequency a p-mode frequency gets, the more the p-mode behave like the fundamental mode. Close to the Lamb separatrix, the higher the radial node, the less the frequency

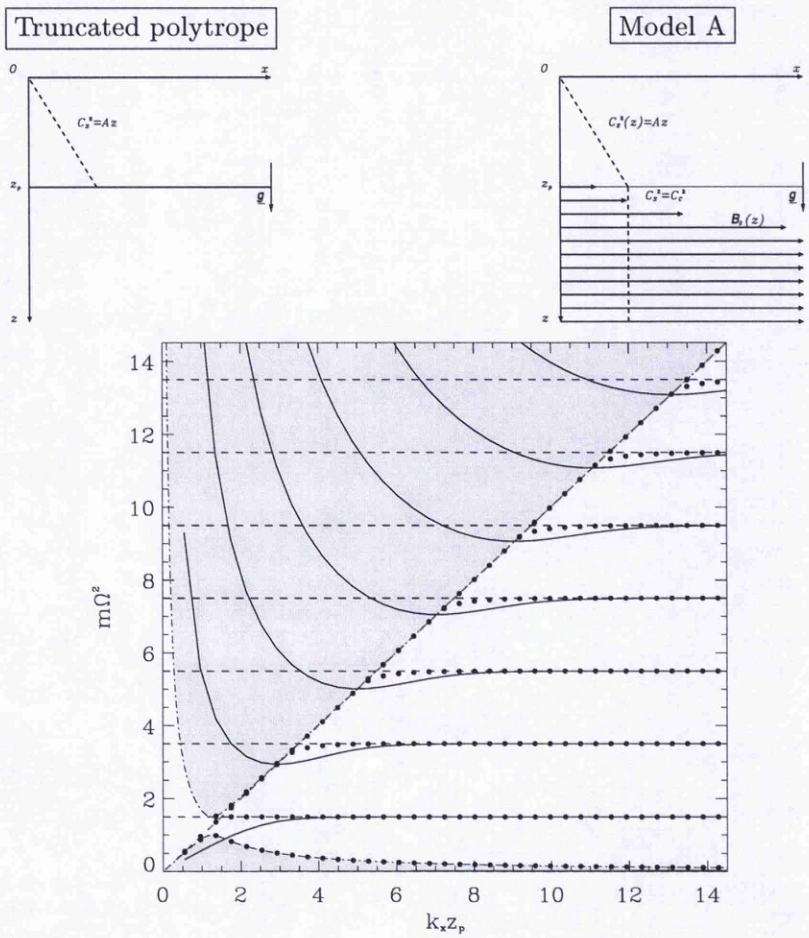

Figure 9.5: Normalised diagnostic diagrams ($m\Omega^2$ against $k_x z_p$) for a truncated polytrope and a polytrope overlaid by the isothermal region (model A). p-modes in a simple polytrope, in a polytrope truncated by a rigid wall (with $V_z = 0$ at $z = z_p$) and a polytrope overlaid by an isothermal region are represented respectively in dashed lines, plain lines and full circles. Each full circle represents a multiplet frequency ν_{nl} for z_p at the base of the convection zone ($z_p \approx 0.391\,\mathrm{R}_\odot$). The oscillatory domain of the isothermal region at $z = z_p$ is shaded; the dispersion line for the Lamb frequency is dash-dotted.

of a p-mode is modified. This is hinted at in the upper dimensional diagram of Figure 9.4, for which z_p is taken to be at the base of the convection zone.

For a truncated polytrope with a free-moving surface boundary condition at $z = z_p$, the shifts are always positive. The two different ridges for p-modes, which result from the two types of lower boundary conditions, turn apart below the Lamb separatrix in the evanescent domain and arrange themselves in two sets of alternate lines, with a separation between them which becomes more and more equidistant as the modes enter the shaded oscillatory domain at $z = z_p$. This divergence between the two

types of ridges illustrates the importance for low-degree modes of well-defined boundary conditions deep in the star.

Finally, Figure 9.5 shows modes in the polytrope with a rigid wall at $z = z_p$, together with the modes of a polytrope overlying an isothermal region (model A). For the parameters of model A, whether the isothermal region is magnetised (with high plasma β) or not, the diagnostic diagrams for such two-layer models are indistinguishable to the eye. Figure 9.5 is therefore concerned not with the effect of magnetic field, but rather the effect of an isothermal region below the polytropic layer. It appears that close to the Lamb separatrix, the ridges are deflected negatively from the discrete levels Ω_n^2 in a way similar to the modes for a polytrope with a rigid wall boundary condition, rather than with a free-moving surface at $z = z_p$.

2. A second series of discrete solutions

The boundary condition at the centre of a star may be understood from a different approach than the one that is usually taken and which was described in Section 4.2. This alternative approach follows from exploring the original solutions to the confluent hypergeometric equation.

The confluent hypergeometric functions The general solution to the confluent hypergeometric equation

$$Z\frac{d^2\psi}{dZ^2} + (b - Z)\frac{d\psi}{dZ} - a\psi = 0 \tag{9.20}$$

can be given under different forms (Slater, 1960; 1965). If ψ_α and ψ_β are two independent solutions, the complete solution of Kummer's equation (9.20) is of the form $\psi = \alpha\psi_\alpha + \beta\psi_\beta$, where α and β are arbitrary constants, which may depend on a and b but not on Z.

The general solution is obtained on substituting into Equation (9.20) the series

$$\psi(Z) = \Sigma_{j=0}^{\infty} a_j Z^{j+s}\,, \tag{9.21}$$

and requiring that the resulting equation hold for arbitrary Z (see Seaborn, 1991, p.42-43). This gives

$$s(s - 1 + b)a_o = 0\,, \tag{9.22}$$

and

$$a_{j+1} = \frac{j+s+a}{(j+s+1)(j+s+b)} a_j \,. \tag{9.23}$$

For a non-trivial solution, $a_o \neq 0$. Thus, either $s = 0$ or $s = 1 - b$, leading to

$$\psi_\alpha(Z) = a_o M(a, b, Z) \,, \quad s = 0 \,, \quad b \neq 0, -1, -2, \ldots \tag{9.24}$$

and

$$\psi_\beta(Z) = a_o Z^{1-b} M(1 + a - b, 2 - b, Z) \,, \quad s = 1 - b \,, \quad b \neq 0, +1, +2, \ldots \,. \tag{9.25}$$

If b is not an integer, then the general solution of Equation (9.20) is

$$\psi(Z) = \alpha_2 M(a, b, Z) + \beta_2 Z^{1-b} M(1 + a - b, 2 - b, Z) \,. \tag{9.26}$$

This general solution is valid for $b \neq 0, \pm 1, \pm 2, \ldots$.

The Tricomi U function is calculated from the two Kummer M functions to improve the domain of validity of b. In fact, U is valid for $b \to 0, \pm 1, \pm 2, \ldots$ (see Slater, 1965, §13.1.3).

Solutions It should be pointed out that in application to the plane-parallel polytrope of index $m = 3/2$, confluent hypergeometric functions are encountered with an argument $b = m + 2$ or $b = m + 3$, *etc.* and so b is not an integer. Thus the general solution of Equation (9.20), with $a = -\Upsilon$ and $b = m + 2$ for the polytropic stratified model, is

$$\psi = \alpha_2 M_\alpha + \beta_2 \frac{M_\beta}{Z^{m+1}} \,, \qquad Z \geq 0, \tag{9.27}$$

where $M_\alpha = M(-\Upsilon, m + 2, Z)$ and $M_\beta = M(-\Upsilon - m - 1, -m, Z)$; for $-\Upsilon$, $m + 2 \neq 0, -1, -2, \ldots$, the arbitrary constants α_2 and β_2 are related to the arbitrary constants α_1 and β_1 for the formal solution ψ (see Equation (4.29)) by the relationship (A.3) (see Appendix A.1) with

$$\begin{aligned} \alpha_2 &= \alpha_1 + \frac{\Gamma(-m-1)}{\Gamma(-\Upsilon - m - 1)} \beta_1 \\ \beta_2 &= \frac{\Gamma(m+1)}{\Gamma(-\Upsilon)} \beta_1 \,. \end{aligned} \tag{9.28}$$

The compressibility is then

$$\triangle = e^{-Z/2}\left[\alpha_2 M_\alpha + \beta_2 \frac{M_\beta}{Z^{m+1}}\right], \; Z \geq 0, \tag{9.29}$$

and the vertical velocity amplitude V_z is determined by (substituting the solution (9.27) for ψ into Equation (4.38))

$$V_z = \frac{e^{-Z/2}}{(1-\Omega^4)}\frac{\gamma}{k_h}\left[\alpha_2 F(M_\alpha) + \beta_2 F\left(\frac{M_\beta}{Z^{m+1}}\right)\right], \qquad Z > 0, \tag{9.30}$$

where one needs the derivative of the second function in M, *viz.*

$$\left(\frac{M_\beta}{Z^{m+1}}\right)' = \frac{M'_\beta}{Z^{m+1}} - (m+1)\frac{M_\beta}{Z^{m+2}}. \tag{9.31}$$

Boundary condition as $z \to \infty$ The solution (9.27) is useful to look at the boundary condition in the centre of the Sun, which in the case of planar geometry, is taken to be the limit $z \to \infty$. The asymptotic expansions of a function M and its derivative have the same leading term (see Equation (A.16) in Appendix A.1), *viz.*

$$M'_\alpha \sim M_\alpha \sim \frac{\Gamma(m+2)}{\Gamma(-\Upsilon)} Z^{-\Upsilon-m-2} e^Z, \qquad Z \to \infty, \tag{9.32}$$

and

$$M'_\beta \sim M_\beta \sim \frac{\Gamma(-m)}{\Gamma(-\Upsilon-m-1)} Z^{-\Upsilon-1} e^Z, \qquad Z \to \infty, \tag{9.33}$$

and one gets $F(M_\alpha) \sim \zeta Z M_\alpha$ and $F\left(\frac{M_\beta}{Z^{m+1}}\right) \sim \zeta Z \frac{M_\beta}{Z^{m+1}}$.

Using both expressions (4.23) of $\rho_o(z)$ and (9.30) of $V_z(z)$, the linearised kinetic energy density E_o for large z (see Equation (4.36)) verifies

$$\begin{aligned} E_o^{1/2} &\sim C^{st} Z^{1+m/2} e^{-Z/2}\left[\alpha_2 M_\alpha + \beta_2 \frac{M_\beta}{Z^{m+1}}\right], \qquad Z \to \infty \\ &\sim C^{st} Z^{-\Upsilon-m/2-1} e^{Z/2}\left[\alpha_2 \frac{\Gamma(m+2)}{\Gamma(-\Upsilon)} + \beta_2 \frac{\Gamma(-m)}{\Gamma(-\Upsilon-m-1)}\right], \qquad Z \to \infty. \end{aligned} \tag{9.34}$$

If the asymptotic expansion $M_\alpha \sim M_\beta \sim e^Z$ is applied to Equation (9.34), then the resulting divergence is incompatible with the proper behaviour of $E_o^{1/2}$ at infinity. To avoid this divergence for large Z, one has to satisfy the relation

$$\alpha_2 \frac{\Gamma(m+2)}{\Gamma(-\Upsilon)} + \beta_2 \frac{\Gamma(-m)}{\Gamma(-\Upsilon-m-1)} = 0. \tag{9.35}$$

In the general case, the constants α_2 and β_2 may be related by an additional boundary condition, applied for instance at the surface of the Sun. In specific cases, the series M_α and M_β may be required to terminate, *i.e.* the M functions must be generalised Laguerre polynomials (see Equation A.18, Appendix A.1). This yields two other possibilities, which are only special cases to Equation (9.35) and which correspond to the truncation values of the respective M functions: either

- Υ is a nonnegative integer and $\beta_2 = 0$,

  or

- $\Upsilon + m + 1$ is a nonnegative integer and $\alpha_2 = 0$.

Upon replacing Υ by its definition (see Equation (4.52)), one obtains two types of series: for nonnegative integer $n_1 = \Upsilon$,

$$(\Omega^2_{n_1})_\alpha = 2\frac{n_1+1}{m} + 1\,, \qquad n_1 = 0, 1, 2, 3\ldots\,; \tag{9.36}$$

for positive integer $n_2 = \Upsilon + m + 1 > m/2 (= 3/4)$,

$$(\Omega^2_{n_2})_\beta = 2\frac{n_2}{m} - 1\,, \qquad n_2 = 1, 2, 3\ldots\,. \tag{9.37}$$

Setting $n_1 + 1 = n_2 = n$, where $n = 1, 2, 3\ldots$ is a positive integer, one gets respectively

$$(\Omega^2_n)_\alpha = \frac{2n}{m} + 1\,; \tag{9.38}$$

$$(\Omega^2_n)_\beta = \frac{2n}{m} - 1\,. \tag{9.39}$$

Hence, looking at the asymptotic expansion of the kinetic energy density at $z \to \infty$ and applying two different types of general solution, it appears that, with the formal solution involving the Tricomi U function, one type of truncation series is missing. This series, $(\Omega^2_n)_\beta$, alternates with the standard series $(\Omega^2_n)_\alpha$.

In the treatment of plane-stratified polytropic models, the original solution ψ (Equation (9.27)) only appears to be given in models of the Earth's atmosphere by Pekeris (1948) or the solar atmosphere by Edwin (1984), yet without noting the truncation values it implies. The original solution ψ involving the two Kummer M functions has been much less adopted than the formal solution ψ involving one M function and the

U function. However, the confluent hypergeometric equation finds also an application in the problem of central force fields in quantum mechanics where the original solution (9.26) applies. In this context, the existence of a second truncation value can become essential.

Solution of Schrœdinger's equation When a particle of mass m_q is in a potential field $V(r)$ which is centrally symmetric about some point (which may be taken to be the origin), the resulting Schrœdinger's equation for eigenvalue E is

$$\nabla^2\psi + \frac{2m_q}{\hbar^2}\left[E - V(r)\right]\psi = 0\,; \tag{9.40}$$

$\hbar$ is the Planck constant.

Expanding ψ in spherical harmonics, the equation for the radial factor, $R(r)$, is (see Morse and Feshbach, 1953, Part II, §12.3, p.1661)

$$\frac{d^2R}{dr^2} + \left[\frac{2m_q}{\hbar^2}\left(E - V(r)\right) - \frac{l(l+1)}{r^2}\right]R = 0\,, \tag{9.41}$$

where, for ψ to be finite everywhere, R must stay finite as $r \to 0$, and must vanish as $r \to \infty$. Eventually this means that the eigen-wave functions of discrete energy levels have a finite number of oscillations, and have an evanescent behaviour at infinity (Merzbacher, 1961; Seaborn, 1991). This is illustrated in Figure 9.6 for a harmonic oscillator potential.

Given the similarity between the wave equation for a polytrope and Schrœdinger's equation in quantum mechanics, which are both amenable to the confluent hypergeometric equation, it is useful to compare some of the cases for which an exact solution is obtained. In particular, it should be noted that the requirement of square integrability in quantum problems, namely that

$$\lim_{A\to\infty}\int_0^A R^2 r\,dr \tag{9.42}$$

must stay finite, is equivalent in the model of the plane-stratified polytrope to the requirement of vanishing kinetic energy density as $z \to \infty$. In fact, the association between the equation for the non-radial stellar oscillations and the Schrœdinger's equation has been investigated by Adam (1994) for square-well potentials though this does not involve the confluent hypergeometric equation.

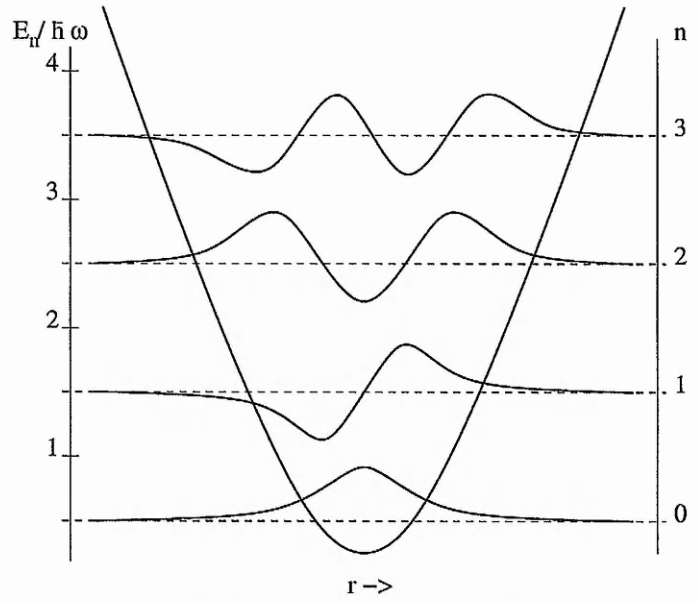

Figure 9.6: Bound states in a harmonic oscillator potential.

The familiar problem of a quantum harmonic oscillator in one dimension with potential energy

$$V(r) = \frac{1}{2} m_q \omega^2 r^2 \,, \tag{9.43}$$

is solved through the two M functions, M_α and M_β; see Seaborn, 1991, p.46-47. The physical constraint that, when the particle is far from the centre of force, the solution must not diverge, requires that the confluent hypergeometric series for M terminates. The energy levels of a particle are obtained (see Figure 9.6), from $E = E_n$ with

$$E_n = (n + \frac{1}{2})\hbar\omega \,, \tag{9.44}$$

where the even and odd levels correspond to the truncation values for the first argument of the respective M functions. By comparison, these eigenvalues correspond to the ones for an infinite polytropic medium, where $z \in [-\infty, +\infty]$, *i.e.* which would not be bounded at the surface.

For the Coulomb potential

$$V(r) = -\frac{\eta^2}{r} \,, \tag{9.45}$$

the equation for the radial factor R is

$$R'' + \left[-\kappa^2 + \frac{2 m_q \eta^2}{\hbar^2 r} - \frac{l(l+1)}{r^2} \right] R = 0 \,. \tag{9.46}$$

The solution in M_β is discarded, so that the general solution is regular at the origin. Only the truncation values given by the M_α function are solutions. The energy levels are of the form (Morse and Feshbach, 1953, Part II, §12.3, p.1664)

$$E_n = -\frac{\hbar^2\kappa^2}{2m_q} = -\frac{m_q\eta^4}{2(n+l)^2\hbar^2}, \qquad n = 1, 2, 3, \ldots . \tag{9.47}$$

For a plane-stratified polytrope with non-vanishing sound speed at the surface, the vertical wavenumber K is given by (see Equation (4.7))

$$K^2(z) = \frac{k_h}{z+z_o}\left[m\Omega^2 - k_h(z+z_o) - \frac{m(m+2)}{4k_h(z+z_o)}\right] \tag{9.48}$$

$$= -k_h^2 + \frac{mk_h\Omega^2}{z+z_o} - \frac{m(m+2)}{4(z+z_o)^2}. \tag{9.49}$$

This form is similar to the coefficient of the radial factor R in Equation (9.46) for a Coulomb potential. If $z_o = 0$, $K^2(z) \to -\infty$ as $z \to 0$. The solutions are obtained in the same way as for the Coulomb potential (note that $\kappa = k_h$, $l \equiv \frac{m}{2}$, $\frac{2m_q\eta^2}{\hbar^2} \equiv \frac{m\omega^2}{g}$), which corresponds to the case of vanishing sound speed at the surface of the Sun.

But if $z_o \neq 0$, then $K^2(0)$ is finite; in such a case, the choice of outer boundary conditions is crucial. Further comparison with problems in quantum mechanics is beyond the scope of this work. But the main fact to remember is that of the existence of a second series of discrete solutions, which in certain applications, become essential. As will be discussed later, they provide a complete theoretical background in order to fully interpret observations of the p-modes.

9.3 Outer boundaries and connected aspects

1. Surface boundary condition

Requiring finite densities, the vanishing property of the Lagrangian pressure perturbation (4.34) is fulfilled in two ways: either the sound speed vanishes at the surface ($z_o = 0$), *viz.*

$$c_s^2|_{z=0} = c_o^2 = 0\,, \tag{9.50}$$

or the compressibility is there zero,

$$\Delta|_{z=0} = 0\,. \tag{9.51}$$

By assuming that the sound speed at the surface of the Sun is zero (*i.e.* $z_o = 0$), one fulfills the boundary condition at the surface through Equation (9.50). Thus, before assuming such sufficient but not necessary condition, it is important to know what the general case where $z_o \neq 0$ implies, and what is neglected when $z_o = 0$.

The general case where $z_o \neq 0$ requires the cancellation of the compressibility at the surface, given by Equation (9.51). The ratios between the constants can then be deduced for the alternative original solution (9.27), *viz.*

$$\frac{\beta_2}{\alpha_2} = -(Z_o)^{m+1} \frac{M(-\Upsilon, m+2, Z_o)}{M(-\Upsilon - m - 1, -m, Z_o)}\,. \tag{9.52}$$

The dispersion relation (9.35) is now

$$\frac{\Gamma(m+2)}{\Gamma(-\Upsilon)} - (Z_o)^{m+1} \frac{M(-\Upsilon, m+2, Z_o)}{M(-\Upsilon - m - 1, -m, Z_o)} \frac{\Gamma(-m)}{\Gamma(-\Upsilon - m - 1)} = 0\,. \tag{9.53}$$

By the use of the relation (A.3) (in Appendix A.1), it can be shown that the dispersion relation (9.53) is also equivalent to solving

$$U(-\Upsilon, m+2, Z_o) = 0\,. \tag{9.54}$$

This dispersion relation arises also from the boundary condition at the centre of the star applied to the formal general solution, in requiring α_1 to be taken zero. This was in fact done by Campbell (1987, p.48) who, from developing Equation (9.54) in the long wavelength limit, derived analytically an approximation to the correction to the value

of Υ from the integral values obtained when the sound speed vanishes at the surface. This underlies that the U function, given in Equation (9.54) and representative of the compressibility Δ at $z = 0$ (see Equation (4.37)), vanishes at the surface when $z_o \to 0$. This is not rigorously true since the U function becomes singular in that limit, and since the condition of the vanishing Lagrangian pressure perturbation at the surface (4.34) is fulfilled because of the special case (9.50) of vanishing sound speed.

On the contrary, the dispersion relation (9.53) is consistent with the two outer limits, $Z_o \to 0$ and $Z_o \to \infty$. First of all, in the limit $Z_o \to 0$ (*i.e.* the limits of vanishing sound speed ($z_o \to 0$) or small wavenumber ($k_h \to 0$)), the M functions are finite and equal one (see Equation (A.12) in Appendix A.1), so the dispersion relation (9.53) reduces to

$$\frac{\Gamma(m+2)}{\Gamma(-\Upsilon)} \to 0\,, \qquad Z_o \to 0\,, \tag{9.55}$$

implying the standard solutions $(\Omega_n^2)_\alpha = \Omega_n^2$.

Secondly, in the limit $Z_o \to \infty$ (*i.e.* the limits of large surface sound speed ($z_o \to \infty$) or large wavenumber ($k_h \to \infty$)), the ratio $\frac{M_\alpha}{M_\beta}$ between the two types of M functions may be obtained from Equations (9.32) and (9.33), *viz.*

$$\frac{M(-\Upsilon, m+2, Z_o)}{M(-\Upsilon-m-1, -m, Z_o)} \sim \frac{\Gamma(m+2)}{\Gamma(-\Upsilon)} \frac{\Gamma(-\Upsilon-m-1)}{\Gamma(-m)} \frac{1}{Z_o^{m+1}}\,, \qquad Z_o \to +\infty\,, \tag{9.56}$$

so that the dispersion relation (9.53) is trivial, which means that no roots are solutions; equivalently this can be seen with the dispersion relation (9.54) since $U \sim Z_o^\Upsilon$ as $Z_o \to \infty$ (see Equation (A.17) in Appendix A.1).

Moreover, in complement to the boundary condition of free-moving surface, one may consider the general polytrope (with non-vanishing sound speed at $z = 0$) to be bounded by a rigid wall, namely that $V_z = 0$ at $z = 0$. The dispersion relation for such medium is similar to Equation (9.13), where M is replaced by U, and Z_p by Z_o, *viz.*

$$\left[1 - 2\frac{(m+1)}{Z_o}\Omega^2 + \Omega^2\right] U(-\Upsilon, m+2, Z_o) - 2\Omega^2 U'(-\Upsilon, m+2, Z_o) = 0\,, \tag{9.57}$$

where the prime denotes the derivative with respect to $Z = 2k_h z$. This dispersion relation may be noted in short $V_z(U) = 0$, in contrast to the dispersion relation (9.13), which may be referred as $V_z(M) = 0$.

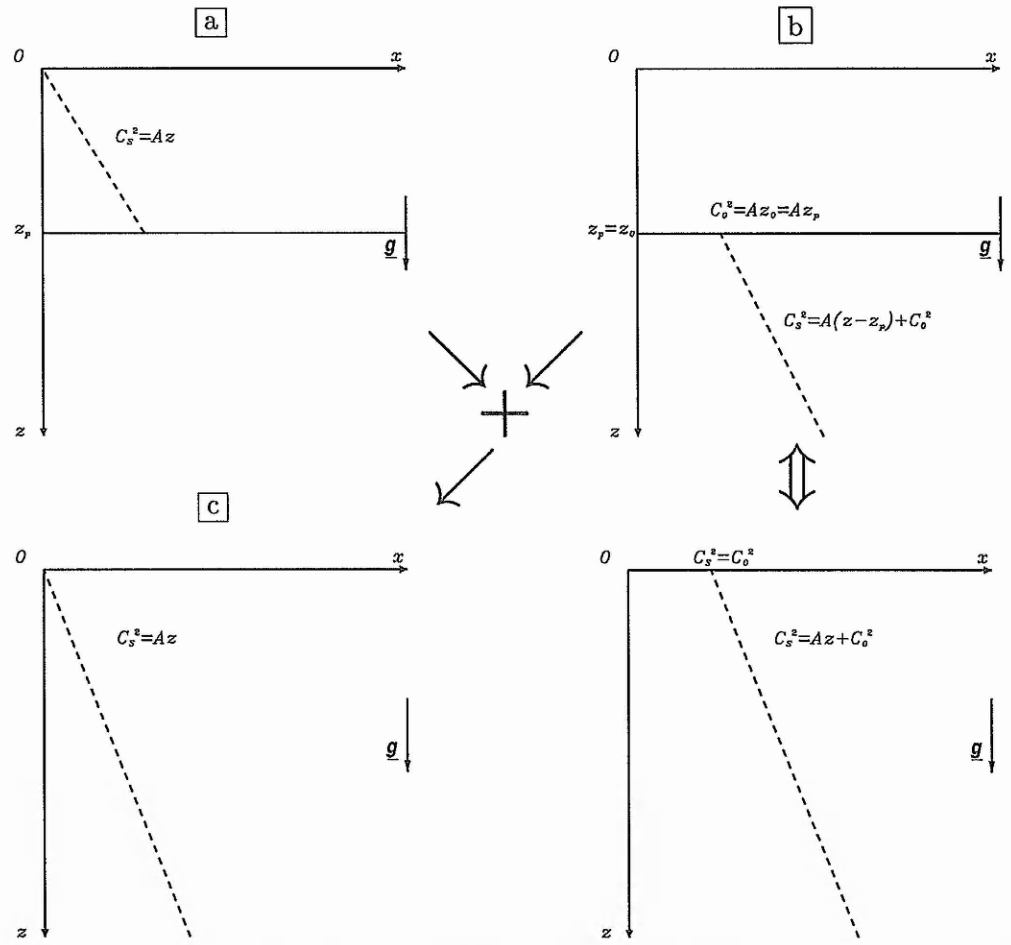

Figure 9.7: Sketch of truncated polytropes, (a) as seen from the surface or (b) from the interior, and forming (c) a simple polytrope. The models (b) sketched on the right represent the same general model for a polytrope terminated at a non-zero temperature level.

The models (b) sketched on the right of Figure 9.7 are representations of the same general model — for a polytrope with non-zero sound speed at its upper boundary — and therefore are solved with the same dispersion relation. Specifically, they yield equivalent results if z_o, the temperature scale-height at the surface of a polytrope terminated at $z = 0$, is chosen to match the temperature scale-height z_p at the upper boundary of a polytrope terminated below the surface level (here at depth $z = z_p$). For a free-moving truncation at depth $z = z_p = z_o$, the roots of the dispersion relation (9.52) or equivalently (9.54) are plotted in full circles in Figure 9.8. This normalised diagram shows consistency with the asymptotic results obtained earlier: namely the standard solutions $(\Omega_n^2)_\alpha$ in the limit (Z_p or) $Z_o \to 0$ (at large wavelength) and no

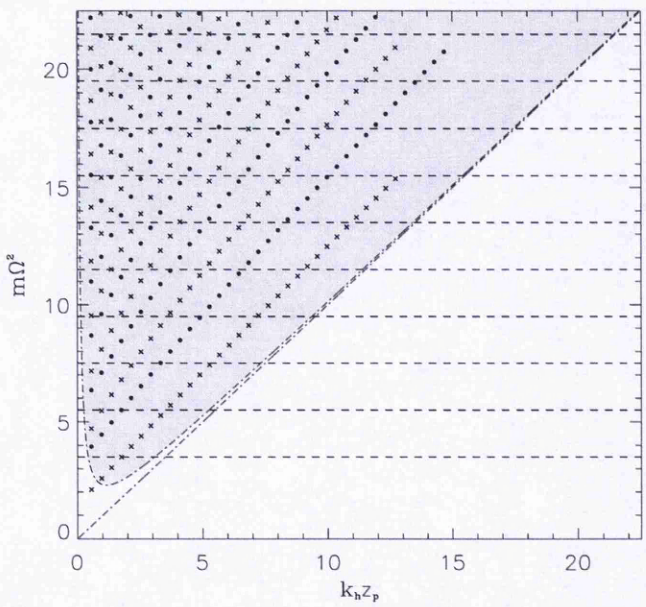

Figure 9.8: Normalised diagnostic diagrams ($k_h z_p$,$m\Omega^2$) for the truncated polytropes with free-moving and rigid wall boundary conditions at the surface of the Sun, represented respectively by full circles and by crosses. The p-mode ridges for a simple polytrope are represented by dashed lines. The oscillatory domain at $z = z_p$ is shaded; the dispersion line for the Lamb frequency is dash-dotted.

solution in the limit (Z_p or) $Z_o \to \infty$ (at small wavelength). Note that these limits are the reverse of those for the p-modes of model (a), discussed in Section 9.2, and which were shown in Figure 9.4.

In addition to the solutions for a polytrope with a free-moving surface boundary condition at $z = 0$, Figure 9.8 shows roots, represented by crosses, for a polytrope with a rigid wall boundary condition ($V_z = 0$ at $z = 0$, given by the dispersion relation (9.57)). The first ridge of this series is the f-mode, which does not exist for a polytrope with a free-moving surface boundary condition at $z = 0$.

The two types of ridges (aligned full circles and crosses) are well separated and alternate mainly in the oscillatory domain. This suggests that, at large wavelength (in the limit (Z_p or) $Z_o \to 0$), the solutions for a polytrope with a rigid wall boundary condition converge to the second series $(\Omega_n^2)_\beta$. With respect to the previous section, this shows here the importance for high-degree modes of well-defined boundary conditions at the Sun's surface. Like the fixed string and the string attached to a ring sliding without stiffness, these two media represent the two outermost limits of what can be

expected for a polytrope with a mixed surface boundary condition. As for the string attached to a ring sliding with finite stiffness, one can expect that a mixed boundary condition would yield p-modes with frequencies aligned on some intermediate ridges.

In the normalised diagrams of this section, shown in Figures 9.8, 9.9 and 9.10, all dispersion relations are calculated for $z_o = z_p$ with an equal value for the sound speed, which is $c_o = c_c = 223\,\mathrm{km\,s^{-1}}$ for the numerical results. Hence each point (full circle or cross) corresponds to a multiplet frequency ν_{nl} for a truncation at the base of the convection zone ($z_p \approx 0.391\,\mathrm{R}_\odot$). It should be noted that, because the diagrams are normalised, any other value for z_p would yield the same ridges, but the multiplets would be different.

2. Node positions

As shown in Figure 9.7, the truncated models (a) as seen from the surface and (b) as seen from the interior are complementary when they are connected at a same truncation depth z_p, in forming a simple polytrope (c) (with vanishing sound speed at the surface). Thus, the above results for models (b) may be viewed and interpreted in relation to the diagnostic diagrams showed in Figure 9.4 for models (a). This connection is useful to shed light on some properties of p-modes in the simple polytrope (c).

For a free-moving truncation at depth $z = z_p$, the roots of the dispersion relation $M = 0$ (Equation (9.14)) for a truncated model (a) may be compared with those of the dispersion relation (9.52) or equivalently (9.54), *i.e.* in short $U = 0$, for a truncated model (b). As seen in Figure 9.9, this illustrates a rather interesting mathematical phenomenon, which was observed in the previous chapter already, namely that the ridges of the single truncated polytropes (with dispersion relations $M = 0$ and $U = 0$ respectively) intersect the ridges of the combined polytropes, which are the discrete ridges Ω_n^2. Therefore, at the intersection points, the modes have zero Lagrangian pressure perturbation at depth $z = z_p$. Hence this normalised graph gives a method to locate the node positions of the p-modes in the interior. Where a p-mode ridge of radial order n_a for a truncated polytrope as seen from the surface intersects a p-mode of order n_b for a truncated polytrope as seen from the interior, those ridges intersect on the ridge

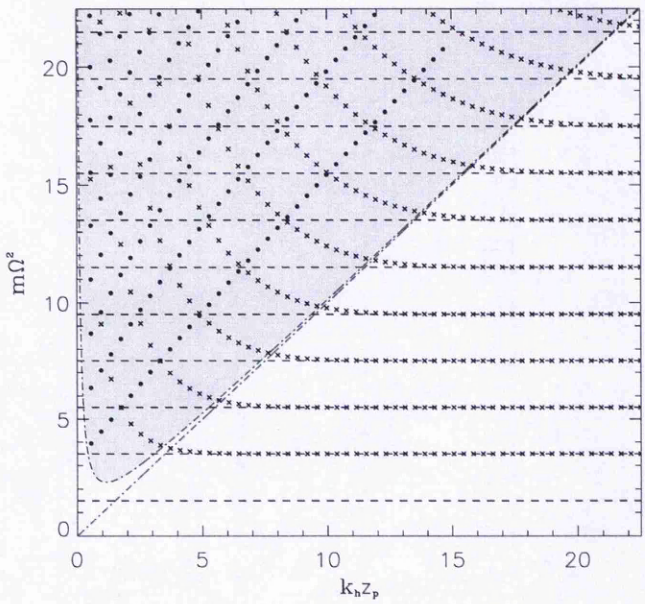

Figure 9.9: Normalised diagnostic diagrams ($k_h z_p$,$m\Omega^2$) for the truncated polytropes of Figure 9.7. The roots of the respective dispersion relations ((a) $M = 0$ and (b) $U = 0$) are represented by crosses and by full circles. The different ridges intersect the p-mode ridges for a simple polytrope (c), represented by dashed lines, at locations giving the nodes in Lagrangian pressure perturbation.

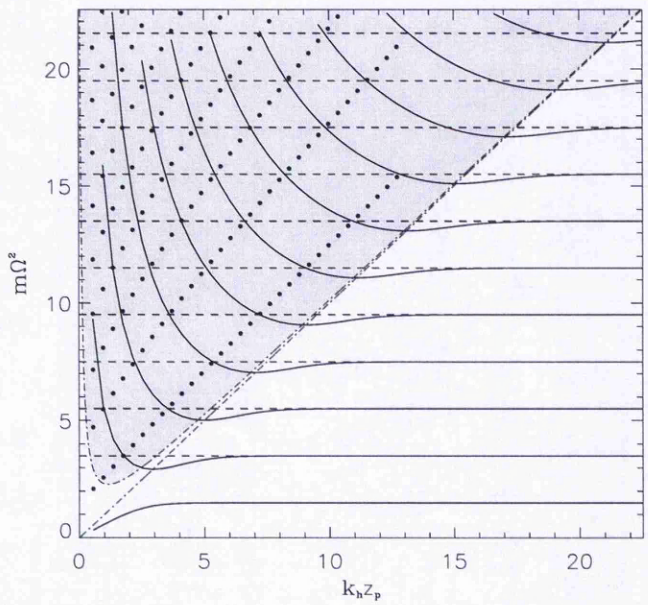

Figure 9.10: Normalised diagnostic diagram ($k_h z_p$,$m\Omega^2$) showing the roots of the dispersion relations (a) $V_z(M) = 0$ and (b) $V_z(U) = 0$, represented respectively by full circles and crosses. As in Figure 9.9, the different ridges intersect the p-mode ridges for a simple polytrope (c), represented by dashed lines, but at locations giving the nodes in velocity.

of a p-mode for a simple polytrope with radial order $n_c = n_a + n_b$. This is simply due to the fact that in combining the two truncated polytropes, the number of nodes in the upper polytrope adds up to the number of nodes in the lower polytrope. Not surprisingly, these positions depend on the horizontal wavenumber k_h or degree l.

But what is less obvious and which does show up nicely in this graph is the fact that one may find the depth of the first, second, or $(n_c - 1)^{th}$ node for which a mode propagates with a given degree l (the n_c^{th} node in pressure is at the surface). For instance p_3, the p-mode of radial order $n = 3$, has two internal nodes: the node at $k_h z_p \approx 3.3$ is the second node as seen from the surface ($n_a = 2$) and the first as seen from the interior ($n_b = 1$); the node at $k_h z_p \approx 1.1$ is the first node as seen from the surface ($n_a = 1$) and the second as seen from the interior ($n_b = 2$). Note that only the intersection points between the ridges of one truncated polytrope (a) or (b) and the simple polytrope (c) are sufficient to indicate the node positions. Nevertheless the demonstration with models (a) and (b) was necessary to prove the consistency of these aspects.

Figure 9.10 combines the roots of the dispersion relations (9.13) and (9.57) for truncated polytropes (a) and (b) respectively, with rigid wall boundary condition at $z = z_p$. In this graph, the intersection points with the p-mode ridges for a simple polytrope (c) give the node positions of the velocity V_z. All nodes are internal since at the surface there is still a pressure node. These node positions alternate with the node positions of the pressure eigenfunction, as one should expect for a pressure wave. But the reason for the deepest internal node is related to the presence of the f-mode, which forms the lowest ridge in both truncated media (a) and (b) with rigid wall boundary condition. In the case of p_3 for instance, there are now three internal nodes, at $k_h z_p \approx 5$ ($n_a = 3$, $n_b = 0$), $k_h z_p \approx 2.3$ ($n_a = 2$, $n_b = 1$) and $k_h z_p \approx 0.7$ ($n_a = 1$, $n_b = 2$).

Moreover, one may always find a mode multiplet for a given combination $k_h z_p$: at any depth $z = z_p$, there exists a mode which has a pressure node (or node in velocity) at that depth, provided that this mode propagates with the required horizontal wavelength. Indeed, the diagnostic diagrams of Figures 9.9 and 9.10 reveal that the entanglement of the nodes in a net of discrete ridges assures that any arbitrary point

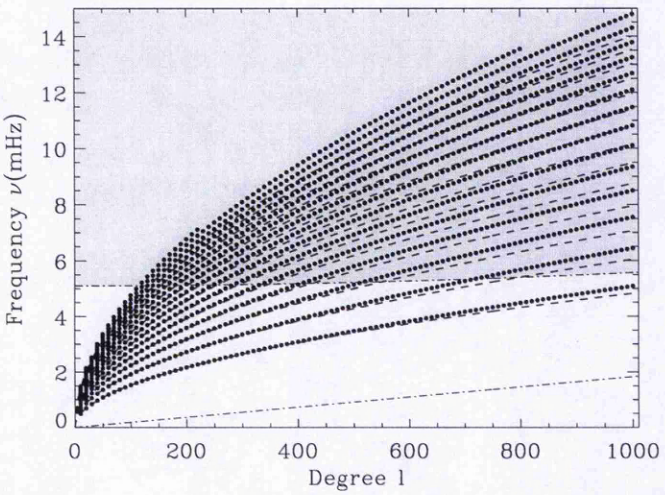

Figure 9.11: Dimensional diagnostic diagram (l, ν), showing the p-mode ridges, starting from the radial order $n = 1$, of the standard polytrope with vanishing sound speed at the surface (in dashed lines) modified in the presence of a non-vanishing sound speed $c_o = 8\,\mathrm{km\,s^{-1}}$ (in full circles). The oscillatory domain at the surface is shaded; the dispersion line for the Lamb frequency is dash-dotted.

$k_h z_p$ would correspond to a node of a p-mode.

3. General frequency corrections

The correction to the standard oscillations due to the presence of the atmosphere increases with degree l and radial order n, and its amplitude is function of the value of the sound speed at the surface. With a value of the sound speed $c_o = 8\,\mathrm{km\,s^{-1}}$, the corrections are as large as 1 or 2 mHz for degree $l = 1000$, as can be seen in Figure 9.11. One can see also that, although the actual atmosphere does not terminate at a level with zero temperature, the simple polytrope (Lamb's original atmosphere) provides an accurate treatment of low-frequency oscillations ($\nu \leq 5$ mHz).

Yet, for these low frequencies, the effects due to the planar geometry and the indetermination in the lower boundary conditions must be taken with care. Moreover, effects due to inhomogeneities in the solar interior must be corrected. For instance, the discontinuity in temperature gradient at the interface between the convective and the subadiabatic radiative zones is associated with phenomena (such as overshooting and turbulent mixing, see Section 2.2) whose effects are taken into account by refined standard models (see, *e.g.*, Gabriel, 1994; Brun et al., 1999). The transition from an

adiabatic temperature gradient A_c within the convection zone to a subadiabatic gradient A_R beneath it is visible as a clear break in the gradient of the sound speed, as inferred by Christensen-Dalsgaard et al. (1985) (see Figure 1.6). These authors do not give a numerical indication of the order of the break in gradient from the convective to the radiative region. But it is very roughly in agreement with a factor $A_c/A_R \sim 2$, as in the models of Basu, Antia and Narasimha (1994). This indicates that for modelling adiabatic stratifications of the solar interior with constant g, the polytropic index m_R in the radiative zone is twice the value of the one in the marginally stable convective zone, *i.e.* $m_R \sim 3$.

Modelling the solar interior with a convection layer above a sub-adiabatic radiative zone with such a polytropic index is an attractive idea (Foullon, 1999). The idea was taken up by Vanlommel and Čadež (2000; see also Vanlommel, 2001) and developed for a wide range of subadiabatic temperature profiles where $0 < A_R \leq A_c$, studying in particular the cases $A_R = 0.2A_c$ and $A_R = 0.8A_c$. As discussed previously, the case $A_R \approx 0.5A_c$ would perhaps have been more appropriate to study.

The effect of the thin superadiabatic layer at the top of the convection zone may also be investigated by way of a superadiabatic polytropic stratification (*e.g.*, Daniell, 1998) or be introduced through a discontinuity in temperature or density at the surface in contact with an isothermal atmosphere (see, *e.g.*, Gough, 1990a, p.291; Price, 2001). As a matter of fact, helioseismology is useful to probe not only the solar interior but also the solar atmosphere, which can be regarded simply as a boundary with inertia that resists the pressure fluctuations (Gough, 1990a).

If indeed the effect of the atmosphere is not ignored, one may regard the boundary surface in equilibrium with an isothermal atmosphere extending to $z \to -\infty$. This, however, ignores the importance of magnetism in the atmosphere. The solar atmosphere may be modelled with an isothermal region or several (essentially two) superposed isothermal regions. By assuming that the wave is evanescent outwards (*i.e.* the frequency ω is limited to be smaller than the plus cut-off ω_+ and greater than the minus cut-off ω_-, see Equation (5.74)), and requiring the solution of the form $V_z = D_1 e^{\Lambda^+ z}$ for $z \leq 0$, one obtains from Equation (4.3) a mechanical boundary condition (Ando and

Osaki, 1975). Christensen-Dalsgaard and Gough (1980) used such a model to estimate the importance of the atmosphere on vertical ($l = 0$) oscillations (with the use of the Bessel functions) at frequencies below the cut-off frequency in the atmosphere. They showed the increasing importance of the atmosphere as the frequency rises. Moreover, their results solved the otherwise apparent discrepancy between observations and the predictions of a standard solar model with normal abundances of helium and heavy elements.

Note however that for a model studying the effect of rotation and a buried magnetic field on stellar oscillations, Gough and Thompson (1990, p.27) have confirmed that their numerical results are unchanged when the simpler boundary condition of vanishing Lagrangian pressure perturbation replaces that derived for an isothermal atmosphere.

4. Conjectures

At frequencies above the cut-off $\omega_a/(2\pi) \sim 5.3$ mHz, high frequency p-modes of low horizontal wavenumbers $k_h \ll 0.2\,\mathrm{Mm}^{-1}$ (*i.e.* $l \ll 140$), can propagate in the corona and some of their wave energy is leaked to the corona by running waves, but their energy is quickly dissipated (Libbrecht and Woodard, 1991). Indeed, the evanescent zone between the inner cavity of the acoustic waves (mainly in the convection zone) and the outer propagation zone of the corona is so wide that the wave energy is reduced greatly when waves appear in the corona. In the case of high horizontal wavenumbers $k_h \gg 0.2\,\mathrm{Mm}^{-1}$, p-modes are evanescent and there is no leakage of waves in the corona.

Energy leakage damps the modes, but the solar interior continues to exhibit discrete, albeit broadened, resonant frequencies as a result of reflection. Careful observations by Jefferies et al. (1997) support the assumption that there is one more partial refection layer above the photosphere, probably at the corona-chromosphere transition region, where waves are reflected by the high density gradient. This interface may well play an important role in explaining the high frequency pseudo-modes observed above the acoustic cut-off. Moreover, as concluded by Rosenthal and Gough (1994) from an idealised model, the solar f-mode may be characterised as an interfacial mode localised near the chromosphere-corona transition layer.

Below the magnetic canopy an idealised model of the chromosphere may be considered, with a temperature profile increasing linearly with height from the photospheric level at $z = 0$ to a reflecting layer at height $z < 0$. To represent the high density gradient and side-step the consideration of magnetic aspects, an appropriate boundary condition at the reflecting level could be that of a rigid wall ($V_z = 0$). This atmospheric polytropic layer should be coupled at the photospheric level, where the sound speed does not vanish, to another polytrope standing for the convection zone. This model still needs to be developed, but one may conjecture from the analogy with the quantum harmonic oscillator that modes with frequencies related to the truncation values of the second type (leading to the series $(\Omega_n^2)_\beta$) appear in these conditions. If the existence of these modes is proven, this could help to explain the oscillations observed on the Sun, as one can expect from the following.

The series $(\Omega_n^2)_\alpha$ and $(\Omega_n^2)_\beta$ alternate, with a spacing of $1/m$ between ridges. Under the assumption that these two types of ridges co-exist, like the even and odd energy levels of a particle for a quantum harmonic oscillator, a general series $(\Omega_n^2)_\gamma$ may be defined, where

$$(\Omega_n^2)_\gamma = \frac{n}{m} + 1 = \frac{n+m}{m} \qquad n = 1, 2, 3 \ldots , \tag{9.58}$$

with the even and odd integers n indicating the 'even' series $(\Omega_n^2)_\alpha$ and the 'odd' series $(\Omega_n^2)_\beta$. The normalised ridges are horizontal and, comparable to energy levels in quantum mechanics, represent frequency levels $m(\Omega_n^2)_\gamma$ of quantum radial orders n.

The merit of this combined series is that it is able to reproduce exactly a relationship between the p-modes that are observed on the Sun. This relationship has been discovered by Duvall (1982), who plotted $(n + \phi)\pi/\omega$ as a function of the horizontal phase speed ω/k_h and obtained the collapse of all ridges onto a single curve, with a value of ϕ close to 3/2. Duvall noted also that frequencies of the fundamental mode with $(n = 0)$ do not fall along the curve. Figure 9.12 shows the graphical expression of the law for month 50 of GONG data (see Appendix A.2), presented as Duvall plotted it.

In the formal approach, only the even series $(\Omega_n^2)_\alpha$ is a solution, and this yields the

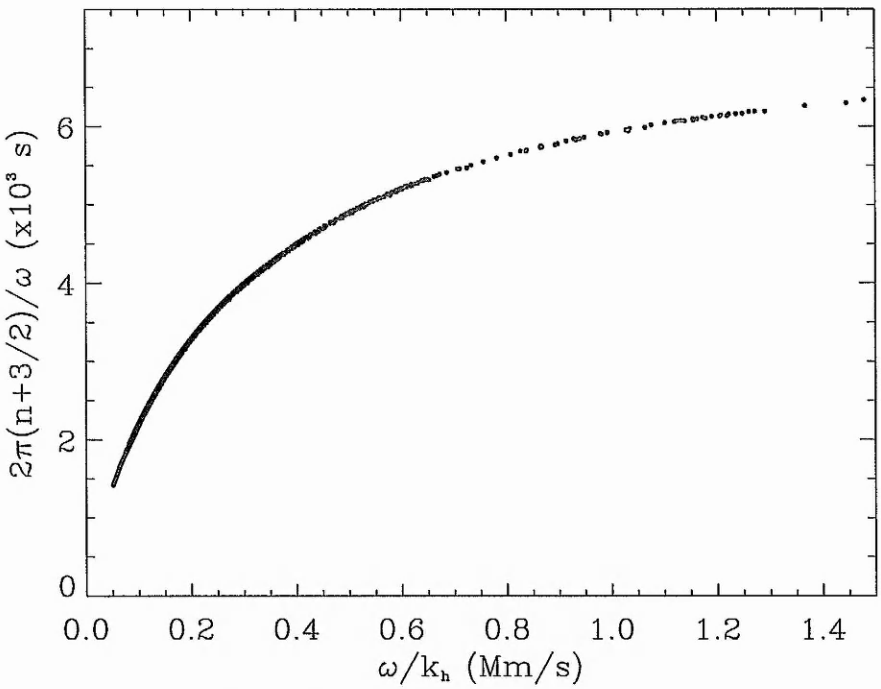

Figure 9.12: Duvall's law, computed from month 50 of GONG data. When the ratio $(n+\phi)\pi/\omega$ is plotted against the horizontal phase speed ω/k_h, all p-mode ridges of radial order n collapse onto one single ridge, with $\phi \approx 3/2$.

relation

$$\frac{(n+\phi)\pi}{\omega} = \frac{m\pi}{2g}\frac{\omega}{k_h}, \qquad \phi = \frac{m}{2}, \qquad n = 1, 2, 3 \ldots . \tag{9.59}$$

The phase factor $\phi = m/2$ does not correlate with the observations. To agree with Duvall's result, one would need a polytropic index $m = 3$ (instead of $m = 3/2$), which introduces differences between modes of different radial order n that are larger than the observed scatter. Although Equation (9.59) is consistent but not fully adequate with Duvall's law, the discrepancy was reported to be due to partial use of the information contained in the data (Christensen-Dalsgaard et al., 1985).

And yet, the direct applicability of the polytropic model to account for the Duvall's law is shown here to be possible. Indeed, the combined series (9.58) yields the law

$$\frac{(n+\phi)\pi}{\omega} = \frac{m\pi}{g}\frac{\omega}{k_h}, \qquad \phi = m, \qquad n = 1, 2, 3 \ldots , \tag{9.60}$$

with a phase-factor $\phi = m = 3/2$ consistent with the observed one. In the law, observed in Figure 9.12, the slope of the curve is function of the horizontal phase speed ω/k_h, and should be related to the coefficient $2\pi\frac{m}{g}$ in Equation (9.60). Knowing that the

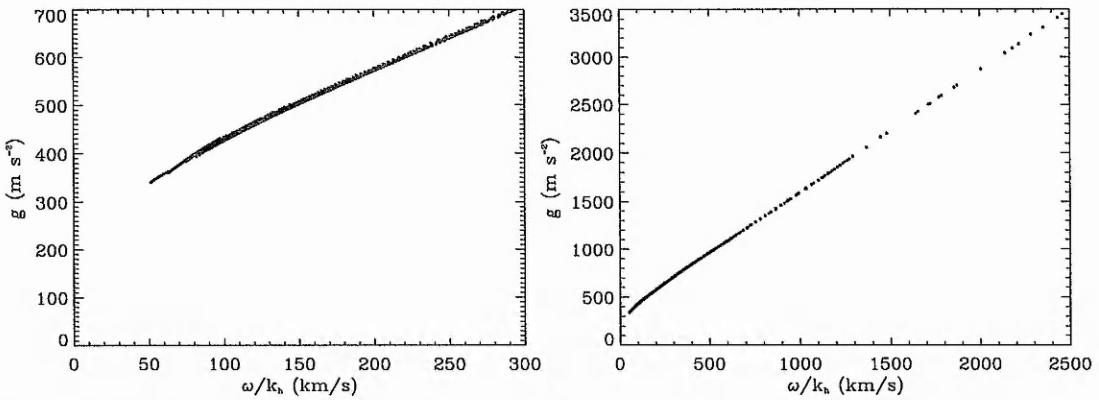

Figure 9.13: The value of g deduced from the combined series of a polytropic model and Duvall's law, computed from month 50 of GONG data, versus the horizontal phase speed ω/k_h: (*left*) is a snapshot of the (*right*) plot for smaller values of g and ω/k_h.

horizontal phase speed gives the local sound speed at the turning point of the mode, the decreasing value of the slope for p-modes of higher phase speed would then be explained by the effect of the increasing gravity at deeper depths, where are determined the conditions of the resonance. Equation (9.60) may be reformulated in the form

$$g = \frac{m\omega}{(n+\phi)}\frac{\omega}{k_h}, \qquad \phi = m, \qquad n = 1, 2, 3 \ldots . \tag{9.61}$$

Following this equation, Figure 9.13 shows that the p-mode ridges fall also onto one single curve. If one extends the curve to values of the horizontal phase speed close to the value of the sound speed at the surface (*i.e.* $10\,\mathrm{km\,s^{-1}}$), one can read a corresponding value for g consistent with the value $g = 274\,\mathrm{m\,s^{-2}}$ at the solar surface. However, for large horizontal phase speeds, the curve reaches unrealistic large values for g. It is likely that this inconsistency is related to the difference between the dispersion law obtained in planar geometry and the one that could be obtained in spherical geometry with gravity gradients.

Conclusion In Section 9.2, it was shown that the approximation of plane geometry introduces some uncertainty on the precision of frequencies of low-degree modes. Moreover, a second series of eigensolutions was left concealed in the formal helioseismic approach. The existence of the series depends on the surface boundary conditions and, as was discussed in Section 9.3, more modelling remains to be done to explain the observed solar oscillations. The effects of the atmosphere, introducing some uncertainty

on the precision of high frequencies or frequencies of high-degree modes, are also important to explain observed frequency shifts over the solar cycle. In the coming chapter, these effects will be reviewed. This will serve as a preamble to study the isolated effect of a buried magnetic field on p-mode oscillations.

Though here at journey's end I lie
in darkness buried deep,
beyond all towers strong and high,
beyond all mountains steep,
above all shadows rides the Sun
and Stars for ever dwell:
I will not say the Day is done,
nor bid the Stars farewell.

John R.R. Tolkien (1892 - 1973)
"The Lord of the Rings" (1954-55), "The Tower of Cirith Ungol"

Chapter 10

Theoretical Frequency Shifts

10.1 Atmospheric frequency shifts

Helioseismic frequency shifts mimic the solar activity cycle (see Section 2.2). As a result, time-dependent variations in the near surface magnetism and temperature are thought to be responsible for the intermediate or high-degree frequency shifts. Before reviewing the theoretical analyses involving the effect of the solar atmosphere, further light may be shed on the observations, in order to allow some comparison with the theoretically determined frequency shifts.

Frequency shifts $\Delta\nu$ between a maximum and a minimum of solar activity,

$$\Delta\nu = \nu(max) - \nu(min)\,, \tag{10.1}$$

can be plotted as a function of angular degree l or base cyclic frequency $\nu(min)$, as displayed in Section 2.1 (see Figures 2.1 and 2.2). To produce these graphs, the cyclic frequency ν $(= \omega/2\pi)$ observed at some period of the solar cycle is an average of the central multiplets ν_{nl} over all degrees and frequency bins. Frequency bins used by observers are horizontal slices of the diagnostic diagram (l, ν) that contain branches of p-mode ridges increasing in number and of radial orders decreasing in n as the range of degrees considered increases. Therefore, frequency shifts obtained with a set of intermediate-degree observations are averaged over a number of points for modes with high l and low n which, *a priori*, do not contribute to the shifts due to variations in the interior, but to shifts due to variations in the surface layers.

If there is a possibility to remove contributions due to the near surface perturbations, it is therefore prudent not to average the observations and to extract any appropriate information that can be compared with theoretical results. In Figures 10.1 and 10.2, contrary to what is often the case in observations, no averaging of ν is carried out, thus incurring no loss of information about the radial order n and degree l. The frequency shifts $\Delta\nu_{nl}$ are obtained between a maximum and a minimum of activity, by taking the difference in central cyclic frequencies between month 50 and month 9 of GONG data (see Appendix A.2). The shifts with the same radial order n are plotted with the same symbol, and each line represents a second order polynomial fit to these shifts. Figure 10.2 in particular shows how shifts belonging to the same ridge increase globally with radial order n.

It was suggested by Kuhn (1988) that the frequency shifts are due to changes in the observed photospheric latitudinal temperature distribution and are correlated with the variation in the surface temperature. Libbrecht and Woodard (1990) have argued on the basis of observations of intermediate-degree modes that the source of the perturbations must lie near the solar surface. Ignoring the magnetism of the solar atmosphere, the influence of its stratification on the form of p-mode ridges is studied by a number of authors (*e.g.*, Belvedere et al., 1983; Hindman and Zweibel, 1994; Steffens and Schmitz, 2000; Dzhalilov et al. 2000; Geyer and Schmitz, 2000).

But it is possible that the frequency shifts are due to variation in thin magnetic fibrils (Bogdan and Zweibel, 1985; Zweibel and Bogdan, 1986) or in the mean magnetic field near the photosphere (Gough and Thompson, 1988). Goldreich et al. (1991) theoretically showed that the variations in the solar p-mode eigenfrequencies are related to the perturbations in the magnetic flux at the Sun's surface. Through a perturbation in the convective heat flux, Balmforth et al. (1996) concluded also that the observed frequency changes reflect a surface disturbance.

Table 10.1 summarises publications which model the upper atmosphere's magnetism by a horizontal or vertical magnetic field. The models with vertical magnetic fields are intended to apply to the magnetised atmosphere near sunspots. But the main consequence of the presence of sunspots is to decrease the frequency (due to dissipation

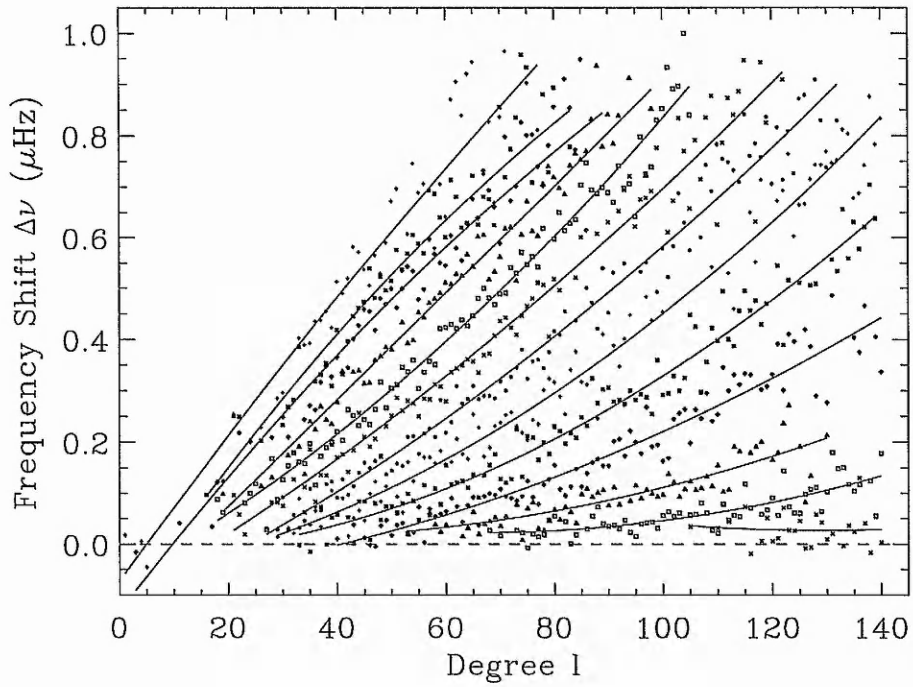

Figure 10.1: Frequency shifts $\Delta\nu$, between month 50 and month 9 of GONG data, versus degree l. Ridges of the same radial order are drawn starting from $n = 1$ at the bottom right to $n = 13$ at the top left.

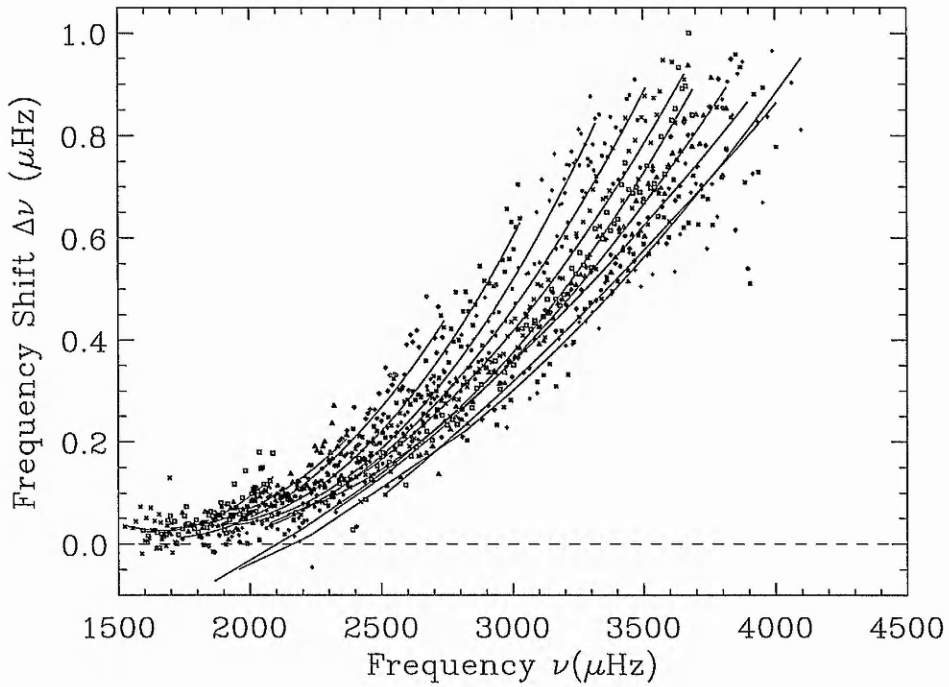

Figure 10.2: Frequency shifts $\Delta\nu$, between month 50 and month 9 of GONG data, versus base frequency of GONG month 9. Ridges of the same radial order are drawn starting from $n = 1$ to $n = 13$ as the base frequency increases.

Horizontal $\mathbf{B_o}$	$k_h = 0$	$k_y = 0$	$(k_x, k_y) \neq 0$
Constant v_A	Daniell, 98.	Campbell, 87; Campbell & Roberts, 89; Wright &Thompson,92; Jain, 92; Pintér, 99; Pintér & Goossens, 99.	Chen & Lykoudis, 72 ($k_x = 0$ & piecewise constant atmosphere); Jain & Roberts, 94a; Pintér, 99.
Uniform B_o	Daniell, 98.	Evans, 90; Evans & Roberts, 90, 92; Wright &Thompson,92; Jain, 92; Jain & Roberts, 93, 94b, 96; Johnston, Roberts & Wright, 95; Daniell, 98; Vanlommel, 01.	Zhukov, 97.
Hybrid and other non-homogeneous profiles	Goldreich et al., 91; Jain et al., 96 (p-mode surface amplitudes).	Tirry, 98; Pintér, 99; Vanlommel & Goossens, 99; Vanlommel, 01; Zhukov, 01.	
Vertical $\mathbf{B_o}$	*e.g.*, Banerjee et al., 95; Bogdan and Cally, 97; Cally and Bogdan, 97; and references therein.		

Table 10.1: Classified references for various models considering the influence of magnetised atmospheres on global solar oscillations.

of acoustic energy), while the observed global frequencies increase near sunspot maximum. As seen in Chapter 5, models with an atmosphere threaded by a horizontal magnetic field allow analytical solutions for the profiles producing a constant Alfvén speed or, when $k_y = 0$, producing a uniform magnetic field. Such profiles were first considered, respectively by Campbell (1987) and Evans (1990), to study the influence of a chromospheric magnetic field on the frequencies of global solar oscillations, with

parallel propagation with respect to the magnetic field. Wright and Thompson (1992) developed a perturbation method approach, based on the WKB approximation to the frequency shifts.

For a simple model consisting of a polytropic solar interior and an overlying isothermal atmosphere with constant Alfvén speed, Campbell and Roberts (1989) revealed that, with increasing magnetic field strength squared, the f-mode suffers a frequency increase for all degrees l, while the p-modes undergo a frequency decrease, except p_1 — the p-mode of radial order $n = 1$ — which suffers a frequency increase at low to moderate values of l.

A model with uniform magnetic field was considered by Evans and Roberts (1990; 1992). They found that the frequencies of both the f- and p-modes are raised by the presence of the overlying magnetic field with the magnitude of the effect increasing with the degree l, the radial order n and the square of the chromospheric magnetic field strength. The extension to a third intermediate isothermal field-free layer showed how the height of the magnetic canopy influences the behaviour of acoustic oscillations (Evans and Roberts, 1991). For an atmosphere with uniform magnetic field, Jain and Roberts (1993; 1994b; 1996) and Johnston et al. (1995) combined the effect of an increase of mean chromospheric magnetic field strength with an increase in chromospheric temperature, in relation with the solar cycle; evidence of these effects is reproduced in Figure 10.3, where it is shown that the theoretically determined frequency shifts go some way towards explaining the observed ones.

These analyses were restricted to motions that have a horizontal wave vector parallel to the horizontal equilibrium magnetic field. Non-parallel propagation was the subject of study by Jain (1992). For an atmosphere with constant Alfvén speed, the effects of non-parallel propagation on p- and f-modes were shown to be non-negligible (Jain and Roberts, 1994a). In a sense, the constant Alfvén and uniform magnetic field models represent two extreme situations with the actual profile of the Alfvén speed lying in between the profiles of these two models. These theoretical approaches, however, did not allow for resonances in the atmosphere, by neglecting the non-parallel propagation and/or the nonuniformity of the overlying magnetic region, hence removing the

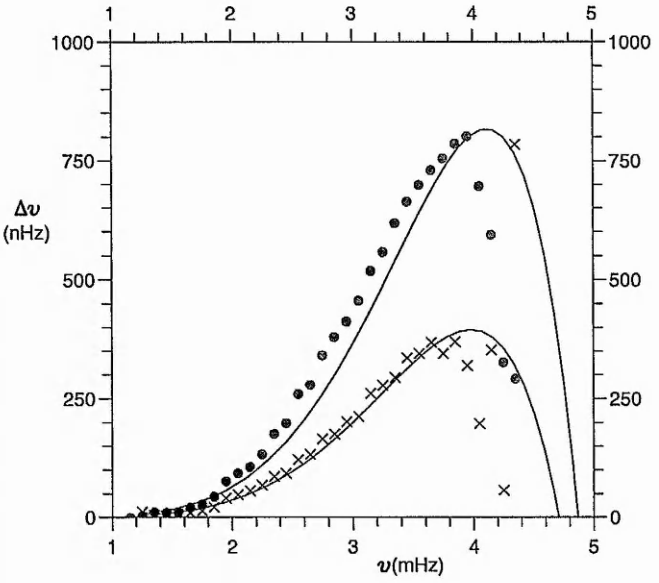

Figure 10.3: The observationally determined frequency shifts $\Delta\nu$ (in nHz) of intermediate p-modes as a function of frequency ν (in mHz) for the years 1988 (crosses) and 1989 (filled circles), compared with 1986 (Libbrecht and Woodard, 1990). Also shown are the results from model calculations by Jain and Roberts (1994b), for oscillations of degree $l = 75$. The theoretically determined frequency shifts (shown as full curves) arise from an increase in chromospheric magnetic field strength (from 30G to 50G (lower curve) or 61G (upper curve)) combined with a simultaneous rise in chromospheric temperature (from 4170K to 6370K (lower curve) or 7770K (upper curve)).

interaction of the p-modes with the continuum Alfvén waves and/or slow MHD waves. Indeed p-modes with characteristic frequencies lying within the range of continuous spectra may resonantly couple to localised Alfvén and/or slow continuum modes. Due to the transfer of energy from the global p-mode oscillation to a localised continuum oscillation, the p-mode is damped and the chromosphere is heated by dissipation occurring in a narrow layer embracing the resonant magnetic surface. The tunnel leakage of wave energy into the region of Alfvén and/or cusp resonances not only results in some heating of the solar upper atmosphere, in a nonradiative manner (see, *e.g.*, Goossens, 1991), but also contributes to frequency changes (see, *e.g.*, Tirry, 1998).

Acoustic oscillations with a horizontal propagation component oblique to the magnetic field in a non-uniform chromosphere were studied for the first time by Zhukov (1997), who reports acoustic energy absorption of Alfvén resonant levels in the chromosphere and computes oscillation frequencies and damping rates. A detailed study was undertaken by Tirry (1998), who incorporates the relevant physical process of resonant absorption of p-modes by localised magnetic waves in a small transition region imbedded in the model used by Campbell and Roberts (1989). An extension of this three-layer model was presented by Pintér (1999), for a wider range of parameters. In particular, Pintér focuses on the possible interaction of global solar acoustic oscillations with the

slow continuum waves for motions that propagate parallel to the magnetic field (see also Pintér and Goossens, 1999). This study was extended to non-parallel propagation by Vanlommel and Goossens (1999).

The jump τ in temperature between the isothermal region (standing for the corona) and the surface temperature — at the interface between the intermediate layer (standing for the chromosphere) and the field-free solar interior — is an important parameter for defining the conditions for resonant absorption. Resonances are excluded for $\tau = 1$, which was the case (in the limit of no intermediate layer) in the Campbell, Evans or Jain models. For τ (> 1) taking a more realistic value, the otherwise negative frequency shifts become positive as the field strength is increased (see Vanlommel and Goossens, 1999, Figure 8). Finally, Vanlommel (2001) makes a rather complete mathematical study based on the model of Evans and Roberts (1990) but for $\tau \neq 1$. There are cases including resonances for modes absorbed by localised slow modes in the coronal layer.

In Figure 10.4, theoretically determined frequency shifts for the model in Vanlommel and Goossens (1999) are shown as broken lines. They arise from an increase in coronal magnetic field strength from a reference value of $B_o(min) = 50$G and for different parameters τ. The dotted and the dashed lines are for $\tau = 150$, while the dashed-dotted and the dashed-triple-dotted lines are for $\tau = 200$. The shifts are calculated for an increase in magnetic field strength to 60G (dotted and dashed-dotted lines) and to 65G (dashed and dashed-triple-dotted lines). The behaviour of the theoretical shifts for the lower degrees is due to the cut-off of the isothermal atmosphere.

In Figure 10.4 I added the observed frequency shifts between a maximum and a minimum of activity, obtained as for Figure 10.1 by taking the difference in central cyclic frequencies between month 50 and month 9 of GONG data (see Appendix A.2). These data sets were not averaged, allowing a comparison of shifts in each radial ridge of order n. One can see that where data is available, the order of magnitude of the theoretical frequency shifts coincide with the observed shifts. The trends in the theoretical shifts follow the observed ones. For the p_2 mode, the theoretical shifts, which compare the best to the second order polynomial fitted to the observations, are obtained for an increase in magnetic field strength of 10G for modes of degree l between 80 and 110,

and 15G for modes of higher degree.

Hence, shifts in the modes of degree $l = 75$ could be as well explained by the effect of a 31G rise in chromospheric field strength combined with a rise in chromospheric temperature over a period of three years, as seen in Figure 10.3, or by a 10G rise in the coronal field strength over a period of 4 years, as in Figure 10.4. These comparisons do not allow for any conclusions about the exact value of τ or the magnetic field strength in the different layers of the solar atmosphere. Instead they underline the uncertainty of the large atmospheric effects on solar oscillations. Moreover, in the solar atmosphere, the temperature increases exponentially. This is not considered so far in those models, which at most deal with linear temperature profiles connected by temperature jumps.

Conclusion and outline Through an increase in magnetic field strength, solar magnetic fields in the atmosphere or sub-surface of the Sun can explain the frequency shifts observed on the timescale of the solar activity cycle. Given the large influence of the changing atmosphere, a separate study of the contribution of internal magnetic layers will clarify the relative importance of these effects. The remainder of this chapter treats the isolated effects of internal magnetic layers, such as at the base of the convection zone and in the sunspots' anchoring zone, where the magnetic field and layer thickness are presumed to vary over the solar activity cycle. Properties that can be derived analytically are presented in Section 10.2. They are applied in particular to the case of the three-layer model and illustrated by numerical results for parallel propagation. Such results are obtained from comparing the resonant frequencies of the models presented in Section 8.2 with those for field-free models. In Section 10.3, these results are further interpreted by an analytical approximation of the dispersion relation. This approximation serves in turn to evaluate the amplitude of the shifts for perpendicular propagation.

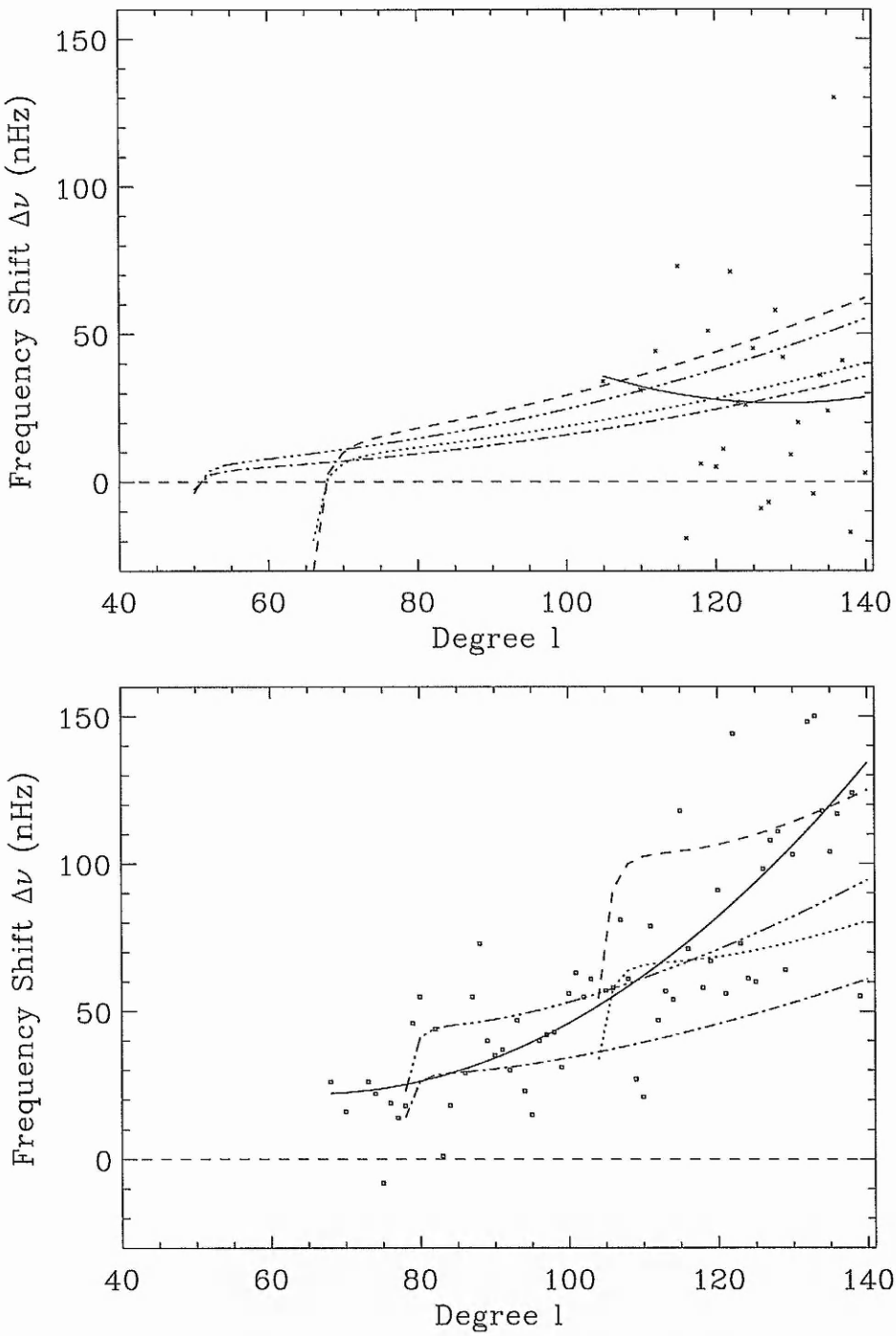

Figure 10.4: Frequency shifts versus degree l, combining observations from GONG data and theoretical numerical results from model calculations by Vanlommel and Goossens (1999), are shown by lines joining shifts for p-modes with the same radial order n: (*top*) p_1 for $n = 1$ and (*bottom*) p_2 for $n = 2$. The solid line shows a second order polynomial fitted to the observationally shifts, which otherwise are crosses for p_1 and squares for p_2.

10.2 Analytical and numerical properties

Properties of the frequency shifts may be explained analytically by invoking some fundamental relations developed earlier in this thesis. In this section, derived properties will elaborate from the most general approach up to the more specific characteristics observed in the numerical results. The frequency shifts considered are generally the cyclic frequency difference $\Delta\nu_{nl}$, between $\nu_{nl}(max)$ obtained with a magnetic field and $\nu_{nl}(min)$ in the absence of a magnetic field; no averaging of ν is made. Numerical results for parallel propagation ($k_y = 0$) are presented in this section. Results for the most evolved model involving a buried magnetic layer at the base of the convection zone are first displayed in Figure 10.5 below, where the frequency shifts are shown against the base frequency $\nu = \nu_{nl}(min)$. A sketch on the left of the graph makes clear the model considered.

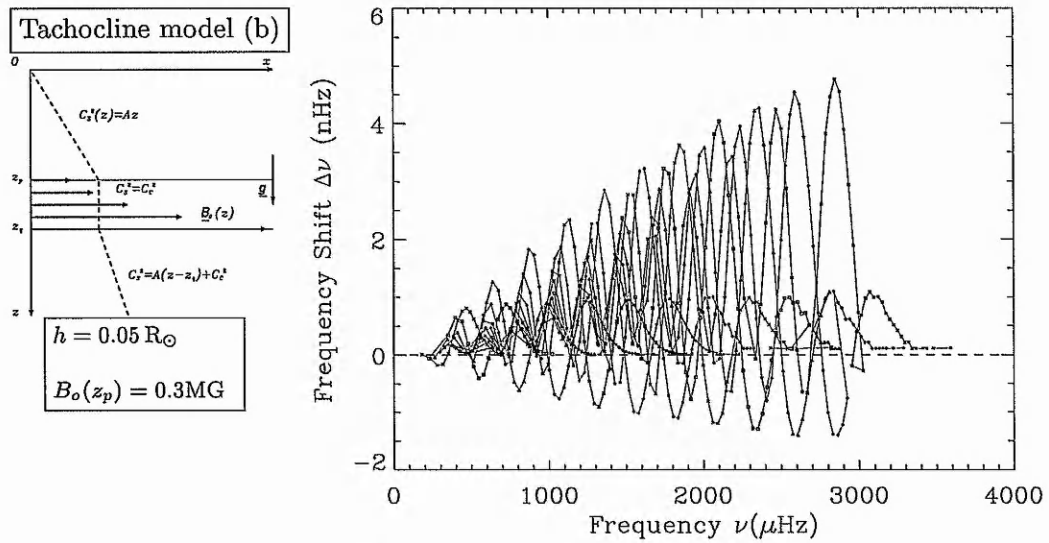

Figure 10.5: Frequency shifts $\Delta\nu$ versus frequency ν for the tachocline model (b).

1. General trends

An increase in magnetic field strength raises the shifts proportionally to the square of the field strength. For instance, a magnetic slab of field strength ten times larger than the original yields shifts of amplitude hundred times bigger. With the same three-layer model, Daniell (1998) reached a similar conclusion from his numerical results for both

low- and high-degree modes. Campbell (1987), using a semi-infinite region below the base of the convective zone, rather than a layer, also obtained this result numerically for high-degree modes. This property was first obtained analytically for fibril magnetic fields (Bogdan and Zweibel, 1985; Zweibel and Bogdan, 1986), and in the case of a magnetic layer, for parallel propagation to an horizontal magnetic field (Roberts and Campbell, 1986; Campbell, 1987). In Zweibel and Bogdan (1986), the dependence on the magnetic field strength was also expressed for a polytropic slab.

This property can be understood as follows. For a change in pressure δp in a medium of density ρ_o, the local sonic speed c is given (see Equations (1.33) and (1.34)) by

$$c^2 = \frac{\delta p}{-\rho_o \Delta}, \tag{10.2}$$

where Δ is the compressibility of the gas. In the Cartesian system (x, y, z), where the perturbations of the ideal linearised MHD equations are Fourier analysed proportionally to $\exp i(\omega t - k_x x - k_y y)$, wave propagation can be described in the z-direction through the vertical velocity perturbation V_z and the Lagrangian pressure perturbation, which, in the presence of a horizontal magnetic field (see Equation (3.40) when Fourier analysed), is given by

$$\mathcal{P}_T = -\rho_o c_s^2 \left[\Delta + \frac{v_A^2}{c_s^2} \Delta_\perp \right], \tag{10.3}$$

for adiabatic sound speed c_s, Alfvén speed v_A and the perpendicular components of compressibility $\Delta_\perp$ as defined in Equation (3.37).

Hence, in the presence of a horizontal magnetic field, the wave experiences an effective magnetosonic speed c given by

$$c^2 = c_s^2 \left[1 + \frac{v_A^2}{c_s^2} \frac{\Delta_\perp}{\Delta} \right], \tag{10.4}$$

indicating that the resulting change in frequency is inversely proportional to the plasma β and so broadly proportional to the square of the magnetic field strength (note that $1/\beta$ and $B_o^2(z_p)$ are not strictly proportional; see Equation (7.40)).

Moreover, Equation (10.4) shows that the effect increases with the normalised component of compressibility perpendicular to the magnetic field lines, $\Delta_\perp/\Delta$. Gough and Thompson (1990) obtained a similar result through perturbation theory. They found

(see their Equation (4.10)) that the effect increases instead with $\sin^2\psi$, where ψ is the angle between the magnetic field and the direction of propagation of the wave. Hence the magnitude of the perturbation depends on the direction of propagation of the wave. However, one cannot argue that the change in frequency is generally inversely proportional to the plasma β: the dependence of $\Delta_\perp/\Delta$ on β must be studied more carefully.

From Equations (3.37) and (3.55),

$$\Delta_\perp = \frac{dV_z}{dz} + \frac{k_y^2 c_\perp^2}{\omega^2}\Delta + \frac{g k_y^2}{\omega^2} V_z \,, \tag{10.5}$$

which means that

$$\frac{\Delta_\perp}{\Delta} = \frac{1}{\Delta}\frac{dV_z}{dz} + \frac{k_y^2}{\omega^2}\left(c_\perp^2 + g\frac{V_z}{\Delta}\right) . \tag{10.6}$$

But also, with Equation (3.63), the ratio $\Delta_\perp/\Delta$ is given in every case by

$$\frac{\Delta_\perp}{\Delta} = 1 - \frac{k_x^2 c_s^2}{\omega^2} - \frac{g k_x^2}{\omega^2}\frac{V_z}{\Delta} . \tag{10.7}$$

If $k_x = 0$, the mode propagates perpendicular to the magnetic field lines and $\Delta_\perp = \Delta$, so that the fast magnetoacoustic speed $(c_s^2 + v_A^2)^{\frac{1}{2}}$ is the characteristic speed of this mode; this agrees also with the value of $c_\perp$ as defined through Equation (3.58). Thus, for propagation perpendicular to magnetic field lines, the effective fast magnetoacoustic speed serves to increase the frequency of the mode.

Parallel propagating modes ($k_y = 0$) have

$$\frac{\Delta_\perp}{\Delta} = \frac{1}{\Delta}\frac{dV_z}{dz} = 1 - \frac{k_x^2 c_s^2}{\omega^2} - \frac{g k_x^2}{\omega^2}\frac{V_z}{\Delta} , \tag{10.8}$$

which supports the idea that the parallel propagating modes would be less affected by the magnetic field. In the limit of zero gravity, this is clear, but in the general case, unless V_z and Δ have the same sign, the effect requires further study.

Zweibel and Bogdan (1986) showed that for a submerged layer of horizontal flux tubes, modes which turn within the layer are more strongly affected. At the turning radius of the mode, the propagation is parallel to the horizontal direction, but not necessarily to the magnetic field lines. Zweibel and Bogdan also showed clearly that the effect is larger for modes propagating perpendicular to the symmetry axis of the

tubes at the turning radius (*i.e.* $k_y \to \infty$), rather than parallel propagating modes ($k_y = 0$).

Hence it appears that the model of parallel propagation is lacking of the mode propagation in the $\mathbf{g} \times \mathbf{B_o}$-direction. Moreover, the low-degree modes ($k_h = 0$) are not necessarily the most affected. And yet, because low-degree modes propagate nearly perpendicular to the magnetic field lines in the vertical direction, this has been a source of confusion in the idea that low-degree modes should be the modes to study for probing the presence of magnetic fields in the solar interior. It should additionally be understood that the modes that are the most affected propagate in the $\mathbf{g} \times \mathbf{B_o}$-direction, hence in the y-direction, and that the mode which only propagates in the z-direction will be the less affected.

The force of gravity involves the vertical velocity V_z. Without gravity, the terms in V_z in Equations (10.6) and (10.7) are ignored and so

$$\frac{\Delta_\perp}{\Delta} = \frac{1}{\Delta}\frac{dV_z}{dz} + \frac{k_y^2 c_\perp^2}{\omega^2} = 1 - \frac{k_x^2 c_s^2}{\omega^2}, \qquad (g = 0). \tag{10.9}$$

The effect of magnetism would be the largest at fixed frequency for perpendicular propagating modes ($k_x = 0$), or at fixed degree for high-frequency modes ($\omega \to \infty$), and would be null at the Lamb frequency ($\omega^2 = k_x^2 c_s^2$). The sign of the effect depends whether $\omega^2 > k_x^2 c_s^2$ or $\omega^2 < k_x^2 c_s^2$. This separation corresponds approximately to the modes with respectively oscillatory and evanescent behaviour in the layer. The oscillatory modes would be up-shifted, while the evanescent modes would be down-shifted. However, this rule does not apply when gravity is introduced.

The correction to Equation (10.9) due to gravity is obtained by rewriting the right-hand side of Equation (10.7) in replacing Δ from Equation (3.63), *viz.*

$$\frac{\Delta_\perp}{\Delta} = \left(1 - \frac{k_x^2 c_s^2}{\omega^2}\right)\left(1 - \frac{1}{1 + \frac{k_y^2}{k_x^2}\frac{\omega^2}{(\omega^2 - k_x^2 v_A^2)} + \frac{\omega^2}{g k_x^2}\frac{1}{V_z}\frac{dV_z}{dz}}\right). \tag{10.10}$$

This expression indicates that the correction due to gravity is increased as k_y increases. Moreover, if $k_y \neq 0$ and if the frequency matches the Alfvén frequency ($\omega^2 = k_x^2 v_A^2$), the effect is expected to be as large as without gravity. The correction term also involves the ratio between the gradient in vertical velocity amplitude with

depth to the amplitude itself. This effect is amplified for low parallel wavenumbers ($k_x \to 0$), which is also indirectly related to high wavenumbers k_y.

2. Application to the three-layer model

Now, for the case where the magnetic layer has constant sound and Alfvén speeds, the vertical velocity amplitude V_z is given by Equation (5.36) for surface modes, *viz.*

$$V_z = D_1 e^{\Lambda^+ z} + D_2 e^{\Lambda^- z} . \tag{10.11}$$

Thus V_p, the value V_z at depth $z = z_p$, is

$$V_p = V_z(z_p) = D_1 e^{\Lambda^+ z_p} + D_2 e^{\Lambda^- z_p} . \tag{10.12}$$

Besides the eigenvalues of the dispersion relation must satisfy Equation (7.21), which is

$$D_1 \mathcal{E}_p^+ e^{\Lambda^+ z_p} + D_2 \mathcal{E}_p^- e^{\Lambda^- z_p} = 0 . \tag{10.13}$$

In order to eliminate the constant D_2, Equations (10.12) and (10.13) are combined to give

$$V_p = D_1 e^{\Lambda^+ z_p} \left(1 - \frac{\mathcal{E}_p^+}{\mathcal{E}_p^-} \right) . \tag{10.14}$$

Now in the isothermal layer, the constants D_1 and D_2 in the vertical velocity amplitude (Equation (10.11)) are respectively obtained from Equations (10.14) and (10.13), giving in the layer

$$V_z = \frac{V_p}{1 - \frac{\mathcal{E}_p^+}{\mathcal{E}_p^-}} \left(e^{\Lambda^+ (z - z_p)} - \frac{\mathcal{E}_p^+}{\mathcal{E}_p^-} e^{\Lambda^- (z - z_p)} \right) . \tag{10.15}$$

Hence

$$\frac{dV_z}{dz} = \frac{V_p}{1 - \frac{\mathcal{E}_p^+}{\mathcal{E}_p^-}} \left(\Lambda^+ e^{\Lambda^+ (z - z_p)} - \Lambda^- \frac{\mathcal{E}_p^+}{\mathcal{E}_p^-} e^{\Lambda^- (z - z_p)} \right) , \tag{10.16}$$

and the ratio $\frac{1}{V_z} \frac{dV_z}{dz}$ is

$$\frac{1}{V_z} \frac{dV_z}{dz} = \frac{\Lambda^+ e^{2\kappa (z - z_p)} - \Lambda^- \frac{\mathcal{E}_p^+}{\mathcal{E}_p^-}}{e^{2\kappa (z - z_p)} - \frac{\mathcal{E}_p^+}{\mathcal{E}_p^-}} . \tag{10.17}$$

Therefore, the effect of the buried magnetic layer is related to the internal and external environment of the layer, as can be seen through the ratio $\frac{1}{V_z}\frac{dV_z}{dz}$ taken at some depth z in the layer, *viz.*

$$\frac{1}{V_z}\frac{dV_z}{dz} = -\frac{1}{2H_o} + \kappa \frac{e^{2\kappa(z-z_p)} + \frac{\mathcal{E}_p^+}{\mathcal{E}_p^-}}{e^{2\kappa(z-z_p)} - \frac{\mathcal{E}_p^+}{\mathcal{E}_p^-}}. \tag{10.18}$$

Modes are affected not only as a function of how deep they propagate, but also on the mode wavelength relative to the distance $h = z - z_p$ travelled inside the layer. Just as a register hole in a flute, the effect on p-mode frequencies of a thin horizontal magnetic layer is to 'encourage' higher harmonics. It follows that a thin buried magnetic slab affects high frequency (or high degree) modes rather more than low frequency (or low degree) modes (see also Figure 10.5).

The consideration of equations in the plane-wave approximation may not be valid for low-degree modes. However, the plane-wave approximation may be considered valid locally if there is no significant variation along a wave front over a distance comparable to the local wavelength λ. In the isothermal layer, this condition corresponds to $\lambda \ll H_o$, where H_o is both the density and pressure scale-heights (see Section 5.1). The local wavelength of a p-mode in the isothermal layer is roughly $\lambda \simeq \frac{c_c}{\nu}$. With a frequency $\nu \simeq 3.3$ mHz and $c_c = 223\,\mathrm{km\,s^{-1}}$ at the base of the convection zone, $\lambda \simeq 0.1\,\mathrm{R}_\odot$. For the tachocline model, this is a reasonable approximation since $H_o \simeq 0.15\,\mathrm{R}_\odot$. But for a shallow field model, with $c_c = 80\,\mathrm{km\,s^{-1}}$, $\lambda \simeq 0.03\,\mathrm{R}_\odot > H_o \simeq 0.02\,\mathrm{R}_\odot$ (see Table 8.1). This should be bear in mind when interpreting the resulting frequency shifts.

For a mode with long wavelength, *viz.* $\kappa \ll 1$, the ratio $\frac{\mathcal{E}_p^+}{\mathcal{E}_p^-} \approx 1$. More specifically, for modes with a wavelength much longer than the thickness of the layer, *i.e.* $\kappa h \ll 1$, the exponential term can be expanded $e^{2\kappa h} \approx 1 + 2\kappa h$, and the expression (10.18) approximated by

$$\frac{1}{V_z}\frac{dV_z}{dz} \sim \frac{1}{h} - \frac{1}{2H_o}. \tag{10.19}$$

If $h \sim 2H_o$, the vertical velocity amplitude stays constant. If $h \gg H_o$, then the vertical velocity amplitude decreases. This explains why low degree modes are the most affected in the top graph of Figure 10.6 for a model with $h \to \infty$. For a thin layer with $h \ll H_o$,

the vertical velocity amplitude increases on the spatial scale of the layer and is slightly decreased by the effect of the density stratification in the layer.

The pressure or density scale-height in the isothermal layer is increased by the presence of the magnetic field, which adds support to the plasma through the finite plasma β (see Equations (5.10)-(5.11)), *viz.*

$$H_o = \frac{c_c^2}{\gamma g}\left(1 + \frac{\gamma}{2\beta}\right). \tag{10.20}$$

Hence, through the background equilibrium the magnetic field helps to increase the vertical gradient of the vertical velocity. As regards Equation (10.10), this globally illustrates a rather complex dependence of $\Delta_\perp/\Delta$ on β, which may be avoided for large plasma β.

3. The Lamb cut-off and the peaks in the shifts for modes around it

Turning now to the numerical results in the case of parallel propagation (with $k_y = 0$), one can see that shifts from any given p-mode ridge of order n occur close to the Lamb cut-off frequency; the shifts are larger where $\omega_n \approx Lc_c/R_\odot$ or $L \approx gR_\odot\Omega_n^2/c_c^2$, *i.e.* for l close to

$$\frac{gR_\odot}{c_c^2}\left(1 + \frac{2n}{m}\right) \approx 3.8\left(1 + \frac{2n}{m}\right). \tag{10.21}$$

Shifts in the ridge of a given p-mode become negligible for degrees higher than this value. This can be seen in Figure 10.6, where each p-mode of radial order n shows a peak in frequency shift, starting from $n = 1$ at low frequency. Note also that the degrees of the modes affected increase linearly with radial order n. Thus the graphs of $\Delta\nu$ plotted as a function of l will be similar to these graphs.

For the most evolved model including a polytropic region below the layer, the shifts are shown for individual modes in radial order n as function of degree l in Figures 10.7 and 10.8, with the last two graphs summing them all. In these figures, the results for a shallow field model are also presented. In the region of evanescence for a ridge of a given p-mode, a peak in the shifts is present around the Lamb cut-off, as it was detected for simple models. For degrees higher than this peak-value, the shifts have the same evanescent behaviour. These last peaks in the shifts of successive p-modes mark the

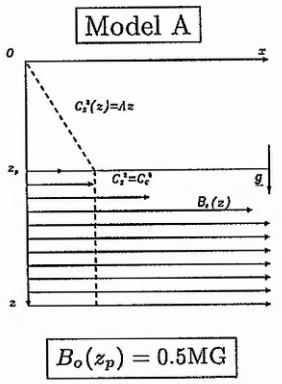

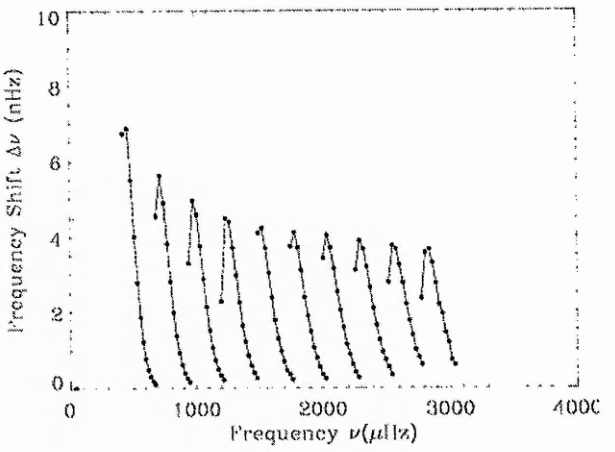

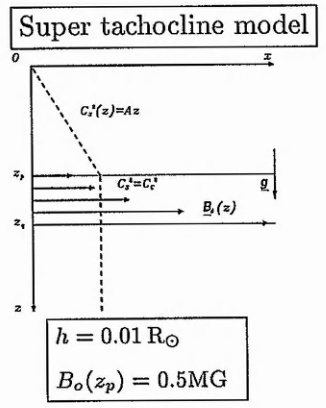

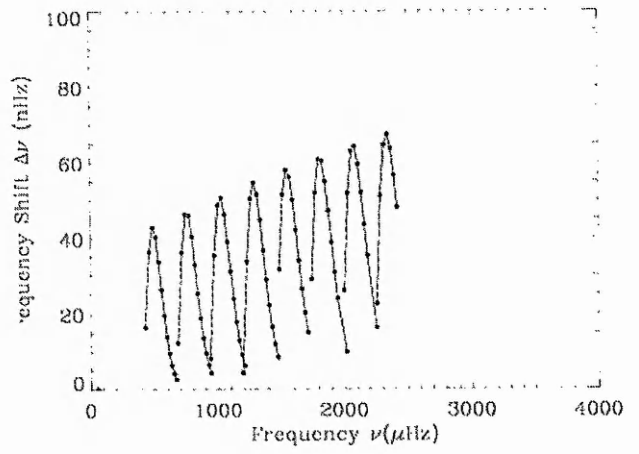

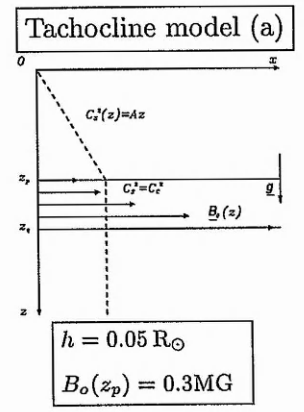

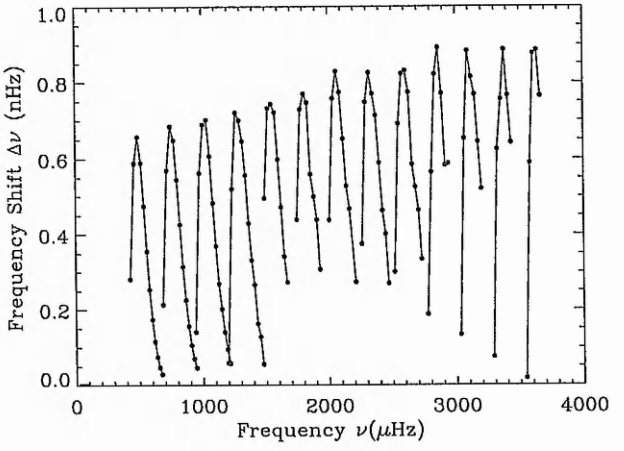

Figure 10.6: Frequency shifts $\Delta\nu$ versus frequency ν, for the magnetic models shown respectively on the left of each graph.

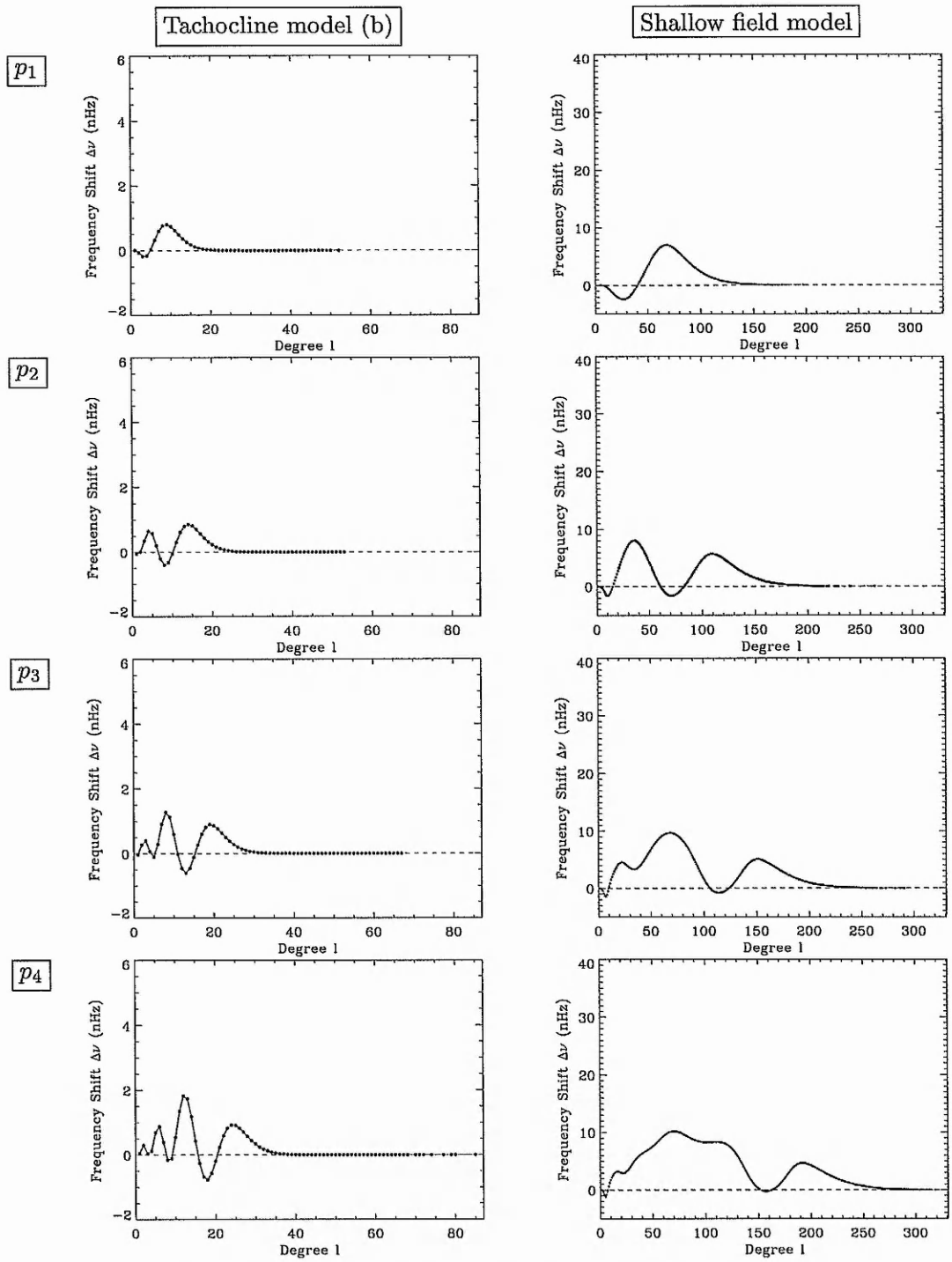

Figure 10.7: The difference $\Delta\nu$ in cyclic frequency between $\nu_{nl}(max)$ obtained with a magnetic slab and $\nu_{nl}(min)$ in the absence of a magnetic field, as a function of degree l, for (*left*) the tachocline model (b) and (*right*) the shallow field model; rows (*1*) to (*4*) are respectively for p-modes of radial orders $n = 1$ to $n = 4$.

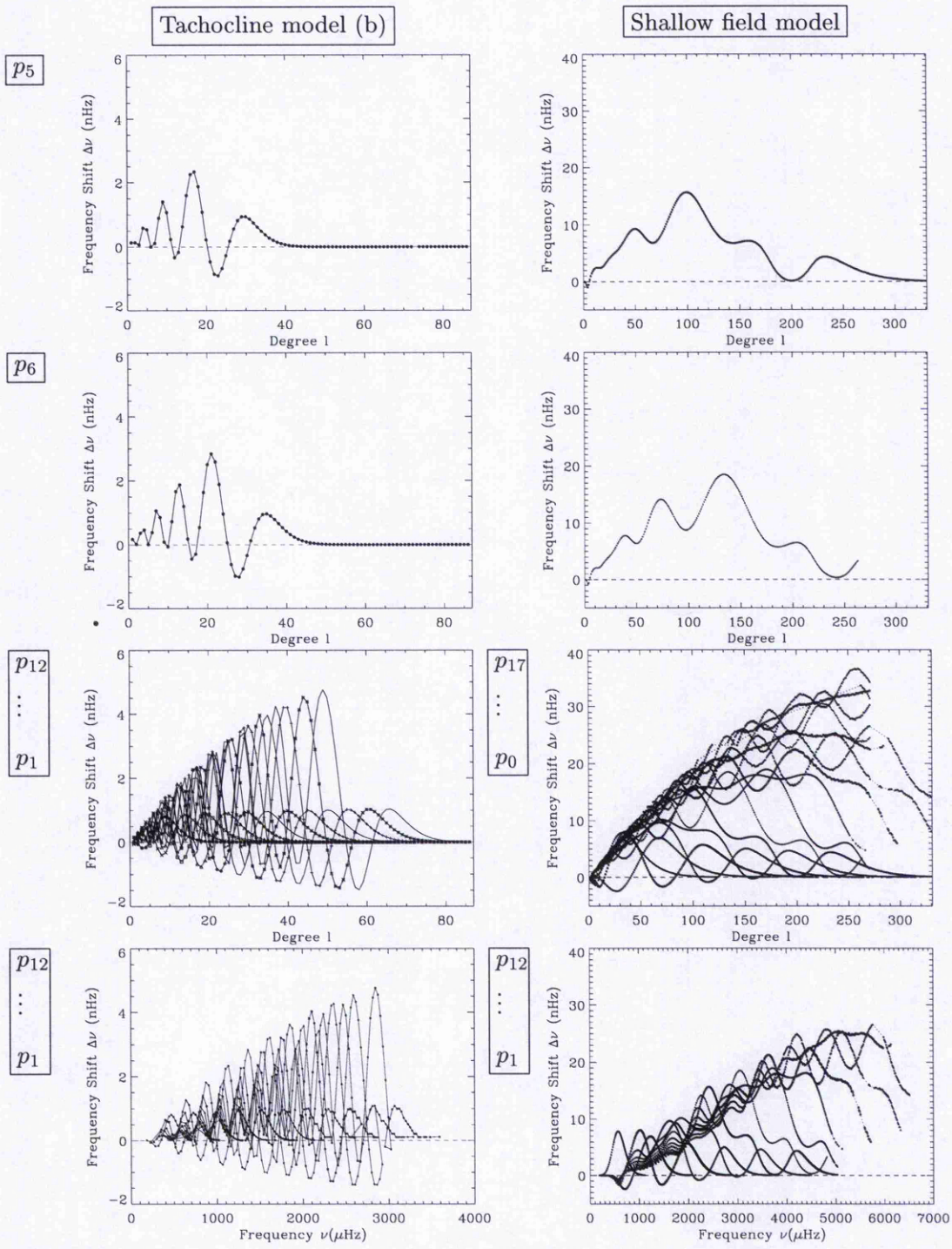

Figure 10.8: As in Figure 10.7, the difference $\Delta\nu$ as a function of degree l for p-modes of radial orders $n = 5$ and $n = 6$, and for all p-modes with $n = 1, 2, \ldots, 12$ for the tachocline model or from $n = 0$ to $n = 17$ for the shallow field model; also shown is $\Delta\nu$ as a function of base frequency $\nu = \nu_{nl}(min)$ for all p-modes of radial orders $n = 1$ to $n = 12$.

separation between oscillatory and evanescent behaviour of the p-mode inside the layer. Because of the polytropic stratification below the layer, as opposed to an isothermal region, the oscillatory solutions are allowed above the Lamb cut-off and there exist shifts for these solutions that could not be seen otherwise.

In the case of parallel propagation, $k_y = 0$, Equation (10.10) obtained in the long wavelength approximation (10.19) is

$$\frac{\Delta_\perp}{\Delta} = \frac{1}{\Delta}\frac{dV_z}{dz} = \left(1 - \frac{k_x^2 c_c^2}{\omega^2}\right)\left(1 - \frac{1}{1 + \frac{\omega^2}{k_x^2}(\frac{1}{hg} - \frac{1}{2H_o g})}\right) . \qquad (10.22)$$

The effect of the modified background equilibrium is balanced by the thickness of the layer (see Equation (10.19)). For a relatively thin layer or a relatively weak magnetic field, the geometry is dominant, and so $\Delta_\perp/\Delta$ does not depend much on β but depends rather on h: the thinner the layer is, the larger the effect. This is why for the tachocline model, which has $h \ll H_o$, one obtains a change in frequency inversely proportional to β. On the other hand, for a relatively intense magnetic field or a relatively thick layer, the wave is more affected by the modified background equilibrium in the presence of the magnetic field than by the geometry (as long as $h \gg H_o$). This concerns in particular the tachocline model A, with $h \to \infty$, and also the shallow field model, which, despite a plasma β almost as large as in the tachocline model, marks its difference by having $h \gg H_o$. Then the effect of $\Delta_\perp/\Delta$ is the largest for modes with $\Omega^2 \sim 2k_x H_o$. The modes with $\Omega^2 \sim 2k_x H_o$ have phase speeds slightly above the sound speed c_c in the oscillatory domain; in a normalised diagnostic diagram they are represented by a line very similar to the fundamental cut-off frequency reported as dash-dotted line(s) in Figure 6.4 of Section 6.2. The intersection between this line and the p-mode ridges is indeed another privileged location for the shifts. In Figure 10.7 for p_2 and p_3 in the shallow field model, this location is identified as corresponding to the highest peak in the shifts.

The sign of $\Delta_\perp/\Delta$ depends also whether $\omega^2 > k_x^2 c_c^2$ or $\omega^2 < k_x^2 c_c^2$. When the right-hand side of Equation (10.22) is small, the mode has no variation in the vertical direction. This occurs if $h \sim 2H_o$ or for frequencies around the Lamb mode ($\omega^2 \approx k_x^2 c_c^2$) as in the case of no gravity. The effect for low-degree modes ($k_x = 0$) at fixed frequency,

or for high-frequency modes ($\omega \to \infty$) at fixed degree, would also be the same with a characteristic fast magnetosonic speed.

Returning to Equation (10.22) that was obtained with the long wavelength approximation ($\kappa h << 1$), *viz.*

$$\frac{\Delta_\perp}{\Delta} \sim \left(1 - \frac{k_x^2 c_c^2}{\omega^2}\right)\left[1 - \frac{1}{1 + \frac{\omega^2}{k_x^2}\left(\frac{1}{gh} - \frac{\gamma}{2c_c^2}\frac{1}{1+\frac{\gamma}{2\beta}}\right)}\right], \tag{10.23}$$

it is possible to reduce the expression, when β is large and $\frac{h}{z_p} \lesssim 1$ (*i.e.* $gh \lesssim c_c^2$), in two cases: for $\frac{\omega}{k_x} \ll \sqrt{gh}$ and for $\frac{\omega}{k_x} \gg c_c$.

For high-degree and/or low-frequency modes ($\frac{\omega}{k_x} \ll \sqrt{gh}$),

$$\begin{aligned}
\frac{\Delta_\perp}{\Delta} &\sim \left(1 - \frac{k_x^2 c_c^2}{\omega^2}\right)\frac{1}{gh}\frac{\omega^2}{k_x^2}\left[1 - \frac{\gamma gh}{2c_c^2}\left(1 - \frac{\gamma}{2\beta}\right)\right] \\
&\sim \frac{1}{gh}\frac{\omega^2}{k_x^2}\left[1 - \frac{h}{z_p}\left(\frac{m+1}{2}\right)\left(1 - \frac{\gamma}{2\beta}\right)\right] - \frac{1}{m}\frac{z_p}{h}\left[1 - \frac{\gamma}{2}\left(1 - \frac{\gamma}{2\beta}\right)\right] \qquad (10.24) \\
&\sim -\frac{1}{m}\frac{z_p}{h} + \frac{1}{gh}\frac{\omega^2}{k_x^2} \qquad \text{for } \frac{h}{z_p} \ll 1\,. \qquad (10.25)
\end{aligned}$$

For low-degree and/or high-frequency modes ($\frac{k_x}{\omega} \ll \frac{1}{c_c}$), *viz.*

$$\begin{aligned}
\frac{\Delta_\perp}{\Delta} &\sim 1 - \frac{1}{\left[\frac{1}{m}\frac{z_p}{h} - \frac{\gamma}{2}(1 - \frac{\gamma}{2\beta})\right]}\frac{c_c^2 k_x^2}{\omega^2} \qquad (10.26) \\
&\sim 1 - m\frac{h}{z_p}\frac{k_x^2 c_c^2}{\omega^2} \qquad \text{for } \frac{h}{z_p} \ll 1\,. \qquad (10.27)
\end{aligned}$$

In both cases, one can see that the effect depends now on the thickness of the magnetic layer as seen from the surface. For a model with $\frac{h}{z_p} \ll 1$, the effect is slightly down-shifted for modes of low-degree and/or high-frequency (Equation(10.27)) while it is mainly negative for high-degree and/or low-frequency modes (Equation(10.25)). As the thickness of the layer increases, the effect might even become negative for low-degree and/or high-frequency modes while it becomes null for high-degree and/or low-frequency modes.

These analytical properties can be observed in Figures 10.7 and 10.8 in the negative extrema of the oscillatory pattern of the shifts versus degree. Considering all p-modes, the negative trends are reversed passing from the tachocline to the shallow field model. In the results for the shallow field model, the shifts dip negatively at low-degree and fall to zero as the degree increases.

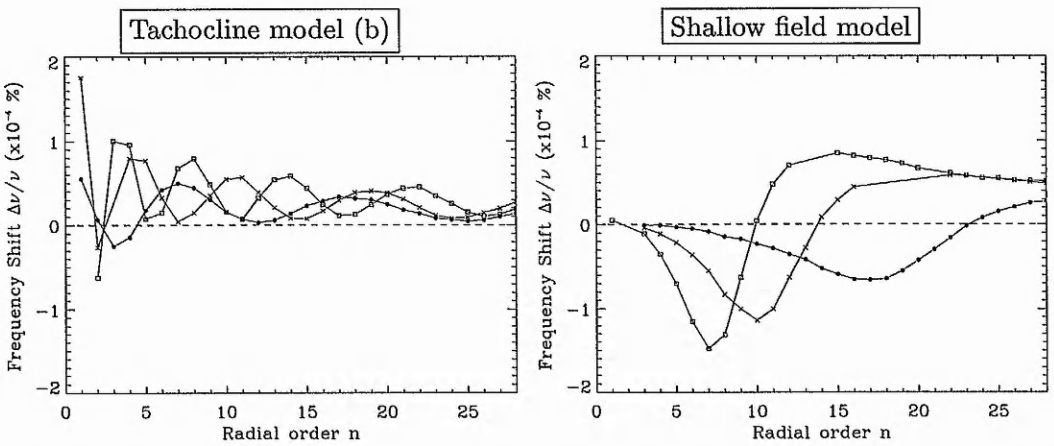

Figure 10.9: Fractional percentage frequency shifts versus radial order n, with lines joining shifts from modes of same degree l, for $l = 1$ (filled circles), $l = 2$ (crosses) and $l = 3$ (open squares); (*left*) is for the tachocline model (b) and (*right*) is for the shallow field model.

Considering the individual ridges of very low degree l, increasing in radial order n as the frequency increases, the above analytical descriptions in terms of frequency rather than degree is also observed in the numerical results. In Figure 10.9, fractional frequency shifts $\Delta\nu/\nu$ are plotted in percentages with respect to the base frequency $\nu(min)$, against the radial order n of the mode. At low radial order n, the negative dips are consistent with Equation (10.25) and the difference of amplitude between the two models is explained by the difference in the ratio $\frac{z_p}{h}$. As the radial order increases, the shifts become positive, again consistent with the approximate result (10.27).

Finally, in Figures 10.7 and 10.8 the global appearance of the shifts differ between the two models. As opposed to the tachocline model, in place where the shifts may become negative, the shifts wind less sharply down and are mainly positive for the shallow field model. On the other hand, looking at expressions (10.24) and (10.26), these effects can be explained by the density stratification, which balances the effect of the thickness of the layer.

Remark: g-modes Contrary to p-modes, parallel propagation of g-modes is expected to yield the largest effect, because of their oscillatory domain confined at large wavenumbers between the Alfvén and the cusp frequencies. Figure 10.10 shows the numerically determined frequency shifts in g-modes, obtained for propagation parallel to the field lines of a shallow magnetic layer. The modes with the largest frequencies, as the radial order n decreases, are the most affected.

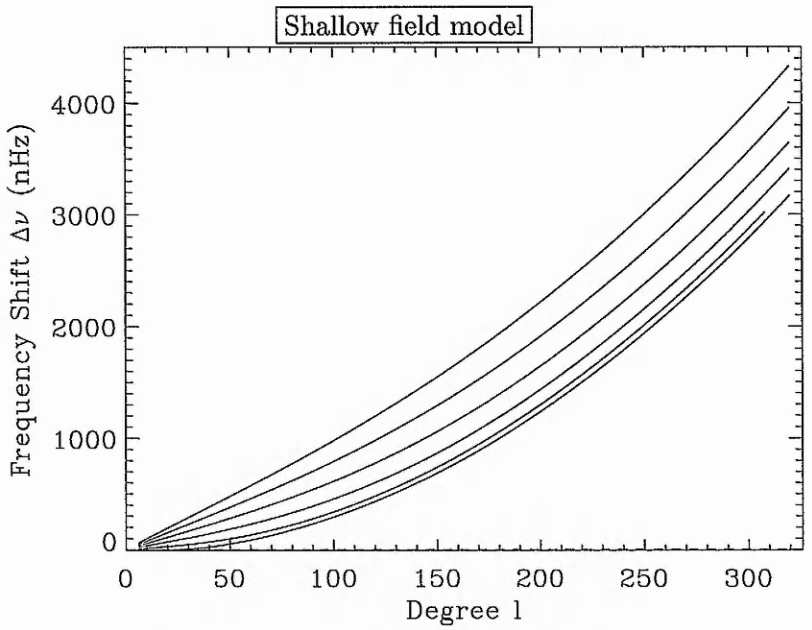

Figure 10.10: Frequency shifts for g-modes propagating parallel to a shallow field. The shifts decrease with radial order from $n = 1$ (upper curve) to $n = 6$ (lower curve).

10.3 Interpretations and inferences

1. Discussion on the choice of parameters

By showing the dependence of frequency shifts with the magnetic field strength, authors face two possibilities for discussion: either they speculate which field strength at the base of the convection zone is required to provide an observable effect or reproduce the amplitude of the observed frequency shifts (*e.g.*, Roberts and Campbell, 1986; Vorontsov, 1988; Dziembowski and Goode, 1989; 1991), or they conclude that the effect of the magnetic field for realistic conditions at the base of the convection zone is negligible as compared to observations (*e.g.*, Bogdan and Zweibel, 1985; Zweibel and Bogdan, 1986; Vorontsov, 1988; Paternó, 1990; Foullon and Roberts, 2000). The interests in the solar physics community are varied. Two major interests may be distinguished regarding the frequency shifts. One is to interpret the frequency shifts observed over the solar cycle (Roberts and Campbell, 1986; Vorontsov, 1988; Foullon and Roberts, 2000). The other is to interpret the variations between the standard solar model and helioseismic inversions for the sound speed profile (Paternó, 1990; Eff-Darwich and Korzennik, 2000), in particular the conspicuous peak near the base of the convection zone (see Figure 1.5 in Section 1.3).

Bogdan and Zweibel (1985) referred to the field strength 10^5G from the lithium argument by Parker (1984a, b) to conclude to the negligible effect of magnetism from bundles at the base of the convection zone (they took the value of pressure at the base of the convection zone $p_o(z_p) \approx 6.6 \times 10^{13}\mathrm{dyn\,cm^{-2}}$ from the standard model of Spruit (1974), yielding $\beta \gtrsim 16667$). Early considerations of the shifts in ν_{nl} on the basis of an evolving magnetic field considered to reside at the base of the convection zone suggested a field strength larger than 1 MG (Roberts and Campbell, 1986; Vorontsov, 1988). Roberts and Campbell (1986), Gough and Thompson (1988) and Paternó (1990) concluded that magnetic fields with strength significantly below 10^6G located near the base of the convection zone have no observable influence on p-modes.

The WKB analytical approximation of Roberts and Campbell (1986) is for low-degree modes propagating parallel to an horizontal magnetic layer and with horizontal

phase speed $\omega/k_x \gg v_A$ (see also Campbell, 1987). By comparing their approximate theoretical frequency shifts with the observations of Woodard and Noyes (1985), Roberts and Campbell (1986) estimated that the peak field strength at solar maximum has to be at least $\sim 5 \times 10^5$G, and increased this minimum value to $\sim 2 \times 10^6$G to account for when the magnetic field is confined to a layer of thickness $\sim 10^5$ km.

This analytical approximation was tested numerically by Campbell (1987), who considered the effect of a semi-infinite magnetic region below the base of the convection zone, similar to model A (see the top of Figure 10.6). Campbell took the isothermal sound speed to be $c_c = 200\,\mathrm{km\,s^{-1}}$, yielding $z_p \approx 0.31\,\mathrm{R}_\odot$. With a gas density $\rho = 0.2\,\mathrm{g\,cm^{-3}}$ (from Spruit, 1974) and a field strength $B_o(z_p) = 0.1$ MG, the Alfvén speed was $v_A = 0.63\,\mathrm{km\,s^{-1}}$, yielding $\beta \approx 100781$. In comparing this model with a field-free one, Campbell obtains numerically a peak in shifts for p_1, the p-mode of radial order $n = 1$, of order 0.15 nHz. Note that he proves the dependence of the shifts on magnetic field strength, as discussed previously, in yielding the peak in shift at the value 15 nHz, by taking $B_o(z_p) = 1$ MG instead. For a field of strength $B_o(z_p) = 0.5$ MG, Campbell would obtain numerically $25 \times 0.15 = 3.75$ nHz, much smaller than the shift value of $0.42\,\mu$Hz predicted by Roberts and Campbell (1986). This inconsistency between the analytical prediction and the numerics could be due to analytical inaccuracies generated in approximations made by Roberts and Campbell (1986).

For $B_o(z_p) = 0.5$ MG, Campbell's numerical results of Campbell (1987) are of the same order as presented here for a similar model, as can be seen in the top graph of Figure 10.6, showing shifts no larger than 7 nHz for p_1. The peak shift of order $n = 1$ has to be compared with the 3.75 nHz-value that Campbell would obtain with a plasma $\beta \approx 100530/25 \approx 4021$. The small difference in the value of the shifts no doubt relates to small difference in the choice of parameters: for the model presented here, the isothermal sound speed is $c_c = 223\,\mathrm{km\,s^{-1}}$, yielding the depth of the base of the convection zone at $z_p \approx 0.39\,\mathrm{R}_\odot$, and the gas pressure is different, yielding a plasma $\beta \approx 4405$. The ratios between the reciprocal $1/\beta$ ($\approx .91$) is different from the ratio between the shifts (≈ 1.87) by a factor of about 2, which accounts almost certainly for the difference in the depth of the base of the convection zone z_p.

This last factor has a non-negligible effect on the frequency shifts, but does not have a straight-forward proportional dependence. This is illustrated by the analytical approximation obtained in the next Section, derived for a more evolved three-layer model. However, as was pointed out already (*cf.* p.159), z_p appears in the dispersion relation through the wavenumber combination $k_x z_p$ and in the ratio $\frac{h}{z_p}$. The roots obtained numerically are the normalised eigenfrequencies $\Omega^2 = \frac{\omega^2}{gk_x}$, and g is not directly specified in the dispersion relation. Without changing the value of the sound speed at the base of the convection zone, *viz.* $c_c = \frac{gz_p}{m} = 223\,\mathrm{km\,s^{-1}}$, nor the ratio $\frac{h}{z_p} \sim 0.125$, it is therefore possible to obtain results for a new model just by scaling the numerical results through a change in g, where z_p and h are scaled accordingly. If α is the scaling factor between two different values for the gravitational acceleration, denoted by the subscripts 1 and 2, *viz.* $(g)_2 = \alpha(g)_1$, then the conditions that

$$(gz_p)_2 = (gz_p)_1 = [\alpha(g)_1]\left[\frac{(z_p)_1}{\alpha}\right], \qquad (k_x z_p)_2 = (k_x z_p)_1 = [\alpha(k_x)_1]\left[\frac{(z_p)_1}{\alpha}\right] \quad (10.28)$$

lead to

$$\begin{aligned}
(\Delta\omega)_2 &= \left(\sqrt{\Omega^2(max)gk_x} - \sqrt{\Omega^2(min)gk_x}\right)_2 , \\
&= \left(\sqrt{gk_x}\right)_2 \left(\sqrt{\Omega^2(max)} - \sqrt{\Omega^2(min)}\right)_2 , \\
&= \alpha\left(\sqrt{gk_x}\right)_1 \left(\sqrt{\Omega^2(max)} - \sqrt{\Omega^2(min)}\right)_2 , \\
&= \alpha(\Delta\omega)_1 . \qquad (10.29)
\end{aligned}$$

If $g = 530\,\mathrm{m\,s^{-2}}$ (Basu et al., 1994, p.214), the scale factor is almost two ($\alpha \sim 1.934$); $z_p \sim 0.202\,\mathrm{R}_\odot$ and $h \sim 0.026\,\mathrm{R}_\odot$. The resulting shifts are shown in Figure 10.11. By comparing with the results of Figure 10.8, one can see that, although the layer is almost half as wide, the change in g from $274\,\mathrm{m\,s^{-2}}$ to $530\,\mathrm{m\,s^{-2}}$ produces shifts that are almost twice as large, and the change in z_p from $0.391\,\mathrm{R}_\odot$ to $0.202\,\mathrm{R}_\odot$ extends the shifts from a range of degree $l = 0$ to $l = 70$, doubled to $l = 140$. This shows the importance of the choice of constant gravitational acceleration g on the dimensional results, which confirms early comments in Section 3.1 on the practical but inappropriate assumption of constant g in a problem embodying the convection zone. This also points to the need to consider a geometry treatment with gradients in the gravitational acceleration.

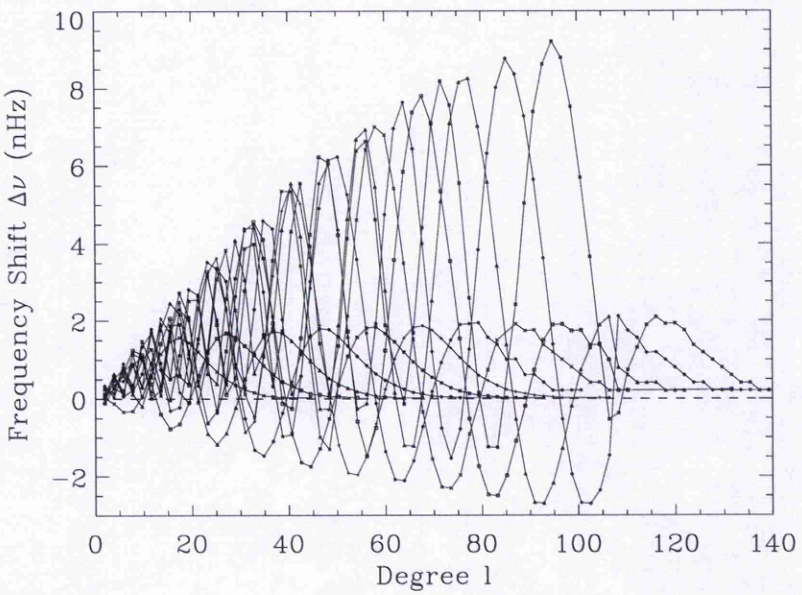

Figure 10.11: Frequency shifts for p-modes propagating parallel to the magnetic field lines of the tachocline model (with $B_o(z_p) = 0.3$MG), but with $g = 530\,\mathrm{m\,s^{-2}}$, $h \sim 0.026\,\mathrm{R}_\odot$ and $z_p \sim 0.202\,\mathrm{R}_\odot$.

The shifts resulting from considering modes propagating parallel to a semi-infinite isothermal magnetic region are the largest at low degree. By confining the magnetic field to a slab, the trend is reversed (see Figures 10.6 and 10.7-10.8). The shifts increase with frequency or degree. If the trend of the absolute frequency shifts is reversed when the magnetic field is confined to a layer, this is however not true for the relative shifts, which still decrease. The graphs of Figure 10.12 show the same results as in Figure 10.6 for the 'super tachocline model', but shifts are plotted versus degree l, instead of frequency; in the left graph, absolute shifts increase globally with degree l, while in the right graph, relative shifts decrease.

In view of the physical constraints discussed in Section 2.2, the value of magnetic field strength $B_o(z_p) = 0.3$ MG is likely to be a realistic upper value for a magnetic field considered to reside at the base of the convection zone. With a field strength $B_o(z_p) = 0.5$ MG, the middle graph of Figure 10.6 shows that an increase of the magnetic layer thickness from 0 to $0.01\,\mathrm{R}_\odot$ produces frequency shifts not larger than 80 nHz at base frequency 3900 μHz. By reducing the field strength to $B_o(z_p) = 0.3$ MG, one can expect a frequency shift of the order 29 nHz. Therefore, one must conclude that

an increase of the magnetic layer thickness from 0.01 to $0.05\,R_\odot$ has a negative effect on frequency shifts, which reduce to values not larger than 1 nHz at base frequency 3900 μHz; such shifts are much smaller than actually observed.

But this last result does not include an increasing temperature profile in the radiative zone, such that p-modes may undergo refraction there. In Figure 10.5, and in greater detail in Figures 10.7 - 10.8, this improvement of the model shows that larger shifts can be obtained for frequencies in the oscillatory domain of the mode propagating in the layer up to a value 6 nHz at base frequency 3900 μHz.

Although he investigated almost the same three-layer model, Daniell (1998) proceeded differently and presented the frequency shifts only for two degrees: $l = 30$ 'so as to display modes which penetrate to the depth of the magnetic layer and below', and $l = 100$ 'for modes being confined much closer to the surface'. Including a base frequency determined for a field of strength $B_o(min) = 10^5$G, he considered shifts to this frequency due to an increase of field strength to $B_o(max) = 3 \times 10^5$G (among other values). His results are comparable to those presented here, having $B_o(min) = 0$ instead, although a limited number of data points prevents a detailed comparison. Daniell finds that for $l = 100$, modes of radial order $n \leq 9$ suffer no change in frequency (his Figure 4.4, p.131). This is in agreement with what can be seen in Figure 10.5, where the shifts obtained up to order $n = 12$ would be negligible beyond $l = 80$. Comparison is possible for p-modes of degree $l = 30$ only, and the best can be done for p_6, the p-mode of order $n = 6$, for which Daniell obtains shifts not larger than 3

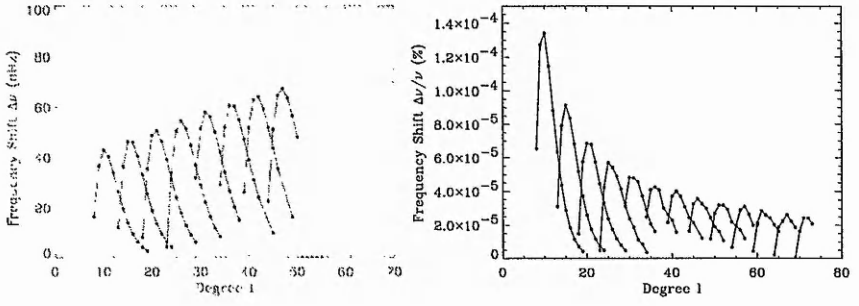

Figure 10.12: The difference in trends between (*left*) absolute and (*right*) relative frequency shifts, plotted versus degree l and for modes propagating parallel to the field lines of the super tachocline model (with $B_o(z_p) = 0.5$MG and $h = 0.01$, *cf.* Figure 10.6).

nHz (his Figure 4.2, p.129). This is in agreement with results for p_6 in Figure 10.8, which show shifts not larger than 3 nHz at degree $l \sim 20$ (instead of 30). Although shifts are not larger than 1 nHz for degree $l = 30$, at least for ridges of order $n \leq 6$, the amplitude of the shifts is recovered. Both treatments adopted the same plasma pressure $p_o(z_p) = 5.25855 \times 10^{12}$ Pa, with reference to the same standard solar model (Guenther et al., 1992), hence the same value of plasma beta $\beta \approx 12236$ for a field strength $B_o(max) = 3 \times 10^5$G. However, Daniell modelled a non-zero surface temperature and, at the base of the convection zone, given by a depth $z_p \approx 0.28\,\mathrm{R}_\odot$, he took an isothermal sound speed of $c_c = 191\,\mathrm{km\,s^{-1}}$, giving $v_A \approx 1.73\,\mathrm{km\,s^{-1}}$. Although this sound speed is lower than expected, the effect of small z_p might be compensated by the effect of non-zero surface temperature, while the non-zero 'base field' introduces effects likely to be negligible in the overall result. Making a tentative comparison of his numerical results with observations, Daniell obtains (p.150) a peak field strength of $3 \times 10^6 - 5 \times 10^6$G.

So far the present research has not changed the main conclusion from Campbell (1987) and Daniell's (1998) investigations that the model is unable to reproduce the observed solar cycle variation in the p-mode frequencies (see, *e.g.*, Daniell, 1998, p.151). Invoking the necessity to prove the numerical results, and thus hopefully to suggest more possibilities to pursue further work in the future, the most important novelty and argument of this thesis comes in the next section. Indeed, it will be shown that the dispersion relation is amenable to an analytical approximation — contrary to what Daniell thought (p.132) — and that this analytical approximation confirms the magnitude of the numerical results for all degrees — as opposed to the analytical approximation derived by Roberts and Campbell (1986), which holds for low-degree modes only.

2. Analytical approximation

The analytical approximation to the dispersion relation derived below will prove to be useful as an insight into the numerical results. In addition, the approximated shifts turn out to have properties that reproduce the main shape of the oscillatory pattern in the shifts obtained numerically. This property of the approximation offers encouragement to deduce analytically shifts for modes with perpendicular propagation.

Consider first the hydrodynamical effect of a thin isothermal layer. The dispersion relation (7.23) is simplified for a field-free ($\beta \to \infty$) isothermal slab (see Equation (8.9)) to

$$\epsilon_p^- \epsilon_q^+ e^{2\kappa h} - \epsilon_p^+ \epsilon_q^- = 0\,, \tag{10.30}$$

where

$$\epsilon_p^\pm = \left(k_h + \Lambda_i^\pm\right) M - 2k_h M'\,, \qquad \epsilon_q^\pm = \left(k_h + \Lambda_i^\pm\right) U - 2k_h U'\,; \tag{10.31}$$

κ is real for surface modes and imaginary for oscillatory modes in the layer. Two first order approximations are applied.

First, the isothermal layer of thickness $h = z_q - z_p$ is considered to be thin so that $\frac{h}{z_p} << 1$. Then the exponential term $e^{2\kappa h} \approx 1 + 2\kappa h$, and the dispersion relation can be expanded

$$D \approx D_o + \frac{h}{z_p} D_1\,, \tag{10.32}$$

where D_o corresponds to the dispersion relation for a model without the layer (*i.e.*, a simple polytrope) and D_1 is the first order correction to that dispersion relation in the presence of an isothermal layer of thickness h.

The eigenfrequency ω is the result of the effect of this thin layer on the original eigenfrequency ω_o, so that $\omega = \omega_o + \Delta\omega$. The second analytical approximation comes from assuming *a priori* that the frequency change is small, so that $\Delta\omega \ll \omega$, a result found numerically. Then, a first order Taylor expansion can be applied to the D_o term around the base frequency ω_o, *viz.*

$$D_o(\omega) \approx D_o(\omega_o) + D_o'(\omega_o)\Delta\omega\,. \tag{10.33}$$

Since $D(\omega) = 0$ and $D_o(\omega_o) = 0$, Equations (10.32) and (10.33) combine to give the analytical approximation to the frequency shift, *viz.*

$$\Delta\omega \approx -\frac{h}{z_p}\frac{D_1(\omega)}{D_o'(\omega_o)} \approx -\frac{h}{z_p}\frac{D_1(\omega_o)}{D_o'(\omega_o)}\,, \tag{10.34}$$

which appears directly proportional to the thickness h of the layer.

From

$$D(\omega) = \frac{\epsilon_p^- \epsilon_q^+ e^{2\kappa h} - \epsilon_p^+ \epsilon_q^-}{4k_h\kappa} = 0\,, \tag{10.35}$$

the terms D_o and D_1 are

$$D_o = \frac{\epsilon_p^- \epsilon_q^+ - \epsilon_p^+ \epsilon_q^-}{4k_h\kappa}\,, \qquad D_1 = z_p\frac{\epsilon_p^- \epsilon_q^+}{2k_h}\,. \tag{10.36}$$

Developing D_o yields

$$\begin{aligned} D_o &= MU' - UM' && (10.37)\\ &= W[M,U] && (10.38)\\ &= -\frac{\Gamma(m+2)}{\Gamma(-\Upsilon)}\frac{e^{2k_h z_p}}{(2k_h z_p)^{m+2}}\,, && (10.39) \end{aligned}$$

where $\Upsilon = [m\Omega^2 - (m+2)]/2$. When taking the first derivative of D_o with respect to ω, only the term in Υ is variable. Writing $u = -\Upsilon$, it is necessary to consider

$$\begin{aligned} \frac{\partial\frac{1}{\Gamma(u)}}{\partial u} &= -\frac{\Gamma'(u)}{(\Gamma(u))^2} && (10.40)\\ &= -\frac{\Psi(u)}{\Gamma(u)}\,. && (10.41) \end{aligned}$$

This derivative must be estimated around $u \approx 1 - n$, where n is a non-zero and positive integer. For such points, the functions Ψ and Γ are two poles (see definitions in Appendix A.1). The problem is solved by applying the reflection formulae (A.7) and (A.9), so that

$$\lim_{u\to 1-n}\frac{\partial\frac{1}{\Gamma(u)}}{\partial u} = (-1)^{n-1}(n-1)!\,. \tag{10.42}$$

This finally gives the derivative of D_o with respect to ω evaluated at ω_o,

$$D_o'(\omega_o) = \frac{m\Omega_o^2}{\omega_o}(-1)^{n-1}(n-1)!\Gamma(m+2)\frac{e^{2k_h z_p}}{(2k_h z_p)^{m+2}}\,. \tag{10.43}$$

In $D_1(\omega_o)$, the confluent hypergeometric functions can be simplified in terms of generalised Laguerre polynomials.

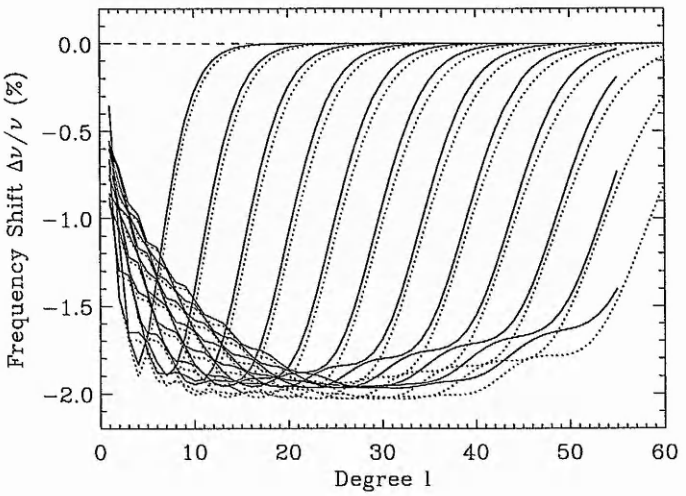

Figure 10.13: Percentages of fractional frequency shifts versus degree l, due to the effect of a buried layer below the convection zone. Numerical and analytical results are shown respectively in bold and dotted lines, joining shifts of the same radial order n, from $n = 1$ (confined to low l) to $n = 12$ (seen at higher l).

After some algebra, the fractional frequency shift is determined as

$$\frac{\Delta\nu}{\nu} = -\frac{h}{k_h} \cdot \frac{(2k_h z_p)^{m+2}}{e^{2k_h z_p}} \cdot \frac{Re(\Pi)(L_1)^2(n-1)!}{2m(1+\frac{2n}{m})\Gamma(n+m+1)}, \tag{10.44}$$

where

$$\Pi = \left[\left(1+2\frac{L_2}{L_1}\right)k_h - \frac{1}{2H_o} - \kappa\right]\left[\left(1+2\frac{L_2}{L_1}\right)k_h - \frac{1}{2H_o} + \kappa\right] \tag{10.45}$$

and L_1, L_2 are generalised Laguerre polynomials

$$L_1 = L_{n-1}^{m+1}(2k_h z_p)\,, \qquad L_2 = L_{n-2}^{m+2}(2k_h z_p)\,. \tag{10.46}$$

These polynomials and Equation (10.44) were evaluated with the mathematical software *Mathematica*. As shown in Figure 10.13, the analytical approximation to account for the presence of a thin isothermal field-free layer in a polytrope ($h = 0.05\,\mathrm{R}_\odot$ and $z_p \approx 0.39\,\mathrm{R}_\odot$) confirms the shape and the magnitude of the shifts obtained numerically.

In reality, these numerical results contain tiny shifts, not discernible on the graph, due only to the presence of a magnetic field ($\beta \approx 12236$ for $B_o(z_p) = 0.3$ MG). These are difficult to determine analytically. Yet, by replacing the layer terms H_o and κ by their magnetic counterparts (*cf.* Table 5.1, p.103) in the product Π of the analytical approximation, one obtains an approximation to the shifts between the model including

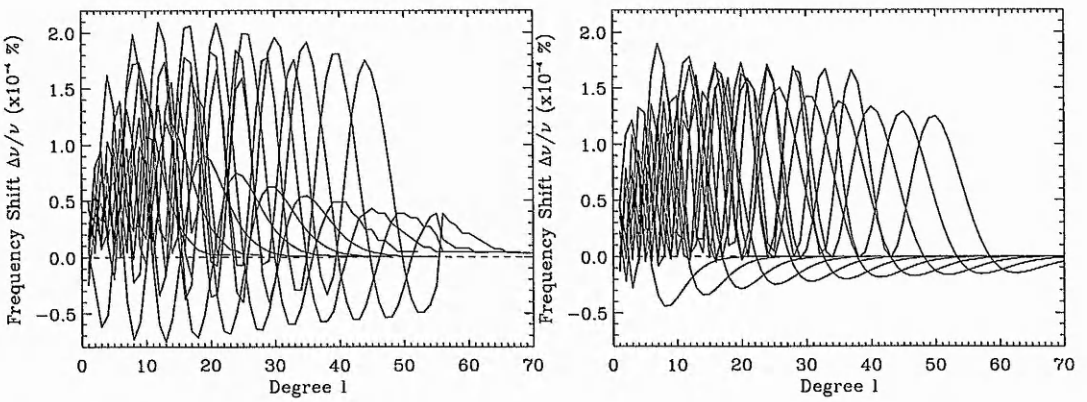

Figure 10.14: Percentages of fractional frequency shifts versus degree l, due to the sole effect of a magnetic field in a buried layer below the convection zone ($B_o(z_p) = 0.3$ MG), for parallel propagation: *(left)* numerical and *(right)* analytical results are shown by lines joining shifts of the same radial order n, from $n = 1$ to $n = 11$ (seen at higher l).

the magnetic layer and the simple polytrope. Subtracting from them the analytical shifts due to the field-free layer, one can even find the magnitude of these tiny shifts, as shown in Figure 10.14 for parallel propagation (Foullon, 2001).

The sole effect of a magnetic field on central p-mode frequencies is to 'encourage' higher harmonics, just as a register hole in a flute. For realistic parameters in the solar interior, this effect is negligible for parallel propagation: $\Delta\nu/\nu \sim 2 \times 10^{-4}\%$ for the tachocline model, which includes a buried layer of thickness $h = 0.05\,\mathrm{R}_\odot$, with maximum field strength $B_o(z_p) = 0.3$ MG; $\Delta\nu/\nu \sim 10^{-3}\%$ for a shallow layer of same thickness at $z_p \approx 0.05\,\mathrm{R}_\odot$ for $B_o(z_p) = 30$ kG (with $\beta \approx 12176$). These shifts are to be compared with the observations, $\Delta\nu/\nu \sim 2 \times 10^{-2}\%$ over a solar cycle.

Moreover, for the tachocline model, the relative effect on p-mode frequencies of a buried magnetic layer is much larger for waves propagating perpendicular rather than parallel to the magnetic field lines (see Figure 10.15). This result is consistent with the consideration in Section 6.1 of an isothermal waveguide, where the p-mode ridges are affected by the anisotropic nature of the magneto-atmospheric cut-off frequencies.

As the solar cycle rises, the x and y-directions are presumed to flip by 90 degrees — the field lines passing from poloidal to toroidal at the base of the convection zone (see, *e.g.*, Dikpati and Charbonneau, 1999). Thus, instead of searching for an explanation through a variation in field strength, one may also interpret the observed shifts

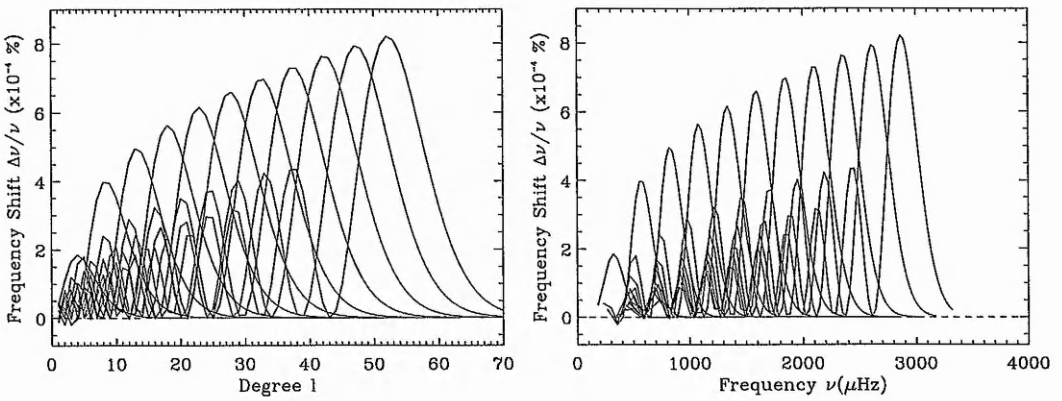

Figure 10.15: Percentages of fractional frequency shifts due to the sole effect of a magnetic field in a buried layer below the convection zone ($B_o(z_p) = 0.3$ MG), for perpendicular propagation ($k_x = 0$), are shown by lines joining shifts of the same radial order n, from $n = 1$ to $n = 11$ (left) versus degree l; and (right) versus base frequency.

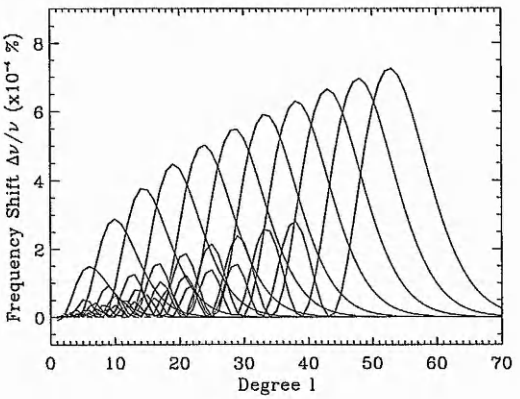

Figure 10.16: Percentages of fractional frequency shifts versus degree l, due to the effect of perpendicular propagation ($k_x = 0$) with respect to parallel propagation ($k_y = 0$), for a magnetic field at the base of the convection zone ($B_o(z_p) = 0.3$ MG), are shown by lines joining shifts of the same radial order n, from $n = 1$ to $n = 11$.

in global frequencies by a change in orientation of the magnetic field lines (Foullon, 2002). At solar maximum, the 'global' waves (*i.e.* as if the Sun were not rotating) propagate perpendicular to a toroidal field; at solar minimum, they propagate parallel to a poloidal one. This change of configuration would produce maximum relative frequency shifts almost as large as the sole effect of the field strength would have on perpendicular propagating waves (see Figure 10.16). These last results lead essentially to the conclusion that at the base of the convection zone the presumed cyclical change of orientation of magnetic field lines has a larger effect on global mode frequencies than an increase in field strength alone. However, the frequency cutoffs and large influence

of the changing atmosphere prevent from comparing these internal effects with observations. An effect as large as $\Delta\nu/\nu \sim 9 \times 10^{-4}\%$ at the peak shift frequency 3900 μHz (see right diagram of Figure 10.15) is still negligible in comparison to the observations, which give $\Delta\nu/\nu \sim 2 \times 10^{-2}\%$ over a solar cycle.

The analytical approximation to the frequency shifts cannot be applied to the shallow field model, for which $h \approx z_p$. It is likely that, as for the tachocline model, shifts for perpendicular propagation would be larger than for parallel propagation. One should then rely on numerical methods to assess whether the sunspot's anchoring zone could contribute efficiently to the global frequency shifts observed over the solar activity cycle. However, more careful modelling would be needed: it would be relevant to include the superadiabatic gradient below the surface, an atmosphere or at least a non-zero sound speed at the surface, which might be more crucial than for the tachocline model.

Still round the corner there may wait
A new road or a secret gate
And though I oft have passed them by,
A day will come at last when I
Shall take the hidden paths that run
West of the Moon, East of the Sun.

John R.R. Tolkien (1892 - 1973)
"The Lord of the Rings" (1954-55), "The Grey Havens"

Part IV

CONCLUSIONS

Chapter 11

Open Questions and Discussions

Daniell (1998) already pointed out that it may take a model utilising more sophisticated physics to study the effects of a buried magnetic layer in the Sun. Any possibility to follow this advice and to make progress by reducing the number of physical restrictions could have led to considering a more complex geometry with variations in the gravity field, a more complex thermal or background flow structure or a more complex magnetic profile in the magnetic layer and/or in its environment. Section 11.1 explores briefly all these directions. But such improvements in the mathematical modelling of the solar interior must be fed by the understanding of the solar context and take into account any physical interpretation (or even intuition) which could be of use at a later stage. These pieces of the solar puzzle are collected in Section 11.2.

11.1 More complex structures

1. Hydrodynamical processes

Thermal structures If one is trying to interpret central frequencies (as opposed to splittings) to infer a magnetic field, one needs to disentangle the effect of magnetism from other effects that can perturb the frequencies. For instance, there might be a source of confusion between the effect of magnetism and the effect of radial stratification at the base of the convection zone, which is in some sense an abrupt transition for the modes. The amplitude of the signal observed in the data is associated with the

discontinuities in the derivatives of the sound speed, used to determine the extent of overshoot (Basu et al., 1994; Basu and Antia, 1994; Monteiro et al., 1994; Christensen-Dalsgaard et al., 1995; Basu, 1997).

More complex thermal structures have been mentioned in Section 9.3. A fourth layer could indeed be added to the three-layer model: a superadiabatic layer below the surface or an atmosphere above the photosphere; a subadiabatic radiative profile below the magnetic slab at the base of the convection zone could also be included. Yet, whatever the nature of changes held responsible for the frequency shifts, these changes must vary over the solar cycle. If temperature changes are the indirect effect of the internal solar dynamics, they can only be deduced in the framework of hydrodynamic or MHD studies. By adding more complexity to the temperature structure of the solar model, eigenfrequencies are likely to be modified.

As regards the modelling of a magnetic field at the base of the convection zone varying with time, embedded in more complex temperature structures, frequency shifts are not likely to be influenced by much. Passing from the tachocline model (a) to the tachocline model (b), *i.e.* with a temperature profile below the magnetic slab passing from isothermal to adiabatic, increased the amplitude of the shifts by a factor of 5 (see the last graph in Figure 10.6 and Figure 10.5 in Section 10.2). Moreover, there is as yet no evidence for changes in the convection zone depth or the extent of overshoot (Basu and Antia, 2000; 2001). The conditions at the surface do not seem to affect the results strongly either. With the simple boundary condition of vanishing Lagrangian pressure perturbation at the surface, the results of Daniell (1998), for a model with non-zero sound speed at $z = 0$, do not differ by very much from those obtained here for a model with zero sound speed (see Section 10.3). Moreover Gough and Thompson (1990, p.27) have confirmed that their numerical results are unchanged when the simpler boundary condition of vanishing Lagrangian pressure perturbation replaces that derived for an isothermal atmosphere.

As regards the modelling of the sunspots' anchoring zone, arguments are stronger for expecting frequency shifts that can explain partly the observed ones. In this case, the superadiabatic layer, an atmosphere or at least a non-zero sound speed at the

surface would be needed for a more thorough investigation.

Yet, independently of a consideration of the effect of a buried layer, a more complex atmosphere, with for instance a non-zero temperature gradient, might play a role in explaining the observed oscillations, in particular the dispersion law discovered by Duvall (1982). As discussed in Section 9.3, further modelling of the Sun with such an atmosphere needs to be explored.

Background flow One could consider vertical and horizontal variations in a background flow. Random vertical and horizontal velocity fields associated with granulation have been studied, in a plane-parallel model of the upper layers of the Sun, for their effects on the f-mode (see, *e.g.*, Murawski and Roberts, 1993a, b; Murawski, 2000). These works argue that the effect of convective flows is to lower the f-mode eigenfrequencies. Also there are indications for solar-cycle changes of the granulation. At the solar maximum, size and flow speed seem somewhat reduced, but this modulation needs further exploration. This might, however, point towards global solar cycle fluctuations in the vertical velocity field associated with convection. The effect of large-scale convection on solar eigenfrequencies was studied by Swisdak (1999), who demonstrates that the effect of convective structures is to lower the p-mode eigenfrequencies (see also Swisdak and Zweibel, 1999). This effect which is approximately proportional to $(V_o/c)^2$, where V_o is the convective velocity and c is the sound speed, can account for the positive discrepancy in sound speed in the outer portion of the convection zone between current solar models and helioseismic observations.

2. Magnetohydrodynamical processes

Critical shear flow Backward propagating surface modes may appear for non-parallel propagation in the presence of a shear flow, when this flow exceeds a critical value, which is of the order of the Alfvén speed (see Joarder and Narayanan, 2000). In theories developed in the atmospheric context such a critical flow is much larger than any flow observed. However, such theories could apply to the region at the base of the convection zone, where flows are likely to be of the order of the Alfvén speed.

Magnetic profile Another more sophisticated model would be to consider a magnetic profile which leads to a non-constant Alfvén speed in the magnetic layer. This suggestion was weighted by L.M.B.C. Campos at the occasion of a 'Workshop on MHD Waves in Astrophysical Plasmas' (INTAS, Mallorca, May 9-11 2001). The underlying reason is to allow interaction of the p-modes with Alfvén oscillations. However, it is likely that resonances of various types (mode coupling, absorption and heating — see, *e.g.*, Tirry, 1998; Vanlommel, 2001), occurring for non-zero k_y in the solar atmosphere, will not take place in realistic buried magnetic structures, because of the large plasma β. This can be seen by examining the diagnostic diagrams presented in Chapter 8, which show that for models with realistic buried magnetic layers, p-mode frequencies lie far above the Alfvén frequency, so that no interaction is likely to take place.

Spherical geometry The spherical geometry of the problem has been ignored in this thesis, although the applicability of plane wave approximation for the spherical geometry of the Sun is not clearly defined. Indeed the approximation of plane wave geometry generates inaccuracies, related to curvature effects and gravity gradients, for modes of low-degree (Christensen-Dalsgaard, 1980); see Chapter 9. One cannot therefore estimate with confidence how low-degree modes are affected by a buried magnetic field in the solar interior until a complementary study in spherical geometry is carried out.

In much the same way that through the 'tokamak expansion' one tries to model a torus by a straight cylinder, one could obtain some condition (on the mode wavelength, for instance) by expanding equations and solutions in the spherical geometry as power series in terms of a curvature parameter, such that the zero-order approximation matches the plane geometry solutions. This will generally be solved with WKB theory (Van der Linden, 2001).

Another possibility is to modify the existing hydrodynamical pulsation code of J. Christensen-Dalsgaard which computes realistic oscillations of stars (Aarhus adiabatic pulsation package[1]), by introducing a magnetic field.

[1]Available from World Wide Web: http://www.obs.aau.dk/~jcd/adipack.n/

In any case, one needs to examine an equilibrium profile in spherical geometry. A toroidal magnetic field at the base of the convection zone may be described in a system of spherical polar coordinates (r, θ, ϕ), with unit vectors $[\mathbf{e_r}, \mathbf{e}_\theta, \mathbf{e}_\phi]$. Denoting equilibrium quantities with the subscript o, the equilibrium field is for instance

$$\mathbf{B_o} = [0, 0, B_o(r, \theta) = a(r) \frac{d}{d\theta} P_k(\cos\theta)] \tag{11.1}$$

where $P_k(\cos\theta)$ is a Legendre polynomial in $\cos\theta$ of degree k, and a is a function of r.

The profile $a(r)$ could be of the form (Gough and Thompson, 1990)

$$a(r) = B_o\left(r_o, \frac{\pi}{2}\right)\left[1 - \frac{(r - r_o)^2}{d^2}\right]^2, \qquad |r - r_o| < d, \tag{11.2}$$

where d is the half-thickness and r_o is the centre position of the magnetic layer; $a(r) = 0$ elsewhere. Or the profile could be chosen so as to be similar to the cartesian model developed in this thesis, *e.g.*,

$$a(r) = B_o\left(r_o, \frac{\pi}{2}\right)\left[\frac{\rho(r)}{\rho(r_o)}\right]^{\frac{1}{2}} = B_o\left(r_o, \frac{\pi}{2}\right) e^{\frac{r_o - r}{2H_o}}, \qquad r_o - h \leq r \leq r_o, \tag{11.3}$$

where H_o is the pressure or density scale-height in an isothermal layer, h is the thickness and r_o is the upper radial position of the magnetic layer; $a(r) = 0$ elsewhere.

Contrary to a horizontal magnetic field in a cartesian model, the toroidal field in spherical geometry carries a tension, which exists when the magnetic field lines are curved. For the equilibrium field, one obtains the Lorentz force

$$\mathbf{j} \times \mathbf{B_o} = -\frac{B_o(r, \theta)}{\mu r^2}\left[\frac{\partial(rB_o)}{\partial r}\mathbf{a_r} + \frac{1}{\sin\theta}\frac{\partial(\sin\theta B_o)}{\partial\theta}\mathbf{a}_\theta\right]. \tag{11.4}$$

This greatly complicates the derivation of equilibrium profiles and the possibility to derive any governing equation is compromised.

To overcome the difficulty of the magnetic equilibrium in spherical geometry, one can probably approximate the effect of the magnetic field on the equilibrium structure, simply by replacing the thermodynamic pressure in the pulsation code with total (hydrostatic and magnetic) pressure. Such techniques appear to have been already developed (Endal et al., 1985; Lydon and Sofia, 1995) and applied as an alternative explanation for the observed frequency shifts in terms of the effect of sub-surface magnetism on p-modes (Lydon et al., 1996).

3. Application to other astrophysical plasmas

Before closing this section, it is worth noting that very similar work to the modelling undertaken here is done, or could be done, for other astrophysical plasmas than the Sun. In particular, p- and g-modes are obtained in polytropic accretion disks (Korycansky and Pringle, 1995) and the effect of an isothermal atmosphere that joins smoothly on to the underlying polytropic layer is explored (Ogilvie and Lubow, 1999). Besides, one can be hopeful that some of the work developed in this thesis could be extended to other solar-like stars, whose oscillations are not yet detected unambiguously, but which may be resolved in the near future by space missions devoted to asteroseismology (see, *e.g.*, Pérez Hernández and Christensen-Dalsgaard, 1998).

11.2 The solar puzzle

1. Correlated surface effects

For a realistic magnetic field at the base of the convection zone, the observed shifts cannot be reproduced, while an explanation must be found through surface effects. This conclusion was also reached by Libbrecht and Woodard (1990), who noted observationally that the frequency increment (considered as a function of frequency ν and degree l) is inversely proportional to the inertia, or mass M, of the modes (M is defined as the ratio of the mode energy to the square of the surface velocity). These properties may be seen in Figures 2.1 and 2.2, reproduced from Howe et al. (1999). Moreover, Woodard et al. (1991) showed that the shifts are correlated with surface magnetic activity, as indicated in magnetogram measurements and in activity latitudes. Because modes of different degree sample the Sun differently with respect to latitude, this implies (assuming the Sun to be axisymmetric) that the cyclic variation is predominantly spherically symmetric (Gough, 1990b).

Not only do the oscillation frequencies vary with the sunspot cycle, but the even component of the degeneracy splitting reported by Libbrecht and Woodard (1990) is consistent with the latitudinal variation of activity determined by limb photometer measurements. The magnitude of the temporal variation in the degeneracy splitting is small compared with the overall frequency shift, confirming the conclusion from the whole-disk data that the structural change is predominantly spherically symmetric. Furthermore, it has recently been suggested that the low-degree shifts are consistent with near surface magnetic flux distributions (Moreno-Insertis and Solanki, 2000) to explain the observed hysteresis shapes seen in the low-degree modes. Only if one could remove contributions due to the near surface perturbations, can one hope to evaluate the independent signals from the solar interior (Dziembowski and Goode, 1997).

2. Vertical mode and low-degree shifts

The $l = 0$ mode penetrates to the core of the Sun and is reflected much higher up in the atmosphere than the other modes. As such it holds a unique position in determining the

structure of the solar interior, and more specifically the core (Gough and Kosovichev, 1993). Based on the idea that low-degree modes propagate deeper in the solar interior than high-degree modes, it was suggested that the effect of a buried magnetic field on the properties of p-modes may be of significance in an explanation of the observed low-degree frequency shifts over the solar activity cycle (Campbell and Roberts, 1986; Roberts and Campbell, 1986).

Observations show a linear dependence between the frequency spectrum and the radial order n, for the mode of degree $l = 0$ (Libbrecht et al., 1990; Elsworth et al., 1994). This is different than for modes with $l \neq 0$, where the dependence is approximately $\propto n^{1/2}$. However, the amplitudes of frequency shifts do not differ greatly between modes of degree $l = 0$ and the other modes of low-degree. From whole-disk data, Elsworth et al. (1990) found that the mean frequencies of oscillation modes of degree $l = 0$, 1 and 2, averaged over the order n of the mode, within the frequency range $2.5 - 3.5$mHz, are each modulated in phase with the sunspot cycle with the same peak-to-peak amplitude (of about $0.46\,\mu$Hz for a shorter period than the solar cycle). Furthermore, despite the slight amplitude differences found in Chaplin et al. (1998), the variations for low-degree modes is quite similar to the ones for high-degree modes (Libbrecht and Woodard, 1990). It is thus likely that the variations of low- and higher-degree modes have a common origin.

The point for which $k_h = 0$ was avoided in the numerical evaluation of the dispersion relations involving the confluent hypergeometric functions (see Appendix A.1). Although the shifts for modes with degree as low as $l = 1$ are not large enough to explain the observed low-degree frequency shifts over the solar activity cycle, one needs additional theoretical arguments to confirm that, for a realistic value of the buried field, modes of degree $l = 0$ are not strongly affected and cannot explain the observations either. In fact, these arguments exist. They are given by theoretical models exploring the case of vertical propagation (Daniell, 1998).

Vertical wave propagation (for $l = 0$) in a plane-parallel polytrope was first investigated by Lamb in 1909, who obtained analytical solutions in terms of Bessel functions. Note however that the mode of degree $l = 0$ in a plane-stratified model of the Sun

cannot propagate further than the centre of the Sun. Jain et al. (1995, 1996) devoted attention to modes with vertical propagation, obtaining solutions in terms of Bessel functions, but considered they could not obtain any quantisation in frequency because of the plane-stratified geometry. With the same equation, but by deriving the dispersion relation for a simple polytropic model of the solar interior bounded at the centre of the Sun by a rigid wall and overlaid on the top by a field-free isothermal atmosphere, Daniell (1998) was able to reproduce the quantisation in n and the behaviour of the modes of degree $l = 0$.

Daniell (1998) studied the mode of degree $l = 0$ in a plane-stratified model including more specifically a uniform chromospheric magnetic field and showed that it is non-negligibly affected by the chromospheric layer. An increase in magnetic field strength coupled with a rise in chromospheric temperature reproduces the observed frequency variations in the p-modes of degree $l = 0$ (see his Figure 2.12, p.59). Daniell (1998) solved numerically his dispersion relation with $k_h = 0$ for a model of the buried magnetic field at the base of the convection zone. The frequency shifts he obtains, resulting from an increase in field strength from 1×10^5G to 3×10^5G, are not larger than 4 nHz at peak frequency 3.2 mHz (see his Figure 4.12, p.147). These numerical results of Daniell (1998) imply a surface effect, rather than an effect at depth, as being responsible for the observed frequency shifts.

3. How p-modes are affected by a buried magnetic layer

Starting from theoretical results and considerations which can always be improved, some imagination is required to interpret physically how p-modes are affected. This suggestive vision should of course be taken with care but, at this stage, it may give a basis of understanding worth keeping in mind.

First, the idea that low-degree modes would be the most affected by a buried magnetic layer because they propagate deeper in the solar interior, is misleading. This idea originates on the ground that modes having their turning point in the perturbative layer would be the most affected. In the presence of a magnetic field this would be especially true for modes propagating in the $\mathbf{g} \times \mathbf{B_o}$-direction (Bogdan and Zweibel,

1985; Zweibel and Bogdan, 1986). Modes which do not propagate in that direction are less affected. This holds true for all modes, including the mode of degree $l = 0$.

On the contrary, one can see that higher harmonics or modes of higher degrees are affected by solar magnetic fields. The chromosphere and even the corona is able to influence the properties of solar p-modes by acting on the evanescent tail of the modes. The acoustic oscillations are modulated mainly by changing conditions in a region in which the waves are evanescent, and not by a change in the cavity in which they propagate (Gough, 1990b).

The situation at the lower turning point of the mode is to be compared with the upper turning point at the solar surface. With respect to this refractive or reflective point, what happens at the base of the convection zone is symmetric to what happens in the solar atmosphere. A given mode which propagates in the solar interior, with a cavity depth above the perturbative layer, may still be affected by the presence of the layer, through its evanescent tail sweeping the lower region. The amplitude of the effect does not depend only on *how deep* the mode propagates in the interior or *how high* it is reflected in the atmosphere (in fact, low-degree modes are reflected higher up in the atmosphere than the high-degree modes are). The effect of a horizontal magnetic layer on p-modes depends in *how far* and *how long* a mode propagates in a sub-horizontal direction. At a given frequency, high-degree modes stay longer in a sub-horizontal direction around the lower turning point than modes of lower degree. Indeed, at their cavity depth, they get refracted where the sound travels slowest. As they propagate sub-horizontally in this region, the evanescent tail of high-degree modes is sweeping the bottom of the convection zone with a contrast in time larger than what would be obtained for low-degree modes.

In this sub-horizontal direction, the more perpendicular to the field lines the mode propagates, the larger is the effect. Thus, the largest effect to explain a predominantly spherically symmetric variation seen in central p-mode frequencies, that is seen also in the latitude-dependent even splitting coefficients but not in the latitudinally symmetric odd splitting coefficients, may be obtained for horizontal propagation in a north-south direction, perpendicular to a toroidal magnetic field.

4. Correlation with solar activity from the interior

Considering a change in field strength in the buried magnetic layer with increasing activity at the surface, frequency shifts due to internal magnetic layers are expected to be out of phase or even anti-correlated with the observed shifts that are themselves correlated with surface activity. This complies with the basic ideas for a dynamo based on magnetic flux tubes. In the progress of injection of a flux tube into the convection zone, the deeper it originates, the more amplified is its magnetic field strength when it emerges from the overshoot layer, the faster it rises and the lower in latitude it emerges at the solar surface as the cycle evolves (Fan et al., 1993). Hence, as the activity increases at the solar surface, the effect on perpendicular propagating modes of a buried toroidal magnetic field decreasing in strength would be expected to yield independent negative frequency shifts. Because the shifts due to a buried magnetic field would not be correlated with the observed ones as the solar activity increases, this also gives ground for inferring that the observed frequency shifts are more a consequence of surface magnetism than of a buried magnetic field.

This reflection is confirmed by observations of Eff-Darwich and Korzennik (2000), who have used the central frequencies to look for changes in the radial structure of the Sun's interior. They found small variations of the sound speed distribution with time at the boundary between the radiative and convective zones. Attempting to find out if the temporal variations in the conspicuous peak or 'hump' at the base of the convection zone are significant and systematic, they isolate the hump and find changes in the area of the hump relative to a grand average over all sound speed profiles, with insignificant error bars. They find a downward trend, as can be seen in Figure 11.1, in both SOI/MDI and GONG data spanning more than two years of observations from December 1995 to July 1998. The downward trend starts much earlier than the rise of the sunspot number, which remains broadly constant until the second half of 1997, therefore indicating that physical processes take place before sunspot activity increases on the solar surface.

Such variations could be an indication of the presence of a toroidal magnetic field stored in this region and whose field strength decreases as the solar activity increases

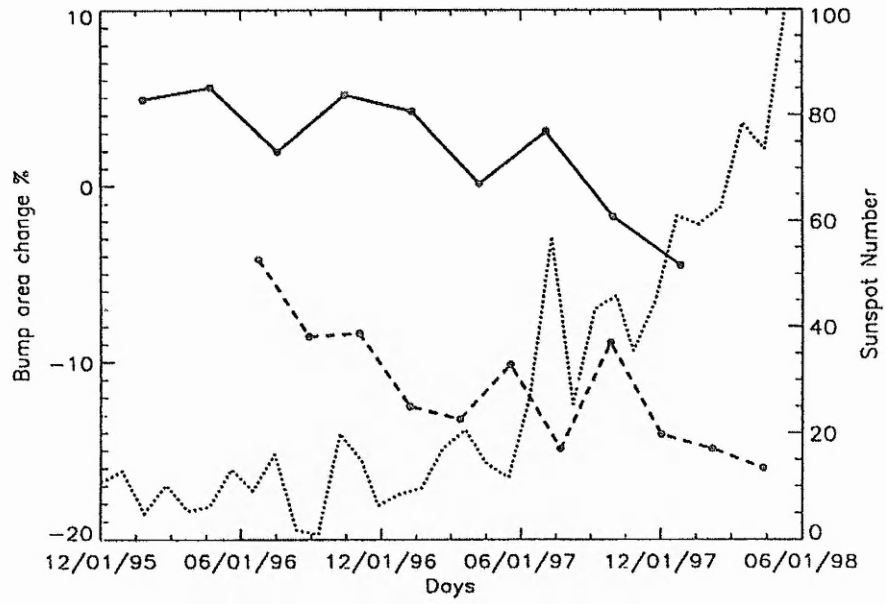

Figure 11.1: Temporal evolution of the area of the 'humps' for both GONG (solid line) and SOI/MDI (dashed line) data. The dotted line corresponds to sunspot number recorded by the National Oceanic and Atmospheric Administration. From Eff-Darwich and Korzennik (2000).

at the surface. Over the rising phase of the solar cycle, these changes would then be associated with independent negative and very small frequency shifts.

5. Playing music with magnetic fields, a musical interpretation

The underlying idea of the phenomenon studied in this thesis may be expressed through a simple analogy, where the standing waves in the Sun are like those in an organ pipe. Consider, more specifically, a flute: near the driven end and also in the vicinity of the open holes in the flute body, the pressure deviates substantially from that in an ideal pipe. Thus, the effective wavelengths of harmonic waves in a flute are not related in a simple way as are wavelengths in an ideal pipe (see, *e.g.*, Fletcher and Rossing, 1991). In a similar way, the gas pressure in the vicinity of a magnetic field deviates from that in a field-free Sun. By analogy with a flute, solar magnetic fields (as well as temperature changes) introduce pressure deviations that play a significant role in modulating the resonant frequencies of p-mode oscillations. The effect of a thin horizontal buried magnetic layer on central p-mode frequencies is to 'encourage' higher harmonics, just as a register hole in a flute (Foullon, 2001). As in a flute, where pressure deviations

result in more pleasant tones, a similar complication exists in the Sun, where pressure deviations over a given period of time produce frequency shifts. The resulting change in frequency is approximately proportional to the square of the magnetic field strength.

This analogy may serve to understand the oscillatory pattern of the shifts obtained for a magnetic field trapped in a layer of plasma. The oscillatory pattern of the frequency shifts that is obtained for $l \neq 0$ increases as the radial order n increases (see Figure 10.9; these patterns were also seen by Daniell (1998) for the mode of degree $l = 0$, see his Figure 4.12). The oscillatory patterns may be interpreted as manifestations of the resulting adjustment of the nodes at the interfaces of the layer. Recent observations seem to indicate the existence of such an oscillatory pattern in low-l shifts (Jiménez-Reyes et al., 2001). These new details need further investigation, but if confirmed they may prove of interest for linking theoretical interpretations to the observations.

Perpendicular to magnetic field lines (with $k_x = 0$), the characteristic wave speed is the fast magnetoacoustic speed $(c_c^2 + v_A^2)^{1/2}$, which serves to increase the frequency of modes propagating in that direction. Pushing the analogy further, perpendicular wave propagation corresponds to playing the flute with a source of heat in front of an open hole, while parallel propagation ($k_y = 0$) indicates the ambient temperature at which the flute is played (Foullon, 2002).

Chapter 12

Summary

By introducing the conditions in which the Sun oscillates (Chapter 1) and the dynamics taking place in the solar interior (Chapter 2), Part I was setting the stage for theoretical modelling. The objective was to examine the role played by horizontal magnetic layers buried in the solar interior, with the view to gain more analytical insight and explain changes observed in the global solar oscillations over the cyclic activity of the Sun.

As a preliminary to an investigation of more complicated models, the dynamics of simple plane-stratified layers was considered in Part II. In Chapter 3, the perturbations of the ideal linearised MHD equations were Fourier analysed proportionally to $\exp i(\omega t - k_x x - k_y y)$, where ω is the angular frequency of a mode of horizontal wavenumber $k_h = (k_x^2 + k_y^2)^{1/2}$ (related to the degree l through $k_h = L/\mathrm{R}_\odot$, for $L = \sqrt{l(l+1)}$ and solar radius $\mathrm{R}_\odot$). Although it precludes variations in the gravity field, the general governing equation that was derived for plane stratified layers is analytically complex and had to be considered in limiting cases. Chapter 4 developed the field-free case — Lamb's equation — and described basic aspects of helioseismology by obtaining p- and g-modes for a polytropic profile. This work lays the foundations for a discussion of a field-free Sun. Chapter 5 developed the magnetic case with constant sound and Alfvén speeds, restricting propagation to parallel or perpendicular directions so as to illustrate the anisotropic nature of magneto-atmospheric waves: the acoustic and gravity cut-off frequencies in a field-free plasma stratified under gravity become anisotropic in the magnetic case. This also modifies the nature of p- and g-modes that can be obtained

with an isothermal stratified atmosphere serving as a waveguide, as discussed in Chapter 6; in this chapter also, fundamental and Lamb modes in an isothermal magnetic layer were obtained and discussed in connection with those for a polytropic layer.

The plane-parallel polytrope with constant gravity and uniform temperature gradient is a convenient model to describe many basic aspects of helioseismology. For this reason, in Part III, a buried magnetic layer was inserted between two polytropic layers. In a Cartesian system (x, y, z), a field-free polytropic medium overlies a horizontal magnetic slab (with field lines aligned in the x-direction) of constant sound and Alfvén speeds, the slab being on top of a field-free polytrope; the adiabatically stratified field-free media are assumed marginally stable to convective motions.

The theoretical foundations of layered models were laid out in Chapter 7, where the general dispersion relation was explored so as to identify the different wavefield contributions and discuss stability aspects. In Chapter 8, some first applications were developed: on the one hand, the dispersion relations were adapted to field-free layered models and, on the other hand, diagnostic diagrams for more or less realistic model conditions were obtained for waves propagating parallel to the magnetic field lines. The properties obtained in Chapter 6, pertinent to the p- and g-modes in an isothermal magnetic waveguide and the magnetically-modified f-mode, proved useful to disentangle the properties of modes in a multi-layer model, which included a magnetic layer. Other general properties across interfaces were investigated, such as the occurrence of magneto-atmospheric surface waves on the magnetic field at the base of the polytrope.

Chapter 9 gave a closer look at the boundary conditions of the field-free model. It was confirmed that the approximation of plane geometry introduces some uncertainty on the precision of frequencies of low-degree modes. Moreover, it was suggested that more modelling remained to be done in order to establish the existence of a second series of eigensolutions, left concealed in the formal helioseismic approach, which depends on the surface boundary conditions and could help to explain the observed solar oscillations.

Through an increase in magnetic field strength, solar magnetic fields in the atmosphere or sub-surface of the Sun can explain the frequency shifts observed on the

timescale of the solar activity cycle. To clarify the relative importance of these effects, further diagnostics of the internal magnetic layers were drawn in Chapter 10, by comparing frequencies obtained for a model with magnetic field and those of a standard field-free model. Frequency shifts due to a stored magnetic field were found to be negligible in comparison with the low- and intermediate-degree frequency shifts reported over the solar activity cycle. Nonetheless, there are grounds for inferring the signature of such buried layers through examining shifts of various degree. Several aspects may be distinguished. First, the p-mode frequencies are increased proportionally to $1/\beta$, where β is the squared ratio between the sound and Alfvén speeds in the magnetic layer. This effect may be directly related to the Lagrangian rate of change in magnetic pressure perturbation, which compresses the volume perpendicular to the magnetic field lines. When the plasma β is large, one can say approximately that magnetism acts only through the dynamics (the magnetic pressure perturbation), but in general the effect is more subtle because the magnetic field affects also the equilibrium pressure distribution. This second aspect involves the variation of the vertical velocity amplitude, which approximately increases on the spatial scale of the layer thickness and decreases on a scale of two (magnetically-modified) density or pressure scale-heights. In particular, when the plasma β is large, it may be said that the frequency changes depend upon the layer thickness 'as seen from the surface'.

The form of the dispersion relation derived in Chapter 7 proved useful in obtaining an analytical approximation to the effect of the buried layer in a polytrope. This analytical approximation was consistent with the numerical results for parallel propagation and served to evaluate the amplitude of the shifts for perpendicular propagation. For realistic solar parameters at the base of the convection zone (with maximum field strength $B_o = 0.3$ MG), the relative effect on p-mode frequencies of a buried magnetic layer of thickness $h = 0.05\,\mathrm{R}_\odot$ is much larger for waves propagating perpendicular rather than parallel to the magnetic field lines. These last results opened a new possibility to obtain frequency shifts, not through a variation in magnetic field strength as usually explained, but by a change in orientation of the magnetic field lines. For a change of magnetic topology at the base of the convection zone, it is expected that the

'global' waves (*i.e.* as if the Sun were not rotating) would propagate perpendicular to a toroidal field at a time which was out of phase with the maximum of solar activity seen at the surface, and that they would propagate parallel to a poloidal field at a time with about the same phase difference with solar minimum. This change of configuration would produce frequency shifts anti-correlated or out of phase with the solar cycle. Nonetheless, for the tachocline model, an effect as large as $\Delta\nu/\nu \sim 9 \times 10^{-4}\%$ at the peak shift frequency 3900 μHz is still negligible in comparison to the observed fractional frequency shift ($\Delta\nu/\nu \sim 2 \times 10^{-2}\%$ over a solar cycle), suggesting that the observed shifts are much more likely to be explained by the influence of the changing chromospheric and coronal atmosphere. However, results from this thesis suggest also that the sunspots' anchoring zone might be relevant, and that a more thorough modelling of this region is needed.

Appendix A

Reference Material

A.1 Special mathematical functions and numerical codes

This appendix lists a series of useful definitions and relations which may be found in 'Handbook of Mathematical Functions' edited by Abramovitz and Stegun, especially Chapter XIII written by Lucy Joan Slater (1965) and entitled 'Confluent Hypergeometric Functions'. The 'Atlas of Functions' edited by Spanier and Oldham is also recommended for graphical sketches of the functions.

Relationships

The functions M and U are respectively the *Kummer* and *Tricomi* confluent hypergeometric functions, defined respectively as follows:

$$M(a,b,z) = \sum_{j=0}^{\infty} \frac{(a)_j}{(b)_j} \frac{z^j}{j!}\,, \tag{A.1}$$

where

$$(a)_j = a(a+1)(a+2)\ldots(a+j-1)\,, \qquad (a)_0 = 1\,; \tag{A.2}$$

and

$$U(a,b,z) = \frac{\Gamma(1-b)}{\Gamma(1+a-b)} M(a,b,z) + \frac{\Gamma(b-1)}{\Gamma(a)z^{b-1}} M(a+1-b, 2-b, z)\,. \tag{A.3}$$

Γ and Ψ functions

The Γ function never takes the value 0 but comes very close to it between consecutive large negative integers. The reciprocal $\frac{1}{\Gamma(z)}$ has no discontinuities and is zero at $z = 0, -1, -2, \ldots$.

The recurrence relation

$$\Gamma(1+z) = z\Gamma(z)\,, \tag{A.4}$$

indicates the reduction of $\Gamma(1+n)$ to the factorial function for a positive integer n,

$$\Gamma(n+1) = n!\,, \tag{A.5}$$

and can be generalised to

$$\Gamma(n+z) = z(1+z)(2+z)...(n-1+z)\Gamma(z) = (z)_n\Gamma(z)\,. \tag{A.6}$$

$\Gamma(z)$ obeys the reflection formula

$$\Gamma(z)\Gamma(1-z) = \frac{\pi}{\sin \pi z}\,. \tag{A.7}$$

The Psi (or Digamma) function is defined as

$$\Psi(z) = \frac{\Gamma'(z)}{\Gamma(z)}\,, \tag{A.8}$$

and obeys the reflection formula

$$\Psi(1-z) = \Psi(z) + \pi \cot \pi z. \tag{A.9}$$

Derivatives

$$\frac{dM(a,b,z)}{dz} = \frac{a}{b}M(a+1,b+1,z)\,; \tag{A.10}$$

$$\frac{dU(a,b,z)}{dz} = -aU(a+1,b+1,z)\,. \tag{A.11}$$

These relations are illustrated in Figure A.1 for parameters appropriate for a polytropic stratified layer.

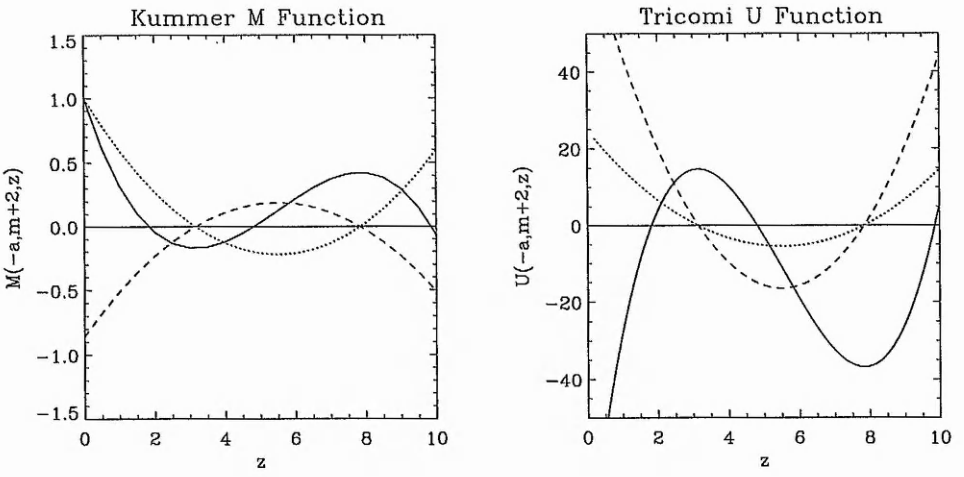

Figure A.1: The confluent hypergeometric functions $X(a,b,z)$ versus z: for different arguments (a,b), $X(-\Upsilon,m+2,z)$ is the full line; $X(-\Upsilon+1,m+3,z)$ is the dotted line; $X'(-\Upsilon,m+2,z)$ is the dashed line, for $\Upsilon=3$ and $m=\frac{3}{2}$. On the *left*, the Kummer functions $X=M$ are given, with $M'(-\Upsilon,m+2,z)=-\frac{\Upsilon}{m+2}M(-\Upsilon+1,m+3,z)$; on the *right*, the Tricomi functions $X=U$ are given, with $U'(-\Upsilon,m+2,z)=-U(-\Upsilon+1,m+3,z)$.

Limiting Forms

At $z=0$

$$M(a,b,0)=1\,, \tag{A.12}$$

irrespective of the parameter values a and b.

The representation (A.3) of U may be combined with the property (A.12) of M to obtain the asymptotic behaviour

$$\lim_{z\to 0}U(a,b,z)=\frac{\Gamma(1-b)}{\Gamma(1+a-b)}+\frac{\Gamma(b-1)}{\Gamma(a)z^{b-1}}\,. \tag{A.13}$$

Two cases emerge as $z\to 0$:

$$\begin{aligned} & b<1\,, && U(a,b,z)\sim\tfrac{\Gamma(1-b)}{\Gamma(1+a-b)}\,,\\ \text{or}\quad & b\geq 1\,, && U(a,b,z)\sim\tfrac{\Gamma(b-1)}{\Gamma(a)z^{b-1}}\,. \end{aligned} \tag{A.14}$$

In application to the polytropic stratified layer, b is equal to $m+2$ or $m+3$, which are >1 since $m+1=\frac{\gamma g}{(c^2)'}>0$. Therefore only the case when the U function is singular at $z=0$ may be encountered in the polytropes discussed here, *viz.*

$$\lim_{z\to 0}U(a,b,z)=\infty\,,\quad \text{for}\quad b\geq 1. \tag{A.15}$$

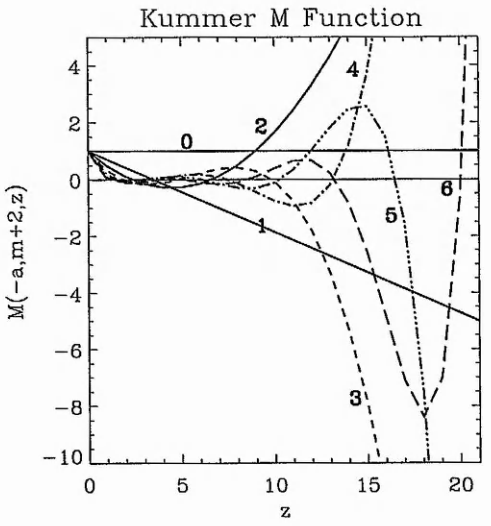

Figure A.2: The Kummer functions $M(-\Upsilon, m+2, z)$ versus z for $m = \frac{3}{2}$ and where $\Upsilon = [0, 6]$ is an integer.

At $z \to +\infty$

$$M(a, b, z) \sim \frac{\Gamma(b)}{\Gamma(a)} z^{a-b} e^{z}\,; \tag{A.16}$$

$$U(a, b, z) \sim z^{-a}(1 + O|z|^{-1})\,. \tag{A.17}$$

Termination of the series

When a is a negative integer, $M(-n, b+1, z)$ and $U(-n, b+1, z)$ reduce to polynomials of degree n in z and take the form of a generalised Laguerre polynomial $L_n^{(b)}(z)$, *viz.*

$$\begin{aligned} M(-n, b+1, z) &= \sum_{j=0}^{n} \frac{(-n)_j}{(b+1)_j} \frac{z^j}{j!} \\ &= \frac{n!}{(b+1)(b+2)...(b+n)} \sum_{j=0}^{n} (-1)^j \binom{n+b}{n-j} \frac{z^j}{j!} \\ &= \frac{n!}{(b+1)_n} L_n^{(b)}(z)\,, \end{aligned} \tag{A.18}$$

and

$$\begin{aligned} U(-n, b+1, z) &= (-1)^n (b+1)_n M(-n, b+1, z) \\ &= (-1)^n n! L_n^{(b)}(z)\,. \end{aligned} \tag{A.19}$$

The form taken by the M function in this case is illustrated by Figure A.2.

Numerical evaluation of the confluent hypergeometric functions

In Figures A.1 and A.2, the Kummer M function was evaluated with a Fortran program, using an algorithm written by Nardin et al. (1992). The Tricomi U function was evaluated with an algorithm written by Fullerton (1976).

The numerical codes used to evaluate the dispersion relations in Section 8.2 and Chapter 9 were written in Fortran 77. The primary root finding program was the NAG library routine C05AGF. This routine locates a simple zero of a continuous function from a given starting value. It works with a binary search to locate an interval containing a zero of the function, then a combination of the methods of linear interpolation, extrapolation and bisection to locate the zero more precisely. This routine was employed within nested loops browsing the plane (l, Ω^2). A main program was written for this purpose and was called '*ROOT*'. For each degree l, the function called '*DR*', whose zero is to be determined in a given range in Ω^2, is evaluated by C05AGF at one given starting value, and subsequently for adjacent values, until a root is found (or not). To search for more roots, subsequent values are specified by the browsing in '*ROOT*'. Such browsing may be done with flexibility: to search for unknown modes (such as surface waves), this can be done thoroughly by small steps in Ω^2; to search for roots which can be guessed, specifically those aligned on a p-mode ridge, the starting values at a given degree l are specified by the roots found previously for degree $l-1$. This second method is the less time-consuming.

Depending on specified parameters supplied to the routine C05AGF (such as the step H for use in the binary search for an interval containing the zero, and the accuracy to which the zero is required), the routine C05AGF returns a root, which may be in general close to the starting value, but not always. Within the browsing in Ω^2 for a given degree l, some roots may be returned more than once, but not necessarily with the same accuracy. The program '*ROOT*' checked that all solutions are effectively zeros to the function and that no roots are repeated. The spurious roots are eliminated, and when a root occurred more than once (within the required accuracy) the root which yielded the smallest 'zero' of the function is retained.

The function '*DR*' is one parameter to the routine C05AGF. The results may depend

on its structure. For instance, if the function has roots close to its asymptotes, these roots are difficult to locate. The function must then be written in the most appropriate form to locate these roots. This implies a multiplication or taking the inverse of the function. For instance, if one form is more appropriate at small wavelengths, it may be useful to take the inverse of this function at large wavelengths. Besides the form of the function critical to find its roots, its numerical evaluation can be difficult or generate some inaccuracies due to the presence of the confluent hypergeometric functions.

The Kummer function $M(a, b, z)$ was mainly evaluated with the algorithm of Nardin et al. (1992), called '*conhyp*', which was originally written for complex arguments but here was used for real values only. The technique used is a direct summation of the Kummer series using specialised extended precision complex subroutines and allowing an accuracy of up to thirteen decimal places through the use of large real arrays and a single final division. Although this numerical evaluator is for arguments with large magnitudes (the argument $z = 0$ was always avoided for this reason), it proved to be very stable and to give satisfactory results for the smallest arguments encountered.

On the other hand, to evaluate the Tricomi function $U(a, b, z)$, the Fullerton code, called '*dchu*', is limited for some arguments or combinations of them, and is not stable. A code used by Dr Brad Hindman, a Fortran version of a code called '*DKummerU*', also proved useful. However, this program had some other problems, but generally it yielded results and it was a good starting point for improvement. It was originally written for IDL by Dr Tom Bogdan and modified in 1995 for greater precision and control by Hindman. This code operates by using either an expansion for small arguments, '*USmallArg*', or a separate expansion for large arguments, '*ULargeArg*'. '*DKummerU*' can be programmed to select which expansion to use. This is useful in the case of solar atmospheric models, which imply a dispersion relation with confluent hypergeometric functions to be evaluated for small third argument; therefore only one code is needed, namely the code '*USmallArg*'. But when one considers a dispersion relation where the interface is taken at the base of the convection zone, the last argument of the U function may become large and the code must compute both expansions (which is time-consuming), and then select the expansion with the smallest residuals. Further-

more, arguments of intermediate size are not treated well by either expansion for some parameter regimes. Besides, if

$$z > z_{min} = 2(b-a)\sqrt{4(b-a)^2 + b}\,, \tag{A.20}$$

then '*DKummerU*' chooses the expansion for large arguments.

The expansion for large arguments in '*ULargeArg*' is the one given by §13.5.2 in Abramovitz and Stegun, *viz.*

$$U(a,b,z) = z^{-a} \sum_{n=0}^{R-1} \frac{(a)_n (1+a-b)_n}{n!} (-z)^{-n}\,. \tag{A.21}$$

This series is truncated if the terms in the sum becomes smaller than the numerical precision, the optimal number of terms has been taken in the asymptotic series, or the number of terms exceeds a practical limit ($imax = 5000$).

For the small argument expansion, '*USmallArg*' computes the U function through its definition (A.3) in terms of Gamma and Kummer M functions. The Gamma functions are obtained with a routine provided by Hindman and written according to numerical recipes, but the M functions are evaluated with the large argument expansion (§13.5.1 in Abramovitz and Stegun, from which the leading term is given in Equation (A.16)). This leaves open as to what should be for small arguments.

The program '*DR*' calls '*conhyp*' to evaluate the M function. However, to evaluate the U function, a combination of codes was necessary. First, for small arguments ($z \leq 60$ and $z \leq z_{min}$), the Tricomi function $U(a,b,z)$ is evaluated as for '*USmallArg*', except that the M functions are evaluated with '*conhyp*'. Second, for large arguments ($z > 60$ or $z > z_{min}$), '*ULargeArg*' is employed. If the number of terms taken in the asymptotic series (A.21) exceeds the maximum number $imax = 5000$, without reaching an optimal, then '*dchu*' is used. For the unstable cases of '*dchu*', the program calls the original program '*DKummerU*'.

A.2 GONG data sets and associated activity measures

This work utilises data obtained by the Global Oscillation Network Group (GONG) project, managed by the National Solar Observatory, which is operated by AURA, Inc. under a cooperative agreement with the National Science Foundation. The data were acquired by instruments operated by the Big Bear Solar Observatory, High Altitude Observatory, Learmonth Solar Observatory, Udaipur Solar Observatory, Instituto de Astrofísico de Canarias, and Cerro Tololo Interamerican Observatory.

The Global Oscillation Network Group (GONG) has, to date, contiguous multisite observations since May 1995, covering the end of cycle 22 and the beginning of cycle 23 and making up the longest, most comprehensive and best-quality set of resolved Sun observations so far available. Table A.2 presents the full set of GONG data that was made available to me thanks to Jim Pintar and Sean McManus (http://www.gong.noao.edu/homepage.html). For each GONG Month numeric reference, the table lists the inclusive start and stop dates of observations, the date included in the data product name, and the fill factors of gap-filled time series. This fill factor may be understood as an indicator of the level of confidence in filling the gaps, that is an indicator of the quality of the data. The Introduction, Sections 9.3 and 10.1 refer to observations made at some specific periods. In particular, Month 50 (referred as 000302) includes days between 05/03 to 09/04/2000; Month 9 (referred as 960307) includes days between 19/02 to 25/03/1996.

Although the data so far collected span only about half of the range of activity levels expected for the cycle, the unprecedented accuracy and continuous nature of the observations already confirm and extend earlier conclusions on the secular variation of the mode frequencies (see Section 2.1 and Section 10.1). Associated activity measures are listed for months with the most overlap with respect to each GONG month. The smoothed sunspot number values were taken from S.I.D.C. Brussels International Sunspot Number (http://sidc.oma.be/DATA/monthssn.dat). The 10.7 cm flux values, which measure the integrated emission from the solar disk in solar flux units ($1SFU = 10^{-22}\mathrm{W\,s\,m^{-2}}$), are from Penticton, B.C., Canada (ftp:// ftp.ngdc.noaa.gov/STP/SOLAR_DATA/SOLAR_RADIO/FLUX/MONTHLY.OBS).

Month Index	Start Date	GONG Stop Date	Name	Fill	Year and Month	Monthly Smoothed Sunspot N.	Radio Flux 10.7 cm (SFU)
1	950507	950611	950524	0.74	199505	19.2	75.5
2	950612	950717	950629	0.81	199506	18.2	75.7
3	950718	950822	950804	0.87	199508	15.4	73.8
4	950823	950927	950909	0.84	199509	13.4	72.0
5	950928	951102	951015	0.87	199510	12.1	77.9
6	951103	951208	951120	0.89	199511	11.3	74.2
7	951209	960113	951226	0.87	199512	10.8	72.6
8	960114	960218	960131	0.87	199601	10.4	74.5
9	960219	960325	960307	0.93	199603	9.7	70.7
10	960326	960430	960412	0.90	199604	8.5	69.3
11	960501	960605	960518	0.94	199605	8.0	70.1
12	960606	960711	960623	0.82	199606	8.5	69.6
13	960712	960816	960729	0.73	199607	8.4	71.2
14	960817	960921	960903	0.76	199609	8.4	69.4
15	960922	961027	961009	0.91	199610	8.8	69.2
16	961028	961202	961114	0.93	199611	9.8	78.7
17	961203	970107	961220	0.92	199612	10.4	77.8
18	970108	970212	970125	0.92	199701	10.5	74.0
19	970213	970320	970302	0.89	199703	13.5	73.5
20	970321	970425	970407	0.79	199704	16.5	74.5
21	970426	970531	970513	0.79	199705	18.4	74.6
22	970601	970706	970618	0.84	199706	20.4	71.7
23	970707	970811	970724	0.86	199707	22.7	71.1
24	970812	970916	970829	0.77	199708	25.1	79.0
25	970917	971022	971004	0.87	199710	31.9	84.9
26	971023	971127	971109	0.75	199711	35.1	99.5
27	971128	980102	971215	0.83	199712	39.0	98.8
28	980103	980207	980120	0.82	199801	43.8	93.4
29	980208	980315	980225	0.92	199802	49.0	93.4
30	980316	980420	980402	0.79	199804	56.6	108.3
31	980421	980526	980508	0.77	199805	59.4	106.7
32	980527	980701	980613	0.85	199806	62.5	108.4
33	980702	980806	980719	0.72	199807	65.5	114.0
34	980807	980911	980824	0.82	199808	67.8	136.0
35	980912	981017	980929	0.86	199809	69.5	138.3
36	981018	981122	981104	0.91	199811	73.0	140.2
37	981123	981228	981210	0.95	199812	77.9	150.1
38	981229	990202	990115	0.92	199901	82.6	142.6
39	990203	990310	990220	0.88	199902	84.6	142.0
40	990311	990415	990328	0.83	199903	83.8	126.3
41	990416	990521	990503	0.87	199905	90.5	148.6
42	990522	990626	990608	0.89	199906	93.1	169.8
43	990627	990801	990714	0.83	199907	94.3	165.6
44	990802	990906	990819	0.86	199908	97.5	170.8
45	990907	991012	990924	0.85	199909	102.3	135.7
46	991013	991118	991030	0.84	199910	107.8	164.8
47	991119	991223	991205	0.89	199912	111.1	169.8
48	991224	000128	000110	0.79	200001	112.9	158.1
49	000129	000304	000215	0.91	200002	116.8	173.2
50	000305	000409	000322	0.83	200003	119.9	208.2

Table A.1: Details of the GONG data sets and associated activity measures.

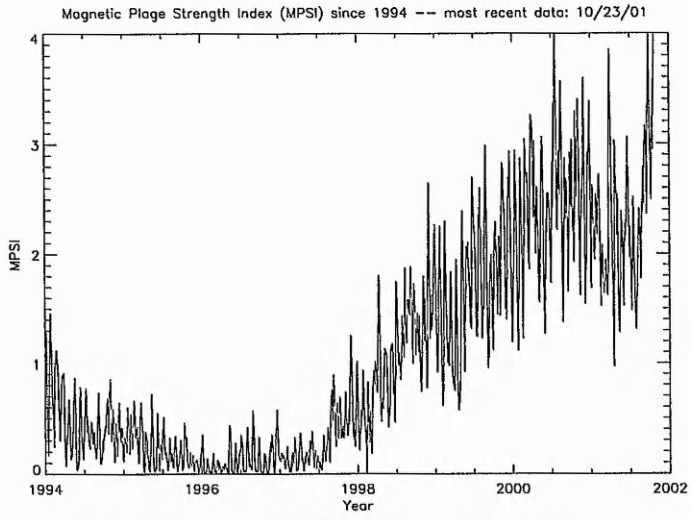

Figure A.3: The Magnetic Plage Strength Index (MPSI) at the end of cycle 22 and in the rising phase of cycle 23 (from 1994 to October 2000). This graph is created with data from the synoptic program at the 150-Foot Solar Tower of the Mt. Wilson Observatory. The Mt. Wilson 150-Foot Solar Tower is operated by UCLA, with funding from NASA, ONR and NSF, under agreement with the Mt. Wilson Institute. From http://www.astro.ucla.edu/ obs/150_data.html

Figure A.3 shows a plot of the Magnetic Plage Strength Index (MPSI) obtained mainly during the rising phase of cycle 23, which covers the time period for GONG data listed in Table A.2. This graph is created with data from the synoptic program at the 150-Foot Solar Tower of the Mt. Wilson Observatory. The MPSI value is obtained by summing the absolute values of the magnetic field strengths for all pixels where the absolute value of the magnetic field strength is between 10 and 100 Gauss. This number is then divided by the total of number of pixels (regardless of magnetic field strength) in the magnetogram.

Figure A.3 is complementary to Table A.2 in order to guide the choice of low-activity GONG data. This is how GONG month 9 (roughly March 1996) was chosen. Figure A.3 also indicates that GONG month 50 (roughly March 2000), which was chosen for being the most recent GONG data set available, corresponds to a fairly high level of solar activity.

Appendix B

Reference Lists

List of Tables

List of Figures

Index

Bibliography

Acheson, D. J.: 1979, *Sol. Phys.* **62**, 23, Instability by magnetic buoyancy

Adam, J. A.: 1977a, *Sol. Phys.* **52**, 293, On the occurrence of critical levels in solar magnetohydrodynamics

Adam, J. A.: 1977b, *Astron. Astrophys.* **60**, 171, Solar magnetoatmospheric waves - A simplified mathematical treatment

Adam, J. A.: 1994, *Astrophys. Space. Sci.* **220**, 179, Non-radial stellar oscillations: A perspective from potential scattering 1: Theoretical foundations

Ando, H. and Osaki, Y.: 1975, *Publ. Astron. Soc. Jpn.* **27**, 581, Nonadiabatic Nonradial Oscillations: An Application to the Five-minute Oscillation of the Sun

Anguera Gubau, M., Pallé, P. L., Pérez Hernández, F., Régulo, C., and Roca Cortés, T.: 1992, *Astron. Astrophys.* **255**, 363, The low l solar p-mode spectrum at maximum and minimum solar activity

Antia, H. M. and Basu, S.: 2000, *Astrophys. J.* **541**, 442, Temporal Variations of the Rotation Rate in the Solar Interior

Antia, H. M., Basu, S., and Chitre, S. M.: 1998, *Mon. Not. R. Astron. Soc.* **298**, 543, Solar internal rotation rate and the latitudinal variation of the tachocline

Antia, H. M., Chitre, S. M., and Thompson, M. J.: 2000, *Astron. Astrophys.* **360**, 335, The Sun's acoustic asphericity and magnetic fields in the solar convection zone

Bachmann, K. T. and White, O. R.: 1994, *Sol. Phys.* **150**, 347, Observations of hysteresis in solar cycle variations among seven solar activity indicators

Balmforth, N., Gough, D., and Merryfield, W.: 1996, *Mon. Not. R. Astron. Soc.* **278**, 437, Structural Changes to the Sun through the Solar Cycle

Banerjee, D., Hasan, S. S., and Christensen-Dalsgaard, J.: 1995, *Astrophys. J.* **451**, 825, The Influence of a Vertical Magnetic Field on Oscillations in an Isothermal Stratified Atmosphere. II

Basu, S.: 1997, *Mon. Not. R. Astron. Soc.* **288**, 572, Seismology of the Base of the Solar Convection Zone

Basu, S. and Antia, H. M.: 1994, *Mon. Not. R. Astron. Soc.* **269**, 1137, Effects of Diffusion on the Extent of Overshoot below the Solar Convection Zone

Basu, S. and Antia, H. M.: 2000, *Sol. Phys.* **192**, 449, Possible solar cycle variations in the convection zone

Basu, S. and Antia, H. M.: 2001, *Mon. Not. R. Astron. Soc.* **324**, 498, A study of possible temporal and latitudinal variations in the properties of the solar tachocline

Basu, S., Antia, H. M., and Narasimba, D.: 1994, *Mon. Not. R. Astron. Soc.* **267**, 209, Helioseismic Measurement of the Extent of Overshoot below the Solar Convection Zone

Basu, S. and Schou, J.: 2000, *Sol. Phys.* **192**, 481, Does the tachocline show solar cycle related changes?

Beck, J. G.: 2000, *Sol. Phys.* **191**, 47, A comparison of differential rotation measurements - (Invited Review)

Belvedere, G., Gough, D., and Paternó, L.: 1983, *Sol. Phys.* **82**, 343, On the Influence of Nonlinearities on the Eigenfrequencies of five-minute Oscillations of the Sun

Berger, M. A.: 1999, *Plasma Phys. Controlled Fusion* **41**, B167, Introduction to magnetic helicity

Bhatnagar, A., Jain, K., and Tripathy, S. C.: 1999, *Astrophys. J.* **521**, 885, GONG p-mode Frequency Changes with Solar Activity

Bogdan, T. J. and Cally, P. S.: 1997, *Proc. R. Soc. London, Ser. A* **453**, 943, Waves in magnetized polytropes

Bogdan, T. J. and Zweibel, E. G.: 1985, *Astrophys. J.* **298**, 867, Effect of a fibril magnetic field on solar p-modes

Braun, D. C. and Fan, Y.: 1998, *Astrophys. J., Lett.* **508**, L105, Helioseismic Measurements of the Subsurface Meridional Flow

Braun, D. C. and Fan, Y.: 1999, *Astrophys. J., Lett.* **510**, L81, Erratum: Helioseismic Measurements of the Subsurface Meridional Flow

Brown, T. M., Christensen-Dalsgaard, J. C., Dziembowski, W. A., Goode, P., Gough, D. O., and Morrow, C. A.: 1989, *Astrophys. J.* **343**, 526, Inferring the Sun's Internal Angular Velocity from Observed p-mode Frequency Splittings

Brown, T. M. and Gilliland, R. L.: 1994, *Ann.Rev.Astron.Astrophysic.* **32**, 37, Asteroseismology

Brun, A. S., Turck-Chièze, S., and Zahn, J. P.: 1999, *Astrophys. J.* **525**, 1032, Standard Solar Models in the Light of New Helioseismic Constraints. II. Mixing below the Convective Zone

Caligari, P., Moreno-Insertis, F., and Schüssler, M.: 1995, *Astrophys. J.* **441**, 886, Emerging Flux Tubes in the Solar Convection Zone. I. Asymmetry, Tilt and Emergence Latitude

Cally, P. S. and Bogdan, T. J.: 1997, *Astrophys. J., Lett.* **486**, L67, Simulation of f- and p-mode Interactions with a Stratified Magnetic Field Concentration

Campbell, W. R.: 1987, *Ph.D. thesis*, University of St Andrews, Scotland, Helioseismological Wave Propagation in Magnetic Structures

Campbell, W. R. and Roberts, B.: 1986, in *IAU Symp. 123: 'Advances in Helio- and Asteroseismology'*, pp 161–165, Magnetic Effects on Solar p-modes

Campbell, W. R. and Roberts, B.: 1989, *Astrophys. J.* **338**, 538, The Influence of a Chromospheric Magnetic Field on the Solar p- and f-modes

Cassinelli, J. P. and MacGregor, K. B.: 1986, in P. A. Sturrock (ed.), *Physics of the Sun*, Vol. 3, pp 47–123, Dordrecht: Reidel, Stellar chromospheres, coronae, and winds

Chandrasekhar, S.: 1961, *Hydrodynamic and Hydromagnetic Stability*, Chapt. X, p. 428, Oxford University Press

Chaplin, W. J., Elsworth, Y., Isaak, G. R., Lines, R., McLeod, C. P., Miller, B. A., and New, R.: 1998, *Mon. Not. R. Astron. Soc.* **300**, 1077, An Analysis of Solar p-mode Frequencies Extracted from BISON Data: 1991-1996

Charbonneau, P., Christensen-Dalsgaard, J., Henning, R., Larsen, R. M., Schou, J., Thompson, M. J., and Tomczyk, S.: 1999, *Astrophys. J.* **527**, 445, Helioseismic Constraints on the Structure of the Solar Tachocline

Chen, C.-J. and Lykoudis, P. S.: 1972, *Sol. Phys.* **25**, 380, Velocity Oscillations in Solar Plage Regions

Choudhuri, A. R. and Gilman, P. A.: 1987, *Astrophys. J.* **316**, 788, The Influence of the Coriolis Force on Flux Tubes rising through the Solar Convection Zone
Christensen-Dalsgaard, J.: 1980, *Mon. Not. R. Astron. Soc.* **190**, 765, On adiabatic non-radial oscillations with moderate or large l
Christensen-Dalsgaard, J.: 1998, *Lecture Notes on Stellar Oscillations*, Available from World Wide Web: http://www.obs.aau.dk/~jcd/oscilnotes/, Institut for Fysik og Astronomi, Aarhus Universitet
Christensen-Dalsgaard, J., Duvall Jr., T. L., Gough, D. O., Harvey, J. W., and Rhodes Jr., E. J.: 1985, *Nature* **315**, 378, Speed of Sound in the Solar Interior
Christensen-Dalsgaard, J. and Gough, D. O.: 1980, *Nature* **288**, 544, Is the Sun helium-deficient?
Christensen-Dalsgaard, J., Gough, D. O., and Thompson, M. J.: 1991, *Astrophys. J.* **378**, 413, The Depth of the Solar Convection Zone
Christensen-Dalsgaard, J., Gough, D. O., and Toomre, J.: 1985, *Science* **229**, 923, Seismology of the sun
Christensen-Dalsgaard, J., Monteiro, M. J. P. F. G., and Thompson, M. J.: 1995, *Mon. Not. R. Astron. Soc.* **276**, 283, Helioseismic estimation of convective overshoot in the Sun
Christensen-Dalsgaard, J. and Mullan, D. J.: 1994, *Mon. Not. R. Astron. Soc.* **270**, 921, Accurate Frequencies of Polytropic Models
Cowling, T. G.: 1941, *Mon. Not. R. Astron. Soc.* **101**, 367, The non-radial oscillations of polytropic stars
Cunha, M. S. and Gough, D.: 2000, *Mon. Not. R. Astron. Soc.* **319**, 1020, Magnetic perturbations to the acoustic modes of roAp stars
Daniell, M.: 1998, *Ph.D. thesis*, University of St Andrews, Scotland, The Influence of Thermal and Magnetic Layers on Solar Oscillation Frequencies
Defouw, R.: 1976, *Astrophys. J.* **209**, 266, Wave Propagation along a Magnetic Tube
Deubner, F. and Gough, D.: 1984, *Ann.Rev.Astron.Astrophysic.* **22**, 593, Oscillations as a diagnostic of the Solar Interior
Dikpati, M. and Charbonneau, P.: 1999, *Astrophys. J.* **518**, 508, A Babcock-Leighton Flux Transport Dynamo with Solar-like Differential Rotation
Duvall, T. L.: 1982, *Nature* **300**, 242, A dispersion law for solar oscillations
Duvall, T. L. and Harvey, J. W.: 1984, *Nature* **310**, 19, Rotational frequency splitting of solar oscillations
Dzhalilov, N. S., Staude, J., and Arlt, K.: 2000, *Astron. Astrophys.* **361**, 1127, Influence of the solar atmosphere on the p-mode eigenoscillations
Dziembowski, W. A. and Goode, P. R.: 1983, *Nature* **305**, 39, Limits on the sun's core magnetism from solar oscillations
Dziembowski, W. A. and Goode, P. R.: 1989, *Astrophys. J.* **347**, 540, The Toroidal Magnetic Field Inside The Sun
Dziembowski, W. A. and Goode, P. R.: 1991, *Astrophys. J.* **376**, 782, Seismology for the fine Structure in the Sun's Oscillations Varying with its Activity Cycle
Dziembowski, W. A. and Goode, P. R.: 1997, *Astron. Astrophys.* **317**, 919, Seismic sounding of the solar core: purging the corruption from the Sun's magnetic activity
Dziembowski, W. A., Goode, P. R., Kosovichev, A. G., and Schou, J.: 2000, *Astrophys. J.* **537**, 1026, Signatures of the Rise of Cycle 23
Eckart, C.: 1960, *Hydrodynamics of Oceans and Atmospheres*, London: Pergamon
Edwin, P. M.: 1984, *Ph.D. thesis*, University of St Andrews, Scotland, Magnetohydro-

dynamic waves in structured atmospheres
Edwin, P. M. and Roberts, B.: 1982, *Sol. Phys.* **76**, 239, Wave propagation in a magnetically structured atmosphere. III - The slab in a magnetic environment
Eff-Darwich, A. and Korzennik, S. G.: 2000, *Sol. Phys.* **193**, 365, Response of the radial stratification at the base of the convection zone to the activity cycle
Elliott, J. R. and Gough, D. O.: 1999, *Astrophys. J.* **516**, 475, Calibration of the Thickness of the Solar Tachocline
Elsworth, Y., Howe, R., Isaak, G. R., McLeod, C. P., Miller, B. A., New, R., Speake, C. C., and Wheeler, S. J.: 1994, *Astrophys. J.* **434**, 801, Solar p-mode frequencies and their dependence on solar activity recent results from the BISON network
Elsworth, Y., Howe, R., Isaak, G. R., McLeod, C. P., and New, R.: 1990, *Nature* **345**, 322, Variation of low-order acoustic solar oscillations over the solar cycle
Endal, A. S., Sofia, S., and Twigg, L. W.: 1985, *Astrophys. J.* **290**, 748, Changes of solar luminosity and radius following secular perturbations in the convective envelope
Evans, D. J.: 1990, *Ph.D. thesis*, University of St Andrews, Scotland, The effects of magnetic fields on oscillations in the solar atmosphere
Evans, D. J. and Roberts, B.: 1990, *Astrophys. J.* **356**, 704, The Influence of a Chromospheric magnetic Field on the Solar p- and f-modes. II. Uniform Chromospheric Field
Evans, D. J. and Roberts, B.: 1992, *Nature* **355**, 230, Interpretation of solar-cycle variability in high-degree p-mode frequencies
Fan, Y., Fisher, G., and DeLuca, E.: 1993, *Astrophys. J.* **405**, 390, The Origin of Morphological Asymmetries in Bipolar Active Regions
Favata, F., Roxburgh, I., and Christensen-Dalsgaard, J.: 2000, *Eddington – A Mission to Map Stellar Evolution through Oscillations and to Find Habitable Planets*, Assessment Study Report ESA-SCI(2000)8, ESA
Ferraro, C. A. and Plumpton, C.: 1958, *Astrophys. J.* **127**, 459, Hydromagnetic Waves in a Horizontally Stratified Atmosphere. V.
Fisher, G., Fan, Y., Longcope, D., Linton, M., and Abbett, W.: 2000, *Phys. Plasmas* **7(5)**, 2173, Magnetic flux tubes inside the sun
Fletcher, N. H. and Rossing, T. D.: 1991, *The Physics of Musical Instruments*, New York: Springer-Verlag
Fossat, E., Gelly, B., Grec, G., and Pomerantz, M.: 1987, *Astron. Astrophys.* **177**, L47, Search for solar p-mode frequency changes between 1980 and 1985
Foukal, P.: 1972, *Astrophys. J.* **173**, 439, Magnetic Coupling of the Active Chromosphere to the Solar Interior
Foullon, C.: 1999, in *ESA SP-448: Ninth European Meeting on Solar Physics, 'Magnetic Fields and Solar Processes', ed. A. Wilson*, pp 87–92, Waves on a Magnetic Slab at the Base of the Convection Zone
Foullon, C.: 2001, in *INTAS Workshop on 'MHD Waves in Astrophysical Plasmas', ed. J.L. Ballester and B. Roberts*, pp 115–118, Playing Music with Magnetic Fields: Effects of Some Internal Magnetic Fields on Solar Oscillations
Foullon, C.: 2002, in *IAU Colloq. 185: 'Radial and Nonradial Pulsations as Probes of Stellar Physics', ed. C. Aerts, T. Bedding and J. Christensen-Dalsgaard, in press*, Playing music with magnetic fields
Foullon, C. and Roberts, B.: 2000, in *AIP CP-537: 'Waves in Dusty, Solar, and Space Plasmas', ed. F. Verheest*, p. 240, The influence of a buried magnetic field on solar p-modes

Freytag, B., Ludwig, H.-G., and Steffen, M.: 1996, *Astron. Astrophys.* **313**, 497, Hydrodynamical models of stellar convection. The role of overshoot in DA white dwarfs, A-type stars, and the Sun

Fullerton, L. W.: 1976, in W. Cowell (ed.), *Lecture Notes in Computer Science*, Vol. 57, pp 452–483, Springer-Verlag, New York, Portable special function routine, in Portability of Numerical Software - Code available from World Wide Web: http://gams.nist.gov/HotGAMS/HotGAMS.html, august 1980 edition

Gabriel, M.: 1994, *Astron. Astrophys.* **292**, 281, Influence of physical effects on the solar p-mode spectrum

Geyer, M. P. and Schmitz, F.: 2000, *Astron. Astrophys.* **361**, 340, Radial stellar oscillations under the influence of the dynamics of the atmosphere – a one-dimensional approach. I. Linear adiabatic oscillations of a special model

Giles, P. M., Duvall, T. L., Scherrer, P. H., and Bogart, R. S.: 1997, *Nature* **390**, 52, A Flow of Material from the Sun's Equator to its Poles

Gilman, P. A.: 1970, *Astrophys. J.* **162**, 1019, Instability of Magnetohydrostatic Stellar Interiors from Magnetic Buoyancy. I

Goedbloed, J. P.: 1971, *Physica* **53**, 412, Stabilization of magnetohydrodynamic instabilities by force-free magnetic fields I. Plane plasma layer

Goedbloed, J. P.: 1983, Rijnhuizen Report 83-145, Lecture Notes on Ideal Magnetohydrodynamics

Goedbloed, J. P.: 1984, *Physica D* **12**, 107, Plasma-Vacuum Interface Problems in Magnetohydrodynamics

Goedbloed, J. P. and Poedts, S.: 1997, *Plasma physics and magnetohydrodynamics*, Course of lectures for PhD students, Free University of Amsterdam

Goldreich, P., Murray, N., Willette, G., and Kumar, P.: 1991, *Astrophys. J.* **370**, 752, Implications of Solar p-mode Frequency Shifts

Gonzalez, A. and Gratton, J.: 1991, *Sol. Phys.* **134**, 233, Magnetoacoustic surface gravity waves

Goossens, M.: 1991, in Priest and Hood (eds.), *Advances in Solar System MHD*, Cambridge University Press, Magnetohydrodynamic Waves and Wave Heating in Non-Uniform Plasmas

Goossens, M.: 2001, *Introduction to Plasma Astrophysics*, Course for undergraduates, Katholieke Universiteit Leuven

Gough, D. O.: 1977, in *IAU Colloq. 36: 'The Energy Balance and Hydrodynamics of the Solar Chromosphere and Corona', ed. R. M. Bonnet and P. Delache, Clermont-Ferrand: G.de Bussac*, p. 3, Random Remarks on Solar Hydrodynamics

Gough, D. O.: 1990a, in *LNP Vol. 367: Progress of Seismology of the Sun and Stars*, pp 283–318, Comments on Helioseismic Inference

Gough, D. O.: 1990b, *Nature* **345**, 768, Helioseismology - Shaky Clues to Solar Activity

Gough, D. O. and Kosovichev, A. G.: 1993, *Mon. Not. R. Astron. Soc.* **264**, 522, The Influence of Low-degree p-mode Frequencies on the Determination of the Structure of the Solar Interior

Gough, D. O. and McIntyre, M. E.: 1998, *Nature* **394**, 755, Inevitability of a magnetic field in the Sun's radiative interior

Gough, D. O. and Thompson, M. J.: 1988, in *IAU Symp. 123: 'Advances in Helio- and Asteroseismology'*, p. 155, Magnetic Perturbations to Stellar Oscillation Eigenfrequencies

Gough, D. O. and Thompson, M. J.: 1990, *Mon. Not. R. Astron. Soc.* **242**, 25, The

Effect of Rotation and a Buried magnetic Field on Stellar Oscillations

Gough, D. O. and Toomre, J.: 1991, *Ann.Rev.Astron.Astrophysic.* **29**, 627, Seismic Observations of the Solar Interior

Guenther, D. B. and Demarque, P.: 1996, *Solar modeling*, Available from World Wide Web: http://apwww.stmarys.ca/~guenther/solar/solar_model.html

Guenther, D. B., Demarque, P., Kim, Y. C., and Pinsonneault, M. H.: 1992, *Astrophys. J.* **387**, 372, Standard solar model

Harvey, J.: 1995, *Phys. Today* **Oct.**, 32, Helioseismology

Hathaway, D., Gilman, P., Harvey, J. W., Hill, F., Howard, R. B., Jones, H. P., Kasher, J., Leibacher, J. B., Pintar, J., and Simon, G. W.: 1996, *Science* **272**, 1306, GONG Observations of Solar Surface Flows

Hindman, B. and Zweibel, E.: 1994, *Astrophys. J.* **436**, 929, The effects of a Hot Outer Atmosphere on Acoustic-Gravity Waves

Hood, A.: 1998, *The Sun : An Introduction to MHD*, Available from World Wide Web: http://www-solar.mcs.st-andrews.ac.uk/~alan/sun_course/solar.html, Course for final year undergraduates, St Andrews University

Howe, R., Christensen-Dalsgaard, J., Hill, F., Komm, R., Larsen, R., Schou, J., Thompson, M., and Toomre, J.: 2000a, *Nature* **287**, 2456, Dynamic Variations at the Base of the Solar Convection Zone

Howe, R., Christensen-Dalsgaard, J., Hill, F., Komm, R. W., Larsen, R. M., Schou, J., Thompson, M. J., and Toomre, J.: 2000b, *Astrophys. J., Lett.* **533**, L163, Deeply Penetrating Banded Zonal Flows in the Solar Convection Zone

Howe, R., Komm, R., and Hill, F.: 1999, *Astrophys. J.* **524**, 1084, Solar Cycle Changes in GONG p-Mode Frequencies, 1995-1998

Hughes, D. W.: 1985, *Geophys. Astrophys. Fluid Dyn.* **32**, 273, Magnetic Buoyancy Instabilities for a Static Plane Layer

Hughes, D. W. and Cattaneo, F.: 1987, *Geophys. Astrophys. Fluid Dyn.* **39**, 65, A New Look at the Instability of a Stratified Horizontal Magnetic Field

Jain, R.: 1992, *Ph.D. thesis*, University of St Andrews, Scotland, The effects of magnetic fields on oscillations in the solar atmosphere

Jain, R., Hindman, B. W., and Zweibel, E. G.: 1995, in *ESA SP-376: Proc. SOHO 4 Workshop, 'Helioseismology', ed. J.T. Hoeksema, V. Domingo, B. Fleck, and B. Battrick*, pp 63–67, Changes in the Upper Turning Point due to Magnetism

Jain, R., Hindman, B. W., and Zweibel, E. G.: 1996, *Astrophys. J.* **464**, 476, The Influence of Magnetism on p-mode Surface Amplitudes

Jain, R. and Roberts, B.: 1991, *Sol. Phys.* **133**, 263, Magnetoacoustic surface waves at a single interface

Jain, R. and Roberts, B.: 1993, *Astrophys. J.* **414**, 898, Do p-mode frequency shifts suggest a hotter chromosphere at solar maximum?

Jain, R. and Roberts, B.: 1994a, *Astron. Astrophys.* **286**, 243, Effects of Non-parallel Propagation on p- and f- Modes

Jain, R. and Roberts, B.: 1994b, *Sol. Phys.* **152**, 261, Solar cycle variations in p-modes and chromospheric magnetism

Jain, R. and Roberts, B.: 1996, *Astrophys. J.* **456**, 399, Discrete High-Frequency p-Modes

Javaraiah, J. and Komm, R. W.: 1999, *Sol. Phys.* **184**, 41, Short-term periodicities of the sun's 'mean' and differential rotation

Jefferies, S. M., Osaki, Y., Shibahashi, H., Harvey, J. W., D'Silva, S., and Duvall, T. L.:

1997, *Astrophys. J., Lett.* **485**, L49, Sounding the Sun's Chromosphere

Jiménez-Reyes, S. J., Corbard, T., Pallé, P. L., Roca Cortés, T., and Tomczyk, S.: 2001, *Astron. Astrophys.* **379**, 622, Analysis of the solar cycle and core rotation using 15 years of Mark-I observations: 1984-1999. I. The solar cycle

Jiménez-Reyes, S. J., Régulo, C., Pallé, P. L., and Roca Cortés, T.: 1998, *Astron. Astrophys.* **329**, 1119, Solar activity cycle frequency shifts of low-degree p-modes

Joarder, P. S. and Narayanan, A. S.: 2000, *Astron. Astrophys.* **359**, 1211, Non-parallel propagation of hydromagnetic surface waves in the presence of steady shear-flows

Johnston, A., Roberts, B., and Wright, A. N.: 1995, in *ASP Conf. Ser. 76: GONG 1994. Helio- and Astero-Seismology from the Earth and Space*, pp 264–267, High Frequency Waves and Chromospheric Magnetism

Kahn, F. D.: 1961, *Astrophys. J.* **134**, 343, Sound Waves Trapped in the Solar Atmosphere.

Kahn, F. D.: 1962, *Astrophys. J.* **135**, 547, Sound Waves Trapped in the Solar Atmosphere. II

Keppens, R.: 1995a, *Ph.D. thesis*, Katholieke Universiteit Leuven and National Center for Atmospheric Research, Belgium, On the interaction of acoustic oscillations with magnetic flux tubes in the solar photosphere

Keppens, R.: 1995b, *Sol. Phys.* **161**, 251, Flux Tubes with a Thin Transition Layer: Scattering and Absorption Properties

Korycansky, D. G. and Pringle, J. E.: 1995, *Mon. Not. R. Astron. Soc.* **272**, 618, Axisymmetric waves in polytropic accretion discs

Kosovichev, A. G.: 1996, *Astrophys. J., Lett.* **469**, L61, Helioseismic Constraints on the Gradient of Angular Velocity at the Base of the Solar Convection Zone

Kosovichev, A. G., Schou, J., Scherrer, P. H., Bogart, R. S., Bush, R. I., Hoeksema, J. T., Aloise, J., Bacon, L., Burnette, A., DeForest, C., Giles, P. M., Leibrand, K., Nigam, R., Rubin, M., Scott, K., Williams, S. D., Basu, S., Christensen-Dalsgaard, J., Dappen, W., Rhodes, E. J., Duvall, T. L., Howe, R., Thompson, M. J., Gough, D. O., Sekii, T., Toomre, J., Tarbell, T. D., Title, A. M., Mathur, D., Morrison, M., Saba, J. L. R., Wolfson, C. J., Zayer, I., and Milford, P. N.: 1997, *Sol. Phys.* **170**, 43, Structure and Rotation of the Solar Interior: Initial Results from the MDI Medium-l Program

Kuhn, J. R.: 1988, *Astrophys. J., Lett.* **331**, L131, Helioseismological splitting measurements and the nonspherical solar temperature structure

Kumar, P. and Goldreich, P.: 1989, *Astrophys. J.* **342**, 558, Nonlinear interactions among solar acoustic modes

Lamb, H.: 1909, *Proc.Lond.Math.Soc.* **7**, 122, On the Theory of Waves Propagated Vertically in the Atmosphere

Lamb, H.: 1932, *Hydrodynamics*, University Press, Cambridge

Lang, K. R.: 1996, *Sky Telesc.* **92**, 24, Unsolved Mysteries of the Sun: Part 2

Lee, M. and Roberts, B.: 1986, *Astrophys. J.* **301**, 430, On the Behavior of Hydromagnetic Surface Waves

Leibacher, J. W., Noyes, R. W., Toomre, J., and Ulrich, R. K.: 1985, *Sci. Am.* **253**, 34, Helioseismology

Leibacher, J. W. and Stein, R. F.: 1971, *Astrophys. Lett.* **7**, 191, A New Description of the Solar Five-minute Oscillation

Leighton, R. B., Noyes, R. W., and Simon, G. W.: 1962, *Astrophys. J.* **135**, 474, Velocity Fields in the Solar Atmosphere. I. Preliminary Report

Libbrecht, K. G. and Woodard, M. F.: 1990, *Nature* **345**, 779, Solar-cycle effects on solar oscillation frequencies

Libbrecht, K. G. and Woodard, M. F.: 1991, *Science* **253**, 152, Advances in helioseismology

Libbrecht, K. G., Woodard, M. F., and Kaufman, J. M.: 1990, *Astrophys. J., Suppl. Ser.* **74**, 1129, Frequencies of solar oscillations

Lydon, T. J., Guenther, D. B., and Sofia, S.: 1996, *Astrophys. J., Lett.* **456**, L127, An Alternative Explanation for the Observed Variation of Solar p-modes with the Solar Cycle

Lydon, T. J. and Sofia, S.: 1995, *Astrophys. J., Suppl. Ser.* **101**, 357, A Method for Incorporating the Effects of Large-Scale Magnetic Fields in the Study of Stellar Structure and Variability

Marion, J. B. and Hornyak, W. F.: 1982, *Physics For Science and Engineering*, Chapt. 20 'Sound', pp 542–577, Holt-Saunders International Editions

Merzbacher, E.: 1961, *Quantum Mechanics*, J. Wiley & Sons, New York

Miles, J. A., Allen, H. R., and Roberts, B.: 1992, *Sol. Phys.* **141**, 235, Magnetoacoustic-gravity surface waves. II.Uniform Magnetic Field

Miles, J. A. and Roberts, B.: 1989, *Sol. Phys.* **119**, 257, On the Properties of Magnetoacoustic Surface Waves

Miles, J. A. and Roberts, B.: 1992, *Sol. Phys.* **141**, 205, Magnetoacoustic-Gravity Surface Waves. I.Constant Alfven Speed

Monteiro, M. J. P. F. G., Christensen-Dalsgaard, J., and Thompson, M. J.: 1994, *Astron. Astrophys.* **283**, 247, Seismic Study of Overshoot at the Base of the Solar Convective Envelope

Moore, D. W. and Spiegel, E. A.: 1964, *Astrophys. J.* **139**, 48, The Generation and Propagation of Waves in a Compressible Atmosphere

Moreno-Insertis, F. and Solanki, S. K.: 2000, *Mon. Not. R. Astron. Soc.* **313**, 411, Distribution of magnetic flux on the solar surface and low-degree p-modes

Morse, P. M. and Feshbach, H.: 1953, *Methods of theoretical physics*, International Series in Pure and Applied Physics, New York: McGraw-Hill

Murawski, K.: 2000, *Astrophys. J.* **537**, 495, Influence of Coherent and Random Flows on the Solar f-Mode

Murawski, K. and Roberts, B.: 1993a, *Astron. Astrophys.* **272**, 595, Random velocity field corrections of the f-mode. I. Horizontal flows

Murawski, K. and Roberts, B.: 1993b, *Astron. Astrophys.* **272**, 601

Musielak, Z. E., An, C.-H., Moore, R. L., and Suess, S. T.: 1989, *Astrophys. J.* **344**, 478, Propagating and Nonpropagating Compression Waves in an Isothermal Atmosphere with Uniform Horizontal Magnetic Field

Nardin, M., Perger, W. F., and Bhalla, A.: 1992, *Transactions on Mathematical Software* **18(3)**, 345, Algorithm 707, CONHYP: A Numerical Evaluator of the Confluent Hypergeometric Function for Complex Arguments of Large Magnitude - Code available from World Wide Web: http://gams.nist.gov/HotGAMS/HotGAMS.html

Newcomb, W. A.: 1961, *Phys. Fluids* **4**, 391, Convective Instability Induced by Gravity in a Plasma with a Frozen-In Magnetic Field

Nye, A. H. and Thomas, J. H.: 1974, *Sol. Phys.* **38**, 399, The nature of running penumbral waves

Nye, A. H. and Thomas, J. H.: 1976, *Astrophys. J.* **204**, 573, Solar Magneto-Atmospheric waves. I. An exact solution for a Horizontal Magnetic Field

Ogilvie, G. I. and Lubow, S. H.: 1999, *Astrophys. J.* **515**, 767, The Effect of an Isothermal Atmosphere on the Propagation of Three-dimensional Waves in a Thermally Stratified Accretion Disk

Parker, E. N.: 1955, *Astrophys. J.* **121**, 491, The Formation of Sunspots from the Solar Toroidal Field

Parker, E. N.: 1966, *Astrophys. J.* **145**, 811, The Dynamical State of the Interstellar Gas and Field

Parker, E. N.: 1967, *Astrophys. J.* **149**, 535, The Dynamical State of the Interstellar Gas and Field. III. Turbulence and Enhanced Diffusion

Parker, E. N.: 1984a, *Astrophys. J.* **286**, 666, Magnetic fields in the radiative interior of stars. I Thermal shadows and forced convection.

Parker, E. N.: 1984b, *Astrophys. J.* **286**, 677, Magnetic Fields in the Radiative Interior of Stars - Part Two - Forced Convection and the ^{7}Li Abundance

Parker, E. N.: 1987, *Astrophys. J.* **321**, 1009, The Dynamical Oscillation and Propulsion of Magnetic Fields in the Convective Zone of a Star. III. Accumulation of Heat and the Onset of the Reyleigh-Taylor Instability

Paternó, L.: 1990, in *LNP Vol. 367: Progress of Seismology of the Sun and Stars*, pp 41–44, Effects of Overshooting and Magnetic Field at the Base of the Solar Convection Zone on the 5-minute p-mode Eigenfrequencies

Pekeris, C. L.: 1938, *Astrophys. J.* **88**, 189, Nonradial Oscillations of Stars

Pekeris, C. L.: 1948, *Phys. Rev.* **73**, 145, The Propagation of a Pulse in the Atmosphere. Part II

Pérez Hernández, F. and Christensen-Dalsgaard, J.: 1998, *Mon. Not. R. Astron. Soc.* **295**, 344, The phase function for stellar acoustic oscillations

Pidatella, R. M. and Stix, M.: 1986, *Astron. Astrophys.* **157**, 338, Convective overshoot at the base of the sun's convection zone

Pijpers, F. P.: 2001, in T. Montmerle and P. André (eds.), *ASP Conf. Ser. 243: From darkness to light: origin and evolution of young stellar clusters*, MONS: a Danish satellite project for asteroseismology

Pintér, B.: 1999, *Ph.D. thesis*, Katholieke Universiteit Leuven, Belgium, The Influence of the Atmospheric Magnetic Field on Solar Oscillation Modes

Pintér, B., Čadež , V. M., and Roberts, B.: 1999, *Astron. Astrophys.* **346**, 190, Waves and instabilities in a stratified isothermal atmosphere with constant Alfvén speed - revisited

Pintér, B. and Goossens, M.: 1999, *Astron. Astrophys.* **347**, 321, Oscillations in a magnetic Solar Model. I.Parallel propagation in a chromospheric and coronal magnetic field with constant Alfvén speed

Price, G. H.: 1996, *Astrophys. J.* **458**, 850, On the High-Frequency Behavior of Acoustic Waves within the Sun

Price, G. H.: 2001, in *ESA SP-464: Proc. SOHO 10/GONG 2000 Workshop, 'Helio- and Asteroseismology at the Dawn of the Millenium'*, pp 231–234, Impact of near-surface solar structure on acoustic wave reflection

Priest, E. R.: 1982, *Solar Magnetohydrodynamics*, D. Reidel Public. Co.

Rae, I. C. and Roberts, B.: 1983, *Phys. Fluids* **26**, 269, Long Wave Dispersion Relations for Surface Waves in a Magnetically Structured Atmosphere

Rhodes, E. J., J., Cacciani, A., Korzennik, S. G., and Ulrich, R. K.: 1993, *Astrophys. J.* **406**, 714, Confirmation of solar cycle-dependent intermediate-degree p-mode frequency shifts

Richard, O., Vauclair, S., Charbonnel, C., and Dziembowski, W. A.: 1996, *Astron. Astrophys.* **312**, 1000, New Solar Models including Helioseismological Constraints and Light-element Depletion

Robe, H.: 1968, *Annales d'Astrophysique* **31**, 475, Les oscillations non radiales des polytropes

Roberts, B.: 1981a, *Sol. Phys.* **69**, 27, Wave Propagation in a Magnetically Structured Atmosphere. I: Surface Waves at a Magnetic Interface

Roberts, B.: 1981b, *Sol. Phys.* **69**, 39, Wave Propagation in a Magnetically Structured Atmosphere. II: Waves in a Magnetic Slab

Roberts, B.: 2001, in P. Murdin (ed.), *Encyclopedia of Astronomy and Astrophysics*, Institute of Physics Publishing (Bristol and Philadelphia) and Nature Publishing Group (London, New York and Tokyo), Solar Interior: helioseismology, influence of Magnetic Fields

Roberts, B. and Campbell, W. R.: 1986, *Nature* **323**, 603, Magnetic Field Corrections to Solar Oscillation Frequencies

Roberts, B. and Webb, A. R.: 1978, *Sol. Phys.* **56**, 5, Vertical Motions in an Intense Magnetic Flux Tube

Ronan, R. S., Kadora, K., and LaBonte, B. J.: 1994, *Sol. Phys.* **150**, 389, Solar Cycle Changes in the High Frequency Spectrum

Rosenthal, C. S. and Gough, D. O.: 1994, *Astrophys. J.* **423**, 488, The Solar f-mode as an Interfacial Mode at the Chromosphere-Corona Transition

Rossing, T. D.: 1992, *Phys. Today* pp 40–47, The Acoustics of Drums

Ruediger, G. and Brandenburg, A.: 1995, *Astron. Astrophys.* **296**, 557, A solar dynamo in the overshoot layer: cycle period and butterfly diagram

Schmitt, J. H. M. M., Rosner, R., and Bohn, H. U.: 1984, *Astron. Astrophys.* **282**, 316, The overshoot region at the bottom of the solar convection zone

Schou, J., Antia, H. M., Basu, S., Bogart, R. S., Bush, R. I., Chitre, S. M., Christensen-Dalsgaard, J., di Mauro, M. P., Dziembowski, W. A., Eff-Darwich, A., Gough, D. O., Haber, D. A., Hoeksema, J. T., Howe, R., Korzennik, S. G., Kosovichev, A. G., Larsen, R. M., Pijpers, F. P., Scherrer, P. H., Sekii, T., Tarbell, T. D., Title, A. M., Thompson, M. J., and Toomre, J.: 1998, *Astrophys. J.* **505**, 390, Helioseismic Studies of Differential Rotation in the Solar Envelope by the Solar Oscillations Investigation Using the Michelson Doppler Imager

Schrijver, C. J. and Title, A. M.: 1999, *Sol. Phys.* **188**, 331, Active regions losing their moorings by subsurface reconnection

Schubert, G.: 1968, *Astrophys. J.* **151**, 1099, The Stability of Toroidal Magnetic Fields in Stellar Interiors

Schüssler, M., Caligari, P., Ferriz-Mas, A., and Moreno-Insertis, F.: 1994, *Astron. Astrophys.* **281**, L69, Instability and Eruption of Magnetic Flux Tubes in the Solar Convection Zone

Schwarzschild, M.: 1958, *Structure and evolution of the stars*, Princeton University Press

Scott, B. D.: 1994, *An Introduction to MHD, or Magnetic Fluid Dynamics*, Available from World Wide Web: http://www.rzg.mpg.de/~bds/lectures/mhd-lecture.html, Summer University for Plasma Physics at the Max-Planck-Institut für Plasmaphysik

Scuflaire, R.: 1974, *Astron. Astrophys.* **36**, 107, The Non Radial Oscillations of Condensed Polytropes

Seaborn, J. B.: 1991, *Hypergeometric Functions and Their Applications*, Texts in

applied mathematics, Springer-Verlag
Singh, A. P. and Talwar, S. P.: 1993, *Sol. Phys.* **148**, 27, Waves in a magnetically structured slab configuration
Skaley, D. and Stix, M.: 1991, *Astron. Astrophys.* **241**, 227, The overshoot layer at the base of the solar convection zone
Slater, J. L.: 1960, *Confluent Hypergeometric Functions*, Cambridge University Press
Slater, J. L.: 1965, in M. Abramovitz and I. Stegun (eds.), *Handbook of Mathematical Functions*, Chapt. XIII, p. 503, National Bureau of Standards, Washington, D.C., Confluent Hypergeometric Functions
Smeyers, P., Vansimpsen, T., de Boeck, I., and van Hoolst, T.: 1996, *Astron. Astrophys.* **307**, 105, Asymptotic representation of high-frequency, low-degree p-modes in stars and in the Sun.
Somasundaram, K. and Uberoi, C.: 1982, *Sol. Phys.* **81**, 19, Compressibility effects on hydromagnetic surface waves
Spiegel, E. A. and Unno, W.: 1962, *Publ. Astron. Soc. Jpn.* **14**, 28, On Convective Growth-rates in a Polytropic Atmosphere
Spiegel, E. A. and Weiss, N.: 1980, *Nature* **287**, 616, Magnetic Activity and Variations in Solar Luminosity
Spiegel, E. A. and Zahn, J.-P.: 1992, *Astron. Astrophys.* **265**, 106, The Solar Tachocline
Spruit, H. C.: 1974, *Sol. Phys.* **34**, 277, A Model of the Solar Convection Zone
Steffens, S. and Schmitz, F.: 2000, *Astron. Astrophys.* **354**, 280, The influence of the solar atmospheric stratification on the form of p-mode ridges
Stein, R. F. and Leibacher, J.: 1974, *Ann. Rev. Astron. Astrophys.* **12**, 407, Waves in the Solar Atmosphere
Stix, M. and Kiefer, M.: 1997, in *SCORe'96 : Solar Convection and Oscillations and their Relationship*, pp 69–72, Solar models with convective overshoot
Swisdak, M. M. I.: 1999, *Ph.D. thesis*, University of Colorado, Boulder, U.S., The Effects of Large-Scale Convection on Solar Eigenfrequencies
Swisdak, M. M. I. and Zweibel, E. G.: 1999, *Astrophys. J.* **512**, 442, Effects of Large-Scale Convection on p-mode Frequencies
Thomas, J. H.: 1983, *Ann.Rev.Fluid.Mech.* **15**, 321, Magneto-atmospheric waves
Thomas, J. H. and Nye, A. H.: 1975, *Phys. Fluids* **18**, 490, Convective instability in the presence of a non-uniform horizontal magnetic field
Thompson, M. J., Toomre, J., Anderson, E., Antia, H. M., Berthomieu, G., Burtonclay, D., Chitre, S. M., Christensen-Dalsgaard, J., Corbard, T., Derosa, M., Genovese, C. R., Gough, D. O., Haber, D. A., Harvey, J. W., Hill, F., Howe, R., Korzennik, S. G., Kosovichev, A. G., Leibacher, J. W., Pijpers, F. P., Provost, J., Rhodes, E. J., Schou, J., Sekii, T., Stark, P. B., and Wilson, P.: 1996, *Science* **272**, 1300, Differential Rotation and Dynamics of the Solar Interior
Tirry, W. J.: 1998, *Ph.D. thesis*, Katholieke Universiteit Leuven, Belgium, MHD quasi-modes and their role in MHD wave heating of solar coronal magnetic structures
Ulrich, R. K.: 1970, *Astrophys. J.* **162**, 993, The Five-minute Oscillations on the Solar Surface
Unno, W., Osaki, Y., Ando, Saio, and Shibahashi: 1989, *Nonradial Oscillations of Stars*, University of Tokyo Press
van Ballegooijen, A. A.: 1982, *Astron. Astrophys.* **113**, 99, The Overshoot Layer at the Base of the Solar Convective Zone and the Problem of Magnetic Flux Storage
Van der Linden, R. A. M.: 2001, private communication

Vanlommel, P.: 2001, *Ph.D. thesis*, Katholieke Universiteit Leuven, Belgium, Effects of the solar atmosphere and sub-photospheric flows on global solar oscillation modes
Vanlommel, P. and Goossens, M.: 1999, *Sol. Phys.* **187**, 357, Influence of a chromospheric magnetic field on solar acoustic modes
Vanlommel, P. and Čadež, V. M.: 2000, *Sol. Phys.* **196**, 227, Solar p- and g-modes in a model with a convection layer above a sub-adiabatic interior
Vorontsov, S. V.: 1988, in *IAU Symp. 123: 'Advances in Helio- and Asteroseismology'*, p. 151, A Search of the Effects of Magnetic Field in the Solar 5-minute Oscillations
Wentzel, D. G.: 1979, *Astrophys. J.* **227**, 319, Hydromagnetic surface waves
Woodard, M. F., Kuhn, J. R., Murray, N., and Libbrecht, K. G.: 1991, *Astrophys. J., Lett.* **373**, L81, Short-term changes in solar oscillation frequencies and solar activity
Woodard, M. F. and Noyes, R. W.: 1985, *Nature* **318**, 449, Change of Solar Oscillation Eigenfrequencies with the Solar Cycle
Wright, A. N. and Thompson, M. J.: 1992, *Astron. Astrophys.* **264**, 701, On the effects of chromospheric magnetic perturbations on solar oscillation frequencies
Yu, C. P.: 1965, *Phys. Fluids* **8**, 650, Magneto-Atmospheric Waves in a Horizontally Stratified Conducting Medium
Yu, C. P.: 1966, *Phys. Fluids* **9**, 412, Convective Stability in a Plasma with Horizontal Magnetic Fields
Zahn, J.-P.: 1992, *Astron. Astrophys.* **265**, 115, Circulation and turbulence in rotating stars
Zhao, J., Kosovichev, A. G., and Duvall, T. L.: 2001, *Astrophys. J.* **557**, 384, Investigation of Mass Flows beneath a Sunspot by Time-Distance Helioseismology
Zhukov, V. I.: 1997, *Astron. Astrophys.* **322**, 302, Resonant Absorption and the Spectrum of 5-min Oscillations of the Sun
Zhukov, V. I.: 2001, *Astron. Astrophys.* **369**, 672, Resonant absorption and the spectrum of 5-min oscillations of the Sun. III. Influence of inhomogeneity of the canopy magnetic field on fine structure
Zweibel, E. G. and Bogdan, T. J.: 1986, *Astrophys. J.* **308**, 401, Effects of fibril magnetic fields on solar p-modes. II - Calculation of mode frequency shifts